STOCHASTIC DYNAMICS IN SOFT MATTER
Non-uniform activity and fluctuating fields

Candidate:
Pietro Luigi Muzzeddu

Advisors:
Andrea Gambassi
Édgar Roldán

A thesis submitted to
Scuola Internazionale Superiore di Studi Avanzati
Physics Area - Physics and Chemistry of Biological Systems
for the degree of Philosopiae Doctor (Ph.D.)

Academic Year 2023-2024

SISSA

Abstract

In this thesis we investigate the stochastic dynamics of particles in contact with active environments or fluctuating correlated media at equilibrium, offering a comprehensive analysis that encompasses both equilibrium and non-equilibrium systems. In the first part, we focus on assemblies of active particles subject to a spatially varying degree of activity. We demonstrate that the interplay between the inter-particle interactions and a non-homogeneous activity leads to unexpected migration properties. In particular, we show that interacting active particles can be directed and localized within specific spatial regions, and we highlight potential applications in the design of autonomous systems able to migrate towards specific target zones. In the second part of the thesis we analyze the equilibrium behavior of particles moving within a fluctuating medium that acquires significant spatio-temporal correlations. Specifically, we first study the extent to which the field-induced forces caused by a fluctuating correlated medium affect the conformational and the dynamical properties of a polymer chain. Secondly, we investigate the self-diffusion coefficient of an odd-diffusive tracer, whose dynamics is characterized by probability fluxes perpendicular to the density gradient, coupled to a Gaussian-core fluid, showing that it can be enhanced by the interaction with the medium. By combining these studies, the thesis advances our understanding of the behavior of particles in correlated and active media, offering new insights into the transport properties and collective behaviors of collodal systems.

Contents

Abstract **2**

1 Introduction **6**

List of publications **6**

2 Theoretical background **12**

2.1 Langevin equation 12
2.2 Stochastic calculus 13
2.2.1 Itô Lemma 15
2.3 Fokker-Planck Equation 16
2.4 Brownian motion 18
2.5 Rotational diffusion 19
2.6 The Ornstein-Uhlenbeck process 22
2.7 Rouse polymer 24
2.8 The Gaussian field 27
2.9 Dean-Kawasaki Equation 29
2.10 Odd diffusion 32

3 Active chiral molecules in activity gradients **36**

3.1 Interacting Active Chiral Particles 38
3.2 Multipole expansion and effective dynamics 40
3.3 Stationary density 42
3.4 Odd-diffusive active particles 47
3.5 Dimer of active magnetic particles 48
3.6 Conclusions 49

4 Taxis of cargo-carrying microswimmers in travelling activity waves **51**

4.1 The model 52
4.2 Transport properties for slow activity waves 54
4.2.1 Stationary density 56
4.2.2 Drift velocity 58

4.3 Transport properties for fast activity waves 60
4.4 Discussion 62

5 Migration and separation of polymers in non-uniform active baths 64
5.1 The model 65
5.2 Effective dynamics 67
5.3 Stationary distribution 69
5.4 Polymer separation 72
5.5 Discussion 72

6 Rouse polymer in a fluctuating correlated medium 74
6.1 The model 75
6.2 Field-induced interactions 80
6.3 Relaxation toward equilibrium 81
  6.3.1 Effective dynamics of the polymer 81
  6.3.2 Linearized dynamics of the polymer 83
  6.3.3 Long-time relaxation of the center of mass 86
6.4 Typical polymer size 88
  6.4.1 Weak-coupling approximation 89
  6.4.2 Typical size in the absence of external forces 91
  6.4.3 Force-extension curve 93
6.5 Conclusions 95

7 Odd tracer dynamics in soft-core media 97
7.1 Introduction 97
7.2 The model 99
7.3 Self-diffusion of the odd tracer 103
  7.3.1 Weak-coupling approximation 104
  7.3.2 Gaussian-core model 105
7.4 Conclusions 110

8 Conclusions and outlook 112

A Appendix of Chapter 3 115
A.1 Dimer of active chiral particles 115
  A.1.1 Case of rigid bond 122
A.2 Single active chiral particle 124
A.3 Active particle under Lorentz force 125
A.4 Active dimer under Lorentz force 127

B Appendix of Chapter 4 132
B.1 Mode equations 132

B.2 Slow active traveling waves 136
B.3 Drift velocity with critical cargo 139
B.4 Fast active traveling waves 140
B.5 Simulation details 145

C Appendix of Chapter 5 146
C.1 Moment expansion 146
C.2 Small gradient approximation 151
C.3 Excluded volume and finite extensibility 156
C.4 Non-equilibrium separation 158
C.5 Numerical simulations 160

D Appendix of Chapter 6 161
D.1 Asymptotic analysis of the memory kernel 161
D.2 Asymptotic analysis of the center-of-mass 164
D.3 Perturbative correction to the gyration radius 166
D.4 Details of the numerical simulation 167

E Appendix of Chapter 7 169
E.1 Velocity marginalization 169
E.2 The interaction-free case 170
  E.2.1 Free dynamics of the odd tracer 170
  E.2.2 Free dynamics of the density field 171
E.3 Weak-coupling approximation 172
E.4 Simulation details 175
  E.4.1 Brownian dynamics simulations 175
  E.4.2 MSD numerical evaluation 177

Acknowledgements 180

List of publications

The results presented in this thesis are reported in the following articles and preprints:

(i) **Pietro Luigi Muzzeddu**, Hidde Derk Vuijk, Hartmut Löwen, Jens-Uwe Sommer, Abhinav Sharma,
Active chiral molecules in activity gradients,
J. Chem. Phys. **157**, 134902 (2022) - published 07 October 2022;

(ii) **Pietro Luigi Muzzeddu**, Édgar Roldán , Andrea Gambassi, Abhinav Sharma,
Taxis of cargo-carrying microswimmers in traveling activity waves,
EPL **142** 67001 (2023) - published 6 June 2023

(iii) **Pietro Luigi Muzzeddu**, Andrea Gambassi, Jens-Uwe Sommer, Abhinav Sharma,
Migration and separation of polymers in non-uniform active baths
Phys. Rev. Lett. **133**, 118102 (2024) - published 11 September 2024;

(iv) **Pietro Luigi Muzzeddu**, Davide Venturelli, Andrea Gambassi,
Rouse polymer in a fluctuating correlated medium
To be submitted

(v) **Pietro Luigi Muzzeddu***, Erik Kalz*, Andrea Gambassi, Abhinav Sharma, Ralf Metzler,
Odd tracer dynamics in soft-core media
To be submitted (* these two authors contributed equally)

Chapter 1

Introduction

The presence of stochasticity (randomness) pervades the most diverse branches of modern scientific fields, from natural to social sciences and economy. In physics, the intent to formalize the motion of a body subject to random forces were stimulated by experimental observations dating back to the nineteenth century. In particular, in 1828, the botanist Robert Brown noticed the tendency of granular particles present inside pollen grains to be in constant erratic motion once dissolved in water [1, 2]. The nature of this motion, essentially unpredictable and irregular, persisted even after the death of the plants, indicating that it was not necessarily associated to animated or living entities. Surprisingly, nearly 80 years passed before Brownian motion was rigorously theorized. It was first Albert Einstein in 1905 [3], and Marian Smoluchowski shortly after [4, 5], who placed it within a physical-mathematical framework, establishing a connection with the molecular-kinetic theory of heat and the theory of diffusion. Equally important was the alternative theory of Brownian motion proposed by the French physicist Paul Langevin [6]. His approach, which led to the same results as Einstein's theory but through a rather different method, was described by the author himself as "une démonstration infiniment plus simple". Specifically, Langevin's theory was the first to incorporate a stochastic element in the equation of motion of a colloidal particle suspended in a fluid. This theory spurred further experiments to verify Einstein's theoretical predictions on the mean squared displacement of a particle in a fluid. Once acquainted with the theory, it was the French physicist Jean Baptiste Perrin to "apply to it the test of experiment" [2, 7].

The problem of finding an effective description for the dynamics of a specific tagged particle (commonly referred to as the *tracer*) in a fluid has attracted significant interest within the statistical mechanics community. Indeed, this requires modeling systems composed by a large number of variables (degrees of freedom) describing interacting agents, in order to study phenomena emerging from such interactions. However, in a complex system like a fluid, the idea of accurately tracking the evolution of each individual degree of freedom is unrealistic, and experimental constraints typically limit the analysis to a restricted set of variables. For example, let us consider a colloidal particle, the typical size of which is within the range $0.1 - 10\,\mu m$, dispersed in a simple fluid such as water. Its motion is strongly affected by repeated collisions with the surrounding fluid molecules in the *bath*, whose exact positions, momenta and internal structures are generally inaccessible. Fortunately, this level of detail is often not needed to accurately describe the dynamics of the colloid, and one can rely on an effective mesoscopic description that ignores the microscopic details of the underlying fluid medium. Such a *coarse-graining* procedure allows one to replace all the microscopic forces acting on the colloid with a single random variable, leading to an effective stochastic equation of motion for the particle. Assuming that the solvent molecules are initially distributed according to a certain statistical distribution, e.g., the canonical one if the fluid medium is at equilibrium, it is intuitive to expect that this initial distribution will impact the statistical properties of the resulting stochastic description [8]. In many cases, the size difference between the tracer and the solvent molecules spans several orders of magnitude, and their motions occur on very different time scales. This separation of time and length scales often allows for a simplified description of the tracer dynamics, in which the possible memory due to its interaction with the fluid can be neglected. In this cases, the stochastic motion of the tracer is described by a *Markovian* process, i.e., its evolution only depends on its current state and it is not affected by its past history. Under this condition, the random interaction of the colloid with the bath can be modeled by a Gaussian (by virtue of the central limit theorem [9]) white noise. In other words, the stochastic forces acting on the tracer are not correlated in time. For this reason, the Langevin dynamics first proposed in Ref. [6], though minimal in the way it describes the motion of a tracer in a fluid at equilibrium, has a widespread application in the field of soft matter.

Based on the simplest stochastic description of Brownian motion, more sophisticated models have been subsequently developed in an attempt to overcome its limitations and to relax some of its underlying assumptions. Notably, some of these extensions use effective stochastic dynamics to describe non-equilibrium situations. They include relaxation processes toward stationary states, systems maintained out of equilibrium by fixed boundary conditions, and more recently, systems within the realm of *active matter* [10]. Active matter refers to all those physical systems driven out of equilibrium by local energy injections occurring at the level of individual agents, which are able to convert the energy stored in the environment into mechanical work and directed motion. Besides several examples of living active systems, such as bacteria or molecular motors [11, 12], many artificial active systems can now be synthesized in the lab [13, 14], with precise characteristics which are well-suited for specific applications. For example, considerable effort has been dedicated to artificially mimick the self-propulsion capabilities of some biological systems such as bacteria, sperm, algae, and fungi [15–18]. This has been achieved with the synthesis of the so-called Janus particles, a type of colloidal particle characterized by the violation of rotational symmetry, which they use to generate directed motion when subjected to specific energy inputs. The propulsion methods are diverse and include, for instance, self-diffusiophoresis via catalytic reactions [19–22] and light-induced self-thermophoresis [23]. Due to their versatility, simplicity, and potential in various fields such as healthcare and sustainability, phoretic active colloids are considered a paradigmatic example of synthetic active matter.

Due to their typical time and length scales, the motion of synthetic self-propelled particles can be analyzed with mesoscopic stochastic dynamics. From a modeling perspective, the self-propulsion is introduced in the form of an additional force along an orientation vector that evolves over time and represents the particle polarity related to its anisotropy. Depending on the stochastic process that regulates the evolution of this polarity, various models have been introduced, among which the most famous are the active Brownian particle, run-and-tumble particle, and active Ornstein-Uhlenbeck particle [24–28]. In all these cases, the decorrelation of the active forces occurs on a typical time scale known as the *persistence time*, as it denotes the characteristic time required for the particle's polarity to reorient. From the perspective of the particle motion, this active force can be interpreted as an additional source of colored noise, as it exhibits temporal correlations on a time scale given by the persistence time. The energy input that comes from the active force violates the detailed balance condition, thus driving the system out of equilibrium. In other words, compared to the case of a Brownian particle in a thermal bath at equilibrium, the dynamics of an active particle is characterized by a broken time-reversal symmetry, meaning that a particular stochastic trajectory and its time-reversed do not have the same probability to occur. This concept can be quantified by calculating the entropy production rate or other appropriate measures of time irreversibility [29, 30]. A rich variety of fascinating phenomena and collective behaviors, forbidden at thermodynamic equilibrium, can emerge when multiple self-propelled particles interact with each other. For instance, an ensemble of repulsively interacting active particles can undergo liquid-gas phase separation through a mechanism now widely studied and known as motility-induced phase separation (MIPS) [10, 31–33]. It should be noted that a liquid-gas phase separation at equilibrium requires the presence of (real or effective) attractive forces, and therefore the transition mentioned above has a purely non-equilibrium nature. Moreover, it has been shown that self-phoretic active particles can exhibit pronounced dynamic clustering in dilute conditions (see, e.g., Refs. [22, 34–36]).

Another extremely interesting aspect concerns the behavior of self-propelled particles in a medium characterized by a spatially varying activity. For example, in living microswimmers such as bacteria, amoebae or sperm cells, this can be due to a non-uniform concentration of chemoattractants dispersed in the environment [37–39], or in the case of synthetic photokinetic Janus particles, to a non-uniform distribution of light intensity [40, 41]. In living organisms such as *E. coli*, the response to a non-uniform concentration of various chemicals is quite elaborate [42] and is due to the presence of chemoreceptors on their body's surface [43]. These receptors allow *E. coli* to make temporal comparisons of the local concentration of attractants in the environment and to modulate their tumbling rate accordingly [44–46]. This modulation of the rate of random reorientation in response to external stimuli, which in the case of *E. coli* is based on a sophisticated ability to process information from the surrounding environment, is known as klinokinesis [47], and it enables *E. coli* to bias its motion towards regions with higher concentrations of attractants. This phenomenon is called *chemotaxis*. An alternative mechanism present in biology, which involves varying the speed of movement in response to external stimuli rather than changing the reorientation rate, is known as orthokinesis [48, 49]. It is natural to ask whether the observed migration of living microswimmers immersed in spatially heterogeneous environments can be reproduced with simpler inanimated objects, and whether these properties can be harnessed to create functional synthetic colloidal structures the motion of which can be controlled and directed using external stimuli.

A first careful theoretical investigation of run-and-tumble particles reported that in presence of a spatially varying self-propulsion force, these particles accumulate in those regions of the surrounding fluid medium where their motion is slower [50]. In the first part of this thesis, we show that this behavior can change significantly when the active particles are put in interaction with each other. Specifically, we examine the case in which the magnitude of the active self-propulsion force, and thus the swim speed of the active particles, vary in space. This setting is analogous to the aforementioned orthokinetic mechanism. We explore various scenarios in which assemblies of colloidal particles turn out to feature a variety of migration properties and of responses to the activity field, depending on the parameters which define their characteristics. In particular, it may happen that these colloidal complexes preferentially localize within specific spatial regions. After the introductory Chapter 2, which summarizes the theoretical background and the tools extensively used in the rest of the thesis, the first part of the presentation is organized as follows:

- In Chapter 3 we study the behavior of two interacting active particles characterized by a certain chirality. This means that the evolution of the polarities of the two colloids is determined by the combination of a stochastic component, related to rotational diffusion, and a deterministic component that models an active torque. The relative importance of these two effects determines the response of the active dimer to a non-homogeneous activity field, establishing its preferential localization in regions of high or low activity. The analysis is extended to the case in which the circular dynamics of the two active particles is induced by the Lorentz force resulting from the application of a magnetic field.

- In Chapter 4 we investigate the possibility of using a self-propelled colloid as a carrier for a passive cargo. We show that the motion of this dimer can be directed by external tactical signals in the form of travelling waves of activity. In particular, the resulting transport significantly depends on the relative size of the two particles and on the propagation velocity of the external stimulus compared to the swim speed of the active colloid. The emergent phenomenology suggests the use of active colloids as potential micrometric vehicles within a fluid.
- In Chapter 5 we examine the behavior of a polymer chain immersed in a non-uniform active bath, which contains self-propelled agents. These agents exert temporally correlated active forces on the polymer, altering its configurational and transport properties. We show that the preferential spatial localization of the polymer within the active bath changes according to its degree of polymerization (i.e., to the number of monomers) and to its connectivity (the structure of its internal interactions). This implies that non-uniform activity fields could be used in order to separate different polymeric species on the basis of their length and/or architecture.

While in the first part of the thesis we characterize the migration properties of interacting active particles in a non-uniform activity field that does not fluctuate and is not affected by the active particles, in the second part we consider the case where the particles are at equilibrium, but the fluctuating medium in which they move is characterized by significant spatio-temporal correlations, as in the case of real fluids. In this case, we relax some assumptions that usually allow the description of the motion of a particle in terms of Brownian motion and we include, from a modeling perspective, some features that characterize more realistic solvents. Specifically, we consider a medium whose relaxation is not instantaneous but potentially occurs on timescales comparable to or longer than those typical of the colloid dynamics. This aspect has already been extensively analyzed in the past and has led to the introduction of the generalized Langevin equation (GLE) [51, 52], an extension of the Langevin dynamics in which the coupling between the tracer and the surrounding fluid is described by means of a friction memory kernel. This type of equation has been used, for example, to characterize the viscoelastic properties of complex fluids such as colloidal dispersions and polymer or self-assembled surfactant solutions [53], by probing the motion of a tracer particle immersed in these fluids. As a second requirement, we want our description to take into account the spatial structure of the fluid, which is inevitably influenced by the presence of the tracer itself. In other words, while ignoring hydrodynamic effects, we introduce spatio-temporal correlations of the fluid into our model. This aspect is essential whenever considering the dynamics of particles dispersed in near-critical fluids characterized by fluctuations of the relevant order parameter over large length scales and by the phenomenon of critical slowing down [54]. An example is given by colloidal particles in a near-critical binary liquid mixture [55, 56]. In this case, it is known that such particles are subject to fluctuation-induced forces [57–59], which can be considered as the thermodynamic analogue of the critical Casimir forces in electrodynamics [60]. In order to describe the dynamics of a tracer (whether a single particle or a collection of interacting sub-units forming a more complex structure) in a correlated medium, we couple its equation of motion to a thermally fluctuating order parameter, described by a scalar field. The latter evolves stochastically and accounts for the spatio-temporal correlations of the fluid. This approach has been frequently used in the last years to characterize the transport properties and the stochastic thermodynamics of colloidal systems in complex fluids [61–71]. In the second part of this thesis, we apply this field-theoretic approach to the following two problems:

- In Chapter 6 we examine the configurational and dynamical properties of a polymer chain dispersed in a correlated medium described by a thermally fluctuating scalar field. We specifically focus on the effect of the field-mediated forces on the typical size of the polymer, and analyze how this changes as a function of the distance of the field from the critical point. Additionally, we investigate the extent to which the fluctuating field affects the relaxation of the internal structure of the polymer and of its center of mass when initially displaced from the resting position of a confining potential. Lastly, we explore how the correlated medium alters the response of a polymer to a stretching force.
- In Chapter 7 we analyze the self-diffusion coefficient of an odd-diffusive tracer particle (which moves, e.g., under the action of the Lorentz force generated by a magnetic field) immersed in a medium which is modeled by a Gaussian core model fluid. Following Refs. [72, 73], we derive a field-theoretic description of the fluid starting from the microscopic dynamics of its constituents. Upon increasing the magnetic field, we reveal a transition from a regime where the self-diffusion of the tracer is suppressed compared to the interaction-free case (as expected in a crowded environment) to one where it is enhanced, meaning the tracer uses the collisions with the fluid particles to speed up its dynamics.

Each Chapter of the thesis is accompanied by an Appendix containing the detailed derivations of the presented results. Some future perspectives and open problems related to the content of this thesis are summarized in Chapter 8.

Chapter 2

Theoretical background

In this Chapter we present the mathematical tools and the stochastic models that will be extensively used in the rest of the thesis.

2.1 Langevin equation

Let us consider the evolution in d spatial dimensions of a single particle coupled to a thermal bath with temperature T. According to the Langevin theory of Brownian motion [6] mentioned in the Introduction, the motion of such a particle is governed by the following stochastic differential equation:

$$m\ddot{\boldsymbol{X}} = -\nu^{-1}\dot{\boldsymbol{X}}(t) + \boldsymbol{F}(\boldsymbol{X}(t), t) + \nu^{-1}\boldsymbol{\xi}(t)\,, \tag{2.1}$$

where $\boldsymbol{X}(t)$ denotes the position of the particle at time t, m its mass and ν the mobility coefficient (i.e., the inverse friction). This equation expresses the variation of the particle momentum on the left hand side as the sum of all the forces acting on the particle. In particular, the term $-\nu^{-1}\dot{\boldsymbol{X}}$ is the friction force proportional to the velocity of the particle, and it represents the average effect of its interaction with the fluid. The force $\boldsymbol{F}(\boldsymbol{X}(t), t)$ consists of a contribution deriving from a potential $\mathcal{U}(\boldsymbol{x})$ and of an external non-conservative force $\boldsymbol{F}_{\mathrm{nc}}(\boldsymbol{x}, t)$ that may drive the system out of equilibrium, namely:

$$\boldsymbol{F}(\boldsymbol{X}(t), t) = -\nabla\mathcal{U}(\boldsymbol{X}(t)) + \boldsymbol{F}_{\mathrm{nc}}(\boldsymbol{X}(t), t)\,. \tag{2.2}$$

Moreover, due to its coupling with the thermal bath, the particle experiences a fluctuating stochastic force $\nu^{-1}\boldsymbol{\xi}(t)$ that describes its random collisions with all the solvent molecules. In a first approximation, these random forces can be considered as statistically uncorrelated, and by virtue of the central limit theorem one can assume that they have a Gaussian distribution. Hence, to completely characterize the Gaussian white noise $\boldsymbol{\xi}(t)$, it is sufficient to provide its first two moments:

$$\begin{aligned}\langle \xi^\alpha(t)\rangle &= 0\,,\\ \langle \xi^\alpha(t)\xi^\beta(s)\rangle &= 2T\nu\delta_{\alpha\beta}\delta(t-s)\,,\end{aligned} \tag{2.3}$$

where the Greek letter $\alpha \in \{1, ..., d\}$ is used to denote the α-component of the noise vector. The amplitude of the noise $\boldsymbol{\xi}$ is proportional to the temperature T of the thermal bath and to the particle mobility ν, so that fluctuations and dissipation are related by the Einstein relation [3]. Note that in Eq. (2.3) as in the rest of this thesis, we work in units where the Boltzmann constant k_B is set equal to 1. In the vast majority of soft matter systems, viscous forces dominate over inertial effects (such that the l.h.s. of Eq. (2.1) is negligible compared to the r.h.s., which can be effectively set to zero), and the Langevin equation (2.1) can be rewritten in its simpler overdamped form as:

$$\dot{\boldsymbol{X}}(t) = \nu \boldsymbol{F}(\boldsymbol{X}(t), t) + \boldsymbol{\xi}(t)\,. \tag{2.4}$$

This form of the Langevin dynamics is very useful when one is interested in phenomena occurring at time scales much longer than the typical relaxation time $m\nu$ of the velocity, as in most cases considered in this thesis. Although it does not directly affect the stochastic dynamics (2.4), there is another important aspect about stochastic differential equations that deserve a thorough clarification. This concerns the formal definition of stochastic integration and the stochastic calculus with which an evolution equation such as Eq. (2.4) has to be interpreted.

2.2 Stochastic calculus

To explain the problem, let us focus on a 1-dimensional stochastic differential equation (SDE) of the form:

$$\dot{X} = a(X(t), t) + b(X(t), t)\xi(t)\,, \tag{2.5}$$

where $\xi(t)$ indicates a zero-mean white Gaussian noise with unit variance, and the generic functions $a(X(t), t)$ and $b(X(t), t)$ control the deterministic and the stochastic contribution to the evolution of the coordinate X, respectively. Note that the main difference compared to Eq. (2.4) is that the amplitude of the noise now depends on the random variable $X(t)$ itself. This type of noise is known as *multiplicative noise*, as opposed to the *additive noise* that characterizes, e.g., Eq. (2.4), where the noise amplitude does not depend on the position of the particle. The formal solution of (2.5) can be easily obtained and reads:

$$X(t) = X(0) + \int_0^t \mathrm{d}s\, a(X(s), s) + \int_0^t \mathrm{d}s\, b(X(s), s)\xi(s)\,. \tag{2.6}$$

Upon introducing the quantity

$$W(t) = \int_0^t \mathrm{d}s\, \xi(s)\,, \tag{2.7}$$

the integral of the noise term, which we refer to as I, can be more conveniently expressed as:

$$I \equiv \int_0^t \mathrm{d}s\, b(X(s), s)\xi(s) = \int_0^t b(X(s), s)\mathrm{d}W(s)\,, \tag{2.8}$$

which is a sort of stochastic Stieltjes integral with a sample function $W(t)$ [9]. The formal definition of this type of integral represents the fundamental aspect from which all the stochastic calculi originate, as briefly shown in the following. As a first step, we note that $W(t)$ is the so-called Wiener process. In particular it is an almost surely continuous Markovian process for all times $t > 0$, characterized by stationary and independent increments. In other words, the quantity $W(t + \Delta t) - W(t)$ is independent of all previous values $W(s)$, with $s < t$. Furthermore, the increments $W(t+\Delta t) - W(t)$ are distributed according to a zero-mean normal distribution with variance Δt, i.e., $W(t+\Delta t) - W(t) \sim \mathcal{N}(0, \Delta t)$. We will now make use of the statistical properties of the Wiener process $W(t)$ to show the subtleties involved in the definition of the stochastic integral (2.8). In particular, we can define (2.8) as a Riemann-Stieltjes integral. This implies dividing the integration domain $[0, t]$ into n sub-intervals delimited by the times $t_0 = 0 < t_1 < t_2 < ... < t_n = t$, and considering the partial sums S_n defined as:

$$S_n = \sum_{i=1}^{n} b(X(\tau_i), \tau_i)[W(t_i) - W(t_{i-1})]\,, \tag{2.9}$$

where $\tau_i = \alpha t_i + (1 - \alpha)t_{i-1}$, with $\alpha \in [0, 1]$. The integral in Eq. (2.8) is then defined as the mean-square limit of the partial sums, i.e. $I \equiv \mathrm{ms}{-}\lim_{n\to\infty} S_n$ [9]. However, it turns out that such definition is not invariant under a change of the parameter α. This can be easily demonstrated by considering for example the stochastic integral $\int_0^t ds\, W(s)dW(s)$, for which the average of the associated partial sums can be exactly computed and yields $\langle S_n \rangle = t\alpha$. This result is strongly dependent on the choice of the intermediate points τ_i, namely on the value of the parameters α. As a consequence, different choices of α lead to distinct definitions of the stochastic integral, and thus to different stochastic calculi. The most frequent prescriptions are those obtained with $\alpha = 1/2$ (Stratonovich) and $\alpha = 0$ (Itô) [9]. Although the latter involves using different rules of calculus, it can nonetheless be useful in some derivations. Interpreting a SDE of the type (2.5) according to different discretization rules (i.e., different stochastic calculi) leads in general to different results, meaning that the average observables assume different values. However, when the stochastic dynamics is characterized by additive noise, as in the case of Eq. (2.4), all stochastic calculi are equivalent. Another scenario where the choice of the discretization rule is irrelevant is when the noise, though multiplicative, is colored, i.e., it has temporal correlations [74–76].

2.2.1 Itô Lemma

As anticipated, whenever the evolution of a stochastic variable is governed by a SDE interpreted with the Itô convention, the rules of calculus need to be modified accordingly. In particular, it is well known that the time derivative of a generic function f of a stochastic process $X(t)$ does not follow the standard chain rule, but it acquires an additional term that we will now briefly justify. Let us assume that the variable $X(t)$ evolves according to Eq. (2.5), which can be equivalently written as

$$\mathrm{d}X = a(X(t),t)\mathrm{d}t + b(X(t),t)\mathrm{d}W\,, \tag{2.10}$$

by using the definition (2.7) of the Wiener process $W(t)$. Let us now consider a differentiable function f, and compute its infinitesimal variation

$$\mathrm{d}f(X(t)) = f'(X(t))\mathrm{d}X + \frac{1}{2}f''(X(t))(\mathrm{d}X)^2 + o(\mathrm{d}t^2)\,. \tag{2.11}$$

Importantly, the second term of the expansion has not been neglected and it can be shown to provide a contribution of order $\mathrm{d}t$ due to the Itô rules of calculus. More precisely, one can prove the formal identity $\mathrm{d}W^2 = \mathrm{d}t$, which derives from the more rigorous statement

$$\int_0^t [\mathrm{d}W(s)]^2 g(s) = \mathrm{ms}-\lim_{n\to\infty}\sum_{i=1}^{n} g(t_{i-1})[W(t_i)-W(t_{i-1})]^2 = \int_0^t \mathrm{d}t\, g(s) \tag{2.12}$$

with $g(s)$ a generic non-anticipating function of s, in the sense that for all times t and s such that $s < t$, one has that $g(s)$ is statistically independent of the increment $W(t) - W(s)$ [9]. This leads to the so-called *Itô lemma*, which states that the infinitesimal variation (and thus the chain rule) of the function $f(X(t))$ is corrected by a term that depends on the noise amplitude, namely:

$$\mathrm{d}f(X(t)) = f'(X(t))\mathrm{d}X + \frac{1}{2}b^2(X(t))f''(X(t))\mathrm{d}t + o(\mathrm{d}t^2)\,. \tag{2.13}$$

The Itô's Lemma can be readily generalized to the case of a multivariate d-dimensional stochastic process $\boldsymbol{X}(t)$ evolving according to

$$\mathrm{d}\boldsymbol{X} = \boldsymbol{a}(\boldsymbol{X}(t),t)\mathrm{d}t + \boldsymbol{b}(\boldsymbol{X}(t),t)\cdot\mathrm{d}\boldsymbol{W}\,, \tag{2.14}$$

where the element of $\boldsymbol{W}$ are d statistically independent Wiener processes, $\boldsymbol{a}$ a d-dimensional vector and $\boldsymbol{b}$ a $d \times d$ matrix. In this case, the multivariate Itô Lemma yields:

$$\begin{aligned} \mathrm{d}f(\boldsymbol{X}(t)) &= \nabla f(\boldsymbol{X}(t)) \cdot \mathrm{d}\boldsymbol{X} \\ &\quad + \frac{1}{2} \sum_{\alpha\beta} [\boldsymbol{b}(\boldsymbol{X}(t), t) \cdot \boldsymbol{b}^T(\boldsymbol{X}(t), t)]_{\alpha\beta} \nabla_\alpha \nabla_\beta f(X(t)) \mathrm{d}t + o(\mathrm{d}t^2)\,. \end{aligned} \tag{2.15}$$

Further below, in Secs. 2.3 and 2.9, we will present some instances where the choice Itô calculus turns out to be useful, leading to a simplification of some derivations compared to using, e.g., Stratonovich calculus and the standard chain rule.

2.3 Fokker-Planck Equation

Let us come back to the overdamped Langevin dynamics in Eq. (2.4). This equation models the stochastic evolution of the variable $\boldsymbol{X}(t)$, and for each noise realization $\boldsymbol{\xi}(t)$ it provides one of its possible random trajectories. A useful tool to study the statistical properties of a stochastic process is the so-called *Master equation*, which describes the deterministic time evolution of the one-time probability density

$$P_1(\boldsymbol{x}, t) = \langle \delta^d(\boldsymbol{X}(t) - \boldsymbol{x}) \rangle\,, \tag{2.16}$$

where the ensemble average is taken over all the possible realizations of the noise $\boldsymbol{\xi}$. In the case of a Markovian process, as the one described by Eq. (2.4), the evolution equation of $P_1(\boldsymbol{x}, t)$ is given by the *Fokker-Planck equation* (FPE) [9, 74, 77–79], the derivation of which is straightforward and is reported in what follows. Among the various ways to derive the FPE, we choose the one that relies on the application of the Itô lemma. We remind that the Langevin equation (2.4) is characterized by additive noise, implying that all discretization rules are equivalent and should lead to the same FPE. For this reason we have the freedom to choose the stochastic calculus which is more suitable for our derivation. If one is faced with an SDE with multiplicative noise and a specified stochastic calculus other than Itô's, such SDE should be converted into its equivalent Itô's form in order to use the following proof. Let us consider the quantity $\delta^d(\boldsymbol{X}(t) - \boldsymbol{x})$: this is a function of the stochastic process $\boldsymbol{X}(t)$ which follows the equation of motion (2.4). This means that, according to the Itô Lemma, its time derivative reads:

$$\frac{\mathrm{d}}{\mathrm{d}t} \delta^d(\boldsymbol{X}(t) - \boldsymbol{x}) = \nabla \delta^d(\boldsymbol{X}(t) - \boldsymbol{x}) \cdot \dot{\boldsymbol{X}}(t) + T\nu \nabla^2 \delta^d(\boldsymbol{X}(t) - \boldsymbol{x})\,. \tag{2.17}$$

Both sides of the above equation are still random variables in that they depend on the stochastic process $\boldsymbol{X}(t)$. Therefore, they can be averaged over all the noise realizations $\boldsymbol{\xi}(t)$. For a generic observable $O(\boldsymbol{X}(t))$ which only depend on the stochastic process $\boldsymbol{X}(t)$ at a single time t, the ensemble average over the noise realizations can be rewritten as:

$$\langle O(\boldsymbol{X}(t))\rangle = \int \mathrm{d}^d\boldsymbol{y}\, O(\boldsymbol{y}) P_1(\boldsymbol{y},t)\,. \tag{2.18}$$

Thus, taking the average of Eq. (2.17) leads to:

$$\partial_t P_1(\boldsymbol{x},t) = \nu \int \mathrm{d}^d\boldsymbol{y} \nabla\delta^d(\boldsymbol{y}-\boldsymbol{x})\cdot\boldsymbol{F}(\boldsymbol{y},t)P_1(\boldsymbol{y},t) + T\nu \int \mathrm{d}^d\boldsymbol{y}\nabla^2\delta^d(\boldsymbol{y}-\boldsymbol{x})P_1(\boldsymbol{y},t)\,, \tag{2.19}$$

where we used $\langle\nabla\delta^d(\boldsymbol{X}(t)-\boldsymbol{x})\boldsymbol{\xi}(t)\rangle = 0$ due to the fact that all Itô processes are non-anticipating. This property is one of the main reasons for which Itô calculus might be advantageous in specific circumstances, as it implies that the noise term $\boldsymbol{\xi}(t)$ and a generic function $f(\boldsymbol{X}(t))$ of the stochastic process $\boldsymbol{X}(t)$ are uncorrelated random variables at the same time t. Integrating by parts Eq. (2.19) finally yields the FPE:

$$\partial_t P_1(\boldsymbol{x},t) = -\nabla\cdot\left[\nu\boldsymbol{F}(\boldsymbol{x},t)P_1(\boldsymbol{x},t) - T\nu\nabla P_1(\boldsymbol{x},t)\right]\,. \tag{2.20}$$

As expected, this equation takes the form of a continuity equation

$$\begin{aligned}\partial_t P_1(\boldsymbol{x},t) &= -\nabla\cdot\boldsymbol{J}(\boldsymbol{x},t)\\ \boldsymbol{J}(\boldsymbol{x},t) &= \nu\boldsymbol{F}(\boldsymbol{x},t)P_1(\boldsymbol{x},t) - T\nu\nabla P_1(\boldsymbol{x},t)\,,\end{aligned} \tag{2.21}$$

with a probability flux given by $\boldsymbol{J}(\boldsymbol{x},t)$. This ensures that, in the domain of definition of $\boldsymbol{x}$, the probability density is a conserved quantity. The probability flux $\boldsymbol{J}(\boldsymbol{x},t)$ consists of two contributions of distinct origin. The first one, $\nu\boldsymbol{F}(\boldsymbol{x},t)P_1(\boldsymbol{x},t)$, is the drift term generated by the deterministic force $\boldsymbol{F}(\boldsymbol{x},t)$ and it is associated to the advective transport. The second one, $-T\nu\nabla P_1(\boldsymbol{x},t)$, is a diffusive flux of the form predicted by the first Fick's law, i.e., it is proportional to the gradient of the probability density. More precisely, whenever the probability density $P_1(\boldsymbol{x},t)$ is non-homogeneous around the position $\boldsymbol{x}$, the diffusion produces a net flux against the gradient in the attempt to compensate for such unbalance and make the distribution spatially homogeneous. The coefficient in front of the probability gradient is the so-called diffusion coefficient and it is denoted by D. In this case, as anticipated in Sec. 2.1, the diffusion coefficient is related to the mobility ν and the temperature T by the Einstein relation

$$D = \nu T\,. \tag{2.22}$$

In the absence of non-conservative forces and external drivings, the advective component of the flux is purely determined by the potential energy $\mathcal{U}(\boldsymbol{x})$. In this case, the stochastic dynamics (2.4) satisfies the detailed balance condition and the time reversal symmetry is preserved. At long times, the one-time probability density associated to this equilibrium dynamics converges to the Boltzmann distribution

$$P_1^{(\mathrm{eq})}(\boldsymbol{x}) \propto e^{-\beta\mathcal{U}(\boldsymbol{x})}\,, \tag{2.23}$$

with $\beta = 1/T$ the inverse temperature. This can be easily verified by checking that the Boltzmann distribution solves the FPE at steady state, i.e., when $\partial_t P_1(\boldsymbol{x}, t) = 0$. An analogous derivation can be carried out for a generic Itô process with multiplicative noise as the one reported in Eq. (2.14). In this case, the corresponding FPE is given by:

$$\begin{aligned} \partial_t P_1(\boldsymbol{x}, t) = &- \sum_\alpha \nabla_\alpha [a_\alpha(\boldsymbol{x}, t) P_1(\boldsymbol{x}, t)] \\ &+ \frac{1}{2}\sum_{\alpha\beta} \nabla_\alpha\nabla_\beta[[\boldsymbol{b}(\boldsymbol{x}, t)\cdot\boldsymbol{b}^T(\boldsymbol{x}, t)]_{\alpha\beta} P_1(\boldsymbol{x}, t)]\,. \end{aligned} \tag{2.24}$$

Finally, note that the FPE reported in Eqs. (2.20) and (2.24) are local in time. This property ultimately comes from the Markovian nature of their underlying stochastic dynamics. For a non-Markovian stochastic process, deriving the associated Master equation can be more involved, and in general it does not lead to a close equation for $P_1(\boldsymbol{x}, t)$.

2.4 Brownian motion

The overdamped Langevin equation (2.4) can be specialized to the case of a single and unconfined colloidal particle diffusing in a simple fluid. In the absence of any deterministic force, the motion of the particle is entirely governed by the collisions with the solvent molecules. Assuming that at the initial time $t_0 = 0$ the particle is located at $\boldsymbol{X}(0)$, its position at a later time t is given by:

$$\boldsymbol{X}(t) = \boldsymbol{X}(0) + \int_0^t \mathrm{d}s\, \boldsymbol{\xi}(s) = \boldsymbol{X}(0) + \sqrt{2\nu T}\boldsymbol{W}(t)\,. \tag{2.25}$$

This means that the stochastic evolution of a freely diffusing particle is statistically equivalent to a Wiener process. In particular, the averaged position $\langle \boldsymbol{X}(t)\rangle = \boldsymbol{X}(0)$ equals its initial value because the Wiener process has zero mean at all times. However the typical distance travelled by the colloidal particle can be computed from the two-point connected correlations

$$\langle (X^\alpha(t) - X^\alpha(0))(X^\beta(s) - X^\beta(0))\rangle = 2\nu T\delta_{\alpha\beta}\min(t, s)\,, \tag{2.26}$$

from which one can derive the mean-squared-displacement:

$$\langle [\boldsymbol{X}(t) - \boldsymbol{X}(0)]^2\rangle = 2d\nu T t\,. \tag{2.27}$$

This implies that the typical distance travelled by the particle at time t grows as $\sim \sqrt{t}$, which is an important characteristic of diffusive motion. Note that the mean-squared-displacement in Eq. (2.27) only features a linear growth with time and does not display an initial ballistic regime $\sim t^2$. Although this should be present as a consequence of inertia, the overdamped Langevin dynamics is unable to capture this effect in that it assumes that the velocity relaxation time νm is vanishingly small. To give an estimate of the typical values assumed by the diffusion coefficient D (see Eq. (2.22)) of a colloidal particle, we first apply the Stoke's law to relate its mobility ν to its radius R and to the dynamic viscosity μ of the fluid it is immersed in. Thus, the diffusion coefficient is given by:

$$D = T/(6\pi\mu R)\,. \tag{2.28}$$

According to this formula, at room temperature, a colloidal particle with a radius $R \approx 1\mu\mathrm{m}$ immersed in water (dynamical friction $\mu \approx 8.9 \cdot 10^{-4}\,\mathrm{Pa}\cdot\mathrm{s}$), is characterized by a diffusion coefficient $D \approx 2 \cdot 10^{-13}\mathrm{m}^2/\mathrm{s}$. This means that during a time interval of 1 second, the colloidal particle travels a typical distance of the order of 1μm, i.e., it moves about its own size in a second.

2.5 Rotational diffusion

In the previous Section, we have seen that as a result of its interaction with the fluid, the position of a colloidal particle evolves according to a diffusive motion. However, it is natural to expect that the fluid will also affect the rotational dynamics of the particle, leading to the so-called rotational diffusion. Let us take an arbitrary point on the surface of the colloidal particle (which we assume to be of spherical shape for simplicity), and consider the line that joins that point to the center of the particle. This line identifies a unit vector $\boldsymbol{n}$ directed from the center of the particle to its surface. In $d = 3$, the overdamped stochastic dynamics of $\boldsymbol{n}$ is given by:

$$\dot{\boldsymbol{n}} = \sqrt{2D_r}\boldsymbol{n} \wedge \boldsymbol{\xi}\,, \tag{2.29}$$

with D_r the rotational diffusion coefficient and $\boldsymbol{\xi}$ a zero-mean Gaussian white noise with unit variance. Importantly, the stochastic rotational dynamics (2.29) is characterized by a multiplicative noise and needs to be interpreted according to the Stratonovich convention. Indeed, this ensures the invariance of the modulus $\|\boldsymbol{n}\| = 1$ along the dynamics, as it can be immediately verified by computing:

$$\frac{\mathrm{d}\|\boldsymbol{n}\|^2}{\mathrm{d}t} = 2\sqrt{2D_r}\boldsymbol{n} \cdot \boldsymbol{n} \wedge \boldsymbol{\xi} = 0\,, \tag{2.30}$$

where we used the (standard) Stratonovich chain rule and the fact that the noise vector $\boldsymbol{n} \wedge \boldsymbol{\xi}$ lies on a plane perpendicular to the unit vector $\boldsymbol{n}$. By introducing the Levi-Civita symbol $\varepsilon_{\alpha\beta\gamma}$ in three dimensions, defined as

$$\varepsilon_{\alpha\beta\gamma} = \begin{cases} +1 & \text{if } (\alpha,\beta,\gamma) \text{ is an even permutation of } (0,1,2), \\ -1 & \text{if } (\alpha,\beta,\gamma) \text{ is an odd permutation of } (0,1,2), \\ 0 & \text{otherwise,} \end{cases} \tag{2.31}$$

the noise term in Eq. (2.29) can be rewritten in the equivalent form:

$$\begin{aligned} \dot{\boldsymbol{n}} &= \boldsymbol{b}(\boldsymbol{n}) \cdot \boldsymbol{\xi}\,, \\ b_{\alpha\beta}(\boldsymbol{n}) &\equiv \sqrt{2D_r} \sum_{\gamma} \varepsilon_{\alpha\gamma\beta} n_\gamma\,. \end{aligned} \tag{2.32}$$

In order to characterize this diffusive motion on a sphere of unit radius, one important quantity to investigate is the orientational autocorrelation function $\langle \boldsymbol{n}(t) \cdot \boldsymbol{n}(0) \rangle$, which will provide a typical time scale after which the orientation vector $\boldsymbol{n}(t)$ is statistically independent from its initial value $\boldsymbol{n}(0)$. To this aim, it is convenient to map the stochastic dynamics (2.32) to its equivalent Itô form. In particular, we want to derive a stochastic dynamics of the form

$$\dot{\boldsymbol{n}} = \boldsymbol{a}^I(\boldsymbol{n}(t)) + \boldsymbol{b}^I(\boldsymbol{n}(t)) \circ \boldsymbol{\xi}\,, \tag{2.33}$$

where we denoted by $\circ$ the Itô product, which renders the same average observables as Eq. (2.32). Following Ref. [9], this mapping does not affect the noise amplitude $\boldsymbol{b}(\boldsymbol{n}(t))$, but it introduces a finite drift term of the form given below:

$$\begin{aligned} a^I_\alpha(\boldsymbol{n}) &= a_\alpha(\boldsymbol{n}) + \frac{1}{2} \sum_{\beta\gamma} b_{\gamma\beta}(\boldsymbol{n}) \nabla_\gamma b_{\alpha\beta}(\boldsymbol{n})\,, \\ b^I_{\alpha\beta}(\boldsymbol{n}) &= b_{\alpha\beta}(\boldsymbol{n})\,, \end{aligned} \tag{2.34}$$

where $a_\alpha(\boldsymbol{n})$ denotes the drift term in the Stratonovich equation (2.32), which is identically zero in the case of rotational diffusion. By using the definition of $b_{\alpha\beta}(\boldsymbol{n})$ in Eq. (2.32), the drift term $a^I_\alpha(\boldsymbol{n})$ which appears in the Itô dynamics can be readily computed as:

$$\begin{aligned} a^I_\alpha(\boldsymbol{n}) &= D_r \sum_{\beta\gamma\sigma\omega} \varepsilon_{\gamma\sigma\beta} n_\sigma \nabla_\gamma \varepsilon_{\alpha\omega\beta} n_\omega = D_r \sum_{\beta\gamma\sigma} \varepsilon_{\sigma\beta\gamma} \varepsilon_{\alpha\gamma\beta} n_\sigma \\ &= -D_r \sum_{\sigma} 2\delta_{\sigma\alpha} n_\sigma = -2D_r n_\alpha\,, \end{aligned} \tag{2.35}$$

where we used the following property of the Levi-Civita symbol

$$\sum_{\beta\gamma} \varepsilon_{\alpha\beta\gamma} \varepsilon_{\sigma\beta\gamma} = 2\delta_{\alpha\beta}\,. \tag{2.36}$$

Thus the equivalent Itô dynamics reads:

$$\dot{\boldsymbol{n}} = -2D_r\boldsymbol{n} + \boldsymbol{b}(\boldsymbol{n}(t)) \circ \boldsymbol{\xi}\,. \tag{2.37}$$

Although the presence of the drift term $-2D_r\boldsymbol{n}$ in the Itô dynamics might appear as counter-intuitive as it is aligned with the orientation vector $\boldsymbol{n}$, it is actually necessary to preserve its norm throughout the dynamics. Indeed, in computing the time derivative of $\|\boldsymbol{n}\|^2$, one should now carefully apply the multivariate Itô Lemma (2.15), obtaining:

$$\begin{aligned}\frac{\mathrm{d}\|\boldsymbol{n}\|^2}{\mathrm{d}t} &= 2\boldsymbol{n}\cdot\boldsymbol{a}^I(\boldsymbol{n}) + D_r\sum_{\alpha\beta\gamma\sigma\omega}\varepsilon_{\alpha\sigma\gamma}\varepsilon_{\beta\omega\gamma}n_\sigma n_\omega\nabla_\alpha\nabla_\beta\boldsymbol{n}\cdot\boldsymbol{n}\\ &= -4D_r\|\boldsymbol{n}\|^2 + 2D_r\sum_{\alpha\gamma\sigma\omega}\varepsilon_{\alpha\sigma\gamma}\varepsilon_{\alpha\omega\gamma}n_\sigma n_\omega\\ &= -4D_r\|\boldsymbol{n}\|^2 + 4D_r\sum_{\sigma\omega}\delta_{\sigma\omega}n_\sigma n_\omega = 0\,,\end{aligned} \tag{2.38}$$

which confirms that the modulus of the vector $\boldsymbol{n}$ is fixed also with the stochastic dynamics in Eq. (2.37). As anticipated, the Itô formalism is more convenient to compute the orientational autocorrelation function [80]. To this purpose, let us denote by $\boldsymbol{n}(0)$ the initial orientation vector. The stochastic dynamics in Eq. (2.37) can be formally solved leading to

$$\boldsymbol{n}(t) = e^{-t/\tau}\boldsymbol{n}(0) + \int_0^t \mathrm{d}s e^{-(t-s)/\tau}\boldsymbol{b}(\boldsymbol{n}(s))\circ\boldsymbol{\xi}(s)\,, \tag{2.39}$$

where we introduced the characteristic time scale $\tau = 1/[(d-1)D_r]$. We can now multiply the formal solution by the initial vector $\boldsymbol{n}(0)$ and then compute the average of the resulting quantity. In this way we obtain:

$$\langle\boldsymbol{n}(t)\cdot\boldsymbol{n}(0)\rangle = e^{-t/\tau} + \boldsymbol{n}(0)\cdot\int_0^t e^{-(t-s)/\tau}\langle\boldsymbol{b}(\boldsymbol{n}(s))\circ\mathrm{d}\boldsymbol{W}(s)\rangle = e^{-t/\tau}\,. \tag{2.40}$$

Importantly, the second average vanishes for all times s because the integrand is a non-anticipating function of s and we are using Itô calculus, thus the noise at a certain time s is not correlated with the value assumed by the random variable $\boldsymbol{n}(s)$ at the same time. By using the orientation autocorrelation function we can also compute the mean-squared-chord, namely the typical length of the segment that joins the points on the sphere identified by $\boldsymbol{n}(t)$ and $\boldsymbol{n}(0)$. This is given by:

$$\langle(\boldsymbol{n}(t)-\boldsymbol{n}(0))^2\rangle = 2 - 2\langle\boldsymbol{n}(t)\cdot\boldsymbol{n}(0)\rangle = 2(1-e^{-t/\tau})\,. \tag{2.41}$$

Interestingly, at short times, when the chord is approximately equal to the travelled arc length, the previous expression becomes:

$$\langle(\boldsymbol{n}(t)-\boldsymbol{n}(0))^2\rangle \overset{t\ll\tau}{\simeq} 2(d-1)D_r t\,, \tag{2.42}$$

which grows linearly in time, as expected for a diffusive dynamics, and is formally equivalent to the mean-squared-displacement of the Brownian motion (see Eq. (2.27)), but in a lower dimensionality because, at short times, the effects of the sphere curvature play a minor role.

By using Eq. (2.24), which provides the expression of the Fokker-Planck equation associated to a given Itô process with multiplicative noise, one can obtain the evolution equation of the one-time probability density $P_1(\boldsymbol{n}, t)$ of the orientation vector undergoing rotational diffusion. This reads:

$$\partial_t P_1(\boldsymbol{n}, t) = D_r \mathcal{R}^2 P_1(\boldsymbol{n}, t)\,, \tag{2.43}$$

where the operator $\mathcal{R} = (\mathbf{1} - \boldsymbol{n} \otimes \boldsymbol{n}) \cdot \nabla$ represents the projection of the nabla operator onto the direction perpendicular to the orientation vector $\boldsymbol{n}$, and $\otimes$ denotes the outer product. In $d = 3$, the unit vector $\boldsymbol{n}$ can be parametrized by the polar angle θ and the azimuthal angle ϕ. Accordingly, the operator $\mathcal{R}^2$ can be rewritten in spherical coordinates as

$$\mathcal{R}^2 = \frac{1}{\sin\theta}\partial_\theta[\sin\theta\partial_\theta] + \frac{1}{\sin^2\theta}\partial_\phi^2\,, \tag{2.44}$$

and it is diagonalized by spherical harmonics $Y_l^m(\theta, \phi)$. This implies that the orientation vector $\boldsymbol{n}$ is itself an eigenfunction of $\mathcal{R}^2$, with eigenvalue $(1 - d)$. Much simpler is the FPE associated to the rotational diffusion in $d = 2$, i.e., the diffusion on a circle, which in polar coordinates reads:

$$\partial_t P_1(\theta, t) = D_r \partial_\theta^2 P_1(\theta, t)\,. \tag{2.45}$$

Indeed, in this case, the underlying stochastic dynamics is expressed in terms of the polar angle θ, and it is characterized by additive noise:

$$\dot{\theta} = \sqrt{2D_r}\xi(t)\,. \tag{2.46}$$

An analogous equation of motion with the addition of an external deterministic torque will be employed in Chapter 3 to describe the rotational dynamics of the polarity of a self-propelled particle.

2.6 The Ornstein-Uhlenbeck process

The behavior of a freely diffusing particle on time scales shorter than the velocity relaxation time $m\nu$ has been first analyzed by Ornstein and Uhlenbeck [81]. In this regime, the role of inertia cannot be neglected, and the stochastic dynamics of the velocity is given by

$$m\nu\dot{\boldsymbol{v}} = -\boldsymbol{v} + \sqrt{2\nu T}\boldsymbol{\xi}\,. \tag{2.47}$$

This stochastic equation of motion is formally equivalent to the overdamped Langevin dynamics of a Brownian particle confined by a harmonic potential $\mathcal{U}(\boldsymbol{x}) = \kappa \boldsymbol{x}^2/2$ with stiffness κ. The latter reads:

$$\dot{\boldsymbol{X}} = -\nu \nabla \mathcal{U}(\boldsymbol{X}(t)) + \sqrt{2\nu T}\boldsymbol{\xi} = -\gamma \boldsymbol{X}(t) + \sqrt{2\nu T}\boldsymbol{\xi}\,, \tag{2.48}$$

with $\boldsymbol{\xi}$ a zero-mean Gaussian white noise and where we introduced the inverse characteristic time

$$\gamma \equiv \tau_X^{-1} = \kappa\nu\,. \tag{2.49}$$

A linear SDE of the type shown in Eqs. (2.47) and (2.48) is called the Ornstein-Uhlenbeck (OU) process, which we briefly discuss here. Due to its linearity, Eq. (2.48) can be solved exactly, giving:

$$\boldsymbol{X}(t) = e^{-\gamma t}\boldsymbol{X}_0 + \sqrt{2\nu T}\int_{t_0}^{t} \mathrm{d}s\, e^{-\gamma(t-s)}\boldsymbol{\xi}(s)\,, \tag{2.50}$$

where we assumed that the particle is initially located at the position $\boldsymbol{X}_0$. From this solution we can readily compute the average position of the particle

$$\boldsymbol{\mu}(t) \equiv \langle \boldsymbol{X}(t)\rangle = e^{-\gamma t}\boldsymbol{X}_0\,, \tag{2.51}$$

which decays exponentially to the rest position of the confining potential with the characteristic time scale τ_X. Moreover, we can compute the two-point connected correlation function $C_{\alpha\beta}(t,s)$ given by:

$$\begin{aligned} C_{\alpha\beta}(t,s) &\equiv \langle [X_\alpha(t) - \mu_\alpha(t)] \cdot [X_\beta(s) - \mu_\beta(s)]\rangle \\ &= 2\nu T \int_{t_0}^{t} \mathrm{d}t' \int_{t_0}^{s} \mathrm{d}s' e^{-\gamma(t+s-t'-s')}\langle \xi_\alpha(t')\xi_\beta(s')\rangle \\ &= \delta_{\alpha\beta}\frac{T}{\kappa}\left[e^{-\gamma|t-s|} - e^{-\gamma(t+s-2t_0)}\right]\,. \end{aligned} \tag{2.52}$$

In the long-time regime, which can be obtained by considering the limit $t_0 \to -\infty$, the system reaches a stationary state and the two-point connected correlation function becomes time-translation invariant, i.e., a function of the difference $t - s$. In particular, from Eq. (2.52) in the long-time limit we can extract the variance of the position at steady state, which is given by

$$\langle [X_\alpha(t) - \mu_\alpha(t)]^2\rangle \overset{t\to\infty}{\to} dT/\kappa\,, \tag{2.53}$$

and, as expected, it is controlled by the entity of the thermal fluctuations and the stiffness of the confining potential. Naturally, this result is in agreement with the fact that stationary density of the position is given by the Boltzmann distribution

$$P^{(\mathrm{eq})}(\boldsymbol{x}) \propto \exp\left(-\frac{\kappa}{2T}\boldsymbol{x}^2\right) \tag{2.54}$$

which, in this case, is Gaussian as a consequence of the harmonic confinement. Equation (2.54) is indeed the long-time solution of the Fokker-Planck equation associated to the OU process, namely:

$$\partial_t P_1(\boldsymbol{x},t) = -\nabla \cdot \left[-\gamma \boldsymbol{x} P_1 - \nu T \nabla P_1\right] . \tag{2.55}$$

2.7 Rouse polymer

The overdamped Langevin dynamics (2.4) can be generalized to model the stochastic equation of motion of many particles interacting with each other to form a polymer chain. In particular, let us consider N particles with position $\boldsymbol{X}_i$, where $i \in \{0, 1, ..., N-1\}$, which we will call monomers. Every pair of interacting monomers is subject to a harmonic attractive potential with a fixed stiffness κ. Hence, the Hamiltonian of the chain is quadratic and is given by:

$$\mathcal{H} = \frac{\kappa}{2} \sum_{i=0}^{N-1} \sum_{j=0}^{N-1} M_{ij} \boldsymbol{X}_i \cdot \boldsymbol{X}_j \, , \tag{2.56}$$

with M_{ij} denoting the connectivity matrix, which establishes which pairs of monomers are interacting. The matrix $\boldsymbol{M}$ is built as follows: each diagonal element M_{ii} contains the degree of connectivity of the monomer i, i.e., the number of monomers to which the latter is connected; the off-diagonal elements M_{ij} are -1 when the monomers i and j are connected, and equal to 0 otherwise. The connectivity matrix defines the architecture of the polymer, namely it determines whether it is a linear chain, a ring, or a more complicate structure. A polymer chain described with a quadratic Hamiltonian as (2.56) is sometimes called a generalized Gaussian structure [82]. The evolution of the polymer in a thermal bath is governed by the following stochastic dynamics:

$$\dot{\boldsymbol{X}}_i = -\nu \nabla_i \mathcal{H}(\{\boldsymbol{X}_i(t)\}) + \boldsymbol{\xi}_i(t) = -\gamma \sum_{j=0}^{N-1} M_{ij} \boldsymbol{X}_j(t) + \boldsymbol{\xi}_i(t) \, , \tag{2.57}$$

where we introduced the relaxation rate $\gamma = \kappa\nu$ as in Eq. (2.49), and where $\{\boldsymbol{\xi}_i\}$ is a set of N independent zero-mean white Gaussian noises with correlations

$$\langle \xi_i^\alpha(t) \xi_j^\beta(s) \rangle = 2\nu T \delta_{ij} \delta_{\alpha\beta} \delta(t-s) \, . \tag{2.58}$$

This model goes under the name of *Rouse model* [83, 84]. Clearly, this is only the simplest possible polymer model because it neglects many features of a real chain, e.g., bending rigidity, torsional stress and excluded volume interaction. Moreover, when a portion of the chain moves, it induces a change in the velocity field of the solvent, which is in principle felt by the neighboring monomers. This kind of hydrodynamic interactions is neglected in the Rouse model, and it is assumed that the only effect of the coupling with the thermal bath is encoded in the friction and in the noise term. Despite this apparently strong simplification, the Rouse model has proved to be useful to describe the dynamics of unentangled dense polymer solutions and melts. In other cases, like in unentangled dilute polymer solutions, the lack of hydrodynamic interactions might represent a serious limitation, and the polymer dynamics is better described by the more elaborate *Zimm model* [84, 85].

The most common approach to analyze the Rouse model is to perform a change of variable from the position of the monomers $\{\boldsymbol{X}_i\}$ to the so-called Rouse modes $\{\boldsymbol{\chi}_i\}$. These can be obtained through the application of a linear transformation $\boldsymbol{\varphi}$, i.e.,

$$\boldsymbol{\chi}_i = \sum_{j=0}^{N-1} \varphi_{ij} \boldsymbol{X}_j \,. \tag{2.59}$$

The transformation $\boldsymbol{\varphi}$ is chosen such that it diagonalizes the connectivity matrix $\boldsymbol{M}$, namely it satisfies:

$$\sum_{jk} \varphi_{ij} M_{jk} \varphi^{-1}_{kl} = \lambda_i \delta_{il} \,, \tag{2.60}$$

with $\{\lambda_i\}$ the N eigenvalues of $\boldsymbol{M}$. This implies that the rows of $\boldsymbol{\varphi}$ are the eigenvectors of $\boldsymbol{M}$, and we choose them to be normalized to unity. Importantly, since the connectivity matrix is symmetric, we have that $\boldsymbol{\varphi}$ is an orthogonal matrix, i.e. $\boldsymbol{\varphi}^{-1} = \boldsymbol{\varphi}^T$. This property will be extensively used in the Chapters 5 and 6, as well as in their corresponding Appendices. Furthermore, we know by construction of $\boldsymbol{M}$ that the sum of the elements of each row (and of each column) is equal to 0. This implies that for a generic connectivity matrix $\boldsymbol{M}$, the vector $(1, 1, ..., 1)/\sqrt{N}$ is always an eigenvector, with associated eigenvalue $\lambda_0 = 0$. By applying the transformation $\boldsymbol{\varphi}$ to the stochastic dynamics (2.57), we get:

$$\dot{\boldsymbol{\chi}}_i = -\gamma_i \boldsymbol{\chi}_i + \tilde{\boldsymbol{\xi}}_i(t) \,, \tag{2.61}$$

where $\{\tilde{\boldsymbol{\xi}}_i\}$ is a set of zero-mean Gaussian white noises with the same statistical properties as $\{\boldsymbol{\xi}_i\}$. This can be easily proved as follows:

$$\begin{aligned} \langle \tilde{\xi}^\alpha_i(t) \tilde{\xi}^\beta_j(s) \rangle &= \sum_{mn} \varphi_{im} \varphi_{jn} \langle \xi^\alpha_m(t) \xi^\beta_n(s) \rangle = 2\nu T \delta_{\alpha\beta} \delta(t-s) \sum_n \varphi_{in} \varphi_{jn} \\ &= 2\nu T \delta_{\alpha\beta} \delta_{ij} \delta(t-s) \,, \end{aligned} \tag{2.62}$$

where we used $\varphi_{jn} = \varphi^T_{nj} = \varphi^{-1}_{nj}$. Moreover, we introduced in Eq. (2.61) the relaxation rate

$$\gamma_i = \gamma \lambda_i \tag{2.63}$$

of the i-th Rouse mode, which is proportional to the i-th eigenvalue of the connectivity matrix. Let us focus first on the 0-th order Rouse mode, which can be easily shown to be proportional to the coordinate $\boldsymbol{X}_{\text{com}}$ of the center of mass of the chain, namely $\boldsymbol{\chi}_0 = \sqrt{N}\boldsymbol{X}_{\text{com}}$. As anticipated, for an arbitrary connectivity matrix one has $\lambda_0 = 0$, implying that the dynamics of the center-of-mass is characterized by an infinite typical time scale because of $\gamma_0 = 0$. In particular, one can see that $\boldsymbol{X}_{\text{com}}$ evolves according to a simple Brownian motion with diffusion coefficient D/N. Conversely, all other modes are characterized by a typical relaxation rate γ_i and their stochastic evolution follows an OU process. The advantage of the transformation $\boldsymbol{\varphi}$ is that it provides a set of variables, the Rouse modes, which are decoupled from each other, as can be seen from (2.61). We will show in Chapters 5 and 6 two problems where the last property does not hold any longer, and the internal structure of the polymer is coupled to its center of mass. Following the solution of the OU process presented in Section 2.6, we can immediately write down the expression of the steady state amplitude of the Rouse modes, also known as power spectrum, i.e.,

$$\langle \boldsymbol{\chi}_i^2 \rangle = \frac{d\nu T}{\gamma_i} \,. \tag{2.64}$$

This quantity diverges for the center of mass in absence of confinement, as the latter keeps diffusing in space and the variance of its position monotonically increases as $\sim t$ without ever reaching a stationary state. From the power spectrum, we can evaluate what the typical size of the polymer is in the stationary state. One way to quantify this in the case of a linear chain is via the end-to-end distance $\boldsymbol{R}_{\text{ee}} = \boldsymbol{X}_{N-1} - \boldsymbol{X}_0$. From symmetry arguments, it is easy to see that on average $\langle \boldsymbol{R}_{\text{ee}} \rangle = 0$, because for each configuration $\{\boldsymbol{X}_i\}$ there exist another one that can be obtained by sending $\boldsymbol{X}_i \to -\boldsymbol{X}_i$, which is characterized by the opposite end-to-end distance and has the same statistical weight. Thus one can compute the mean-squared end-to-end distance

$$\begin{aligned}\langle \boldsymbol{R}_{\text{ee}}^2 \rangle = \langle (\boldsymbol{X}_{N-1} - \boldsymbol{X}_0)^2 \rangle &= \sum_{ij} (\varphi^{-1}_{N-1,i} - \varphi^{-1}_{0,i})(\varphi^{-1}_{N-1,j} - \varphi^{-1}_{0,j}) \langle \boldsymbol{\chi}_i \cdot \boldsymbol{\chi}_j \rangle \\ &= \sum_{i=1}^{N-1} (\varphi_{i,N-1} - \varphi_{i,0})^2 \langle \boldsymbol{\chi}_i^2 \rangle\end{aligned} \tag{2.65}$$

and express it as a function of the stationary power spectrum. The typical size of the polymer can then be obtained by taking the square root of the previous quantity. Note that, as expected, the typical size of the polymer does not depend on the position of the center of mass. In the case of a linear chain the transformation $\boldsymbol{\varphi}$ reads

$$\varphi_{kj} = \sqrt{\frac{2 - \delta_{k0}}{N}} \cos\left(\frac{k\pi}{N} \left(j + \frac{1}{2} \right) \right) \,, \tag{2.66}$$

and the relaxation rates are given by

$$\gamma_j = 2\gamma \left(1 - \cos\left(\frac{j\pi}{N} \right) \right) = 4\gamma \sin^2\left(\frac{j\pi}{2N} \right) \,. \tag{2.67}$$

However, $\sqrt{\langle \boldsymbol{R}_{\mathrm{ee}}^2 \rangle}$ can be used as a proxy for the typical polymer size only in the case of a linear chain. A more appropriate observable that can be used for a generic polymer structure is given by the gyration radius $\boldsymbol{R}_{\mathrm{g}}$, which is defined as:

$$\boldsymbol{R}_{\mathrm{g}}^2 = \frac{1}{N} \sum_{i=0}^{N-1} (\boldsymbol{X}_i - \boldsymbol{X}_{\mathrm{com}})^2 \,. \tag{2.68}$$

Analogously to the end-to-end distance, also the average gyration radius can be expressed in terms of the power spectrum:

$$\begin{aligned} \langle \boldsymbol{R}_{\mathrm{g}}^2 \rangle &= \frac{1}{N} \sum_{i=0}^{N-1} \left\langle \left(\sum_{j=0}^{N-1} \varphi_{ji} \boldsymbol{\chi}_j - \frac{\boldsymbol{\chi}_0}{\sqrt{N}} \right)^2 \right\rangle = \frac{1}{N} \sum_{i=0}^{N-1} \left\langle \left(\sum_{j=1}^{N-1} \varphi_{ji} \boldsymbol{\chi}_j \right)^2 \right\rangle \\ &= \frac{1}{N} \sum_{j=1}^{N-1} \sum_{k=1}^{N-1} \left(\sum_{i=0}^{N-1} \varphi_{ji} \varphi_{ki} \right) \langle \boldsymbol{\chi}_j \cdot \boldsymbol{\chi}_k \rangle = \frac{1}{N} \sum_{j=1}^{N-1} \langle \boldsymbol{\chi}_j^2 \rangle \,. \end{aligned} \tag{2.69}$$

This expression will be used later on in Chapter 6 to describe the effect of a correlated medium on the structure of a polymer chain.

2.8 The Gaussian field

All stochastic dynamics discussed in the previous Sections are given by d-dimensional stochastic processes, or in the case of the Rouse model by a set of N interacting d-dimensional stochastic processes. In this Section we describe the stochastic evolution of a thermally fluctuating scalar field $\phi(\boldsymbol{x}, t)$, with $\boldsymbol{x} \in \mathbb{R}^d$. In this case, for each of the infinitely many spatial labels $\boldsymbol{x}$, the value taken by the field in that point is a fluctuating degree of freedom. For simplicity, we assume that the field $\phi(\boldsymbol{x}, t)$ is Gaussian, i.e., it is characterized by the quadratic Hamiltonian

$$\mathcal{H} = \int \mathrm{d}^d \boldsymbol{x} \left[\frac{1}{2} (\nabla \phi)^2 + \frac{r}{2} \phi^2 \right] , \tag{2.70}$$

where the parameter $r = 1/\xi_\phi^2$ is related to the correlation length ξ_ϕ of the field, and therefore it determines its distance from the critical point $r = 0$. The stochastic evolution of the field is assumed to be given by [54]:

$$\partial_t \phi(\boldsymbol{x}, t) = -D_\phi (i\nabla)^a \frac{\delta \mathcal{H}}{\delta \phi(\boldsymbol{x}, t)} + \zeta(\boldsymbol{x}, t) = -D_\phi (i\nabla)^a \left[(r - \nabla^2) \phi(\boldsymbol{x}, t) \right] + \zeta(\boldsymbol{x}, t) \,, \tag{2.71}$$

where $\delta/\delta\phi$ denotes the functional derivative and D_ϕ is the field mobility. The exponent a can assume two distinct values: with $a = 0$ we get what is called model A dynamics, whereas with $a = 2$ we obtain model B dynamics. This nomenclature was first given in [86]. Model A describes the stochastic evolution of a non-conserved order parameter, while in model B the scalar field $\phi(\boldsymbol{x}, t)$ is locally conserved throughout the dynamics. This implies that in the latter case, the equation of motion (2.71) can be rewritten as a continuity equation $\partial_t \phi = -\nabla \cdot \boldsymbol{J}(\boldsymbol{x}, t)$, with a suitable fluctuating flux $\boldsymbol{J}(\boldsymbol{x}, t)$. The noise term $\zeta(\boldsymbol{x}, t)$ is a zero-mean Gaussian white noise field, with correlations:

$$\langle \zeta(\boldsymbol{x}, t)\zeta(\boldsymbol{y}, s)\rangle = 2D_\phi T(i\nabla)^a \delta^d(\boldsymbol{x} - \boldsymbol{y})\delta(t - s)\,. \tag{2.72}$$

To ensure that the system reaches the equilibrium Boltzmann distribution $P^{(\mathrm{eq})}[\phi] \propto \exp(-\beta \mathcal{H}[\phi])$ at steady state, the noise amplitude in the previous equation is actually determined by the field mobility D_ϕ and by the temperature T according to a continuum version of the Einstein relation. Analytical progresses can be made by rewriting the field dynamics (2.71) in the Fourier domain. Precisely, for the Fourier mode $\phi_{\boldsymbol{q}}$, we obtain the following dynamics:

$$\dot{\phi}_{\boldsymbol{q}} = -\alpha_{\boldsymbol{q}}\phi_{\boldsymbol{q}} + \zeta_{\boldsymbol{q}}(t)\,, \tag{2.73}$$

where

$$\alpha_{\boldsymbol{q}} = Dq^a(r + q^2) \tag{2.74}$$

denotes the inverse relaxation time of $\phi_{\boldsymbol{q}}$. This means that all Fourier components are decoupled and evolve according to Ornstein-Uhlenbeck processes. Note that, here as in the rest of the thesis, we use the convention for that the Fourier transform of a function $f(\boldsymbol{x})$ is given by

$$f_{\boldsymbol{q}} = \int \mathrm{d}^d\boldsymbol{x}\, f(\boldsymbol{x}) \exp(-i\boldsymbol{q} \cdot \boldsymbol{x})\,. \tag{2.75}$$

The quantity $\zeta_{\boldsymbol{q}}(t)$ denotes the Fourier transform of the noise, and its correlations read:

$$\langle \zeta_{\boldsymbol{q}}(t)\zeta_{\boldsymbol{q}'}(t')\rangle = 2DT(2\pi)^d q^a \delta^d(\boldsymbol{q} + \boldsymbol{q}')\delta(t - s)\,. \tag{2.76}$$

As expected, large-wavelength modes (i.e., those characterized by small $|\boldsymbol{q}|$) always exhibit a longer relaxation time. In particular, when the field is poised at the critical point $r = 0$, the relaxation time grows arbitrarily large as $|\boldsymbol{q}| \to 0$, as a consequence of the critical slowing down [54]. The last property holds even off-criticality in the case of model B dynamics, as implied by the underlying conservation law that regulates the evolution of $\phi(\boldsymbol{x}, t)$. Since (2.73) is an OU process, we know from Section 2.6 that it is solved by:

$$\phi_{\boldsymbol{q}}(t) = G_{\boldsymbol{q}}(t - t_0)\phi_{\boldsymbol{q}}(t_0) + \int_{t_0}^{t} \mathrm{d}s\, G_{\boldsymbol{q}}(t - s)\zeta_{\boldsymbol{q}}(s)\,, \tag{2.77}$$

where $G_{\boldsymbol{q}}(t) = \Theta(t)\exp(-\alpha_{\boldsymbol{q}} t)$ is the dynamic free field propagator and $\Theta(t)$ the Heaviside step function. Here, we denoted the initial configuration assumed by the field with $\phi_{\boldsymbol{q}}(t_0)$. According to Eq. (2.52) it is immediate to show that the two-point connected correlation function reads:

$$\langle \phi_{\boldsymbol{q}}(t)\phi_{\boldsymbol{q}'}(s)\rangle_c = (2\pi)^d\delta^d(\boldsymbol{q}+\boldsymbol{q}')\frac{T}{q^2+r}\left[e^{-\alpha_{\boldsymbol{q}}|t-s|} - e^{-\alpha_{\boldsymbol{q}}(t+s-2t_0)}\right] . \tag{2.78}$$

In the long time limit $t_0 \to -\infty$, the previous formula becomes $\langle \phi_{\boldsymbol{q}}(t)\phi_{\boldsymbol{q}'}(s)\rangle_c = (2\pi)^d\delta^d(\boldsymbol{q}+\boldsymbol{q}')\mathcal{C}_{\boldsymbol{q}}(t-s)$, with $\mathcal{C}_{\boldsymbol{q}}(t-s)$ the time-translation invariant free field correlator given by

$$\mathcal{C}_{\boldsymbol{q}}(t-s) = \frac{T}{q^2+r}e^{-\alpha_{\boldsymbol{q}}|t-s|} . \tag{2.79}$$

This expression shows that at criticality the large-wavelength modes are subjected to large fluctuations. Finally, for both model A and B, we can compute the stationary dynamic susceptibility $\chi_{\boldsymbol{q}}(t)$, which provides information on the response of $\phi(\boldsymbol{x},t)$ to an external field $h(\boldsymbol{x})$. To this aim, we can add to the Hamiltonian (2.70) the linear term $-\int \mathrm{d}^d\boldsymbol{x}\, h(\boldsymbol{x})\phi(\boldsymbol{x})$ and derive a new stochastic dynamics which now depends on the external field. In this way, we can verify that the dynamic susceptibility $\chi_{\boldsymbol{q}}(t)$ is related to the free field propagator $G_{\boldsymbol{q}}(t)$ by the very simple formula:

$$\chi_{\boldsymbol{q}}(t-s) = \left.\frac{\delta\langle\phi_{\boldsymbol{q}}(t)\rangle}{\delta h_{\boldsymbol{q}}(s)}\right|_{h=0} = Dq^aG_{\boldsymbol{q}}(t-s) . \tag{2.80}$$

Following Ref. [54], we can Fourier transform Eq. (2.80) also with respect to the time variable and compute the inverse dynamic susceptibility

$$\chi^{-1}_{\boldsymbol{q},\omega} = q^2\left[r/q^2 + 1 + i\omega/Dq^{a+2}\right] . \tag{2.81}$$

This can be compared with the general scaling form

$$\chi^{-1}_{\boldsymbol{q},\omega} = q^{2-\eta}\hat{\chi}_+(r/q^{1/\nu}, w/Dq^z)^{-1} , \tag{2.82}$$

to extract the static critical exponent $\nu = 1/2$ related to the divergence of the correlation length ξ_ϕ at the critical point, the anomalous scaling dimension $\eta = 0$ for the algebraic decay of the correlations at $r = 0$, and the dynamic critical exponent

$$z = 2 + a = \begin{cases} 2 & \text{model A,} \\ 4 & \text{model B.} \end{cases} \tag{2.83}$$

2.9 Dean-Kawasaki Equation

In this Section, we report a brief derivation of the stochastic dynamics of the global density field $\rho(\boldsymbol{x},t)$ related to an ensemble of N interacting particles. The resulting SDE has been first derived by Dean [72] and Kawasaki [73], and therefore goes under the name of *Dean-Kawasaki equation*. In the following, we will take the route presented by Dean. Let us consider a collection of N particles with positions $\{\boldsymbol{X}_i\}$, interacting via a pairwise potential $V(\boldsymbol{X}_i - \boldsymbol{X}_j)$. These particles are coupled to a thermal bath with temperature T, and their stochastic evolution in the overdamped regime is ruled by the Langevin dynamics

$$\dot{\boldsymbol{X}}_i = -\nu \sum_{j=0}^{N-1} \nabla V(\boldsymbol{X}_i(t) - \boldsymbol{X}_j(t)) + \boldsymbol{\xi}_i(t)\,, \tag{2.84}$$

with ν the mobility coefficient and $\{\boldsymbol{\xi}_i\}$ a set of N independent zero-mean white Gaussian noises with variance $2\nu T$. For simplicity, we assume that the potential $V(\boldsymbol{X}_i - \boldsymbol{X}_j)$ is such that two particles do not experience any interaction force when they overlap, i.e., $\nabla V(\boldsymbol{0}) = \boldsymbol{0}$. Importantly, note that Eq. (2.84) is characterized by additive noise, and thus all stochastic calculi would produce the same results. In particular, for convenience in the forthcoming derivation, we will adopt the Itô interpretation. As anticipated, the aim of this Section is to derive a SDE that describes the hydrodynamic fluctuations of the global density $\rho(\boldsymbol{x}, t)$, which is defined as:

$$\rho(\boldsymbol{x}, t) = \sum_{i=0}^{N-1} \rho_i(\boldsymbol{x}, t) = \sum_{i=0}^{N-1} \delta^d(\boldsymbol{X}_i(t) - \boldsymbol{x})\,, \tag{2.85}$$

with $\rho_i(\boldsymbol{x}, t) = \delta^d(\boldsymbol{X}_i(t) - \boldsymbol{x})$ the density of a single particle i. The evolution of $\rho_i(\boldsymbol{x}, t)$ can be obtained by considering a generic function $f(\boldsymbol{X}_i)$ of the position $\boldsymbol{X_i}$, which can be rewritten as

$$f(\boldsymbol{X}_i(t)) = \int \mathrm{d}^d\boldsymbol{x}\, \rho_i(\boldsymbol{x}, t) f(\boldsymbol{x}) \tag{2.86}$$

due to the definition of the particle density $\rho_i(\boldsymbol{x}, t)$, and by computing its time derivative. Using the multivariate Itô lemma (2.15) and integrating by parts, it is straightforward to get:

$$\partial_t \rho_i(\boldsymbol{x}, t) = -\nabla \cdot \left[-\rho_i(\boldsymbol{x}, t) \sum_{j=0}^{N-1} \nabla V(\boldsymbol{x} - \boldsymbol{X}_j(t)) - T\nabla\rho_i(\boldsymbol{x}, t) + \rho_i(\boldsymbol{x}, t)\boldsymbol{\xi}_i(t) \right]\,, \tag{2.87}$$

which shows that each particle density ρ_i evolves according to a continuity equation with a fluctuating flux. Moreover, by using again the definition of ρ_i, we can rewrite the drift term as

$$-\rho_i(\boldsymbol{x}, t) \sum_{j=0}^{N-1} \nabla V(\boldsymbol{x} - \boldsymbol{X}_j(t)) = -\rho_i(\boldsymbol{x}, t) \int \mathrm{d}^d\boldsymbol{y}\, V(\boldsymbol{x} - \boldsymbol{y}) \rho(\boldsymbol{y}, t)\,. \tag{2.88}$$

By summing Eq. (2.87) over the index i, we get the fluctuating dynamics of the global density

$$\begin{aligned}\partial_t \rho(\boldsymbol{x}, t) = &- \nabla \cdot \left[-\rho(\boldsymbol{x}, t) \int \mathrm{d}^d \boldsymbol{y} \, V(\boldsymbol{x} - \boldsymbol{y}) \rho(\boldsymbol{y}, t) - T \nabla \rho(\boldsymbol{x}, t) \right] \\ &+ \sum_{i=0}^{N-1} \boldsymbol{\xi}_i(t) \cdot \nabla \rho_i(\boldsymbol{x}, t) \,.\end{aligned} \tag{2.89}$$

However, differently from the deterministic part of this continuity equation, which only depends on the global density ρ, the noise term in the second line is still a function of the particle densities $\{\rho_i\}$. For later convenience, we call this noise

$$\zeta(\boldsymbol{x}, t) = \sum_{i=0}^{N-1} \boldsymbol{\xi}_i(t) \cdot \nabla \rho_i(\boldsymbol{x}, t) \,. \tag{2.90}$$

Let us analyze the statistical properties of $\zeta(\boldsymbol{x}, t)$. It is easy to verify that its average vanishes at all times, i.e.,

$$\langle \zeta(\boldsymbol{x}, t) \rangle = \sum_{i=0}^{N-1} \langle \boldsymbol{\xi}_i(t) \rangle \cdot \langle \nabla \rho_i(\boldsymbol{x}, t) \rangle = 0 \,, \tag{2.91}$$

where the average factorizes by virtue of the Itô calculus. Analogously, the two-point correlations are given by:

$$\langle \zeta(\boldsymbol{x}, t) \zeta(\boldsymbol{y}, s) \rangle = \sum_{ij} \sum_{\alpha\beta} \nabla_{\boldsymbol{x}}^\alpha \nabla_{\boldsymbol{y}}^\beta \langle \xi_i^\alpha(t) \xi_j^\beta(s) \rho_i(\boldsymbol{x}, t) \rho_j(\boldsymbol{y}, s) \rangle \,. \tag{2.92}$$

When $t > s$, the average above can be split into $\langle \xi_i^\alpha(t) \rangle \langle \xi_j^\beta(s) \rho_i(\boldsymbol{x}, t) \rho_j(\boldsymbol{y}, s) \rangle = 0$ because of Itô calculus, which makes the noise at time t independent also of the density at the same time. Similarly, the correlation vanishes also when $s > t$. This implies that the noise $\zeta(\boldsymbol{x}, t)$ is actually white, namely:

$$\begin{aligned}\langle \zeta(\boldsymbol{x}, t) \zeta(\boldsymbol{y}, s) \rangle &= \sum_{ij} \sum_{\alpha\beta} \nabla_{\boldsymbol{x}}^\alpha \nabla_{\boldsymbol{y}}^\beta \langle \xi_i^\alpha(t) \xi_j^\beta(s) \rangle \langle \rho_i(\boldsymbol{x}, t) \rho_j(\boldsymbol{y}, s) \rangle \\ &= 2\nu T \sum_{i=0}^{N-1} \sum_{\alpha=0}^{d-1} \nabla_{\boldsymbol{x}}^\alpha \nabla_{\boldsymbol{y}}^\alpha \delta(t - s) \langle \rho_i(\boldsymbol{x}, t) \rho_i(\boldsymbol{y}, t) \rangle \\ &= 2\nu T \sum_{\alpha=0}^{d-1} \nabla_{\boldsymbol{x}}^\alpha \nabla_{\boldsymbol{y}}^\alpha \delta(t - s) \delta^d(\boldsymbol{y} - \boldsymbol{x}) \langle \rho(\boldsymbol{x}, t) \rangle \,.\end{aligned} \tag{2.93}$$

Note that $\langle \rho_i(\boldsymbol{x}, t) \rangle = \langle \delta^d(\boldsymbol{X}_i(t) - \boldsymbol{x}) \rangle$ is actually equal to the deterministic one-body and one-time probability density as defined in Eq. (2.16). By an analogous argument as the one reported for the two-point correlations, one can derive the n-point correlations with the help of Itô calculus and verify that the noise $\zeta(\boldsymbol{x},t)$ is Gaussian. Interestingly, this implies that $\zeta(\boldsymbol{x},t)$ is statistically equivalent to the noise $\zeta'(\boldsymbol{x},t)$ defined as:

$$\zeta'(\boldsymbol{x},t) = \nabla \cdot \left(\sqrt{2\nu T \rho(\boldsymbol{x},t)} \boldsymbol{\Lambda}(\boldsymbol{x},t) \right) , \tag{2.94}$$

with $\boldsymbol{\Lambda}(\boldsymbol{x},t)$ a zero-mean Gaussian white noise field with correlations

$$\langle \Lambda^\alpha(\boldsymbol{x},t) \Lambda^\beta(\boldsymbol{y},s) \rangle = \delta_{\alpha\beta} \delta(t-s) \delta^d(\boldsymbol{y}-\boldsymbol{x}) \, . \tag{2.95}$$

Hence, we can replace $\zeta(\boldsymbol{x},t)$ with $\zeta'(\boldsymbol{x},t)$ in Eq. (2.89) and finally obtain the Dean-Kawasaki equation

$$\begin{aligned} \partial_t \rho(\boldsymbol{x},t) = &- \nabla \cdot \left[-\rho(\boldsymbol{x},t) \int \mathrm{d}^d \boldsymbol{y} \, V(\boldsymbol{x}-\boldsymbol{y}) \rho(\boldsymbol{y},t) - T \nabla \rho(\boldsymbol{x},t) \right] \\ &+ \nabla \cdot \left(\sqrt{2\nu T \rho(\boldsymbol{x},t)} \boldsymbol{\Lambda}(\boldsymbol{x},t) \right) , \end{aligned} \tag{2.96}$$

which has to be interpreted according to the Itô convention. This stochastic differential equation is non-linear and features a multiplicative noise, in that the amplitude of the global density fluctuations depends on the density itself, as evident from Eq. (2.94). This is expected, as the intuition suggests that in those regions where the number of particles is very small, the density fluctuations should also be moderate. Furthermore, being a continuity equation, (2.96) models the evolution of a locally conserved density field. In Chapter 7 we will comment on the relation between the Dean-Kawasaki equation and the model B dynamics described in the Section 2.8.

2.10 Odd diffusion

In the last Section of this Chapter, we discuss the stochastic dynamics of a single colloidal particle with electric charge q under the action of Lorentz force induced by a magnetic field $\boldsymbol{B} = B\hat{\boldsymbol{z}}$ oriented along the z-axis. From this paradigmatic example we shall introduce the concept of odd diffusion, showing that the derivation of the overdamped regime requires a more careful analysis than what previously done in Section 2.1, in that the small mass limit $m \to 0$ hides some subtleties. The colloid motion occurs in the two-dimensional plane perpendicular to the magnetic field $\boldsymbol{B}$, and it is modeled by the underdamped dynamics

$$\begin{cases} \dot{\boldsymbol{X}} = \boldsymbol{v}, \\ m\dot{\boldsymbol{v}} = -\boldsymbol{\Gamma}\boldsymbol{v} + \sqrt{2T/\nu}\boldsymbol{\xi}, \end{cases} \tag{2.97}$$

where $\boldsymbol{\xi}$ is a zero-mean Gaussian white noise with unit variance and the effect of the magnetic field is captured by the friction tensor $\boldsymbol{\Gamma} = \nu^{-1}[\mathbf{1} - \kappa\boldsymbol{\varepsilon}]$. Here,

$\kappa = \nu B$ is the dimensionless *oddness parameter* and $\boldsymbol{\varepsilon}$ the two-dimensional Levi-Civita symbol. Note that we work for simplicity in units such that the electric charge is $q = 1$. The equation for the velocity $\boldsymbol{v}$ is linear and thus can be solved exactly (more details can be found in Appendix E) leading to the following dynamics for the position

$$\dot{\boldsymbol{X}} = \boldsymbol{G}(t - t_0)\boldsymbol{v}(t_0) + \boldsymbol{\eta}(t)\,, \tag{2.98}$$

with $\boldsymbol{v}(t_0)$ the initial velocity of the colloid and the matrix $\boldsymbol{G}(t)$ defined as:

$$\begin{aligned} \boldsymbol{G}(u) &= \Theta(u) e^{-u/\tau_\nu} \boldsymbol{M}(u), \\ \boldsymbol{M}(u) &= \begin{pmatrix} \cos(u/\tau_B) & \sin(u/\tau_B) \\ -\sin(u/\tau_B) & \cos(u/\tau_B) \end{pmatrix}, \end{aligned} \tag{2.99}$$

where we introduced the time scales $\tau_\gamma = \nu m$ and $\tau_B = m/B$. The resulting Gaussian noise term

$$\boldsymbol{\eta}(t) = \sqrt{2T/\tau_\nu m} \int_{t_0}^{t} ds\, \boldsymbol{G}(t-s)\boldsymbol{\xi}(s) \tag{2.100}$$

is colored and characterized by the correlations

$$C_{\alpha\beta}(t,s) = \langle \eta^\alpha(t)\eta^\beta(s)\rangle = \frac{T}{m}\left[e^{-\frac{|t-s|}{\tau_\gamma}} - e^{-\frac{t+s-2t_0}{\tau_\gamma}} \right] M_{\alpha\beta}(t-s)\,. \tag{2.101}$$

In other words, the correlations of the noise $\boldsymbol{\eta}$ decay after a typical time scale τ_ν, which is indeed the characteristic velocity relaxation time, and exhibit oscillations with a period $\tau_B/2\pi$. Starting from the equation of motion in Eq. (2.98) for the position $\boldsymbol{X}$, we want to derive the evolution of the one-time probability density $P_1(\boldsymbol{x}, t)$ as defined in Eq. (2.16), i.e., the Master equation. Note that in this case, the latter does not correspond to the Fokker-Planck equation (2.24) because the underlying stochastic dynamics in Eq. (2.98) is non-Markovian, and therefore we shall use a different route to derive it. For simplicity, we assume that $\boldsymbol{v}(t_0) = 0$. Moreover, we interpret the SDE (2.98) according to the Stratonovich convention, so that the standard rules of calculus apply, and we get:

$$\begin{aligned} \partial_t P_1(\boldsymbol{x}, t) &= -\sum_{\alpha=1}^{d} \nabla_{\boldsymbol{x}}^{\alpha} \langle \delta^d(\boldsymbol{x} - \boldsymbol{X}(t))\eta_\alpha(t)\rangle \\ &= -\sum_{\alpha=1}^{d} \nabla_{\boldsymbol{x}}^{\alpha} \int \mathcal{D}[\boldsymbol{\eta}] \delta^d(\boldsymbol{x} - \boldsymbol{X}(t))\eta_\alpha(t) e^{-\mathcal{S}[\boldsymbol{\eta}]}\,. \end{aligned} \tag{2.102}$$

In the second equality, we used the definition of the average over the noise realizations by introducing the statistical weight $e^{-\mathcal{S}[\boldsymbol{\eta}]}$ (the normalization is absorbed in the measure $\mathcal{D}[\boldsymbol{\eta}]$), with the action $\mathcal{S}$ defined as:

$$\mathcal{S}[\boldsymbol{\eta}] = \frac{1}{2}\sum_{\gamma,\beta=1}^{d}\int_{t_0}^{\infty}\mathrm{d}u\int_{t_0}^{\infty}\mathrm{d}s\,\eta_\gamma(u)C^{-1}_{\gamma\beta}(u,s)\eta_\beta(s)\,. \tag{2.103}$$

For the coming derivation it is useful to compute the following functional derivative of the action $\mathcal{S}$:

$$\frac{\delta\mathcal{S}[\boldsymbol{\eta}]}{\delta\eta_\alpha(t)} = \frac{1}{2}\sum_{\beta=1}^{d}\int_{t_0}^{\infty}\mathrm{d}s\,\eta_\beta(s)\left[C^{-1}_{\alpha\beta}(t,s)+C^{-1}_{\beta\alpha}(s,t)\right]\,, \tag{2.104}$$

with $t > t_0$, which implies

$$\sum_{\gamma=1}^{d}\int_{t_0}^{\infty}\mathrm{d}s\,C_{\alpha\gamma}(t,s)\frac{\delta e^{-\mathcal{S}[\boldsymbol{\eta}]}}{\delta\eta_\gamma(s)} = -\eta_\alpha(t)e^{-\mathcal{S}[\boldsymbol{\eta}]}\,. \tag{2.105}$$

The previous identity can substituted into (2.102), leading to:

$$\begin{aligned}\partial_t P_1(\boldsymbol{x},t) &= \sum_{\alpha,\beta=1}^{d}\nabla^\alpha_{\boldsymbol{x}}\int\mathcal{D}[\boldsymbol{\eta}]\delta^d(\boldsymbol{x}-\boldsymbol{X}(t))\int_{t_0}^{\infty}\mathrm{d}s\,C_{\alpha\beta}(t,s)\frac{\delta e^{-\mathcal{S}[\boldsymbol{\eta}]}}{\delta\eta_\beta(s)}\\ &= -\sum_{\alpha,\beta=1}^{d}\nabla^\alpha_{\boldsymbol{x}}\int_{t_0}^{\infty}\mathrm{d}s\,C_{\alpha\beta}(t,s)\int\mathcal{D}[\boldsymbol{\eta}]e^{-\mathcal{S}[\boldsymbol{\eta}]}\frac{\delta}{\delta\eta_\beta(s)}\delta^d(\boldsymbol{x}-\boldsymbol{X}(t))\\ &= \sum_{\alpha,\beta,\gamma=1}^{d}\nabla^\alpha_{\boldsymbol{x}}\int_{t_0}^{\infty}\mathrm{d}s\,C_{\alpha\beta}(t,s)\nabla^\gamma_{\boldsymbol{x}}\left\langle\delta^d(\boldsymbol{x}-\boldsymbol{X}(t))\frac{\delta X_\gamma(t)}{\delta\eta_\beta(s)}\right\rangle\end{aligned} \tag{2.106}$$

where in the second line we used integration by parts and in the third one the standard chain rule. The average in the last line can be exactly computed due to the linearity of Eq. (2.98), which admits the simple solution $X_\alpha(t) = X_\alpha(t_0) + \int_{t_0}^{t}\mathrm{d}s\,\eta_\alpha(s)$. Therefore, the functional derivative of the position with respect to the noise at a previous time is given by $\delta X_\gamma(t)/\delta\eta_\beta(s) = \delta_{\alpha\beta}\Theta(t-s)$. Thus, the Master equation becomes:

$$\partial_t P_1(\boldsymbol{x},t) = \sum_{\alpha,\beta=1}^{d}\nabla^\alpha_{\boldsymbol{x}}\nabla^\beta_{\boldsymbol{x}}[D_{\alpha\beta}(t)P_1(\boldsymbol{x},t)]\,, \tag{2.107}$$

with the diffusion tensor $D_{\alpha\beta}(t)$ defined as:

$$D_{\alpha\beta}(t) = \int_{t_0}^{t}\mathrm{d}s\,C_{\alpha\beta}(t,s)\,. \tag{2.108}$$

From the solution of the integral above, one can work out the small-mass limit $m \to 0$, and verify that it produces a diffusion tensor characterized by the presence of finite antisymmetric elements proportional to the oddness parameter κ, i.e.,

$$\boldsymbol{D}(t) \overset{\tau_\nu \ll t}{\sim} \frac{\nu T}{1+\kappa^2} \begin{pmatrix} 1 & -\kappa \\ \kappa & 1 \end{pmatrix} , \tag{2.109}$$

and thus the Master equation:

$$\partial_t P_1(\boldsymbol{x}, t) = \frac{\nu T}{1+\kappa^2} \nabla_{\boldsymbol{x}} \cdot \left[\begin{pmatrix} 1 & -\kappa \\ \kappa & 1 \end{pmatrix} \cdot \nabla_{\boldsymbol{x}} P_1(\boldsymbol{x}, t) \right] . \tag{2.110}$$

This implies that the diffusive flux $\boldsymbol{J} = \boldsymbol{D}(t) \cdot \nabla P_1$ is generically not aligned with the gradient of the probability density, but it has a non-zero component also in the direction perpendicular to it, caused by the magnetic field. Note that the effect of the oddness is two-fold: not only it produces fluxes perpendicular to ∇P_1, but also it reduces the scalar diffusion coefficient νT by a factor $(1 + \kappa^2)$. In the derivation above, the evolution of P_1 in the overdamped regime has been obtained by first computing the Master equation from the non-Markovian dynamics in Eq. (2.98) and subsequently by taking the small-mass limit. In what follows, we show that the alternative route that consists in deriving the overdamped dynamics by naively substituting $m = 0$ in Eq. (2.97), actually produces a different and incorrect result. Indeed, in this case, one would get the following stochastic dynamics for the position:

$$\dot{\boldsymbol{X}} = \sqrt{2T/\nu}\, \boldsymbol{\Gamma}^{-1} \cdot \boldsymbol{\xi}(t) , \tag{2.111}$$

which, on the basis of Eq. (2.24), would give a Fokker-Planck equation of the form:

$$\partial_t P_1(\boldsymbol{x}, t) = \frac{T}{\nu} \sum_{\alpha\beta\gamma} \nabla_{\boldsymbol{x}}^{\alpha} \nabla_{\boldsymbol{x}}^{\beta} [\Gamma^{-1}_{\alpha\gamma} \Gamma^{-1}_{\beta\gamma} P_1(\boldsymbol{x}, t)] = \frac{\nu T}{1+\kappa^2} \nabla^2_{\boldsymbol{x}} P_1(\boldsymbol{x}, t) . \tag{2.112}$$

One can immediately see that this FPE correctly captures the reduction of the scalar diffusion coefficient $\nu T/(1+\kappa^2)$, but it misses the off-diagonal terms of the diffusion tensor. From the point of view of the one-time probability density, this is not necessarily a problem. Indeed, Eqs. (2.112) and (2.110) are solved by the same $P_1(\boldsymbol{x}, t)$ at all times t. However, if one is interested in any observable that depends on the fluxes, the correct equation to look at is Eq. (2.110). The subtlety about the overdamped limit of odd diffusive systems discussed here will turn out to be useful later on in Chapter 7.

Chapter 3

Active chiral molecules in activity gradients

Living matter at the micron scale is able to perform a wide variety of complex motions and behaviors, see, e.g., Refs. [87, 88]. This requires sensing chemical and structural properties of the environment, processing this information by complex biochemical networks, and adapting the behavior accordingly [89–91]. For example, the bacterium *E. coli* measures the local nutrient concentration while it swims, and compares that with the concentration in the past. If the current concentration is getting lower (higher), it increases (decreases) its tumble rate. This strategy results in chemotaxis, i.e., in a preferential accumulation in spatial regions where the nutrient concentration is larger [92, 93].

Active particles are regarded as the simplest models for motility in living systems. While they share the essential features with the bacteria, namely self-propulsion and persistence, their response to local fuel concentration is rather simple: they merely adjust their speed in proportion to the local fuel concentration [94–98], a mechanism known as orthokinesis [49]. As a consequence, active particles subjected to fuel gradients, preferentially accumulate in regions where the fuel concentration is low [50, 99], i.e., where they are less agitated. Nevertheless, the ability to steer active particles towards specific and predetermined target zones – artificial chemotaxis – remains a highly sought property of synthetic active matter. While this has been demonstrated experimentally via elaborate feedback mechanisms [100–102], where an external stimulus is applied to the particle as a function of its state (position and/or orientation), the continuous monitoring of the particle state might not always be possible. Therefore, an autonomous approach where some form of feedback emerges spontaneously is much more desirable, and can correctly steer the active particle towards the target without requiring external stimuli. Recently, it has been shown that a chemotactic-like behavior can emerge in a system of cargo-carrying active particles [103]. While active particles with a light cargo accumulate in regions of low activity, a crossover occurs upon increasing the cargo such that the active-passive complex accumulates in regions of high activity. In the case of a heavy cargo, which moves much more slowly than the active particle, the latter *performs* a local integration of the activity profile in the neighborhood of the attached cargo, resulting in a net force towards the regions of higher activity and thus giving rise to chemotactic behavior. Active particles connected in a chain to form polymers, have also recently attracted significant attention [104–109]. In particular, the interaction of the active sub-units might lead to fascinating behaviors when the chain is dispersed in a non-uniform active bath (see Chapter 5 for a detailed description).

In this Chapter, we extend the idea of emergent chemotaxis to colloidal molecules made of active chiral particles (ACPs). Specifically, we consider a dimer composed by two interacting self-propelled particles, whose rotational dynamics is driven by opposite active torques (see the left sketch in Figure 3.1). This dimeric complex evolves in a medium characterized by an activity gradient. We show that upon increasing the torque, the active chiral dimer switches its behavior from antichemotactic to chemotactic and it accumulates in regions of high activity. While the behaviour of active colloidal molecules is well understood for a constant activity [110, 111], the effect of activity gradients is much less explored. Recent studies showed how a rigid dimer composed by two active particles with orientations fixed with respect to the connecting bond behaves in activity gradients [112]. By contrast, in the case of interacting active chiral particles analyzed in this Chapter, the orientation of the two particles evolves freely due to thermal fluctuations and active torques.

Active chiral particles exhibit odd-diffusive motion on time scales longer than the persistence time [113–115]. The diffusion tensor that characterizes their overdamped motion contains both a symmetric and an antisymmetric part. Both passive and self-propelled charged Brownian particles also perform odd-diffusive motion under the effect of the Lorentz force, see, e.g., [116–119] and the derivation presented in Sec. 2.10. While active chiral particles rotate due to the microscopic active torque, in the case of charged particles under magnetic field a certain handedness is introduced by the Lorentz force. On a coarse grained level, where one integrates out the orientational degree of freedom, the two systems present many similarities. The two model systems can even be mapped into one another for homogeneous magnetic field, activity and torque. However, the mapping does not hold in general. We show this explicitly by analyzing their chemotactic behavior: a dimer composed of oppositely charged active particles always accumulates in the regions of low activity independently of the applied magnetic field. Note that in the derivation presented here, we neglect the electrostatic interaction between the two monomers.

The present Chapter is organized as follows. In Sec. 3.1, we present our model of a dimer composed of two active chiral particles, the polarity of which is driven

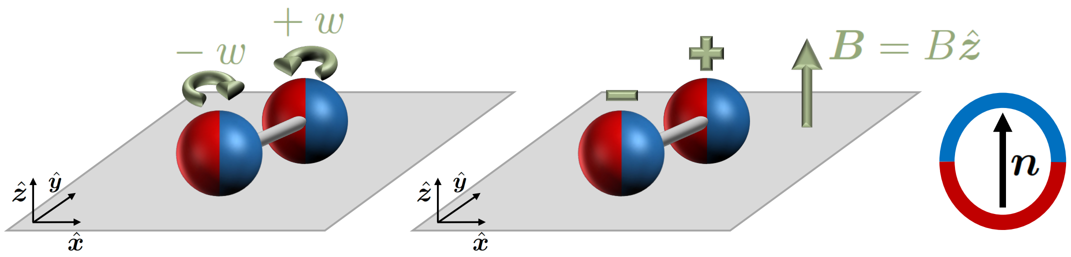

Figure 3.1: Schematic representation of the dimeric molecules analyzed in this Chapter. Left panel: interacting self-propelled particles (depicted as Janus particles) the polarity of which is subjected to an active torque (green circular arrows). The two monomers experience opposite torques $\pm w$. Central panel: interacting, self-propelled particles with opposite electric charges subjected to a magnetic field $\boldsymbol{B}$ along the z-direction. The effect of the Lorentz force induces the odd-diffusive behavior of the two particles. Right panel: sketch of the polarity vector $\boldsymbol{n}$ for a Janus-like particle, which sets the direction of the self-propulsion force.

by opposite active torques with the same magnitude. In Sec. 3.2, with the help of a multipole expansion and of the small-gradient approximation, we derive an effective coarse-grained Fokker-Planck equation for the one-time probability density of the center of mass of the dimer. Its analytical solution at steady state is then given and discussed in Sec. 3.3. In Secs. 3.4 and 3.5, inspired by the similarity between an ACP and a charged self-propelled particle subject to the Lorentz force in terms of their odd-diffusive behaviour, we construct a dimer of active charged particles under the action of a magnetic field, as sketched in the central panel of Figure 3.1, showing that its chemotactic-like behavior, contrary to ACPs, does not change. Finally, in Sec. 3.6, we discuss possible experimental realizations and present a brief outlook for future works.

The analysis presented in this Chapter has been published in Ref. [120].

3.1 Interacting Active Chiral Particles

We consider two active chiral particles interacting via an attractive potential $U(\boldsymbol{x})$ (e.g., an harmonic potential with zero rest length or a rigid rod) and evolving in a 2-dimensional medium. Their positions at time t are denoted with the vectors $\boldsymbol{X}_0(t)$ and $\boldsymbol{X}_1(t)$. The two particles are coupled to a thermal bath with temperature T and are subject to additional self-propulsion forces along their orientation vectors $\boldsymbol{n}_i = (\cos\theta_i, \sin\theta_i)$, with $i \in \{0, 1\}$, which are parametrized by their polar angles $\{\theta_i\}$. These active forces introduce a violation of the fluctuation-dissipation relation, thus driving the system out of equilibrium. We neglect the effects of inertia compared to the viscous forces and describe the stochastic evolution of the dimer by means of the following overdamped Langevin dynamics:

$$\begin{cases} \dot{\boldsymbol{X}}_i = -\nu \nabla_i U(\boldsymbol{X}_0 - \boldsymbol{X}_1) + \nu f_a(\boldsymbol{X}_i)\boldsymbol{n}_i + \sqrt{2D_T}\boldsymbol{\xi}_i(t)\,, \\ \dot{\theta}_i = \omega_i + \sqrt{2D_R}\eta_i(t)\,, \end{cases} \tag{3.1}$$

where $\{\boldsymbol{\xi}_i\}$ and $\{\eta_i\}$ are independent zero-mean Gaussian white noises with the following statistical properties:

$$\begin{aligned} \langle \xi_i^\alpha(t)\xi_j^\beta(s)\rangle &= \delta_{ij}\delta_{\alpha\beta}\delta(t-s)\,, \\ \langle \eta_i(t)\eta_j(s)\rangle &= \delta_{ij}\delta(t-s)\,. \end{aligned} \tag{3.2}$$

The two ACPs have the same mobility coefficient ν, translational diffusion coefficient $D_T = \nu T$ and rotational diffusion coefficient D_R. Note that the translational diffusion coefficient D_T is related to the temperature T and the mobility ν by the Einstein relation, so that, in the absence of activity, the stochastic dynamics in Eq. (3.1) satisfies the detailed balance condition. As anticipated, the two ACPs are self-propelled along the direction given by their orientation vectors $\{\boldsymbol{n}_i\}$. Importantly, the modulus of the active forces is non-uniform in space and modulated by the function $f_a(\boldsymbol{x})$, which we assume to be determined by some local fuel concentration. In the following, we will denote with $v_a(\boldsymbol{x}) = \nu f_a(\boldsymbol{x})$ the typical swim speed of the particles due to activity, which we will sometimes call activity field. In addition to (thermal) rotational diffusion, both particles experience homogeneous torques $\{w_i\}$ along the direction perpendicular to the plane of motion, which produce a systematic rotation of their polarity around the fixed z-axis. In this Chapter, we restrict our analysis to the case in which the two active particles are subject to opposite torques of the same magnitude, i.e., $\omega_0 = -\omega_1 = \omega$. Note that in the rotational dynamics (3.1) we do not consider any explicit alignment of the polarities with the activity gradient [40, 121]. In fact, their possible interaction with $\nabla v_a(\boldsymbol{x})$ would introduce an explicit bias for the particles to move along or against the activity gradient, depending on the sign of their coupling. However it would depend on the specific self-propulsion mechanism which we would like to keep unspecified in our model. As a consequence, we neglect this possible mesoscopic coupling. We also ignore the hydrodynamic interaction between the two particles, and its effect on the self-propulsion [122–125]. In spite of these simplifications, the interplay between the rotational diffusion due to thermal fluctuations and the active torque determines the behaviour of the dimer in a non-homogeneous activity field, as shown in the following Sections.

3.2 Multipole expansion and effective dynamics

Our primary goal of this Section is to analyze the response to activity gradients of two interacting active chiral particles forming a dimer. In particular, we want to understand whether in the long-time limit this dimer preferentially localizes in regions of high or low activity. To this aim, we derive an effective dynamics for the probability density of the center of mass $\boldsymbol{R} = (\boldsymbol{X}_0 + \boldsymbol{X}_1)/2$, and integrate out the polarity variables $\{\theta_i\}$ as well as the relative distance $\boldsymbol{r} = \boldsymbol{X}_0 - \boldsymbol{X}_1$ between the active particles. Our starting point is the Fokker-Planck equation that governs the evolution of the one-time joint probability density $P_1(\boldsymbol{R}, \boldsymbol{r}, \theta_1, \theta_2, t)$. This is given by:

$$\partial_t P_1(\boldsymbol{R}, \boldsymbol{r}, \theta_0, \theta_1, t) = [\mathcal{L}_{\boldsymbol{R}} + \mathcal{L}_{\boldsymbol{r}} + \mathcal{L}_w + \mathcal{R}^2] P_1 \tag{3.3}$$

where the operators $\mathcal{L}_{\boldsymbol{R}}$ and $\mathcal{L}_{\boldsymbol{r}}$ are related to the stochastic dynamics of the center of mass $\boldsymbol{R}$ and the relative distance $\boldsymbol{r}$, respectively, and are defined as:

$$\begin{aligned} \mathcal{L}_{\boldsymbol{R}} &= -\frac{1}{2}\nabla_{\boldsymbol{R}} \cdot \Big[v_a\Big(\boldsymbol{R} + \boldsymbol{r}/2\Big)\boldsymbol{n}_0 + v_a\Big(\boldsymbol{R} - \boldsymbol{r}/2\Big)\boldsymbol{n}_1 - D_T \nabla_{\boldsymbol{R}} \Big] \,, \\ \mathcal{L}_{\boldsymbol{r}} &= -\nabla_{\boldsymbol{r}} \cdot \Big[-2\nu \nabla U(\boldsymbol{r}) + v_a\Big(\boldsymbol{R} + \boldsymbol{r}/2\Big)\boldsymbol{n}_0 - v_a\Big(\boldsymbol{R} - \boldsymbol{r}/2\Big)\boldsymbol{n}_1 - 2D_T \nabla_{\boldsymbol{r}} \Big] \,, \end{aligned} \tag{3.4}$$

whereas $\mathcal{L}_w$ and $\mathcal{R}^2$ derive from the rotational dynamics of the orientation vectors and are given by:

$$\begin{aligned} \mathcal{L}_w &= \omega \left(\frac{\partial}{\partial \theta_1} - \frac{\partial}{\partial \theta_0} \right) \,, \\ \mathcal{R}^2 &= D_R \left(\frac{\partial^2}{\partial \theta_1^2} + \frac{\partial^2}{\partial \theta_0^2} \right) \,. \end{aligned} \tag{3.5}$$

In particular, $\mathcal{L}_w$ depends on the active torque that systematically rotates the orientation vectors producing the circular motion of the two particles, while $\mathcal{R}^2$ is the rotational diffusion operator in 2-dimensions, analogous to the one introduced in Eq. (2.45) for a single particle. To eliminate the orientational degrees of freedom, we expand the joint probability density $P(\boldsymbol{R}, \boldsymbol{r}, \theta_0, \theta_1, t)$ in eigenfunctions of the operator $\mathcal{R}^2$. The first eigenfunctions are given by 1, $\{\boldsymbol{n}_i\}$, $\boldsymbol{n}_0 \otimes \boldsymbol{n}_1$, $\{\boldsymbol{n}_i \otimes \boldsymbol{n}_i - \boldsymbol{1}/d\}$. This leads to the so-called Cartesian multipole expansion (see, e.g., [24, 126]), which reads as follows:

$$\begin{aligned} P_1(\boldsymbol{R}, \boldsymbol{r}, \theta_1, \theta_2, t) = \frac{1}{\Omega_2^2} \Big[&\phi + \boldsymbol{\sigma}_0 \cdot \boldsymbol{n}_0 + \boldsymbol{\sigma}_1 \cdot \boldsymbol{n}_1 + \boldsymbol{\Sigma} : \boldsymbol{n}_0 \boldsymbol{n}_1 \\ &+ \boldsymbol{w}_1 : \Big(\boldsymbol{n}_0 \boldsymbol{n}_0 - \frac{\boldsymbol{1}}{2} \Big) + \boldsymbol{w}_2 : \Big(\boldsymbol{n}_1 \boldsymbol{n}_1 - \frac{\boldsymbol{1}}{2} \Big) + \ldots \Big] \,, \end{aligned} \tag{3.6}$$

where the symbol : denotes the double contraction and Ω_d the solid angle in d spatial dimensions. In particular, in $d = 2$, one has $\Omega_2 = 2\pi$. In Eq. (3.6) we introduced the dipole moments $\{\boldsymbol{\sigma}_i\}$ and the quadrupole moments $\{\boldsymbol{w}_i\}$, which are related to the local polar and nematic order parameters [127], respectively. Moreover, we introduced, the rank-2 tensor $\boldsymbol{\Sigma}$, which is the expansion coefficient associated to the dyadic product $\boldsymbol{n}_0\boldsymbol{n}_1$. Note that all these expansion coefficients depend on the position $\boldsymbol{R}$ of the center of mass, the relative distance $\boldsymbol{r}$, and the time t. Their evolution equation can be obtained by projecting the FPE onto their relative eigenfunctions, as detailed in Appendix A.1. The resulting differential equations are highly coupled and arranged in a hierarchical structure. Analytical progresses can be made by assuming that the activity field is characterized by small spatial variations on a length scale given by the persistence length $\ell_p \sim v_a\tau$, and using the time scale separation between $\phi(\boldsymbol{R}, \boldsymbol{r}, t)$ and the higher-order expansion coefficients. Indeed, while the average polarizations $\{\boldsymbol{\sigma}_i\}$ and nematic parameters $\{\boldsymbol{w}_i\}$ relax on typical time scales proportional to the persistence time τ, the coefficient ϕ is actually related to the coarse-grained probability density

$$\rho(\boldsymbol{R}, t) = \int \mathrm{d}\boldsymbol{r}\, \phi(\boldsymbol{R}, \boldsymbol{r}, t) \tag{3.7}$$

of finding the dimer (i.e., its center of mass) at position $\boldsymbol{R}$ at time t, and thus its evolution is governed by a continuity equation. This implies that large-wavelength perturbations in the density relax very slowly compared to $\{\boldsymbol{\sigma}_i\}$ and $\{\boldsymbol{w}_i\}$. Details about the coarse-graining procedure and the derivation of the effective dynamics for $\rho(\boldsymbol{R}, t)$ are reported in Appendix A.1. In particular, when the attractive interaction between the active particles is given by a harmonic potential with zero rest length and stiffness κ, i.e., $U(\boldsymbol{r}) = \kappa \boldsymbol{r}^2/2$, the coarse-grained density $\rho(\boldsymbol{R})$, follows the following Fokker-Planck equation:

$$\partial_t \rho(\boldsymbol{R}) = -\nabla_{\boldsymbol{R}} \cdot \Big[\boldsymbol{V}(\boldsymbol{R})\rho(\boldsymbol{R}) - \nabla_{\boldsymbol{R}}(D(\boldsymbol{R})\rho(\boldsymbol{R}))\Big] , \tag{3.8}$$

where the effective diffusivity $D(\boldsymbol{R})$ and the effective drift $\boldsymbol{V}(\boldsymbol{R})$ are given, respectively, by

$$\begin{aligned} D(\boldsymbol{R}) &= \frac{1}{1+\Omega^2}\frac{v_a^2(\boldsymbol{R})}{4D_R} + \frac{D_T}{2} , \\ \boldsymbol{V}(\boldsymbol{R}) &= (1-\epsilon/2)\nabla_R D(\boldsymbol{R}) . \end{aligned} \tag{3.9}$$

Here, we introduced the dimensionless quantity

$$\Omega = \omega / D_R \tag{3.10}$$

given by the ratio of the angular velocity ω induced by the active torque and the inverse decorrelation time D_R due to rotational diffusion (see Eq. (2.40)). Moreover, we introduce the dimensionless parameter

$$\tau = D_R/(2\kappa\nu) \tag{3.11}$$

given by the ratio between the rotational diffusion D_R and the relaxation rate $2\kappa\nu$ of the relative distance $\boldsymbol{r}$. In other words, Ω and τ express the active torque and the relaxation time of the relative distance $\boldsymbol{r}$ in units of the rotational diffusion time scale, D_R^{-1}. In terms of the dimensionless quantities Ω and τ, the coupling ϵ that appears in the effective drift in Eq. (3.9) reads

$$\epsilon = \frac{[1+(1-\Omega^2)\tau]\,(1+\Omega^2)}{[1+(1-\Omega^2)\tau]^2 + [\Omega\,(1+2\tau)]^2}\,. \tag{3.12}$$

The important role played by the parameter ϵ is discussed in the Section below.

3.3 Stationary density

Due to the simple derivative relation between the effective drift and diffusion terms in Eq. (3.9), it is straightforward to determine the steady-state density $\rho(\boldsymbol{R})$ without the need of specifying the form of the activity field $v_a(\boldsymbol{R})$. By imposing the zero-flux condition $\boldsymbol{V}\rho = \nabla(D\rho)$ in Eq. (3.8), one obtains for the density

$$\rho(\mathbf{R}) \propto \left[1 + \frac{1}{D_T}\frac{1}{1+\Omega^2}\frac{v_a^2(\mathbf{R})}{2D_R}\right]^{-\epsilon/2}. \tag{3.13}$$

In the absence of activity (i.e., $v_a(\boldsymbol{R}) = 0$) the system reduces to a dimer of passive Brownian particles, so we expect a standard diffusive process leading to flat distribution in the long-time limit. Note that if $v_a(\boldsymbol{R}) = 0$, the position of the dimer is decoupled from the rotational degrees of freedom, and the polarities $\{\boldsymbol{n}_i\}$ do not play any role in the dynamics. In the case of spatially homogeneous activity, i.e., $v_a(\boldsymbol{R}) = v_0$ with a constant v_0, the symmetry of the system imposes again flat steady state distribution. Indeed, the spatial dependence of $\rho(\boldsymbol{R})$ in Eq. (3.13) is a consequence of the broken spatial translation invariance introduced by the non-uniform activity field.

For a generic spatially varying $v_a(\boldsymbol{R})$, the way the activity affects the steady-state density depends on the sign of the coupling ϵ, which, in turn, is determined by the relative importance of the following two terms: $1+\tau$ and $\Omega^2\tau$. At fixed relaxation time of the relative distance $\boldsymbol{r}$, the competition between the rotational diffusion and the deterministic active rotation of $\boldsymbol{n}_i$ can lead to qualitatively different scenarios. In particular if $1+\tau > \Omega^2\tau$, the exponent ϵ in Eq. (3.12) is positive and the density peaks in regions with lower activity. Since the activity

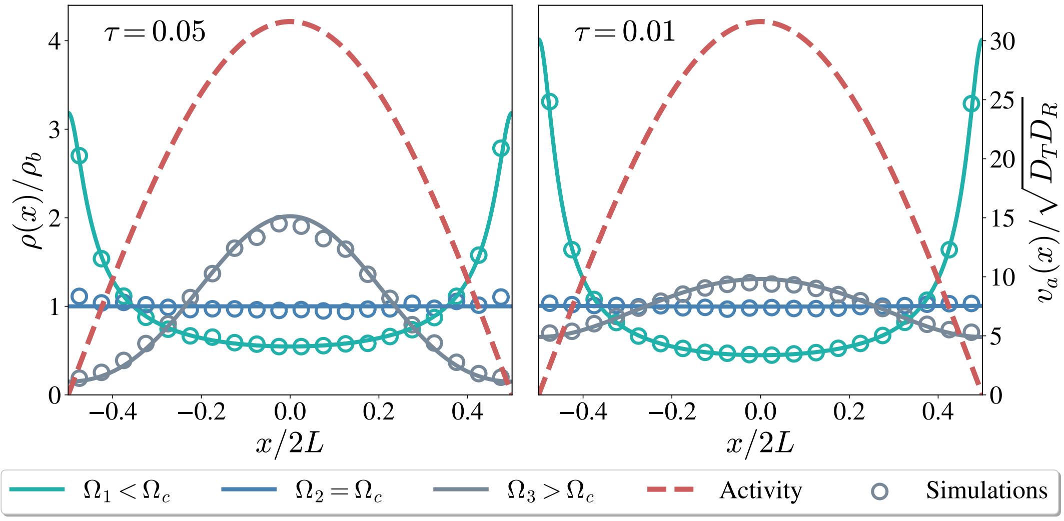

Figure 3.2: Steady-state density of dimers made of active chiral particles with opposite torques, in $d = 2$ spatial dimensions. All lengths and times in the plots are measured in units of $l = \sqrt{D_T/D_R}$ and $\tau_R = 1/D_R$, respectively. The numerical estimation of the spatial density ρ has been carried out by computing the histograms of the time series coming from Brownian dynamics simulations of Eq. (3.1). Both analytical (solid line) and numerical (symbols) results have been obtained by adopting periodic boundary conditions. The dashed red curve represents the activity field, which we take as homogeneous along the y-direction and varying according to $v_a(x) = 10\sqrt{10}\sin\left(\frac{\pi}{2L}x + \frac{\pi}{2}\right)$ (in units of $\sqrt{D_T D_R}$) along the x-direction, with $2L$ the elementary cell size. Since the system is invariant under translations along the y-direction, we report here the marginal distribution $\rho(x)$ divided by the bulk density ρ_b. In each panel, the transition from antichemotactic to chemotactic behavior is clearly observed upon increasing the value of Ω. The two panles are characterized by different spring relaxation times τ. In particular, for higher stiffness κ (i.e., smaller value of τ, right panel), the density peak observed in the chemotactic regime is broader and the dimer is less localized compared to the case of lower stiffness (left panel). Simulations have been carried out with the following parameters: $\Omega_1 = 2 < \Omega_c$, $\Omega_2 = 4.58257 \approx \Omega_c$, $\Omega_3 = 10 > \Omega_c$, $\tau = 0.05$ on the left panel, and $\Omega_1 = 2 < \Omega_c$, $\Omega_2 = 10.05 \approx \Omega_c$, $\Omega_3 = 15 > \Omega_c$, $\tau = 0.01$ on the right panel.

field might reflect some local fuel concentration, we refer to this behavior as antichemotactic. On the contrary, if $1 + \tau < \Omega^2 \tau$, the dimer typically spends more time in high-activity regions. We call this phenomenon chemotaxis. The crossover between these two regimes as a function of Ω occurs at the critical value:

$$\Omega_c = \frac{\omega_c}{D_R} = \sqrt{\frac{1+\tau}{\tau}}, \tag{3.14}$$

at which the steady state is characterized by a homogeneous density distribution. Figure 3.2 shows the stationary density distribution of active dimers for three different values of ω obtained from Brownian dynamics simulations of Eq. (3.1), denoted by the symbols in the various plots. The theoretical predictions of Eq. (3.13), reported as solid lines, turn out to be in very good agreement with the numerical simulations.

At this stage, the following question arises: what is the mechanism responsible for the emergence of a chemotactic phase and why does it require torque values above a certain threshold? To start addressing this point we focus on the limiting case in which the time scale of rotational diffusion is much larger than the relaxation time scale of the relative distance and that of the active torque, i.e., $\tau \ll 1$ and $\Omega \gg 1$, respectively. We qualitatively describe the emergence of the chemotactic behavior predicted by the model in this regime $(1 + \tau \ll \Omega^2 \tau)$ with the help of a schematic representation of the dynamics shown in Figure 3.3. Let us consider a configuration of the dimer in which one of the particles' orientation is in the direction of increasing activity whereas that of the other is in the opposite direction. In this configuration, the dimer is typically stretched and it experiences a translation towards the higher activity region. Accordingly, the dimer climbs up the activity gradient and the distance between the two particles increases. As the dimer climbs up, the orientations of the two particles evolve due to the active torque such that after some time $(\sim 1/(2\omega))$ they point towards each other. In this configuration, the dimer experiences a drift towards the low-activity region. The dimer thus climbs down the activity gradient, however, while the dimer descends the activity gradient, the two particles approach each other such that the net downwards drift continuously decreases before the two particles again point outwards as in the initial configuration. Overall, while climbing up the dimer experiences larger translation due to the two particles getting distant from each other than during the climb down when the two particles approach each other. In a cycle of period $1/\omega$, the dimer performs a forward and backward motion, with net drift towards the region of higher activities. We based our reasoning on a particular initial configuration. In general, if the rotational diffusion is negligible with respect to the deterministic torque, the mechanism will be somewhat different depending on the initial configuration, but in no case it will bias the motion toward region of lower activity. Note that for biased movement along the direction of

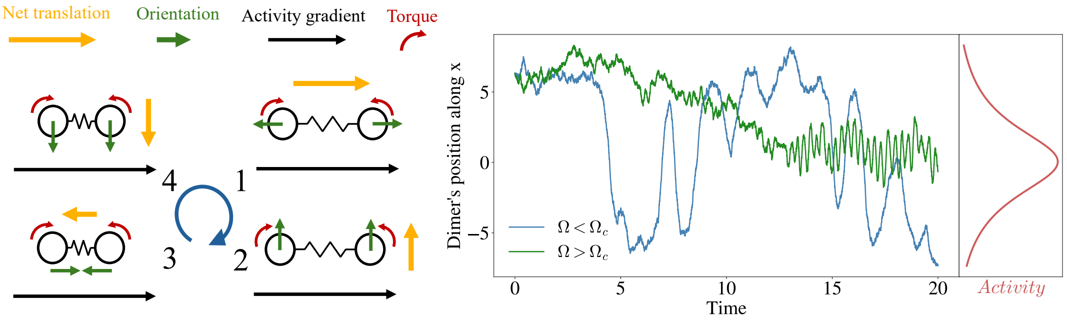

Figure 3.3: Left panel: schematic representation of the mechanism leading to chemotaxis in the case of a dimer made by two active chiral particles with opposite and homogeneous torques (red arrows). The cycle of four configurations (numbered 1, 2, 3, and 4) depicted in the figure refers to the limiting case in which the rotational diffusion time $1/D_R$ is much longer than the time scales characterizing the active torque and the spring relaxation, i.e., $\tau \ll 1$ and $\Omega \gg 1$. The orientation vectors (green arrows) are typically opposite when the dimer is stretched, as shown by the configuration in step 1. For this reason, the dimer experiences a translation (yellow arrows) in the direction of the activity gradient (black arrows). The evolution of the orientation vectors due to the active torque (step 2) leads, after some time $\sim 1/(2\omega)$, to the configuration in step 3, where the system translates towards the low-activity region. However, since the spring in step 3 is typically less extended than in step 1, this drift against the activity gradient is much smaller than the one experienced by the dimer in step 1. Overall, this asymmetry results in a biased motion towards high-activity regions. Right panel: stochastic trajectories obtained from Brownian dynamics simulations of the equations of motion in Eq. (3.1). As in Figure 3.2, lengths and times are measured in units of $l = \sqrt{D_T/D_R}$ and $\tau_r = 1/D_R$, respectively. In contrast to the blue trajectory ($\Omega = 3 < \Omega_c \simeq 4.58257$), where the stochasticity due to rotational diffusion prevails on the deterministic rotation produced by the active torque, the green one ($\Omega = 20 > \Omega_c \simeq 4.58257$) exhibits a directed motion of the dimer toward the region where the activity profile (red curve) is higher.

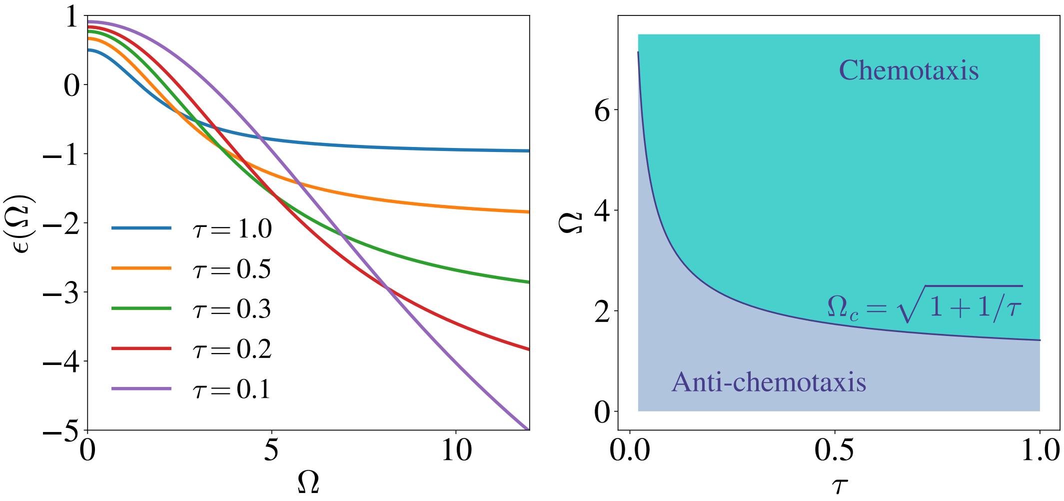

Figure 3.4: Left panel: Value of the exponent ϵ for a dimer of ACPs as a function of the dimensionless torque Ω (see Eq. (3.10)) for different values of τ. Upon increasing the active torque, the dimer switches behavior from antichemotactic ($\epsilon > 0$) to chemotactic $\epsilon < 0$. Right panel: state diagram in (Ω, τ) plane, which shows the regions within which $\epsilon > 0$, corresponding to anti-chemotaxis or $\epsilon < 0$, corresponding to chemotaxis. The blue critical curve separates the chemotactic from the anti-chemotactic region. In particular, for small relaxation time τ of the relative distance between the two particles, it is significantly harder for the dimer to change its tactic behaviour as the threshold torque Ω_c beyond which this change occurs tends to diverge.

the activity gradient only a sufficiently large active torque is necessary. The underlying mechanism does not require temporal integration of the fuel concentration [93], memory [128], or an explicit coupling between the orientation of the particles and the activity gradients [40, 41, 129], which were previously suggested as possible causes.

The mechanism presented here relies solely on the fact that the distance between the two active particles changes during their dynamics. In fact, in the case of a rigid dimer, in which the distance between the two particles is fixed, there is no biased movement towards higher activity regions. We show analytically in Appendix A.1.1 that the tactic coupling ϵ for a rigid dimer is always positive and equal to $\epsilon = 1/2$. Equation (3.14) defines the critical curve in the (Ω, τ) plane separating the chemotactic phase from the anti-chemotactic one, which is presented in the right panel of Figure 3.4. For a fixed D_R, the critical torque diverges in the limit of $\kappa \to \infty$ (i.e., $\tau \to 0$) implying that the dimer preferentially accumulates in the low activity regions. This is indeed expected as, in this case, the two particles are tightly bound to each other and therefore, the dimer is effectively reduced to a single active particle which shows antichemotactic behavior. Similarly, for a fixed κ, it is apparent that upon increasing D_R, increasingly large active torques are required to induce chemotactic behavior. It is important to note that the collective coordinate $\boldsymbol{R}$ can describe the location of the dimer only when the two particles stay sufficiently close to each other. For small κ, the activity gradients may become large on the length scale of the distance between the two particles. In this case, our theory based on the small-gradients approximation does not apply.

3.4 Odd-diffusive active particles

In the previous Section we demonstrated how two interacting self-propelled particles driven by microscopic opposite torques can exhibit, for sufficiently large torques, a chemotactic-like behavior. The single components of this molecule belong to a class of systems defined as odd-diffusive. This kind of systems are characterized by the presence of antisymmetric components in their diffusion tensor and show fluxes perpendicular to the density gradient. Recently the analysis of odd-diffusive systems has attracted a lot of attention for both equilibrium and out-of-equilibrium systems such as passive/active charged particles in magnetic field, see, e.g., [116–119]. In the case of charged self-propelled (active) particles immersed in a magnetic field, rather than a microscopic driving torque, the chirality is induced by the Lorentz force. Despite the different physical origin underlying their odd-diffusive behavior, both kinds of self-propelled particles (i.e., with torque-induced chirality or Lorentz-force induced chirality) are characterized by very similar dynamics. This similarity can be better understood from a comparison of their coarse-grained FPEs (derived in Appendices A.2 and A.3), where one integrates out the rotational degree of freedom. In particular, for a single active chiral particle with spatially homogeneous driving torque ω and activity $v_a(\boldsymbol{r}) = v_C$ in $d = 2$, we have

$$\partial_t \rho(\boldsymbol{r}, t) = \nabla_{\boldsymbol{r}} \cdot \left[\left(\frac{v_C^2}{2D_R} \boldsymbol{M}^{-1} + D_T \mathbf{1} \right) \nabla_{\boldsymbol{r}} \rho(\boldsymbol{r}, t) \right], \tag{3.15}$$

with $\boldsymbol{M} = \mathbf{1} + \Omega \boldsymbol{\varepsilon}$, $\boldsymbol{\varepsilon}$ the totally antisymmetric Levi-Civita tensor in two dimensions, and Ω defined in Eq. (3.10). For a charged self-propelled particle immersed in homogeneous magnetic field B and activity v_B we have, instead,

$$\partial_t \rho(\boldsymbol{r}, t) = \nabla \cdot \left[\left(\frac{v_B^2}{2D_R} \frac{1}{1+\kappa^2} \mathbf{1} + D_T \boldsymbol{\Gamma}^{-1} \right) \nabla \rho(\boldsymbol{r}, t) \right], \tag{3.16}$$

with $\boldsymbol{\Gamma} = (\mathbf{1} - \kappa \boldsymbol{\varepsilon})$ the effective friction tensor and $\kappa = qB\nu$ is the dimensionless oddness parameter. The two equations present a similar structure, with the corresponding diffusion tensors (given by the expressions in round brackets) containing anti-symmetric components. These expressions can even coincide if the following relations hold

$$\begin{cases} v_C^2 = -2D_T D_R \frac{1+\Omega^2}{1+\kappa^2}\frac{\kappa}{\Omega}\,, \\ \\ v_B^2 = 2D_R D_T \kappa\left(\kappa - 1/\Omega\right)\,. \end{cases} \tag{3.17}$$

3.5 Dimer of active magnetic particles

Given the intriguing similarity between the two systems described above, it is natural to wonder whether this extends to their chemotactic behavior. In particular, can two self-propelled oppositely charged interacting particles immersed in a magnetic field $\boldsymbol{B} = B\hat{\boldsymbol{z}}$ cooperate in such a way as to exhibit chemotaxis, similarly to what has been demonstrated for a dimer composed of two active particles driven by opposite microscopic torques?

We show below that, despite the suggestive similarity to dimers made of active chiral particles, the charged dimers are always antichemotactic and they do not show the transition towards chemotactic behavior featured by the former. To prove that, we derive the steady-state density of the charged dimers and analyze how this is affected by a non-uniform activity field. The derivation is similar to the one outlined in Sec. 3.2 for a dimer composed of active particles driven by opposite active torques (see Appendix A.4 for details) and starts from the evolution of the one-time joint probability density:

$$\partial_t P_1(\boldsymbol{X}_0, \boldsymbol{X}_1, \theta_0, \theta_1, t) = \left(\mathcal{L}_0 + \mathcal{L}_1 + \mathcal{R}^2\right) P_1 \tag{3.18}$$

where the Fokker-Planck operators $\mathcal{L}_0$ and $\mathcal{L}_1$ are defined as

$$\begin{aligned} \mathcal{L}_0 &= -\nabla_{\boldsymbol{X}_0} \cdot \left[\boldsymbol{\Gamma}_+^{-1} \cdot \left(-\nu(\nabla_{\boldsymbol{X}_0} U(\boldsymbol{X}_0 - \boldsymbol{X}_1)) + v_a(\boldsymbol{X}_0)\boldsymbol{n}_0 + D_T \nabla_{\boldsymbol{X}_0}\right)\right]\,, \\ \mathcal{L}_1 &= -\nabla_{\boldsymbol{X}_1} \cdot \left[\boldsymbol{\Gamma}_-^{-1} \cdot \left(-\nu(\nabla_{\boldsymbol{X}_1} U(\boldsymbol{X}_0 - \boldsymbol{X}_1)) + v_a(\boldsymbol{X}_1)\boldsymbol{n}_1 + D_T \nabla_{\boldsymbol{X}_1}\right)\right]\,, \end{aligned} \tag{3.19}$$

while the rotational operator $\mathcal{R}^2$ is given in Eq. (3.5). Here, $\boldsymbol{X}_0$ and $\boldsymbol{X}_1$ denote the positions of the two particles, ν the scalar mobility coefficient and D_T the scalar thermal diffusivity. Moreover, $U(\boldsymbol{x}) = \kappa_s \boldsymbol{x}^2/2$ is the harmonic interaction potential describing the attraction between the two monomers, where the stiffness is denoted by κ_s to distinguish it from the oddness paramere κ, and $v_a(\boldsymbol{x})$ is the activity field. The tensors $\boldsymbol{\Gamma}_\pm$ have the same definition as $\boldsymbol{\Gamma}$ given in the previous Section, with the additional subscript denoting the sign of the charge $\pm q$. Rewriting Eq. (3.18) in terms of the center of friction $\boldsymbol{R} = (\boldsymbol{\Gamma}_+ \cdot \boldsymbol{X}_0 + \boldsymbol{\Gamma}_- \cdot \boldsymbol{X}_1)/2$ and the relative distance $\boldsymbol{r} = \boldsymbol{X}_0 - \boldsymbol{X}_1$, and following similar steps to the ones presented in Sec. 3.1, we get an effective FPE for the coarse-grained density

$\rho(\boldsymbol{R}, t)$, characterized by the following drift and diffusion terms

$$D(\boldsymbol{R}) = \frac{v_a^2(\boldsymbol{R})}{4D_R} + \frac{D_T}{2}\,, \qquad \boldsymbol{V}(\boldsymbol{R}) = (1 - \epsilon/2)\nabla_R D(\boldsymbol{R})\,. \tag{3.20}$$

In this case, the coupling ϵ is given by:

$$\epsilon = 1 - \frac{1-\kappa^2}{1+\kappa^2}\left[1 - \frac{1}{1+\tau(1+\kappa^2)}\right]\,, \tag{3.21}$$

with $\kappa = qB\nu$ the dimensionless oddness parameter and $\tau = D_R/2\kappa_s\nu$ the typical relaxation time of the relative distance $\boldsymbol{r}$ in units of the rotational diffusion time scale $1/D_R$. By imposing again zero flux in the steady state, the following density profile can be easily derived

$$\rho(\boldsymbol{R}) \propto \left[1 + \frac{1}{D_T}\frac{v_a^2(\boldsymbol{R})}{2D_R}\right]^{-\epsilon/2}\,. \tag{3.22}$$

We note that the expressions (3.13) and (3.22) are equivalent when both the magnetic field B and the torque ω are zero. Indeed, in this case, both systems reduce to a dimer of simple ABPs. However, for generic non-zero values of B and ω, there is a striking difference between the two systems. In the dimer of ACPs it is possible to change the sign of ϵ by varying the value of the torque ω. This allows the system to explore both a chemotactic and an anti-chemotactic phase. Conversely, for the active charged dimer immersed in a magnetic field, the value of ϵ is strictly positive regardless the intensity of B. This constraint prevents the system from exhibiting a chemotactic phase.

3.6 Conclusions

A single active chiral particle preferentially accumulates in low-activity regions, i.e., it is effectively anti-chemotactic. However, when two such particles with opposite chiralities are connected to each other, the resulting dimer can become chemotactic upon increasing the active torque. Such an assembly of active chiral particles might be possibly realized in experiments by using advanced fabrication techniques that have been used to assemble colloidal particles into desired structures [130–135]. However, at the colloidal scale, it might be challenging to fabricate such dimers without affecting the rotation of the individual chiral particles.

At the millimetre scale, our predictions could be tested in *vibrots* which are miniature robots that convert vibrations into rotational and translational motion [136–139]. Vibrots with chiral leg configurations can rotate in both directions and hence mimic active chiral particles of opposite polarities [140]. They can be connected to each other without affecting their rotation [141]. Activity gradients could be realised in a vibrating plate via surface patterning which modifies the effective friction experienced by a vibrot.

Active chiral particles belong to a class of systems referred to as odd-diffusive. In these systems, probability fluxes are not only along the density gradients but also perpendicular to them [113, 142, 143]. Odd-diffusive behavior is encoded in the diffusion tensor that has an antisymmetric part (See Eqs. (3.15) and (3.16)). We showed that despite sharing the property of odd-diffusion, the two systems, namely active chiral particles and Brownian particles under Lorentz force, exhibit distinct dynamics such that one cannot be mapped into the other in general. We showed this explicitly in the context of the tactic behavior of dimers.

Chapter 4

Taxis of cargo-carrying microswimmers in travelling activity waves

The ability to self-propel at the expense of fuel consumption is a fundamental property of active matter [13, 144–146]. In the biological context, self-propelling microscopic systems perform functions that require accurate directed transport, for instance, white blood cells chase intruders [147], motor proteins transport RNA inside cells [148] and microswimmers such as *E. Coli* [92] and sperm cells [149] steer themselves towards sources of nutrients. Directed transport is a highly desirable property, in particular for applications in drug delivery at the nanoscale [100, 150–153]. For this purpose, bio-hybrid microswimmers have been designed by integrating biological entities with synthetic constructs, e.g., bacteria capable to transport and drop off passive microscopic cargo to specific target locations [154–157].

Bacteria and eukaryotic cells [158, 159] generally navigate in dynamic activating media and react *in vivo* to time-dependent tactic stimuli of various nature. Such an interaction with travelling activity signals, e.g., chemical waves [160, 161], leads to fascinating collective behaviors [162] and sometimes to unexpected migration phenomena, as in the case of the so-called *chemotactic wave paradox* [160, 163]. While synthetic active particles mimic the basic features of self-propulsion and persistence of actual biological active matter, they lack the information processing capacity and motoric control which is essential for directed transport in biological and bio-hybrid systems. Despite their memoryless response to tactic signals, artificial self-propelled particles exhibit directed transport when immersed in travelling waves controlling locally their degree of activity (e.g., their self propulsion velocity), as shown experimentally with phototactic Janus particles exposed to propagating optical pulses [129]. Several theoretical studies have focused on controlling and directing the motion of a single self-propelled particle in a fluctuating environment [99, 164–167]. However, a fundamental understanding of the behavior of cargo-carrying microswimmers in time-dependent activity is still lacking.

It has been already shown that chemically active colloidal particles can be employed as carriers of catalytically-inert cargoes at the micro-scale[122, 168]. Cargo-carrying self-propelled particles have also been analyzed in stationary and spatially inhomogeneous activity fields [103]. While a single self-propelled particle always accumulates in spatial regions with low activity, attaching a passive cargo reverses this tendency. In fact, beyond a certain threshold cargo, the particle accumulates in regions with larger activity [103]. While preferential accumulation could be regarded as a signature of the tactic behavior [103], in the case of stationary activity, it causes no transport of the dimer. By contrast, for a time-dependent activity, such as a source emitting activity pulses, the tactic behavior of an active particle can result in the motion towards or away from the source. With this motivation in mind, in this Chapter, we study active-passive dimers subject to a time-dependent activity in the form of a travelling wave. We analytically show that the dimer exhibits directed transport, characterized by a wave-induced drift. The direction of this drift depends on the wave speed, being always along its propagation direction for a fast wave. For a slow wave, instead, the drift may be along or opposite to the propagation direction of the wave, depending on the friction coefficient of the cargo being larger or smaller than a certain threshold value. Interestingly, the net drift vanishes at that threshold, at least for sufficiently small wave speeds. Our theoretical treatment of the active-passive dimer is based on the active Ornstein-Uhlenbeck particle (AOUP) model of activity [27, 169–171]. Furthermore, our analysis shows that the tactic behavior of a cargo-carrying AOUPs is equivalent to that of a similar active-passive dimeric complex where the active unit is modeled as an active Brownian particle (ABP) [103].

The analysis presented in this Chapter has been published in Ref. [172].

4.1 The model

In this Section we introduce a minimal model for the dynamics of an active microswimmer that drags a passive load in d spatial dimensions within an non-homogeneous and time-dependent environment. The microswimmer at position $\boldsymbol{r}$ and time t interacts with a tactic signal described by the activity field $v_{\mathrm{a}}(\boldsymbol{r} - \boldsymbol{v}_w t)$, which propagates with velocity $\boldsymbol{v}_w = v_w \boldsymbol{e}_0$ along the direction of the unit vector $\boldsymbol{e}_0$, as depicted in fig. 4.1. The shape of the traveling wave $v_{\mathrm{a}}(\boldsymbol{r} - \boldsymbol{v}_w t)$ will remain generic unless specified otherwise. As usually done for μm-sized colloidal particles in a liquid, we assume that viscous forces dominate over inertial effects and therefore we consider an overdamped dynamics for the active-passive dimer,

Figure 4.1: Sketch of the stochastic model described by (4.1) in two spatial dimensions. A self-propelled active microswimmer (blue ellipse) in a fluid drags a passive cargo (gray circle) via a harmonic interaction (blue spring). The instantaneous self-propulsion velocity of the microswimmer (blue arrow) is locally controlled by a sinusoidal traveling wave of activity, which propagates through the fluid with phase velocity v_w along the unit vector $\boldsymbol{e}_0$. The value of the activity field rescaled to its maximum is given in the colorbar on the right. For illustration we sketch here two examples of active-passive dimers, one with a low-friction cargo (q small, left) and the other with a high-friction cargo (q large, right).

which is governed by the following Langevin equations:

$$\dot{\boldsymbol{r}}_1 = -\nu \nabla_{\boldsymbol{r}_1} U(\boldsymbol{r}_1 - \boldsymbol{r}_2) + v_{\mathrm{a}}(\boldsymbol{r}_1 - \boldsymbol{v}_w t)\boldsymbol{\eta} + \sqrt{2D}\boldsymbol{\xi}_1, \tag{4.1a}$$

$$\dot{\boldsymbol{r}}_2 = -\frac{\nu}{q} \nabla_{\boldsymbol{r}_2} U(\boldsymbol{r}_1 - \boldsymbol{r}_2) + \sqrt{\frac{2D}{q}}\boldsymbol{\xi}_2, \tag{4.1b}$$

$$\tau \dot{\boldsymbol{\eta}} = -\boldsymbol{\eta} + \sqrt{\frac{2\tau}{d}}\boldsymbol{\xi}_3; \tag{4.1c}$$

where $\boldsymbol{r}_1$ and $\boldsymbol{r}_2$ denote the positions of the active microswimmer and the passive cargo, respectively. The interaction $U(\boldsymbol{r}_1 - \boldsymbol{r}_2)$ between them is modeled by an isotropic parabolic potential $U(\boldsymbol{r}) = \kappa \boldsymbol{r}^2/2$, with stiffness $\kappa > 0$ and zero rest length. The stochastic terms $\boldsymbol{\xi}_1$, $\boldsymbol{\xi}_2$, $\boldsymbol{\xi}_3$ are three independent zero-mean Gaussian white noises with correlations

$$\langle \xi_i^\alpha(t) \xi_j^\beta(s) \rangle = \delta_{\alpha\beta}\delta_{ij}\delta(t-s)\,, \tag{4.2}$$

where $i, j \in \{1, 2, 3\}$ and $\alpha, \beta \in 1, .., d$, and they account for thermal fluctuations. Moreover, the active carrier exploits local energy injections to self-propel along the direction of the propulsion vector $\boldsymbol{\eta}$, which evolves according to a set of d independent Ornstein-Uhlenbeck processes with variance $1/d$ and characteristic time τ, as reported in (4.1c). It follows that $\boldsymbol{\eta}$ is a zero-mean Gaussian colored noise, whose correlations in the long time limit reads:

$$\langle \eta_\alpha(t) \eta_\beta(s) \rangle = (\delta_{\alpha,\beta}/d) \exp\left(-|t-s|/\tau\right)\,. \tag{4.3}$$

This normalization ensures that the average modulus squared of the propulsion vector is $\langle \|\boldsymbol{\eta}\|^2 \rangle = 1$ for any dimensionality d. While the time scale τ sets the persistence of the self-propulsion force, its strength is modulated in space by the activity field $v_\mathrm{a}(\boldsymbol{x})$. Note that, in this minimal model, the rotational dynamics of the active carrier is not affected by the interaction potential between the two monomers and there is no coupling between the dimer main axis and the polarity of the active particle. In order to recover an equilibrium dynamics in the absence of activity $v_\mathrm{a} = 0$, we connect the mobility ν and the diffusivity D via the Einstein relation $D = \nu T$. Moreover, the cargo and the active carrier are assumed to have different friction coefficients, the ratio of which is given by the parameter q. In a Newtonian fluid and for spherical colloidal carrier and cargo, q equals the ratio of the radius of the cargo to that of the carrier.

The Langevin dynamics in (4.1) can be more conveniently rewritten in terms of the relative distance $\boldsymbol{r}$ and the dimer position in the comoving frame, which we identify with the centre of friction $\boldsymbol{\chi}$, defined as:

$$\begin{aligned} \boldsymbol{\chi} &= \frac{\boldsymbol{r}_1 + q\boldsymbol{r}_2}{1+q} - \boldsymbol{v}_w t \,, \\ \boldsymbol{r} &= \boldsymbol{r}_1 - \boldsymbol{r}_2 \,. \end{aligned} \tag{4.4}$$

In this new coordinate system, we can derive the Fokker-Planck equation for the 1-time probability density $P(\boldsymbol{\chi}, \boldsymbol{r}, \boldsymbol{\eta}, t)$ associated to the stochastic dynamics (4.1). This is given by:

$$\begin{aligned} \partial_t P(\boldsymbol{\chi}, \boldsymbol{r}, \boldsymbol{\eta}, t) = &- \nabla_{\boldsymbol{\chi}} \cdot \left[-\boldsymbol{v}_w P + \frac{1}{1+q} v_\mathrm{a}\left(\boldsymbol{\chi}'\right) \boldsymbol{\eta} P - \frac{D}{1+q} \nabla_{\boldsymbol{\chi}} P \right] \\ &- \nabla_{\boldsymbol{r}} \cdot \left[-\frac{1+q}{q} \nu \nabla_{\boldsymbol{r}} U P + v_\mathrm{a}\left(\boldsymbol{\chi}'\right) \boldsymbol{\eta} P - \frac{1+q}{q} D \nabla_{\boldsymbol{r}} P \right] \\ &+ 1/(d\tau) \hat{\mathcal{L}}_{\boldsymbol{\eta}} P \end{aligned} \tag{4.5}$$

where the vector $\boldsymbol{\chi}' = \boldsymbol{\chi} + q\boldsymbol{r}/(1+q)$ denotes the position of the active carrier in the comoving frame and has to be interpreted as a function of $(\boldsymbol{\chi}, \boldsymbol{r})$. Moreover, we introduced the Fokker-Planck operator $\hat{\mathcal{L}}_{\boldsymbol{\eta}}$ related to the stochastic dynamics of the propulsion vector $\boldsymbol{\eta}$, which is defined as

$$\hat{\mathcal{L}}_{\boldsymbol{\eta}} P = \nabla^2_{\boldsymbol{\eta}} P + d \nabla_{\boldsymbol{\eta}} \cdot (\boldsymbol{\eta} P) \ . \tag{4.6}$$

4.2 Transport properties for slow activity waves

In order to estimate the extent to which the propagating tactic signal affects the directed motion of the cargo-carrying microswimmer, we focus on transport properties induced by the activity travelling wave. Starting from Eq. (4.5), we derive in the Appendix B.1 an effective mean-field dynamics which describes the evolution of the system at time scales longer than τ and length scales larger than the typical persistence length $l_p \sim \langle v_\mathrm{a} \rangle \tau$ analogously to ref. [126]. This provides a generalised hydrodynamics for the relevant fields such as particle density, polarization, etc. In particular, the predictions deriving from it are expected to be valid for an activity which varies slowly on the length scale l_p (*large wavelength* approximation). Importantly, we emphasize that our model ignores the hydrodynamic contributions arising from the interaction of the dimer with the surrounding solvent, thus falling into the class of dry active matter models [146]. In order to identify the fields with a relaxation time which grows indefinitely upon increasing the wavelength (i.e., the slow modes), we perform a moment expansion analogous to, e.g., refs. [126, 173, 174]. The evolution of the modes is described by a hierarchical structure, the detailed derivation of which is reported in Appendix B.1. Importantly, we note that the zeroth order mode $\varphi(\boldsymbol{\chi}, \boldsymbol{r}, t) = \int \mathrm{d}\boldsymbol{\eta}\, P(\boldsymbol{\chi}, \boldsymbol{r}, \boldsymbol{\eta}, t)$, which describes the density related to the spatial marginal variables $\boldsymbol{\chi}$ and $\boldsymbol{r}$, is the only slow mode of the system. Indeed, $\varphi(\boldsymbol{\chi}, \boldsymbol{r}, t)$ is associated with a conservation law and its dynamics has the form of a continuity equation:

$$
\begin{aligned}
\partial_t \varphi(\boldsymbol{\chi}, \boldsymbol{r}, t) = &- \partial_\alpha \left[-v_w \delta_{\alpha,0} \varphi + \frac{v_\mathrm{a}(\boldsymbol{\chi}')\, \sigma_\alpha}{(1+q)} - \frac{D}{1+q} \partial_\alpha \varphi \right] \\
&- \partial'_\alpha \left[-\frac{(1+q)}{q} \nu \partial'_\alpha U \varphi + v_\mathrm{a}(\boldsymbol{\chi}')\, \sigma_\alpha - \frac{(1+q)D}{q} \partial'_\alpha \varphi \right],
\end{aligned}
\tag{4.7}
$$

where we introduced the shorthand notation $\partial_\alpha \equiv \partial_{\chi_\alpha}$ and $\partial'_\alpha \equiv \partial_{r_\alpha}$, while repeated indices imply summation. In the dynamics above, σ_α is the α-th component of the first-order mode $\boldsymbol{\sigma}(\boldsymbol{\chi}, \boldsymbol{r}, t) = \int \mathrm{d}\boldsymbol{\eta}\, \boldsymbol{\eta} P(\boldsymbol{\chi}, \boldsymbol{r}, \boldsymbol{\eta}, t)$, which is related to the conditional average polarization of the active carrier at fixed spatial variables. Its dynamics is governed by

$$
\begin{aligned}
\partial_t \sigma_\alpha(\boldsymbol{\chi}, \boldsymbol{r}, t) = &- \frac{\partial_\alpha \left[v_\mathrm{a}(\boldsymbol{\chi}')\, \varphi \right]}{(1+q)d} - \frac{\partial'_\alpha \left[v_\mathrm{a}(\boldsymbol{\chi}')\, \varphi \right]}{d} \\
&+ \frac{(1+q)}{q} \nu \partial'_\beta \left[\partial'_\beta U \sigma_\alpha \right] - \tau^{-1} \sigma_\alpha + \mathcal{O}(\partial^2),
\end{aligned}
\tag{4.8}
$$

where dependencies on higher-order modes are included in $\mathcal{O}(\partial^2)$. Notably, the decay rate due to the sink term $-\tau^{-1}\sigma_\alpha$ implies that $\sigma_\alpha(\boldsymbol{\chi}, \boldsymbol{r}, t)$ is a fast mode that is not locally conserved throughout its dynamics. The separation of time scales between φ and $\boldsymbol{\sigma}$ justify the use of the quasi-static approximation in dealing with (4.8) (see Appendix B.2 for details). Moreover, the contribution $\mathcal{O}(\partial^2)$ of higher-order gradients is negligible under the assumption that the activity field is characterized by small spatial variations.

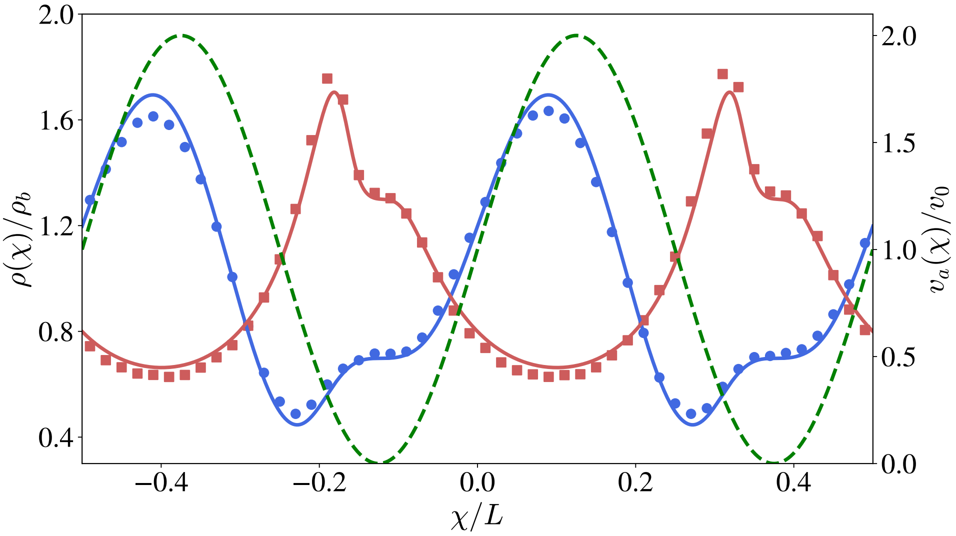

Figure 4.2: Stationary density $\rho(\chi)$ of the dimer (red and blue lines and symbols, left axis), in the comoving frame of the traveling activity wave $v_\mathrm{a}(\chi)$ with sinusoidal shape (green dashed line, Eq. (4.14), right axis), as obtained from numerical simulations (symbols) and from analytical predictions (Eq. (4.15), solid lines). The latter hold under the assumption of long wavelength and slow traveling wave and they are reported for both a high-friction cargo with $q = q_\mathrm{high} > q_\mathrm{th}$ (blue) and a low-friction cargo with $q = q_\mathrm{low} < q_\mathrm{th}$ (red). See the Appendix B.5 for further information on the numerical simulations.

4.2.1 Stationary density

The combination of large-wavelength approximation and quasi-stationarity of $\boldsymbol{\sigma}(\boldsymbol{\chi}, \boldsymbol{r}, t)$ at time scales longer than τ provides a closure scheme for the hierarchy without needing information about higher-order modes. In particular, after integrating out the relative coordinate $\boldsymbol{r}$, we derive an effective drift-diffusion equation for the marginal density $\rho(\boldsymbol{\chi}, t) = \int d\boldsymbol{r}\varphi(\boldsymbol{\chi}, \boldsymbol{r}, t)$ (see Appendix B.2 for the detailed derivation), which reads:

$$\partial_t \rho(\boldsymbol{\chi}, t) = -\nabla_{\boldsymbol{\chi}} \cdot \left[\boldsymbol{V}_\mathrm{eff}(\boldsymbol{\chi})\rho(\boldsymbol{\chi}, t) - \nabla_{\boldsymbol{\chi}}(D_\mathrm{eff}(\boldsymbol{\chi})\rho(\boldsymbol{\chi}, t))\right], \tag{4.9}$$

where the effective drift and effective diffusivity are given, respectively, by

$$\begin{aligned} \boldsymbol{V}_\mathrm{eff}(\boldsymbol{\chi}) &= (1 - \epsilon/2)\nabla_{\boldsymbol{\chi}} D_\mathrm{eff}(\boldsymbol{\chi}) - \boldsymbol{v}_w, \\ D_\mathrm{eff}(\boldsymbol{\chi}) &= \frac{D}{1+q} + \frac{\tau v_\mathrm{a}^2(\boldsymbol{\chi})}{d(1+q)^2}. \end{aligned} \tag{4.10}$$

This expression of D_eff reveals an enhancement of the diffusivity $D/(1+q)$ of the center of friction induced by the activity via a term $\propto v_\mathrm{a}^2(\boldsymbol{\chi})$. Interestingly, the alignment of the effective drift with the activity gradient is controlled by the *tactic coupling*

$$\epsilon = 1 - \frac{q}{1 + \frac{1+q}{q}\frac{\tau}{\tau_\mathrm{r}}}\,, \tag{4.11}$$

where $\tau_\mathrm{r} = 1/\nu\kappa$ is the characteristic spring relaxation time. The role of ϵ can be understood by considering the case of static activity field. In fact, for $v_w = 0$, the stationary density obtained from (4.9) is

$$\rho(\boldsymbol{\chi}) = \mathcal{N}^{-1}\left[1 + \frac{\tau v_\mathrm{a}^2(\boldsymbol{\chi})}{dD(1+q)}\right]^{-\epsilon/2}\,, \tag{4.12}$$

with $\mathcal{N}$ a normalization constant. Accordingly, ϵ determines the preferential accumulation of the dimer in the regions with high or low activity depending on its sign. Equation (4.11) implies that for a fixed τ/τ_r, the tactic coupling ϵ is entirely determined by the friction ratio q, because it changes sign at the threshold value

$$q_\mathrm{th} = \frac{1}{2}\left[1 + \tau/\tau_\mathrm{r} + \sqrt{(1+\tau/\tau_\mathrm{r})^2 + 4\tau/\tau_\mathrm{r}}\right] \geq 1. \tag{4.13}$$

For highly mobile cargoes with $q < q_\mathrm{th}$ one has $\epsilon > 0$ and thus the dimer preferentially accumulates in low-activity regions. For slow cargoes with $q > q_\mathrm{th}$, instead, $\epsilon < 0$ and the dimer preferentially accumulates in high-activity regions. Interestingly, as in the single-particle case (see, e.g., ref. [98]), the equivalence with a cargo-carrying ABP [103] with rotational diffusivity D_r is fully recovered by imposing $\tau^{-1} = (d-1)D_r$.

In order to analyze the general case of an activity travelling wave ($v_w \neq 0$), we assume for simplicity that the activity field v_a varies only along $\boldsymbol{e}_0$. Accordingly, we denote the effective drift and diffusivity with $D_\mathrm{eff}(\chi_0)$ and $V_{\mathrm{eff},\alpha}(\chi_0)$ as they now depend only on $\chi_0 = \boldsymbol{\chi}\cdot\boldsymbol{e}_0$. As an example, we hereafter consider a sinusoidal activity wave

$$v_\mathrm{a}(\chi_0) = v_0\left[1 + \sin(\chi_0/\lambda)\right], \tag{4.14}$$

with wavelength λ, but the derivation can be easily extended to activity traveling waves with different shapes. We determine the resulting stationary density $\rho(\boldsymbol{\chi})$ in the comoving frame

$$\frac{\rho(\boldsymbol{\chi})}{\rho_b} = \frac{L\,D_\mathrm{eff}^{-1}(\chi_0)\int_0^L \mathrm{d}x \exp\left\{-\int_{\chi_0}^{\chi_0+x}\mathrm{d}y\frac{V_{\mathrm{eff},0}(y)}{D_\mathrm{eff}(y)}\right\}}{\int_0^L \mathrm{d}u\int_0^L \mathrm{d}x\,D_\mathrm{eff}^{-1}(u)\exp\left\{-\int_u^{u+x}\mathrm{d}y\frac{V_{\mathrm{eff},0}(y)}{D_\mathrm{eff}(y)}\right\}}, \tag{4.15}$$

by considering a comoving box of size L with periodic boundary conditions. Here, $\rho_b = L^{-d}$ is the value of the uniform distribution over the $d-$dimensional comoving box. The stationary density $\rho(\boldsymbol{\chi})$ is shown in Figure 4.2 and it also features the transition in the preferential accumulation illustrated above for $v_w = 0$.

4.2.2 Drift velocity

The interaction with the propagating activity field induces a non-trivial tactic response in the cargo-carrying complex, which is now able to sustain a non-vanishing stationary flux J_0 in the comoving frame, acquiring an average drift velocity $v_d = (\langle \dot{\boldsymbol{r}}_1 \rangle + q \langle \dot{\boldsymbol{r}}_2 \rangle)/(1+q) = J_0/\rho_b + v_w$ along $\boldsymbol{e}_0$ in the lab frame. This drift is given by [175, 176]

$$v_d = \frac{L\left[1 - \exp\left\{-\int_0^L \mathrm{d}y \frac{V_{\mathrm{eff},0}(y)}{D_{\mathrm{eff}}(y)}\right\}\right]}{\int_0^L \mathrm{d}u \int_0^L \mathrm{d}x \, D_{\mathrm{eff}}^{-1}(u) \exp\left\{-\int_u^{u+x} \mathrm{d}y \frac{V_{\mathrm{eff},0}(y)}{D_{\mathrm{eff}}(y)}\right\}} + v_w, \tag{4.16}$$

and it strongly depends on the tactic coupling ϵ and therefore on q. More precisely, it can be shown analytically that v_d vanishes at the static threshold value $q = q_{\mathrm{th}}$ reported in (4.13) (see Appendix B.3). Additionally, for sufficiently small thermal diffusivity D, the threshold value $q = q_{\mathrm{th}}$ also separates two distinct tactic regimes with respect to the wave propagation: *positive taxis* for $q > q_{\mathrm{th}}$, where the microswimmer navigates along the propagating tactic signal with $v_d/v_w > 0$, and *negative taxis* for $q < q_{\mathrm{th}}$, where the microswimmer navigates against it, with $v_d/v_w < 0$, see fig. 4.3(a). This predicted negative taxis as well as the fact that its magnitude decreases upon increasing D are consistent with what occurs for a single active particle [164, 165], which is retrieved as the limit $q \to 0$ of our model. Conversely, as q increases, the response of the dimeric microswimmer to the traveling tactic signal might become substantially different from that of a single active particle, depending on both q and τ/τ_{r}. More precisely, at fixed τ/τ_{r} the cargo-carrying microswimmer travels along the sinusoidal wave when $q > q_{\mathrm{th}}$, due to its tendency to localize close to the propagating activity crests, performing the *active surfing* shown in Figure 4.3(b). Interestingly, an analogous effect was observed experimentally with single self-polarizing phototactic particles in traveling light pulses [129]. While in ref. [129] this behavior is caused by an aligning torque, in our model it emerges as a cooperative effect between the active carrier and the passive cargo. Note, however, that the ability of the microswimmer to catch up with the travelling wave crests, i.e., $v_d \simeq v_w$ is limited to the case of slowly propagating activity wave, which explains the non-monotonicity of the blue curve in fig. 4.3(a). In order to quantify the efficiency of this surfing, we determine the slope c of the linear relation $v_d \approx c v_w$, which holds at small wave velocities v_w. Its dependence on q and the thermal diffusivity D is reported in the inset of Figure 4.3, which shows, as expected, that $c \leq 1$ and that the directed transport is highly efficient (i.e., $c \simeq 1$) for $D \ll \tau v_0^2$. We recall here that the predictions presented above follow from a coarse graining which assumes that the activity field varies slowly on a length scale of the order of $l_p = v_0 \tau$. In the static case $v_w = 0$, this condition is met for $\lambda \gg l_p$. However, for a traveling wave, the coarse graining additionally requires that the distance $\sim v_w \tau$ traveled

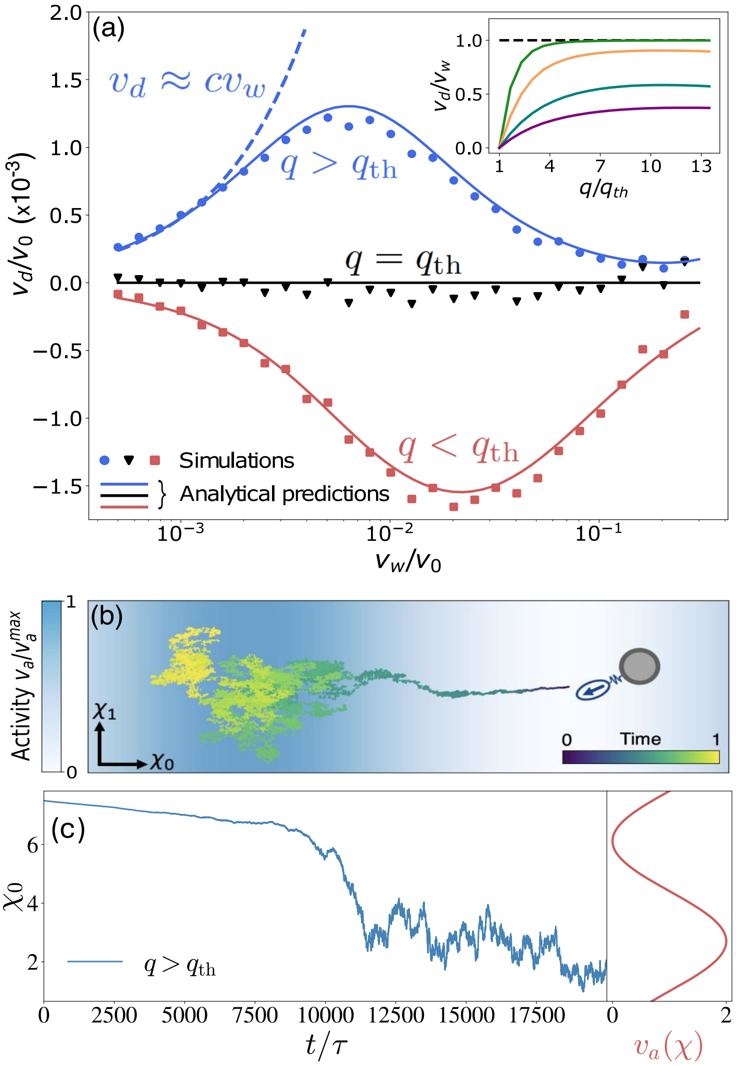

Figure 4.3: (a) Average drift v_d as a function of the phase velocity v_w in the slow-wave regime $v_w < v_0$ (Equation (4.16)). For low-friction cargoes with $q = q_{\text{low}} < q_{\text{th}}$ (red line), the microswimmer exhibits a negative tactic behavior. At the threshold value q_{th} (black line), the average drift vanishes for all wave velocities v_w, whereas for $q = q_{\text{high}} > q_{\text{th}}$ (blue solid line), the dimer is characterized by positive taxis. Details on numerical results (symbols) can be found in Appendix B.5. In the inset, we report the slope of the linear relation $v_d \approx c v_w$ (blue dashed line) at small wave velocities as a function of q, and for thermal diffusivity $D \in \{0.05, 0.03, 0.01, 0.001\}$ (solid lines from bottom to top). (b) and (c): Stochastic trajectory of a cargo-carrying microswimmer in the comoving frame (χ_0, χ_1) in two spatial dimensions. For a high-friction cargo ($q = 20$) and small thermal diffusivity $D = 10^{-3}$ the dimer *surfs* the propagating activity wave by localizing around its maximum while traveling with the same velocity, i.e., $v_d = v_w$.

by the active wave on a time scale $\sim \tau$ does not exceed $\sim l_p$, which happens for $v_w < v_0$. Accordingly, in order to investigate the transport properties in the opposite case $v_w > v_0$, we pursue below an alternative analytical approach.

4.3 Transport properties for fast activity waves

For simplicity, and without loss of generality, we restrict the analysis of the case $v_w > v_0$ to one-dimensional systems and to a sinusoidal traveling wave as in Eq. (4.14). The main difference compared to the slow-wave approximation discussed above lies in the closure scheme used to combine the mode equations (4.7) and (4.8). More precisely, as the small gradients approximation is no longer applicable for $v_w > v_0$, we explore this regime by considering small self-propulsion forces by keeping in the effective dynamics only contributions of the lowest order in v_0 [167, 177, 178]. To this aim, we rewrite (4.8) in the more convenient form

$$\hat{\mathcal{L}}_\sigma \sigma(\chi, r, t) = -\frac{\partial_\chi \left[v_\mathrm{a}(\chi')\varphi\right]}{(1+q)} - \partial_r \left[v_\mathrm{a}(\chi')\varphi\right] + \Upsilon(\chi, r, t), \tag{4.17}$$

where $\chi' = \chi + qr/(1+q)$ is the position of the active carrier in the comoving frame, $\Upsilon(\chi, r, t)$ includes all contributions of higher-order modes, and the operator $\hat{\mathcal{L}}_\sigma$ is defined as

$$\hat{\mathcal{L}}_\sigma = \partial_t + \frac{1}{\tau} - v_w \partial_\chi - \frac{D}{1+q}\partial_\chi^2 - \frac{(1+q)D}{q}\left[\partial_r^2 + \frac{1}{\ell^2}\partial_r r\right], \tag{4.18}$$

with the characteristic length $\ell = \sqrt{D\tau_\mathrm{r}}$.

To solve for $\sigma(\chi, r, t)$, we then determine the Green function of $\hat{\mathcal{L}}_\sigma$ and compute the convolution with the right hand side of (4.17). In doing this, we assume that the contribution $\Upsilon(\chi, r, t)$ of higher-order modes is negligible in the limit of small self-propulsion forces, thus closing the hierarchy. Analogously to the previous approach, after integrating over the relative coordinate r, we obtain a continuity equation for the marginal density $\rho(\chi, t)$, i.e.,

$$\partial_t \rho(\chi, t) = -\partial_\chi \left[I(\chi, t) - \frac{D}{1+q}\partial_\chi \rho - v_w \rho\right], \tag{4.19}$$

where

$$I(\chi, t) = \int_{-\infty}^{\infty} \mathrm{d}r \, \frac{v_\mathrm{a}(\chi')\,\sigma(\chi, r, t)}{(1+q)} = \frac{\langle v_\mathrm{a}(\chi')\eta \,|\, \chi\rangle}{1+q}\rho(\chi, t), \tag{4.20}$$

and $\langle \cdot | \chi \rangle$ denotes the conditional average at fixed χ. We derive a close yet cumbersome analytical expression for $I(\chi, t)$ which is related to the local average swim speed of the center of friction due to self-propulsion (see (4.20)

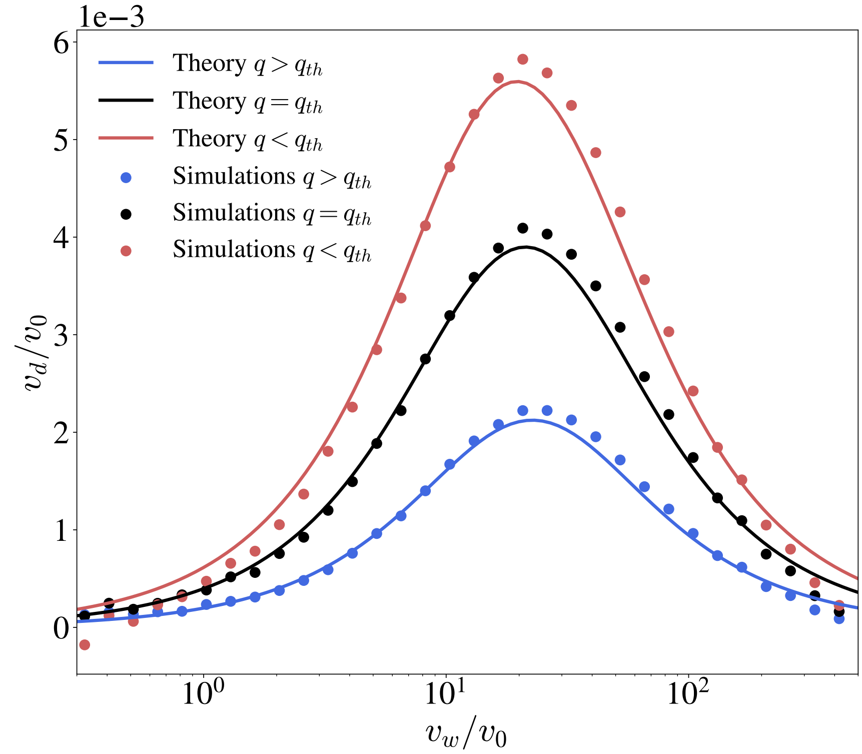

Figure 4.4: Average drift velocity v_d as a function of the phase velocity v_w of the activity wave, in the case for $v_w > v_0$ (see the analytical expression in (4.21)). The cargo-carrying microswimmer acquires a positive drift independently of the value of the friction ratio q, which takes here the same values as those of the corresponding curves in fig. 4.3. The numerical results (symbols) were obtained as discussed in Appendix B.5.

and Appendix B.4). Similarly, we also derive in the Appendix B.4 analytical expressions for the stationary density and the flux in the comoving frame, which we use to analyze the directed transport in the regime of fast active traveling waves. In particular, for $D\tau_r \ll \lambda^2$, the average drift velocity v_d reads

$$\frac{v_d}{v_0} = \frac{l_p}{2\lambda(1+q)^2}\left[\frac{\sin\psi_0}{|z_0|} + q\frac{\sin\psi_1}{|z_1|}\right], \tag{4.21}$$

where we recall that $l_p = v_0\tau$ is the persistence length of the active carrier, while ψ_n and $|z_n|$ are the phase and the modulus, respectively, of the complex number

$$z_n = 1 + \frac{\tau D}{\lambda^2(1+q)} + \frac{(1+q)\tau D}{q\ell^2}n + \mathrm{i}\frac{\tau v_w}{\lambda}, \tag{4.22}$$

where i is the imaginary unit. A general expression of the drift velocity for an arbitrary thermal diffusivity D is given in Appendix B.4.

Figure 4.4 shows the behavior of the average drift v_d as a function of the wave velocity v_w in the regime $v_w > v_0$ of fast traveling waves. Unlike the case of $v_w < v_0$ (see Figure 4.3), the tactic behavior of the microswimmer does not exhibit a qualitative change as a function of the friction ratio q, with the drift occurring always along the direction of the active wave. However, as q increases, this drift decreases because of the reduced mobility of the dimer. The drift velocity of the microswimmer attains its maximum value at a wave speed which scales as $v_w/v_0 \sim \lambda/l_p$. This can be qualitatively understood as following. Consider a single pulse of activity of spatial extent λ travelling with a speed v_w. A microswimmer with its polarization against the direction of the travelling pulse will rapidly exit the pulse from the receding front. However, when the polarization is along the direction of the pulse, the microswimmer will be carried along with it until it switches its polarization which will cause it to exit the pulse. The optimum scenario corresponds to the condition $v_w\tau - v_0\tau \sim \lambda$ in which the microswimmer effectively traverses the whole pulse before switching polarization. This results in a maximum of the drift speed at $v_w \sim \lambda/\tau$. While the drift velocity of the dimer in fig. 4.4 features a single peak, we find both analytically and via numerical simulations that a second peak may appear at larger v_w, for large values of q and persistence time τ. The location of this additional peak depends on the spring relaxation time scale τ_r but we defer a thorough investigation of its features and microscopic origin to future works.

4.4 Discussion

In this Chapter we showed that self-propelled cargo-carrying microswimmers interacting with a traveling wave of activity display a rich tactic behavior. Their response to such a wave is actually independent of the details of the activity, as evidenced by the proved equivalence of cargo-carrying AOUPs and ABPs in terms of their coarse grained-dynamics. The tactic transition which emerges in the presence of slowly propagating waves relies on the possibility to control the preferential localization of the microswimmer in high/low activity regions, by tuning the friction of its cargo. In particular, we find a surfing effect when the directed migration along the activity wave is induced by an effective localization around the slowly propagating wave maxima. Considering, e.g., the experimental realization of Janus microswimmers as in Ref. [129], Eq. (4.13) implies $q_\mathrm{th} \simeq \kappa/(0.02\,\mathrm{pN}/\mu\mathrm{m})$ for $q_\mathrm{th} \gtrsim 1$. Accordingly, assuming for the cargo-carrier binding an elastic constant $\kappa \simeq 0.1\,\mathrm{pN}/\mu\mathrm{m}$, typical for soft matter, the tactic transition is predicted to occur at a cargo radius $\simeq 8\,\mu\mathrm{m}$, which is within experimental reach. By tuning the stiffness κ of the spring between the active carrier and the passive cargo, one can shift the transition. A possible experimental system could be envisaged in which the linker between carrier and cargo is composed of colloidal chains. Recently, colloidal chains have been produced experimentally with tremendous control on length and stiffness, mimicking the behavior of flexible and semiflexible polymers [179, 180]. We speculate that a qualitatively similar tactic behavior may emerge spontaneously in a binary mixture of mutually attractive active and passive particles, upon formation of clusters of different sizes. It has been recently shown that also molecules composed of two rigidly connected active particles [112] exhibit a transition in their effective localization in high/low activity regions, as well as dimers made of two active chiral particles (see Chapter 3). It will be interesting to study such active-matter systems subject to active traveling waves, and in the presence of external potentials [30, 181]. We expect the predictions presented in this Chapter to have an impact on experimental studies on soft matter, biophysics, and nanotechnology. Important examples include cases in which synthetic Janus particles [182] and bacteria [183] have been used to efficiently transport and deliver microscopic objects in specific target sites. Moreover, our investigation could inspire future optimal design of existing *biohybrid* micromachines such as spermbots formed by assembling synthetic materials with sperm cells [184, 185]. The taxis transition unveiled by our minimal stochastic model may also have implications in biological processes at the microscale in which traveling waves play a key role, e.g., signaling waves in cell development [186].

Chapter 5

Migration and separation of polymers in non-uniform active baths

Living systems continuously exchange information and energy with the surrounding environment and their biological function unavoidably relies on mechanisms that are only allowed out of equilibrium [187]. This inherent nonequilibrium state, exemplified by the hallmark feature of self-propulsion, gives rise to a diversity of collective behaviors shared by biological systems across various scales, ranging from molecular motor assemblies [12, 188, 189] to swarming bacteria [190] and flocking birds [191–193]. While a comprehensive theory encompassing the diverse properties of living matter is still elusive due to the astonishing complexity of the biological world, significant efforts have been directed towards constructing a theoretical framework for active matter [146, 194–197]. Prominent examples from biology include flagellated bacteria [92], algae [198, 199] and other motile microorganisms [200], molecular motors on cytoskeletal filaments [201], active worms [202, 203] and many others. Active colloidal molecules are also experimentally synthesized in the lab [13, 111, 200] using techniques such as self-diffusiophoresis via catalytic reactions [20–22], light-induced self-thermophoresis [23], nonreciprocal deformation cycles [204, 205], and the integration of biological components with synthetic structures in biohybrid systems [206].

Numerous active biological systems, including some of the examples mentioned above, appear as filamentous or polymer-like structures. It is well-established that several polymeric molecules in the interior of a cell rely on a variety of active reactions to regulate their biological functions. For example, DNA is continuously processed by enzymes such as DNA-polymerase and helicase to ensure its successful replication [207], ribosomes slide along RNA strands to synthesize proteins [207] and the chromosomal loci dynamics is strongly affected by ATP-dependent non-thermal fluctuations [208]. For this reason, the field of *active polymers* [104, 106] has gained a growing level of attention in recent years, yielding insights into the impact of non-equilibrium fluctuations and activity on structural and dynamic properties of both isolated chains and suspensions of polymers [104, 106, 209–225].

In this Chapter, we focus on the effect of a nonequilibrium bath featuring a spatially non-uniform degree of activity on a polymeric molecule described as an ideal Rouse chain. While recent attention has been devoted to the impact of inhomogeneous activity [26, 40, 41, 50, 98, 99, 103, 120, 172, 226–229], there exists a notable gap in our understanding regarding its influence on polymer-like structures. Here, we reveal a previously unexplored effect in these systems: nonhomogeneous active baths induce qualitatively different spatial distributions in Rouse polymers depending on their contour length and connectivity. More precisely, short polymers preferentially accumulate within spatial regions of low bath activity, whereas long ones in regions of high bath activity. Furthermore, we demonstrate that highly connected structures typically display a tendency to localize where the activity is lower. Note that the model described in this Chapter does not refer to a specific biological or synthetic system, rather it is inspired by the ubiquity of polymeric structures in nature.

The results presented in this Chapter have been published in Ref. [230].

5.1 The model

We study a minimal stochastic $d-$dimensional model of an ideal Rouse polymer composed by N units, subjected to exponentially-correlated noises, which account for the interaction with an active bath. The chain connectivity is encoded in the matrix M_{ij} [82], which determine all the pairs of interacting monomers as introduced in Section 2.7. A sketch of a polymer with linear connectivity dispersed in an active bath characterized by the presence of active agents is shown in Figure 5.1. The polymer is characterized by a quadratic Hamiltonian

$$\mathcal{H} = \frac{\kappa}{2} \sum_{i=0}^{N-1} \sum_{j=0}^{N-1} M_{ij} \boldsymbol{X}_i \cdot \boldsymbol{X}_j, \tag{5.1}$$

with $\boldsymbol{X}_i$ the position of the $i-$th monomer and κ the coupling strength of interacting monomers. We neglect inertial effects compared to viscous forces and assume that the polymer's motion follows the overdamped Langevin dynamics

$$\dot{\boldsymbol{X}}_i(t) = -\nu \nabla_{\boldsymbol{X}_i} \mathcal{H} + \mu \mathrm{f_a}(\boldsymbol{X}_i) \boldsymbol{\eta}_i + \boldsymbol{\xi}_i(t) \, . \tag{5.2}$$

Here, ν denotes the mobility of the monomers and $\{\boldsymbol{\xi}_i(t)\}$ are zero-mean Gaussian white noises with correlation

$$\langle \xi_{i\alpha}(t) \xi_{j\beta}(s) \rangle = 2D \delta_{ij} \delta_{\alpha\beta} \delta(t-s) \, , \tag{5.3}$$

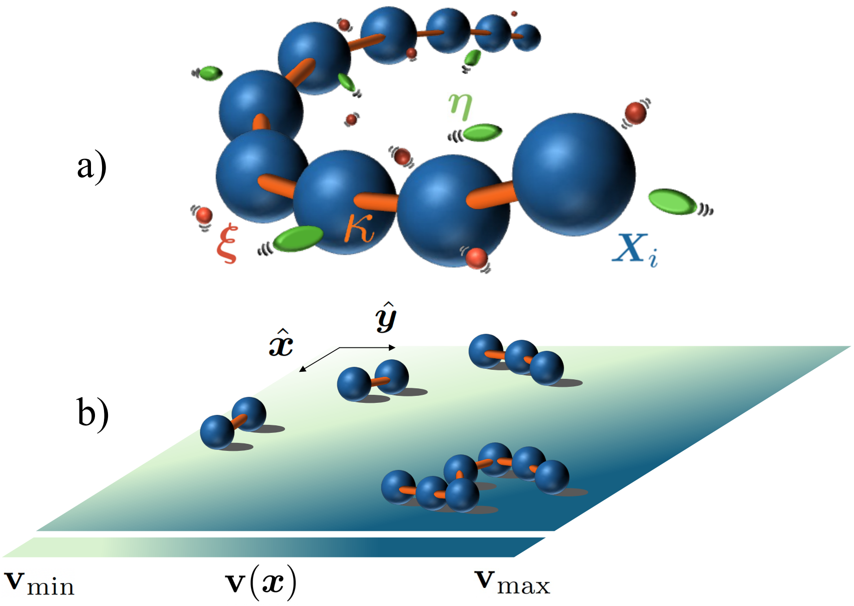

Figure 5.1: a) Sketch of a linear polymer immersed in an active bath. The blue monomers, connected by orange bonds with stiffness κ, interact with the red passive molecules (thermal bath) and are subjected to additional time-correlated forces due to the collision with the green active agents suspended in the surrounding fluid. These nonequilibrium interactions bring in nonequilibrium fluctuations that affect both the conformational and migration properties the polymer. b) Spontaneous separation of polymer species with different length dispersed in a medium characterized by a non-uniform activity field $\mathrm{v}(\boldsymbol{x})$.

describing thermal fluctuations. The thermal diffusivity is related to the mobility via the Einstein's relation $D = \nu T$, with the Boltzmann constant set to $k_{\mathrm{B}} = 1$ as in the rest of the thesis. As a result of the collisions with the active agents dispersed in the bath, the polymer experiences additional non-thermal fluctuations which violate the detailed balance condition and drive it out of equilibrium. This effect is modeled by the active forces $\mathrm{f_a}(\boldsymbol{X}_i)\boldsymbol{\eta}_i$ in the stochastic dynamics (5.2). Such active forces are characterized by a typical magnitude which varies non-homogeneously in space according to the function $\mathrm{f_a}(\boldsymbol{x})$ and are aligned with the orientation vectors $\boldsymbol{\eta}_i$, which evolve as the N independent d-dimensional Ornstein-Uhlenbeck processes

$$\tau\dot{\boldsymbol{\eta}}_i = -\boldsymbol{\eta}_i + \boldsymbol{\zeta}_i(t)\,. \tag{5.4}$$

Here $\{\boldsymbol{\zeta}_i(t)\}$ are N independent zero-mean Gaussian white noises with correlations

$$\langle\zeta_{i\alpha}(t)\zeta_{j\beta}(s)\rangle = 2\tau d^{-1}\delta_{ij}\delta_{\alpha\beta}\delta(t-s)\,, \tag{5.5}$$

and τ is the characteristic relaxation time of the OU processes which sets the persistence time of the active forces. In the long time limit, the time-translation invariant correlation function of the orientation vectors reads

$$\begin{aligned}\langle \eta_{i\alpha}(t)\eta_{j\beta}(s)\rangle &= \delta_{ij}\delta_{\alpha\beta}\mathcal{C}_\eta(t-s)\,,\\ \mathcal{C}_\eta(t-s) &= d^{-1}\exp\left(-|t-s|/\tau\right)\,.\end{aligned} \tag{5.6}$$

The variance of $\zeta_{i\alpha}$ has been chosen such that $\langle \|\boldsymbol{\eta}_i\|^2\rangle = \langle \sum_\alpha \eta_{i\alpha}^2\rangle = 1$ for all d and i. Note that the model can alternatively be used to describe a chain of active particles, each endowed with its own polarity, which use energetic resources distributed in the bath according to the activity $\mathrm{f_a}(\boldsymbol{x})$ to self-propel.

5.2 Effective dynamics

The stochastic dynamics (5.2) can be rewritten within the Rouse domain [84] in terms of the Rouse modes $\boldsymbol{\chi}_i = \sum_j \varphi_{ij}\boldsymbol{X}_j$ where the matrix φ_{ij} is chosen in such a way to diagonalize the symmetric connectivity matrix M_{ij} and with the rows normalized to unity, as presented in Sec. 2.7. The Rouse modes evolve according to the following stochastic equation of motion

$$\dot{\boldsymbol{\chi}}_i = -\gamma_i\boldsymbol{\chi}_i + \sum_j \varphi_{ij}\mathrm{v}(\boldsymbol{X}_j)\boldsymbol{\eta}_j + \tilde{\boldsymbol{\xi}}_i(t), \tag{5.7}$$

where the Gaussian white noise $\tilde{\boldsymbol{\xi}}_i(t)$ has the same statistics as $\boldsymbol{\xi}_i(t)$, and the monomer position $\boldsymbol{X}_j$ can be rewritten in terms of the Rouse modes using the inverse transformation φ^{-1}. The typical swim speed of the monomers due to activity is $\mathrm{v}(\boldsymbol{x}) \equiv \nu\mathrm{f_a}(\boldsymbol{x})$, which we will refer to as the activity field. The relaxation rates $\{\gamma_i\}$ of the Rouse modes in the absence of activity are proportional to the eigenvalues $\{\lambda_i\}$ of the connectivity matrix, i.e. $\gamma_i = \gamma\lambda_i$ where $\gamma = \nu\kappa$. Unlike the case of a Rouse polymer in a thermal bath at equilibrium, the Rouse modes are now coupled via the activity field $\mathrm{v}(\mathbf{X}_i)$, which makes the analytical treatment of the problem more challenging. We denote with $\mathcal{P}(\{\boldsymbol{\chi}\},\{\boldsymbol{\eta}\},t)$ the one-time joint probability density that the Rouse modes and the orientation vectors assume the values $\{\boldsymbol{\chi}\}$ and $\{\boldsymbol{\eta}\}$ at time t, respectively. Being the underlying dynamics of the system Markovian, the time evolution of $\mathcal{P}(\{\boldsymbol{\chi}\},\{\boldsymbol{\eta}\},t)$ follows the Fokker-Planck (FP) equation [9, 74]:

$$\partial_t\mathcal{P} = (\mathcal{L}_0 + \mathcal{L}_\mathrm{a} + \mathcal{L}_{\boldsymbol{\eta}})\mathcal{P}, \tag{5.8}$$

with the set of operators $\{\mathcal{L}_0, \mathcal{L}_{\mathrm{a}}, \mathcal{L}_{\boldsymbol{\eta}}\}$ defined as:

$$\begin{aligned}
\mathcal{L}_0 &\equiv \sum_{i=0}^{N-1} \nabla_i \cdot \Big[\gamma_i \boldsymbol{\chi}_i + D\nabla_i\Big], \\
\mathcal{L}_{\mathrm{a}} &\equiv \sum_{i=0}^{N-1} \nabla_i \cdot \Big[-\sum_j \varphi_{ij} \mathrm{v}(\boldsymbol{X}_j)\boldsymbol{\eta}_j\Big], \qquad (5.9)\\
\mathcal{L}_{\boldsymbol{\eta}} &\equiv \sum_{i=0}^{N-1} (d\tau)^{-1} \Big[\widetilde{\nabla}_i^2 + d\widetilde{\nabla}_i \cdot \boldsymbol{\eta}_i\Big].
\end{aligned}$$

Here, we used the shorthand notation $\nabla_i \equiv \nabla_{\boldsymbol{\chi}_i}$ and $\widetilde{\nabla}_i \equiv \nabla_{\boldsymbol{\eta}_i}$. The operator $\mathcal{L}_0$ corresponds to the FP-operator of a free Rouse chain in contact with an equilibrium thermal bath, while the effect of the activity is brought in by $\mathcal{L}_{\mathrm{a}}$ and $\mathcal{L}_{\boldsymbol{\eta}}$.

To investigate how the spatial localization of the polymer correlates with the bath activity, we look for a description that includes the center of mass of the polymer $\boldsymbol{X}_{\mathrm{com}} = \boldsymbol{\chi}_0/\sqrt{N}$ as the only relevant variable. Accordingly, we perform a coarse-graining procedure based on a moment expansion and a small-gradient approximation, as detailed in the Appendices C.1 and C.2. In particular, we assume that the activity field v has small spatial variations on the length scales of $\ell_{\mathrm{b}} = \sqrt{dT/k}$ and $\ell_{\mathrm{p}} = \mathrm{v}\tau$, which correspond to the bond length and the persistence length of an active particle, respectively. As a consequence, the marginal density $\rho_0(\boldsymbol{\chi}_0, t)$ of the 0-th Rouse mode and its associated probability flux $\boldsymbol{\mathcal{J}}_0$ will also exhibit small gradients on the same length scales. This simplifying assumption makes the gradient expansion (see, e.g., Refs. [25, 26] or Chapter 4) a suitable approach to derive an effective equation for ρ_0. In particular, by neglecting contributions of order $\mathcal{O}(\nabla_0^2)$ and higher in $\boldsymbol{\mathcal{J}}_0$, thus truncating the expansion to the drift/diffusion order (see Appendix C.2 for details), we obtain that $\rho_0(\boldsymbol{\chi}_0, t)$ evolves according to

$$\partial_t \rho_0 = -\nabla_0 \cdot \left[\boldsymbol{\mathcal{V}}\rho_0 - \nabla_0(\mathcal{D}\rho_0)\right], \qquad (5.10)$$

where we introduced the effective drift $\boldsymbol{\mathcal{V}}(\boldsymbol{\chi}_0)$ and diffusivity $\mathcal{D}(\boldsymbol{\chi}_0)$ given by

$$\begin{aligned}
\mathcal{D}(\boldsymbol{\chi}_0) &= D + \frac{\tau}{d}\mathrm{v}^2\Big(\frac{\boldsymbol{\chi}_0}{\sqrt{N}}\Big), \qquad (5.11)\\
\boldsymbol{\mathcal{V}}(\boldsymbol{\chi}_0) &= (1-\epsilon/2)\nabla_0 \mathcal{D}(\boldsymbol{\chi}_0). \qquad (5.12)
\end{aligned}$$

Equation (5.11) shows that the effective diffusivity $\mathcal{D}$ consists of the term D, due to thermal fluctuations, and of the enhancement induced by non-equilibrium fluctuations caused by the active forces. Moreover, the spatial variations of the activity field induce the effective drift $\boldsymbol{\mathcal{V}}$ in Eq. (5.12), which is always aligned with the activity gradient. The entity of this drift depends on the parameter ϵ, which is related to the polymer architecture and to the persistence time τ of the active forces by the following expression:

$$\epsilon = 1 - \sum_{i=1}^{N-1} \frac{1}{1+\tau\gamma_i}\,. \tag{5.13}$$

We recall here that the relaxation rates $\{\gamma_i\}$ carry information on the polymer connectivity, being proportional to the eigenvalues $\{\lambda_i\}$ of the connectivity matrix. In particular, for a linear chain

$$\lambda_j = 4\sin^2(j\pi/2N)\,. \tag{5.14}$$

Furthermore, it should be noted that Eq. (5.13) gives $\epsilon < 1$ for any choice of the model parameters, implying that the effective drift $\boldsymbol{\mathcal{V}}$ always points in the direction of greatest increase of the activity field. This might lead to the wrong conclusion that all polymeric structures tend to accumulate in regions of high bath activity, driven by $\boldsymbol{\mathcal{V}}$. However, high activity regions are also characterized by a larger effective diffusivity $\mathcal{D}$, whose effect is to reduce the typical residence time of the polymer in those areas, thus counteracting the effective drift. The competition between these two effects is governed by ϵ: depending on their degree of polymerization and connectivity, different chains will preferentially localize in different regions of space.

5.3 Stationary distribution

The effective Fokker-Planck equation (5.10) can be easily solved at steady state by imposing the zero-flux condition, due to the simple relation between the drift $\boldsymbol{\mathcal{V}}$ and the diffusion $\mathcal{D}$. By introducing $\rho(\boldsymbol{X}_{\rm com}) \equiv \rho_0(\sqrt{N}\boldsymbol{X}_{\rm com})$, we get:

$$\rho(\boldsymbol{X}_{\rm com}) = \mathcal{N}\left[1 + \frac{\tau \mathrm{v}^2(\boldsymbol{X}_{\rm com})}{dD}\right]^{-\epsilon/2}, \tag{5.15}$$

with $\mathcal{N}$ a normalization constant. Equation (5.15) implies that all chains with $\epsilon > 0$ will typically spend more time in regions of low bath activity, whereas those with $\epsilon < 0$ will preferentially accumulate in high activity areas. At fixed bath conditions, i.e., fixed time scale ratio $\alpha \equiv \tau\gamma = \tau\kappa\nu$, there are only two ways to vary ϵ. The first one is to change the degree of polymerization N of the chain by adding/removing monomeric units. The left panel of Figure 5.2 shows the steady state density of the center of mass for the case of linear chains of various lengths. Theoretical predictions (Eq. (5.15), solid lines) and numerical simulations (symbols) are compared in $d = 2$, for polymers in a box with size

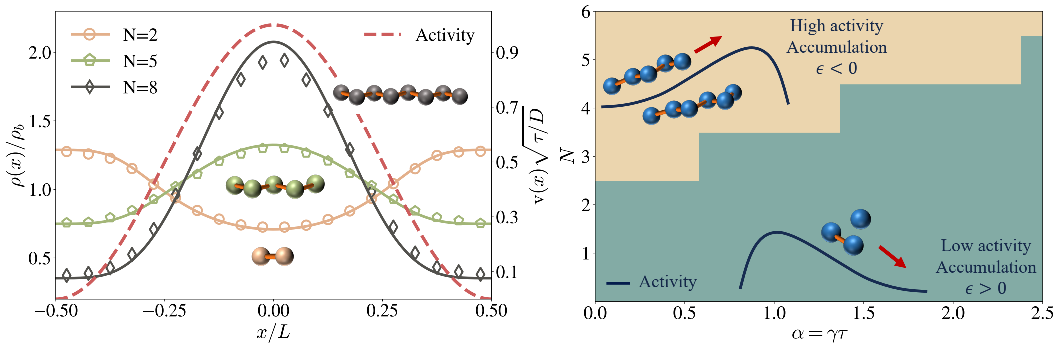

Figure 5.2: Left panel: comparison between the analytical expression of the steady state density ρ of the polymer's center of mass (see Equation (5.15), solid lines, left axis) and numerical simulations (symbols). The red dashed line shows the activity profile (right axis) and ρ is reported in units of $\rho_b = 1/L$. The parameters of the simulation are $T = 0.1$, $\kappa = 1.0$, $\mu = 1.0$, $\tau = 1.0$, $\mathrm{v}_0 = 1.0$, $L = 10$, and the integration time step $\Delta t = 0.001$. Right panel: region of preferential accumulation (corresponding to the sign of ϵ) of linear chains as a function of the time scale ratio $\alpha = \gamma\tau$ and the number of monomers N. For the purpose of visualization, the boundaries between the different signs of ϵ are drawn at half-integer values of N.

L endowed with periodic boundary conditions. The activity field is sinusoidal and varies along the x-axis as

$$\mathrm{v}(x) = (\mathrm{v}_0/2)[1 + \cos(2\pi x/L)]\,, \tag{5.16}$$

while it is uniform along the remaining, orthogonal axis. The plot shows that short chains (e.g., dimers) preferentially localize in low-activity regions, whereas the density of longer chains increasingly peaks around regions of high activity as the number of monomers increases. The minimum number of monomers above which linear chains localize in regions of high activity depends on the persistence time τ of the active forces and on the stiffness κ of the interaction between interconnected monomers. The separation between localization in high/low activity regions is evident in the diagram of Figure 5.2 (right panel), which identifies the domains of the parameter space (N, α) corresponding to these two cases. An immediate conclusion drawn from the diagram is that for single particles and dimers, the effective diffusivity always prevails over the drift contribution, leading to localization in regions of low activity for any value of α. In fact, for $\alpha \to 0$, the coefficient $\epsilon \simeq 2 - N$, implying that only chains with $N > 2$ localize in regions of high activity. For finite α, the dominant contribution to the coefficient ϵ comes from Rouse modes which relax slower than the correlation time τ of the active bath. This corresponds to the observation that with increasing τ, linear chains require a higher degree of polymerization to preferentially localize where the activity is larger (Figure 5.2).

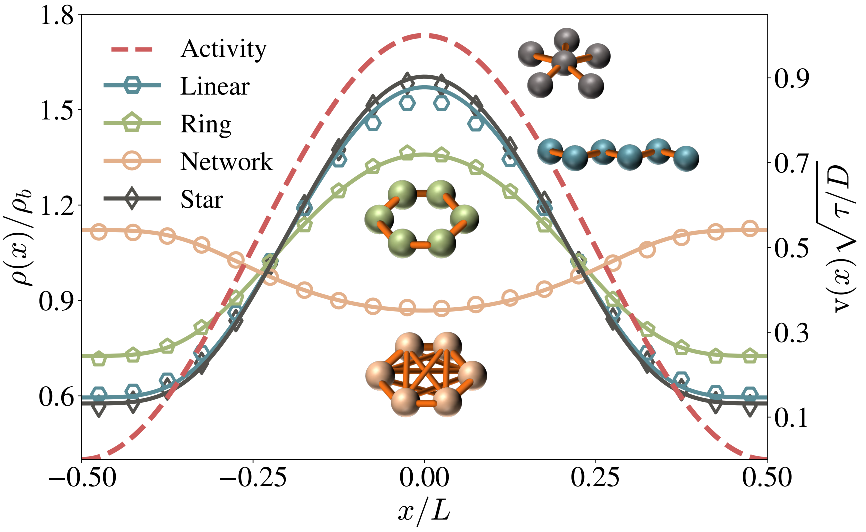

Figure 5.3: Stationary probability density ρ of the center of mass of polymers with $N = 6$ monomers and different connectivity matrix: linear (blue), ring (green), star (gray), and fully connected (light orange) polymer. We compare analytical predictions (Eq. (5.15), solid lines) and simulations results in $d = 2$ dimensions (symbols). The activity field is represented by the red dashed line (right axis). The parameters of the simulation are the same as in Fig. 5.2.

The second way to change the sign of ϵ is to vary the connectivity matrix M_{ij} of the chain by keeping fixed the number N of monomers. In order to demonstrate this, we determined the stationary density $\rho(\boldsymbol{X}_{\text{com}})$ for different structures, i.e. linear, ring, and star polymer as well as fully connected network. Figure 5.3 shows the resulting ρ, obtained with the same activity field (5.16). It turns out that, for a fixed degree N of polymerization ($N = 6$ in Figure 5.3), the most constrained structure from the point of view of internal interactions, i.e., the fully connected network, is unable to localize in the region of high activity, whereas the structures with a lower degree of connectivity typically spend more time where the activity is higher. Moreover, as can be seen in Figure 5.3, the localization is more effective for those chains characterized by the least number of bonds. To understand heuristically the possible preferential localization of the polymers in regions with high activity, we note from (5.13) that negative values of ϵ primarily arise from modes k which are much slower than the correlation time τ of the active forces, i.e., which have $\tau\gamma_k \ll 1$. Accordingly, one can estimate $|\epsilon - 1| \gtrsim K$, where K denotes the number of these slow modes, which do not relax during the persistence time τ of the active forces, thus pinning the polymer motion. In turn, these slow modes effectively play the role of passive cargoes for the remaining active modes, which turn out (see [103] and Chapter 4) to drift preferentially towards the regions in space with higher activity.

5.4 Polymer separation

The fact that polymer chains localize in regions of high or low activity depending on their degree of polymerization and connectivity can lead to the spontaneous spatial separation of different polymer species, when these are immersed in a non-uniform active bath. This can be observed, for example, in molecular dynamics simulations (see details in Appendix C.5) of a mixture of linear chains of various lengths in a sinusoidal activity field, as shown in Figure 5.4. After an initial phase in which all chains are prepared in a mixed phase localized around the center of the box, different species begin to migrate to different regions of space according to their length. In particular, the chains with $N = 20$ and 25 localize where the activity is higher, while the shorter chains spend more time in the region of low activity. To better appreciate the separation along the x-axis, where the activity is non-uniform, a harmonic confining potential along the y-axis (see Figure 5.4) has been introduced. A similar spontaneous separation, will occur even in the presence of steric hindrance (see Appendix C.3) and inter-chain interactions (neglected here), at least for dilute polymer mixtures, and possibly with different time scales, as the initial mixed state will take longer to untangle. Note that the spontaneous separation described above occurs only in non-equilibrium conditions. In fact, it would be absent if the equation of motion of the polymer obeys detailed balance, i.e., if the energy injections introduced by the time-correlated forces are compensated by an additional dissipation modeled by a friction with an appropriate memory kernel (for more details see Appendix C.4).

5.5 Discussion

The ability to segregate and sort biomolecules or synthetic polymer-like structures at micro/nano-meter scale is of paramount importance in a variety of applications, spanning from diagnostics and biomedicine to biological analyses and chemical processing [231]. Nonequilibrium conditions have already proved useful in length-selective accumulation of oligonucleotides subjected to thermal gradients [232] and elasticity-based polymer sorting in active fluids [233]. The mechanism investigated here has potential to be employed in active sorting techniques to separate polymers based on both their length and structural connectivity. In a more realistic setting, the relaxation time scales of the chain will be influenced by additional interactions (e.g., bending rigidity, steric hindrance, and hydrodynamics) and the active bath may also exhibit more than one time scale. Our theoretical predictions might be experimentally tested with synthetic chains assembled from magnetic colloidal beads [234, 235] immersed in a bath with photokinetic bacteria, the swimming speed of which depends on the incident light intensity [236, 237]. Moreover, our results could also be relevant

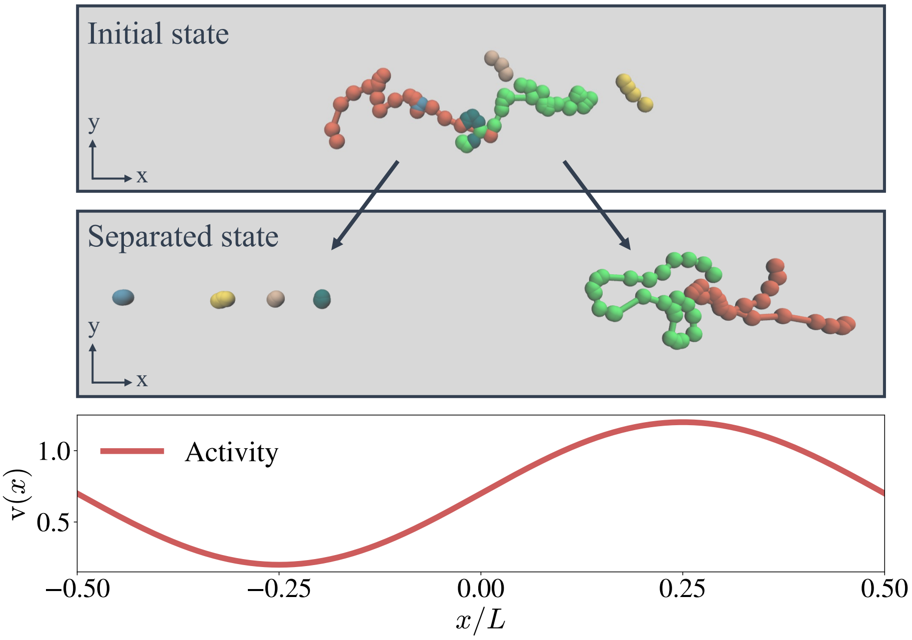

Figure 5.4: Molecular dynamics simulations proving the spontaneous separation of linear polymer chains with various lengths in a sinusoidal activity field $\mathrm{v}(x) = 0.2 + 0.5[1 + \sin(2\pi x/L)]$ (bottom panel) and in $d = 2$. Polymers with $N \in \{2, 3, 4, 5, 20, 25\}$ are initially localized and mixed at the center of the box (top snapshot). Over time, different species migrate to different regions in space, based on their polymerization degree (middle snapshot). Simulation parameters: $T = 0.01$, $\kappa = 3.0$, $\mu = 1.0$, $\tau = 3.0$, $L = 20$. Integration timestep: $\Delta t = 0.001$.

in cells where naturally occurring activity gradients in the actin cytoskeleton influence mechanics. For instance, in mouse oocytes, activity gradients facilitate the central positioning of the nucleus through active diffusion [238–240]. In such cells, the transport behavior of polymer-like structures, whether externally introduced or assembled locally, would depend on their length and topology as predicted by our theory, rather than merely diffusing down the activity gradient. Whether such activity gradient-driven processes are at work in real cells, contributing to the precise localization and transport of biomolecules remains an intriguing possibility that warrants further investigation.

Chapter 6

Rouse polymer in a fluctuating correlated medium

Understanding the behavior of polymeric macromolecules dispersed in a fluid environment is of crucial importance for advancements in biomedical applications [241–243], the design and development of smart materials [244–247], and for understanding several biological processes [248, 249]. In most situations, polymeric molecules are in contact with complex heterogeneous and correlated media, and their behavior is significantly affected by their mutual interaction. For example, this is the case of polymers embedded in composite fluids [250], porous media [251], biological tissues and cellular interiors [252, 253]. Over the last decades, particular emphasis has been put on investigating structural properties of polymeric chains in binary liquid mixtures displaying spatio-temporal correlations [254–261]. The typical length scale of such correlations depends on the distance from the critical demixing point of the binary mixture, and potentially diverges when the mixture is poised at the critical point.

A first theoretical study of this problem has been done by De Gennes and Brochard [254, 255], who showed that a polymer dispersed in a binary liquid mixture would first collapse into a globule-like configuration as the solvent approaches the demixing transition, to eventually re-expand at the critical point itself. The polymer collapse has been physically rationalized by advancing the hypothesis that the better solvent of the binary mixture would form a wetting layer around the polymer, screening the excluded volume repulsion and thus resulting in an effective attraction. The spatial range of these induced interactions caused by the fluctuating medium is given by the correlation length of the latter [254, 262]. In particular, the effective interactions experienced by the polymer become long-range when the underlying medium is critical. When the correlation length of the binary mixture exceeds the typical size of the polymer, the latter is effectively immersed in a droplet enriched with the better solvent, and thus it re-swells again to its size in a pure solvent. Further theoretical investigations have been proposed later on, relying on self-consistent perturbative schemes [263, 264] and field-theoretic methods [262, 265–267]. The analytical predictions on the conformational features of a polymer in a near-critical solvent have been verified by on-lattice Monte Carlo simulations [256, 268] and multiscale simulation methods based on density functional theory [269]. From an experimental perspective, the effect of a correlated environment on the structure of a tracer chain has been explored using dynamic light scattering [270, 271] and small-angle neutron scattering [272]. While many static properties of a polymer in a correlated environment have been widely studied in the past, the effect of the field-mediated forces on its dynamics is much less explored.

In this Chapter, we study conformational and dynamical properties of a polymer chain interacting with a correlated medium, which is described by a thermally fluctuating order parameter field $\phi(\boldsymbol{x}, t)$. The latter evolves according to a dissipative (model A) or conserved (model B) relaxational dynamics, analogously to Refs. [62–64, 66–69, 71], and interacts with the polymer via a translationally invariant linear coupling. Due to this interaction, the polymer and the field affect each other dynamically. To make contact with the case of a polymer chain dispersed in a binary solvent mixture, the scalar field $\phi(\boldsymbol{x}, t)$ can be interpreted as the relative concentration of the two species in the mixture. However, our derivation does not rely on any specific interpretation of the order parameter $\phi(\boldsymbol{x}, t)$. At the same time, the field dynamics presented here neglects hydrodynamic effects, which are necessary to make contact with real fluids. Using two distinct approaches based on the linear response theory or the weak-coupling approximation, we make theoretical predictions on conformational and relaxation properties of the chain.

For this reason, after describing the model in Sec. 6.1 and analyzing the field-induced interaction in Sec. 6.2, we derive in Secs. 6.3.1 and 6.3.2 a linearized effective equation of motion for the polymer, and study the dynamical relaxation of its internal structure as well as the one of its center of mass toward the rest position in a confining potential. In particular, we investigate the extent to which the correlated medium affects such relaxation processes, especially close to the critical point. In Sec. 6.4 we study the typical size of the polymer as a function of its polymerization degree and of the correlation length of the medium. Finally, in Sec. 6.4.3 we analyze the response of a linear polymer to a tensile force acting on its extreme monomers. All analytical predictions are tested using numerical simulations.

6.1 The model

The system consists of an ideal harmonic (Rouse) chain in d spatial dimensions, composed by N monomers with positions $\{\boldsymbol{X}_i(t)\}_{i=0}^{N-1}$, and a fluctuating order

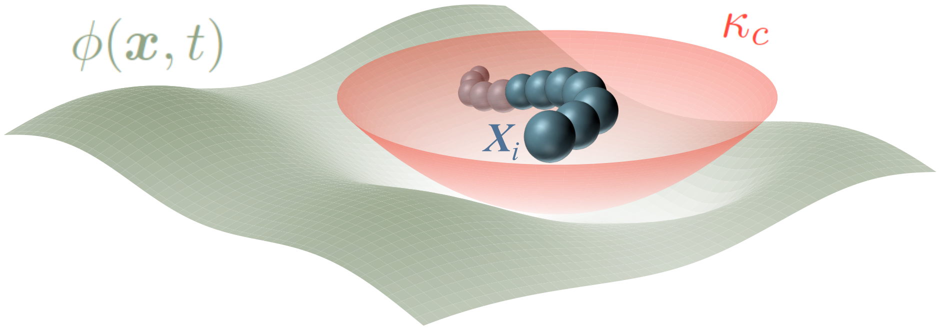

Figure 6.1: Schematic illustration of the model representing a (linear) polymer chain coupled to a thermally fluctuating order parameter field $\phi(\boldsymbol{x},t)$, and confined by a harmonic potential with stiffness κ_c.

parameter field $\phi(\boldsymbol{x},t)$. The structure of the internal interactions among the monomers is encoded in the connectivity matrix M_{ij} (see Sec. 2.7), so that the Hamiltonian of the Rouse polymer is given by:

$$\mathcal{H}_0 = \frac{\kappa}{2}\sum_{ij} M_{ij}\boldsymbol{X}_i\cdot\boldsymbol{X}_j + \frac{\kappa_c}{2}\sum_i \boldsymbol{X}_i^2\,, \tag{6.1}$$

where κ denotes the stiffness of the pairwise attractions between the sub-units of the chain, and κ_c sets the elastic constant of the external harmonic confinement, in case this is present. Note that we neglect, in what follows, the possible energetic contributions coming from the bending of the polymeric chain, as well as excluded volume interactions leading to steric hindrance effects. In fact, our aim here is to investigate the extent to which the spatio-temporal correlations in the underlying medium affect the structural properties of the simplest possible polymer model. For the fluctuating scalar field $\phi(\boldsymbol{x})$ we take a Gaussian Hamiltonian

$$\mathcal{H}_\phi = \int \mathrm{d}^d\boldsymbol{x}\left[\frac{1}{2}(\nabla\phi)^2 + \frac{r}{2}\phi^2\right]\,, \tag{6.2}$$

where the parameter $r \geq 0$ controls the distance of the field from criticality, and determines its correlation length $\xi_\phi = r^{-1/2}$. Analogously to Refs. [65–68], the coupling between the polymer and the field is chosen to be linear and translation invariant, and it is given by:

$$\mathcal{H}_{\text{int}} = -\lambda\sum_{i=0}^{N-1}\sigma_i\int \mathrm{d}^d\boldsymbol{x}\,\phi(\boldsymbol{x})V(\boldsymbol{x}-\boldsymbol{X}_i)\,, \tag{6.3}$$

where $\lambda > 0$ denotes the coupling strength, $V(\boldsymbol{x}) > 0$ the interaction potential and $\{\sigma_i\}_{i=0}^{N-1}$ a set of N binary variables with $\sigma_i \in \{-1,+1\}$. This means that the energetically favoured configurations are those where the field assumes larger (smaller) values in spatial proximity of the monomers with positive (negative) interaction coupling $\lambda\sigma_i$. For simplicity, we focus on isotropic interaction potentials characterized by a single length scale R, such as:

$$V(\boldsymbol{x}) = (2\pi R^2)^{-d/2} \exp\bigl(-\boldsymbol{x}^2/(2R^2)\bigr)\,. \tag{6.4}$$

Here R represents the characteristic length scale of interaction between the field $\phi(\boldsymbol{x}, t)$ and each monomer in the chain, and it might be interpreted as the typical monomer size. In the following, we will denote the total Hamiltonian as

$$\mathcal{H} = \mathcal{H}_0 + \mathcal{H}_\phi + \mathcal{H}_{\text{int}}\,. \tag{6.5}$$

As typically done for biomolecules in solution, we assume that viscous forces dominate over inertial effects, and we model the equation of motion of the polymer with the following set of overdamped Langevin equations:

$$\begin{aligned}\dot{\boldsymbol{X}}_i(t) &= -\nu\nabla_{\boldsymbol{X}_i}\mathcal{H} + \boldsymbol{\xi}_i(t)\\ &= -\nu\kappa M_{ij}\boldsymbol{X}_j - \nu\kappa_c\boldsymbol{X}_i + \nu\lambda\sigma_i\mathbf{f}(\boldsymbol{X}_i) + \boldsymbol{\xi}_i(t)\,,\end{aligned} \tag{6.6}$$

where ν is the monomer mobility, and the force $\mathbf{f}(\boldsymbol{X}_i)$ exerted by the field on the i-th monomer reads:

$$\mathbf{f}(\boldsymbol{X}_i, \phi, t) \equiv -\int \mathrm{d}^d\boldsymbol{x}\, \phi(\boldsymbol{x})\nabla_{\boldsymbol{x}} V(\boldsymbol{x} - \boldsymbol{X}_i)\,. \tag{6.7}$$

Moreover, the polymer is in contact with a thermal bath at temperature T, the effect of which is accounted for by the set of zero-mean independent Gaussian white noises $\{\boldsymbol{\xi}_i(t)\}$, with correlations

$$\langle \xi_i^\alpha(t)\xi_j^\beta(s)\rangle = 2\nu T\delta_{ij}\delta_{\alpha\beta}\delta(t-s)\,. \tag{6.8}$$

Being the system at equilibrium, the amplitude of the noise is chosen such that fluctuations and dissipations are related by Einstein's relation. As explained in Sec. 2.7, the stochastic dynamics of the polymer in Eq. (6.6) can be rewritten within the Rouse domain [84] by introducing the Rouse modes $\{\boldsymbol{\chi}_i\}$ and the orthogonal transformation φ, see Eqs. (2.59) and (2.60). When the coupling to the field is switched off, i.e., $\lambda = 0$, the Rouse modes are decoupled and their time evolution is governed by independent Ornstein-Uhlenbeck processes with inverse relaxation times

$$\tilde{\gamma}_i \equiv \tau_i^{-1} \equiv \gamma_i + \gamma_c\,. \tag{6.9}$$

Here $\gamma_c = \nu\kappa_c$ is the inverse characteristic time scale introduced by the harmonic confinement, while $\gamma_i = \nu\kappa m_i$ denotes the inverse relaxation time of the i^{th} Rouse mode of an unconfined chain, which depends on the eigenvalue m_i of the connectivity matrix $\boldsymbol{M}$. However, when the polymer interacts with $\phi(\boldsymbol{x}, t)$, the field-induced forces couple the Rouse modes yielding to the following dynamics:

$$\dot{\boldsymbol{\chi}}_i = -\tilde{\gamma}_i \boldsymbol{\chi}_i + \nu\lambda \sum_{j=0}^{N-1} \varphi_{ij}\sigma_j \mathbf{f}(\boldsymbol{X}_j, \phi) + \boldsymbol{\eta}_i(t)\,, \tag{6.10}$$

where the noise $\boldsymbol{\eta}_i$ has the same statistics as $\boldsymbol{\xi}_i$, and the monomer position $\boldsymbol{X}_j$ can be rewritten as a linear combination of Rouse modes by means of the inverse transformation $\boldsymbol{\varphi}^{-1}$.

As in Sec. 2.8, the field $\phi(\boldsymbol{x}, t)$ is assumed to evolve according to a purely relaxational dynamics [54]

$$\partial_t \phi(\boldsymbol{x}, t) = -D(i\nabla)^a \left[(r - \nabla^2)\phi - \lambda \sum_{i=0}^{N-1} \sigma_i V(\boldsymbol{x} - \boldsymbol{X}_i)\right] + \zeta(\boldsymbol{x}, t)\,, \tag{6.11}$$

where D denotes the mobility of the field. As explained in Sec. 2.8, the parameter a takes the value $a = 2$ (model B, see Sec. 2.8) if the order parameter field is locally conserved during its dynamics, whereas $a = 0$ (model A, see Sec. 2.8) if it does not satisfy any conservation law. The zero-mean Gaussian white noise field $\zeta(\boldsymbol{x}, t)$ is characterized by the correlations reported in Eq. (2.72). The amplitude of the noise field is proportional to the field mobility D and to the temperature T, as the polymer and the field are assumed to be in contact with the same thermal bath. The stochastic dynamics of the field in Eq. (6.11) can be conveniently rewritten in Fourier space as

$$\dot{\phi}_{\boldsymbol{q}} = -\alpha_{\boldsymbol{q}}\phi_{\boldsymbol{q}} + D\lambda V_{\boldsymbol{q}} q^a \sum_{j=0}^{N-1} \sigma_j e^{-i\boldsymbol{X}_j \cdot \boldsymbol{q}} + \zeta_{\boldsymbol{q}}(t)\,, \tag{6.12}$$

where we introduced the relaxation rates

$$\alpha_{\boldsymbol{q}} \equiv Dq^a(r + q^2) \tag{6.13}$$

and $\zeta_{\boldsymbol{q}}(t)$, from Eqs. (2.73) and (2.76). In the absence of the interaction coupling, i.e. for $\lambda = 0$, the field modes $\phi_{\boldsymbol{q}}$ evolve according to independent Ornstein-Uhlenbeck processes with relaxation times $\tau_\phi(\boldsymbol{q}) = \alpha_{\boldsymbol{q}}^{-1}$. In particular, this implies that the $\boldsymbol{q} = \boldsymbol{0}$ mode features a diverging relaxation time in the case of critical model A dynamics, which is consistent with the phenomenon of critical slowing-down [54]. The same effect is also present in the case of model B dynamics, even off-criticality, as a consequence of the conservation law, whereby large length-scale perturbations relax on arbitrarily large time scales. Note that in the case of model A dynamics the zero-mode $\phi_{\boldsymbol{q}=\boldsymbol{0}}$ diffuses and might become arbitrarily large as the field approaches criticality. However, this fact is irrelevant for what concerns the equation of motion of the polymer, as can be easily

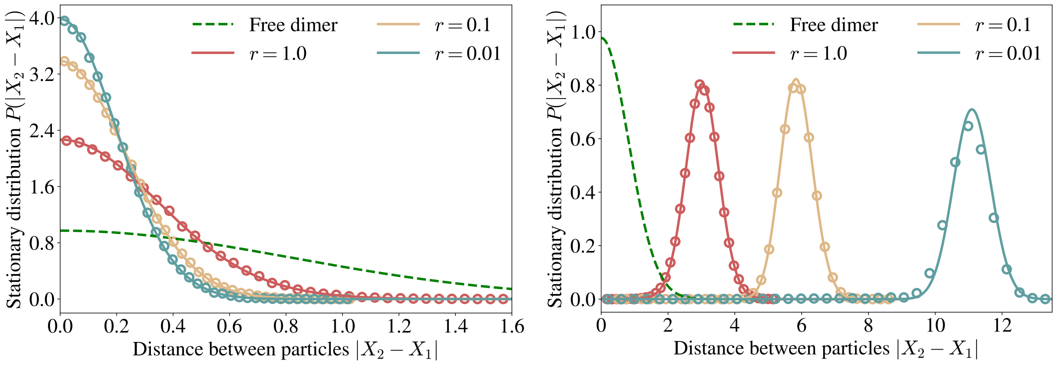

Figure 6.2: Stationary distribution $P(|X_2 - X_1|)$ of the distance $|X_2 - X_1|$ between the two sub-units of a dimer, interacting with a fluctuating field in $d = 1$ and in the absence of confinement. Solid lines represent the theoretical predictions in Eq.(6.16), whereas symbols are obtained with molecular dynamics simulations (see Appendix D.4). Left panel: the monomers are characterized by the same interaction coupling with the fluctuating field. This induces a collapse of the dimer, which is increasingly more effective as the field approaches criticality, i.e., as the value of $r > 0$ is reduced. Right panel: the monomers are characterized by opposite interaction couplings with the field, and thus the dimer is stretched. The results of the simulations (symbols) are obtained with the following parameters: $\kappa = 1$, $\nu = 1$, $T = 1$, $D = 1$, $R = 1$, $\lambda = 10$. The non-vanishing value of the average distance (i.e., of the static equilibrium point) in the right panel emerges from the competition between the inter-monomer attraction and the effective repulsive force induced by the field.

realized by rewriting the field-induced force $\mathbf{f}$ in Eq. (6.7) as:

$$\mathbf{f}(\boldsymbol{X}_j, \phi, t) = \int \frac{\mathrm{d}^d q}{(2\pi)^d}\, i\boldsymbol{q}\phi_{\boldsymbol{q}} V_{-\boldsymbol{q}} e^{\mathrm{i}\boldsymbol{q}\cdot\boldsymbol{X}_j}\,, \tag{6.14}$$

to which the zero-mode $\phi_{\boldsymbol{q}=\boldsymbol{0}}$ does not actually contribute. In a more realistic system, however, one would need to counteract this growth by adding a suitable chemical potential — e.g., $\mathcal{H}_\phi \mapsto \mathcal{H}_\phi + \lambda N \int \mathrm{d}\boldsymbol{x}\, \phi(\boldsymbol{x})$.

To investigate the effect of the correlated medium on structural and migration properties of the polymer, we analyze the behavior of its center of mass $\boldsymbol{X}_{\mathrm{com}} = \boldsymbol{\chi}_0/\sqrt{N}$ and of its internal structure described by the Rouse modes $\boldsymbol{\chi}_j$ with $j > 1$. By computing their amplitudes $\langle \boldsymbol{\chi}_j^2 \rangle$, we can determine the typical size of the polymer given by its mean-squared gyration radius. Note that the definition of the Rouse modes will depend in general on the polymer connectivity $\boldsymbol{M}$, which is kept generic in the analysis presented below.

6.2 Field-induced interactions

Since the stochastic dynamics in Eqs. (6.10) and (6.11) satisfies the detailed balance condition, the stationary joint probability distribution of the polymer and the field follows the Boltzmann distribution

$$P_{\mathrm{eq}}[\phi, \{\boldsymbol{\chi}_j\}] \propto \exp\left\{-\beta \mathcal{H}[\phi, \{\boldsymbol{\chi}_j\}]\right\} , \tag{6.15}$$

with $\beta = 1/T$. Hence, the marginal distribution $P_{\mathrm{eq}}(\{\boldsymbol{\chi}_j\})$ of the polymer can be obtained by integrating out the field ϕ, and it is given by:

$$P_{\mathrm{eq}}(\{\boldsymbol{\chi}_j\}) = \int \mathcal{D}[\phi] P_{\mathrm{eq}}[\phi, \{\boldsymbol{\chi}_j\}] \propto \exp\left\{-\beta(\mathcal{H}_0 + \mathcal{H}_{\mathrm{eff}})\right\} . \tag{6.16}$$

Importantly, the effect of the field now appears in the form of an effective interaction Hamiltonian $\mathcal{H}_{\mathrm{eff}}$ among the monomers, whose expression reads:

$$\begin{aligned} \mathcal{H}_{\mathrm{eff}} &= -\frac{\lambda^2}{2} \sum_{ij} \sigma_i \sigma_j \int \frac{\mathrm{d}^d q}{(2\pi)^d} |V_q|^2 G_{\boldsymbol{q}} \left[e^{i\mathbf{q}\cdot(\mathbf{X}_i - \mathbf{X}_j)} - 1 \right] \\ &= -\frac{\lambda^2}{2} \sum_{ij} \sigma_i \sigma_j \int \frac{\mathrm{d}^d q}{(2\pi)^d} |V_q|^2 G_{\boldsymbol{q}} \left[e^{i\mathbf{q}\cdot \sum_k (\varphi_{ki} - \varphi_{kj}) \boldsymbol{\chi}_k} - 1 \right] , \end{aligned} \tag{6.17}$$

where

$$G_{\boldsymbol{q}} = 1/(r + \boldsymbol{q}^2) \tag{6.18}$$

denotes the Fourier transform of the equal-time propagator within the Gaussian model (see, e.g., Ref. [54]). Notice that in Eq. (6.17) we adopted the convention for which the value of the effective interaction energy is measured with respect to the case of perfectly overlapping monomers, such that $\mathcal{H}(\{\boldsymbol{\chi}_j = \mathbf{0}\}) = 0$. Importantly, the effective Hamiltonian (6.17) is pairwise additive. The absence of many-body interactions is due to the fact the coupling between the monomers and the field is linear, in agreement with what was noted in Ref. [273]. This fact is not merely an equilibrium feature, but it actually carries over to the dynamics, as shown in Ref. [67] using dynamical path-integral methods.

Interesting conclusions on the effects of the field-induced forces can be drawn by considering the limiting case of point-like monomers, i.e., $R \to 0$. In this case, the interaction potential is given by $V(\boldsymbol{x}) = \delta^d(\boldsymbol{x})$, and in $d = 3$ the effective Hamiltonian in Eq. (6.17) takes the form of a Yukawa potential

$$\mathcal{H}_{\mathrm{eff}} = -\sum_{i \neq j} \frac{\lambda^2 \sigma_i \sigma_j}{4\pi} \frac{e^{-|\boldsymbol{X}_i - \boldsymbol{X}_j|/\xi_\phi}}{|\boldsymbol{X}_i - \boldsymbol{X}_j|} , \tag{6.19}$$

with a characteristic decay length which is given by the correlation length ξ_ϕ of the field. This result is consistent with what previously found in Refs. [254, 255, 262] for polymeric molecules in binary fluids. In particular, this implies that the internal structure of the polymer is strongly affected by the field, especially when the latter approaches the critical point and the effective interaction is described by a long-range Hamiltonian. Importantly, the attractive/repulsive nature of the field-induced interaction between two monomers of the chain depends on the sign of their couplings $\lambda\sigma_i$ with the fluctuating field ϕ. More precisely, when the two couplings have the same sign, the monomers attract each other, whereas in the case couplings with opposite signs, they repel. This effect is explicitly shown in Fig. 6.2 for the simplest case of a dimeric molecule ($N = 2$) in $d = 1$ dimensions, and it is known to be a rather general feature of fluctuation-induced forces (see, e.g., Ref. [274]). Here, we plot the stationary distribution of the relative distance between the two monomers for various values of the parameter r, i.e., for fluctuating fields ϕ with various correlation length. Specifically, we show that as the critical point is approached, the typical distance between the monomers decreases (increases) in the case of attractive (repulsive) field-mediated interactions.

6.3 Relaxation toward equilibrium

In order to analyze the influence of the correlations of the medium on the dynamical properties of the polymer, we derive the effective equation of motion of the latter by integrating out the fluctuating order parameter ϕ, analogously to what has been done, in a similar context, in Refs. [62, 65, 67, 68, 71, 275]. For simplicity, we shall focus on the case in which all monomers couple to the field with couplings of the same sign σ, i.e. $\sigma_0 = \sigma_1 = ... = \sigma_{N-1} = \sigma$, implying that all field-mediated interactions are attractive.

6.3.1 Effective dynamics of the polymer

As a first step, we solve exactly the stochastic dynamics (6.12) of the fluctuating field, obtaining:

$$\begin{aligned}\phi_{\boldsymbol{q}}(t) = G_{\boldsymbol{q}}(t-t_0)\phi_{\boldsymbol{q}}(t_0) + \int_{t_0}^{t} \mathrm{d}s\, G_{\boldsymbol{q}}(t-s)\zeta_{\boldsymbol{q}}(s) \\ + D\lambda\sigma \int_{t_0}^{t} \mathrm{d}s\, G_{\boldsymbol{q}}(t-s) V_{\boldsymbol{q}} q^a \sum_{j=0}^{N-1} e^{-i\sum_k \varphi^{-1}_{jk} \boldsymbol{q}\cdot\boldsymbol{\chi}_k(s)}\,,\end{aligned} \tag{6.20}$$

where

$$G_{\boldsymbol{q}}(t) = \Theta(t) e^{-\alpha_{\boldsymbol{q}} t} \tag{6.21}$$

denotes the dynamic field propagator and t_0 the initial time, with $t > t_0$. The solution above is then substituted into the evolution equation (6.10) of the

Rouse modes, yielding the following effective non-Markovian dynamics for the polymer:

$$
\begin{aligned}
\dot{\boldsymbol{\chi}}_j = & \int_{t_0}^{t} \mathrm{d}s\, \boldsymbol{F}_j(\Delta\boldsymbol{\chi}_0(t,s), \{\boldsymbol{\chi}_k(s)\}_{k>0}, \{\boldsymbol{\chi}_k(t)\}_{k>0}) \\
& - \tilde{\gamma}_j \boldsymbol{\chi}_j + \boldsymbol{v}_j^{\mathrm{ic}}(\{\boldsymbol{\chi}_k(t)\}) + \Xi_j(\{\boldsymbol{\chi}_k(t)\}, t)\,, \qquad (6.22)
\end{aligned}
$$

where we denoted by $\Delta\boldsymbol{\chi}_0(t,s) = \boldsymbol{\chi}_0(t) - \boldsymbol{\chi}_0(s)$ the displacement of the rescaled center of mass. Let us discuss the various terms entering this dynamics. The interaction of the polymer with the fluctuating field introduces a space- and time-dependent memory kernel $\boldsymbol{F}_j$ given by:

$$
\begin{aligned}
\boldsymbol{F}_j(\Delta\boldsymbol{\chi}_0(t,s), \{\boldsymbol{\chi}_k(s)\}_{k>0}, \{\boldsymbol{\chi}_k(t)\}_{k>0}) = & D\nu\lambda^2 \int \frac{\mathrm{d}^d q}{(2\pi)^d}\, i\boldsymbol{q} q^a |V_{\boldsymbol{q}}^2| G_{\boldsymbol{q}}(t-s) \\
\times \sum_{n,k=0}^{N-1} \varphi_{jk} e^{\frac{i\boldsymbol{q}\cdot\Delta\boldsymbol{\chi}_0(t,s)}{\sqrt{N}}} & \exp\left\{ -i\boldsymbol{q} \cdot \sum_{m=1}^{N-1} [\varphi_{nm}^{-1}\boldsymbol{\chi}_m(s) - \varphi_{km}^{-1}\boldsymbol{\chi}_m(t)] \right\}. \qquad (6.23)
\end{aligned}
$$

Note that the memory kernel depends in a non-linear way on the spatial coordinates. Furthermore, its functional dependence on the various Rouse modes is qualitatively different: while the center of mass only appears via its displacement $\Delta\boldsymbol{\chi}_0(t,s)$, the higher-order modes $\boldsymbol{\chi}_j(s)$ and $\boldsymbol{\chi}_j(t)$ at two different times t and s contribute separately to the memory term. The relevance of this apparently secondary fact and its effect on the dynamical properties of the polymer will be clarified in Sec. 6.3.2.

Another interesting point to be noted is the fact that the memory kernel does not depend on the sign of the interaction coupling, as it is proportional to $\lambda^2\sigma^2 = \lambda^2$. This property is a consequence of the fact that the original dynamics in Eqs. (6.10) and (6.12) is invariant under the transformation $(\lambda, \phi) \leftrightarrow (-\lambda, -\phi)$ [66]. Importantly, the effective dynamics in Eq. (6.22) does not hinge on any approximation, and it is therefore exact to any order in the interaction coupling λ. The statistics of the noise Ξ_j of the effective dynamics is also affected by the interaction of the polymer with the order parameter ϕ. In particular, it consists of a white noise term $\boldsymbol{\xi}_j$ which describes the interaction with the thermal bath, and a temporally correlated term resulting from the coarse graining of the field. In fact:

$$
\begin{aligned}
\Xi_j(t) = \boldsymbol{\xi}_j(t) + \lambda\sigma\nu \int \frac{\mathrm{d}^d q}{(2\pi)^d} i\boldsymbol{q} V_{-\boldsymbol{q}} & \int_{t_0}^{t} \mathrm{d}s\, G_{\boldsymbol{q}}(t-s)\zeta_{\boldsymbol{q}}(s) \\
& \times \sum_{j,k=0}^{N-1} \varphi_{jk} \exp\left[i\boldsymbol{q} \cdot \sum_{n=0}^{N-1} \varphi_{kn}^{-1}\boldsymbol{\chi}_n(t) \right]. \qquad (6.24)
\end{aligned}
$$

For each wavevector $\boldsymbol{q}$, the temporal convolution over the variable s between the free-field propagator $G_{\boldsymbol{q}}$ and the noise $\zeta_{\boldsymbol{q}}$ corresponds to an exponentially colored noise with correlation time $1/\alpha_{\boldsymbol{q}}$. Thus, as expected, each mode of the field contributes to the stochastic part of Eq. (6.22) by introducing some memory over its own typical relaxation time. For this reason, the correlation of $\boldsymbol{\Xi}_j$ might extend for arbitrarily long times in the case of locally conserved dynamics or critical fields. Moreover, the noise $\boldsymbol{\Xi}_j$ is multiplicative in that its amplitude depends on the value assumed by the Rouse modes at time t.

Finally, at short times, the effective dynamics of the polymer is reminiscent of the initial configuration of the field $\phi_{\boldsymbol{q}}(t_0)$ via the following term:

$$\boldsymbol{v}_j^{\mathrm{ic}}(t) = \lambda\sigma\nu \int \frac{\mathrm{d}^d q}{(2\pi)^d} i\boldsymbol{q} V_{-\boldsymbol{q}} G_{\boldsymbol{q}}(t-t_0)\phi_{\boldsymbol{q}}(t_0) \sum_{k=0}^{N-1} \varphi_{jk} \exp\left[i\boldsymbol{q} \cdot \sum_{n=0}^{N-1} \varphi_{kn}^{-1} \boldsymbol{\chi}_n(t) \right], \tag{6.25}$$

which decays to zero after the longest relaxation time of the field. Note that for an initial spatially homogeneous field one has $\phi_{\boldsymbol{q}}(t_0) \propto \delta^d(\boldsymbol{q})$, so that $\boldsymbol{v}_j^{\mathrm{ic}}(t)$ vanishes at all times.

6.3.2 Linearized dynamics of the polymer

Unfortunately, the effective dynamics in Eq. (6.22) does not lend itself to an analytical treatment, due to its non-linear nature and to the complicated statistics of the multiplicative and colored noise $\boldsymbol{\Xi}_j(t)$. However, since in the following we will be interested in the long-time behavior close to equilibrium, we now focus on the *linear* response of the system. Besides, note that linearizing the dynamics may provide an accurate approximation even moderately far from equilibrium. For example, one can notice that the non-linear dependence on the Rouse modes in the memory kernel in Eq. (6.23) is weighted by the factor $\boldsymbol{q}q^a|V_{\boldsymbol{q}}^2|G_{\boldsymbol{q}}(t-s)$, which decays exponentially to zero for large wavevectors (see Eq. (6.21)). This means that the momentum integral in Eq. (6.23) has an effective cutoff which depends on the time lag $t-s$. For example, in the case of model A, the weight factor is proportional to a Gaussian with standard deviation $\sigma_w = [2R^2 + 2D(t-s)]^{-1}$. Therefore, all contributions to the memory kernel coming from momenta $q > q_{\mathrm{cutoff}} \sim 3\sigma_w$ are substantially negligible. This implies that, whenever the displacement of the center of mass $\Delta\boldsymbol{\chi}_0(t,s)$ and higher-order Rouse modes at times t and s are much smaller than $1/q_{\mathrm{cutoff}}$, the memory kernel can be linearized around $\Delta\boldsymbol{\chi}_0(t,s) = \boldsymbol{\chi}_j(s) = \boldsymbol{\chi}_j(t) = \boldsymbol{0}$. We then linearize the effective dynamics in Eq. (6.22), obtaining first of all the non-linear memory kernel $\boldsymbol{F}_j$

$$\boldsymbol{F}_j(\Delta\boldsymbol{\chi}_0(t,s),\{\boldsymbol{\chi}_k(s)\}_{k>0},\{\boldsymbol{\chi}_k(t)\}_{k>0}) \simeq D\nu\lambda^2\int\frac{\mathrm{d}^dq}{(2\pi)^d}\,\boldsymbol{q}q^a|V_{\boldsymbol{q}}^2|G_{\boldsymbol{q}}(t-s)$$
$$\times\,\boldsymbol{q}\cdot\sum_{m,n,k=0}^{N-1}\varphi_{jk}[\varphi^{-1}_{nm}\boldsymbol{\chi}_m(s)-\varphi^{-1}_{km}\boldsymbol{\chi}_m(t)]\,. \quad (6.26)$$

Furthermore, the last line can be simplified by using some properties of the transformation $\boldsymbol{\varphi}$ introduced in Sec. 2.8. Specifically, we remind that it contains along its rows the eigenvectors of the connectivity matrix $\boldsymbol{M}$ normalized to unity. This implies that $\boldsymbol{\varphi}$ is orthogonal, i.e. $\boldsymbol{\varphi}^{-1}=\boldsymbol{\varphi}^T$, because $\boldsymbol{M}$ is symmetric, and that $\varphi_{0j}=1/\sqrt{N}$ for all $j\in\{0,...,N-1\}$. This can be used to prove the following simple identity:

$$\sum_j\varphi^{-1}_{ji}=\sum_j\varphi_{ij}=\sqrt{N}\sum_j\varphi_{ij}\varphi_{0j}=\sqrt{N}\delta_{i0}\,, \quad (6.27)$$

which can be used to rewrite Eq. (6.26) as

$$\boldsymbol{F}_j(\Delta\boldsymbol{\chi}_0(t,s),\{\boldsymbol{\chi}_k(s)\}_{k>0},\{\boldsymbol{\chi}_k(t)\}_{k>0}) \simeq \dot{\Gamma}(t-s)[\boldsymbol{\chi}_j(t)-\delta_{j0}\boldsymbol{\chi}_0(s)]\,, \quad (6.28)$$

where we introduced the linear memory kernel

$$\Gamma(t)=\frac{ND\nu\lambda^2}{d}\int\frac{\mathrm{d}^dq}{(2\pi)^d}\,\frac{q^{2+a}|V_{\boldsymbol{q}}|^2G_{\boldsymbol{q}}(t)}{\alpha_{\boldsymbol{q}}}\,. \quad (6.29)$$

Already from Eq. (6.28) one can anticipate that the center of mass and the higher-order Rouse modes will behave differently. Indeed, by specializing Eq. (6.28) to $j=0$, one can see that the result of the linearization still depends on the displacement $\Delta\boldsymbol{\chi}_0(t,s)$, which involves the position of the center of mass at two times t and s. Conversely, for $j>0$, Eq. (6.28) only depends on the Rouse mode $\boldsymbol{\chi}_j(t)$ at the single time t. Integrating Eq. (6.28) over s we get:

$$\int_{t_0}^t\mathrm{d}s\,\boldsymbol{F}_0(\Delta\boldsymbol{\chi}_0(t,s),\{\boldsymbol{\chi}_k(s)\}_{k>0},\{\boldsymbol{\chi}_k(t)\}_{k>0}) \simeq$$
$$-\int_{t_0}^t ds\,\Gamma(t-s)\dot{\boldsymbol{\chi}}_0(s)+\Gamma(t-t_0)\Delta\boldsymbol{\chi}_0(t,t_0) \quad (6.30)$$

for the center of mass, and

$$\int_{t_0}^t\mathrm{d}s\,\boldsymbol{F}_j(\Delta\boldsymbol{\chi}_0(t,s),\{\boldsymbol{\chi}_k(s)\}_{k>0},\{\boldsymbol{\chi}_k(t)\}_{k>0}) \simeq -[\Gamma(0)-\Gamma(t-t_0)]\boldsymbol{\chi}_j(t) \quad (6.31)$$

for higher-order Rouse modes $\boldsymbol{\chi}_j$ with $j > 0$. Equations (6.30) and (6.31) suggest that the long-time relaxation of all Rouse modes will be affected by how fast $\Gamma(t)$ decays to zero upon increasing the time t. The behavior of $\Gamma(t)$ at long times turns out to be

$$\Gamma(t) \sim \begin{cases} t^{-d/2-1} e^{-Drt} & \text{if } r > 0 \ , \\ t^{-d/2} & \text{if } r = 0 \ , \end{cases} \tag{6.32}$$

in the case of model A and

$$\Gamma(t) \sim \begin{cases} t^{-d/2-1} & \text{if } r > 0 \ , \\ t^{-d/4} & \text{if } r = 0 \ , \end{cases} \tag{6.33}$$

in the case of model B, as detailed in Appendix D.1 by inspecting the analytic structure of its Laplace transform (in particular, without assuming any specific form of the interaction potential $V_{\boldsymbol{q}}$). The algebraic decay of these kernels appears as a manifestation of the slow modes that characterize the medium in model A at criticality ($r = 0$), due to the phenomenon of critical slowing down [54, 86], and in model B even off criticality, due to the underlying local conservation of the order parameter ϕ [66].

Next, we consider a suitable linearization for the noise term $\Xi_j(t)$. Keeping only the lowest-order contribution in the Rouse modes in Eq. (6.24) leads to the linearized noise $\boldsymbol{\Lambda}_j(t)$ defined as:

$$\boldsymbol{\Lambda}_j(t) = \boldsymbol{\xi}_j(t) + \delta_{j0}\sqrt{N}\lambda\sigma\nu \int \frac{\mathrm{d}^d q}{(2\pi)^d} i\boldsymbol{q} V_{-\boldsymbol{q}} \int_{t_0}^{t} \mathrm{d}s \, G_{\boldsymbol{q}}(t-s)\zeta_{\boldsymbol{q}}(s) \, . \tag{6.34}$$

The statistics of the linearized noise $\boldsymbol{\Lambda}_j$ is substantially different for the center of mass ($j = 0$) and for the higher-order Rouse modes ($j > 0$). More precisely, for the former, the memory effects persist at the level of the linearized dynamics as prescribed by the last term of Eq. (6.34), whereas for the latter they vanish and $\boldsymbol{\Lambda}_j$ actually reduces to the white noise $\boldsymbol{\xi}_j$. Importantly, it is easy to verify that the stationary time-correlations of $\boldsymbol{\Lambda}_0(t)$, which we denote by $C_\Lambda^{\alpha\beta}(t-s)$, are related to the linear memory kernel $\Gamma(t-s)$ by the fluctuation-dissipation theorem:

$$C_\Lambda^{\alpha\beta}(t-s) \equiv \langle \Lambda_0^\alpha(t)\Lambda_0^\beta(s)\rangle = \nu T \delta_{\alpha\beta}[2\delta(t-s) + \Gamma(t-s)] \, , \tag{6.35}$$

with $t > s$. This is expected, as the system evolves according to an equilibrium dynamics.

Finally, one can linearize the contribution $\boldsymbol{v}_0^{\mathrm{ic}}$ around $\{\boldsymbol{\chi}_j(t) = 0\}$, which gives, for a generic initial configuration $\phi_{\boldsymbol{q}}(t_0)$ of the field,

$$\bar{\boldsymbol{v}}_j^{\mathrm{ic}}(t) = \lambda\sigma\nu \int \frac{\mathrm{d}^d q}{(2\pi)^d} i\boldsymbol{q} V_{-\boldsymbol{q}} G_{\boldsymbol{q}}(t-t_0)\phi_{\boldsymbol{q}}(t_0) \left[\sqrt{N}\delta_{j0} + i\boldsymbol{q}\cdot\boldsymbol{\chi}_j(t)\right] \, . \tag{6.36}$$

Combining together Eqs. (6.30), (6.34) and (6.36), the effective linearized dynamics of the center of mass takes the form of a generalized Langevin equation (GLE), given by:

$$\begin{aligned}\dot{\boldsymbol{\chi}}_0(t) = &-\int_{t_0}^{t} ds\,\Gamma(t-s)\dot{\boldsymbol{\chi}}_0(s) - [\tilde{\gamma}_0 - \Gamma(t-t_0)]\boldsymbol{\chi}_0(t) \\ &- \Gamma(t-t_0)\boldsymbol{\chi}_0(t_0) + \boldsymbol{\Lambda}_0(t) + \bar{\boldsymbol{v}}_0^{\mathrm{ic}}(t)\,. \end{aligned} \tag{6.37}$$

In addition to the non-Markovian nature of the above dynamics, we can immediately see that marginalizing the field introduces a correction to the typical relaxation time $\tilde{\gamma}_0$ associated to the harmonic confining potential, as well as a further time-dependent force proportional to the initial position of the center of mass $\boldsymbol{\chi}_0(t_0)$, and decaying with increasing time in the same way as the linear memory kernel $\Gamma(t-t_0)$. For the case of the higher-order Rouse modes $\boldsymbol{\chi}_j$ with $j > 0$, the effective linearized dynamics reads, instead,

$$\dot{\boldsymbol{\chi}}_j(t) = -\,[\tilde{\gamma}_j + \Gamma(0) - \Gamma(t-t_0)]\boldsymbol{\chi}_j(t) + \boldsymbol{\xi}_j(t) + \bar{\boldsymbol{v}}_j^{\mathrm{ic}}(t)\,. \tag{6.38}$$

As anticipated, this dynamics is Markovian, as the memory effects introduced by the coarse graining of the fluctuating order parameter ϕ did not survive the linearization procedure. Also in this case, integrating out the field from the dynamics, introduces a time-dependent correction to the relaxation rate $\tilde{\gamma}_j$. However, in this case such correction will persists also at long times, asymptotically reaching the value of $\Gamma(0)$. Interestingly, all Rouse modes are affected by the same correction.

6.3.3 Long-time relaxation of the center of mass

We first analyze the non-equilibrium relaxation of the center of mass towards the bottom of the confining potential, after an initial displacement $\boldsymbol{\chi}_0(t_0)$. An analogous problem has been already investigated in Ref. [66] for a single particle coupled to a fluctuating Gaussian field. In this case, after an initial rearrangement around the neighborhood of the particle, the field lags behind it and produces a slowing down of the relaxation process.

Without loss of generality, let us assume that $t_0 = 0$ and that the center of mass is initially displaced from the rest position of the trap by an amount $\bar{\chi}_0$ along the α-direction, i.e., $\chi_0^\beta(t_0) = \bar{\chi}_0\delta_{\alpha\beta}$. The problem can be conveniently analyzed in the Laplace domain [276] by first solving for $\hat{\chi}_0^\alpha(z) = \int_0^\infty dt\ \langle\chi_0^\alpha(t)\rangle\, e^{-zt}$, i.e., the Laplace transform of the average position of the center of mass along the α-direction, and then by studying its analytic structure in the complex z plane [68, 277]. Unfortunately, Eq. (6.37) cannot be immediately diagonalized by taking its Laplace transform because of the presence of the terms $\Gamma(t-t_0)\boldsymbol{\chi}_0(t)$ and $\bar{\boldsymbol{v}}_0^{\mathrm{ic}}(t)$, which involve products of t-dependent

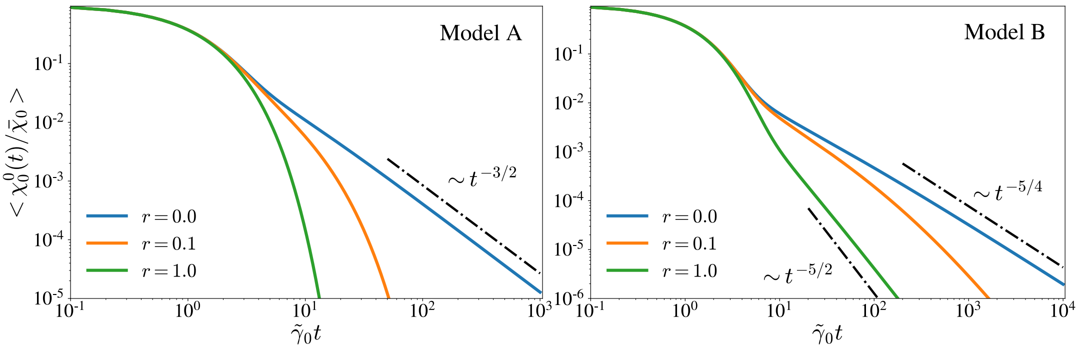

Figure 6.3: Nonequilibrium relaxation of the position $\chi_0^0(t)$ of the center-of-mass of a dimer initially displaced from the rest position of the trap by an amount $\bar{\chi}_0$ in $d = 1$ spatial dimensions, as a function of time t measured in units of the relaxation time $1/\tilde{\gamma}_0$. The two monomers are characterized by the same coupling with the field. The solid lines represent the result of molecular dynamics simulations (see Appendix D.4 for details) with the field initialized in the spatially homogeneous configuration $\phi_{\boldsymbol{q}} = 0$ for all momenta $\boldsymbol{q}$. As specified in the legend, different colors pertains to different correlation lengths $\xi_\phi = r^{-1/2}$ of the field. Left and right panels report the relaxation curves obtained with the field evolving according to model A and model B dynamics, respectively. Moreover, the theoretically predicted algebraic behavior at long times, given in Eqs. (6.42) and (6.43), is shown by black dashed-dotted lines. The plot shows how the relaxation of the center of mass of the dimer toward the bottom of the confining harmonic potential is slowed down by the field order parameter, especially when the latter is critical. The asymptotic behaviors obtained with numerical simulations are in very good agreement with the analytical predictions. The values of the various parameters used in the simulations are: $\kappa = 1$, $\nu = 1$, $T = 0$, $D = 1$, $R = 1$, $\lambda = 1$, $\sigma_1 = \sigma_2 = 1$.

functions. However, in the following we consider the case where the field is initialized in the configuration it would assume if the whole system were in its minimum energy configuration. In Fourier space, this is given by:

$$\phi_{\boldsymbol{q}}(t_0) = \frac{ND\lambda\sigma V_{\boldsymbol{q}} q^a}{\alpha_{\boldsymbol{q}}} \,. \tag{6.39}$$

With this initial condition, the linearization of Eq. (6.25) can be shown to give $\boldsymbol{v}_0^{\mathrm{ic}}(t) = -\Gamma(t - t_0)\boldsymbol{\chi}_0(t)$, which simplifies the GLE in Eq. (6.37) as

$$\dot{\boldsymbol{\chi}}_0(t) = -\int_{t_0}^{t} ds\, \Gamma(t-s)\dot{\boldsymbol{\chi}}_0(s) - \tilde{\gamma}_0 \boldsymbol{\chi}_0(t) - \Gamma(t-t_0)\boldsymbol{\chi}_0(t_0) + \boldsymbol{\Lambda}_0(t) \,. \tag{6.40}$$

The potential impact of this seemingly arbitrary choice of initial condition in Eq. (6.39) will be tested a posteriori using numerical simulations. The average solution $\langle \boldsymbol{\chi}_0(t) \rangle$ of Eq. (6.40) can now be expressed in Laplace domain as

$$\hat{\chi}_0^\alpha(z) = \frac{\bar{\chi}_0}{\tilde{\gamma}_0 + z + z\hat{\Gamma}(z)}, \tag{6.41}$$

where $\hat{\Gamma}(z)$ is the Laplace transform of $\Gamma(t)$ in Eq. (6.29). This shows (as expected) that the asymptotic behavior of the average position of the center of mass is strictly related to that of the linear memory kernel $\Gamma(t)$, which we studied above in Eqs. (6.32) and (6.33). In particular, in Appendix D.2 we derive the following asymptotic behaviors:

$$\langle \chi_0^\alpha(t) \rangle \sim \begin{cases} t^{-(2+d/2)} & \text{for} \quad r > 0, \\ t^{-(1+d/4)} & \text{for} \quad r = 0, \end{cases} \tag{6.42}$$

for model B, while

$$\langle \chi_0^\alpha(t) \rangle \sim t^{-(1+d/2)} e^{-Drt} \tag{6.43}$$

for model A with $r \ll \tilde{\gamma}_0/D$, whereas the decay becomes purely exponential for $r \gg \tilde{\gamma}_0/D$ (see Appendix D.2 for details). The results presented above are shown in Fig. 6.3, where the non-equilibrium relaxation of the position of the center of mass $\boldsymbol{\chi}_0(t)$ as a function of time is plotted for the simple case of a dimer in $d = 1$ spatial dimensions. The solid lines in Fig. 6.3 denote the results of numerical simulations, whereas the black dashed-dotted lines are the theoretical predictions of the asymptotic behaviors reported in Eqs. (6.42) and (6.43). The position of the center of mass exhibits an algebraic decay for model B (right panel), with an exponent that depends on whether the medium is critical ($r = 0$) or not ($r > 0$). As mentioned above, this originates from the conservation law that underlies the medium in model B dynamics, thus producing slow modes $\boldsymbol{q} \sim 0$ [54, 86]. By contrast, for model A (left panel), an algebraic decay is only found when $r = 0$, since in this case the relevant mechanism is the critical slowing down that affects the medium when $r = 0$ [54, 66, 86].

6.4 Typical polymer size

In this Section we study the average squared gyration radius $\langle R_g^2 \rangle$ and the average end-to-end distance $\langle \boldsymbol{R}_{\text{ee}} \rangle$ of the polymer in the steady state, when its internal structure has already relaxed to an equilibrium configuration. Both quantities are a measure of the typical polymer size, and are defined as

$$R_g^2 = \frac{1}{N} \sum_{n=0}^{N-1} (\boldsymbol{X}_n - \boldsymbol{X}_{\text{com}})^2 = \frac{1}{N} \sum_{n \neq 0} \boldsymbol{\chi}_n^2 \,, \tag{6.44}$$

$$\boldsymbol{R}_{\text{ee}} = \boldsymbol{X}_{N-1} - \boldsymbol{X}_0 = \sum_{n \neq 0} (\varphi_{n,N-1} - \varphi_{n,0}) \boldsymbol{\chi}_n \,. \tag{6.45}$$

However, while the first one is appropriate for any topology of the chain, i.e., for any connectivity matrix $\boldsymbol{M}$, the second one is only informative for a linear chain, where the two ends are defined. Although the derivation of $\langle R_g^2 \rangle$ would be analogous for a generic topology of the polymer, in the following we focus on a linear chain with extreme monomers given by $\boldsymbol{X}_0$ and $\boldsymbol{X}_{N-1}$.

To make the derivation more general, we consider the potential presence of a stretching force $\boldsymbol{f}_s$ that acts on the end-to-end distance $\boldsymbol{R}_{\text{ee}}$. In particular, we add the following stretching potential

$$\mathcal{U}_s = -\boldsymbol{f}_s \cdot \boldsymbol{R}_{\text{ee}} = -\boldsymbol{f}_s \cdot \sum_i (\varphi_{i,N-1} - \varphi_{i,0}) \boldsymbol{\chi}_i \tag{6.46}$$

to the total Hamiltonian $\mathcal{H}_0 + \mathcal{H}_{\text{eff}}$ reported in Eq. (6.16). The response of the polymer to such a stretching force, described by the so-called force-extension curve, is analyzed in the dedicated Sec. 6.4.3. In general, both $\langle R_g^2 \rangle$ and $\langle \boldsymbol{R}_{\text{ee}} \rangle$ are affected by the fluctuating order parameter ϕ of the medium. The effect of the field-mediated forces on the typical size of the polymer is studied in the following Section with the help of a perturbative expansion in the interaction coupling λ. Whenever this is possible, we compare the results of this weak-coupling approximation with the theoretical predictions coming from the linearized theory derived in Sec. 6.3.2.

6.4.1 Weak-coupling approximation

As in Sec. 6.3, we consider the case in which all monomers have the same coupling with the field, i.e., $\sigma_i = \sigma$ for all i, and thus they experience an effective attraction. In the framework of the weak-coupling approach, we find convenient to define the average $\langle \cdots \rangle_{f,\lambda}$, where the modulus f of the stretching force and the magnitude λ of the interaction coupling with the field are explicitly indicated as subscripts. In particular, we want to obtain the first non-trivial correction to $\langle R_g^2 \rangle_{f,0}$ and $\langle \boldsymbol{R}_{\text{ee}} \rangle_{f,0}$, which is induced by the coupling of the polymer with the field. Using a standard perturbative expansion in λ, we get:

$$\langle O \rangle_{f,\lambda} - \langle O \rangle_{f,0} = -\,\beta\,[\langle O \mathcal{H}_{\text{eff}} \rangle_{f,0} - \langle O \rangle_{f,0} \langle \mathcal{H}_{\text{eff}} \rangle_{f,0}] + \mathcal{O}(\lambda^4)\,, \tag{6.47}$$

where the observable O can be replaced by either R_g^2 or $\boldsymbol{R}_{\text{ee}}$. Note that the correction on the r.h.s of this equation only depends on averages calculated when the polymer is decoupled from the field (i.e., $\lambda = 0$), and it is of order λ^2. In fact, all corrections proportional to odd powers of λ vanish because the original equations of motion in Eqs. (6.10) and (6.12) are invariant under the transformation $(\lambda, \phi) \leftrightarrow (-\lambda, -\phi)$.

All the averages needed to evaluate the r.h.s. of Eq. (6.47) can be computed with the help of the generating functional $\mathcal{Z}[\{\mathbf{j}_i\}]$ of the free Rouse chain, which is defined as:

$$
\begin{aligned}
\mathcal{Z}[\{\mathbf{j}_i\}] &= \Big\langle \exp\Big(\sum_{i=0}^{N-1} \mathbf{j}_i \cdot \boldsymbol{\chi}_i\Big)\Big\rangle_{f,0} \qquad (6.48)\\
&= \exp\left[\frac{1}{2\beta}\sum_{i=0}^{N-1}\frac{1}{\mathcal{M}_i}[\mathbf{j}_i^2 + 2\beta(\varphi_{i,N-1}-\varphi_{i,0})\boldsymbol{f}_s\cdot\mathbf{j}_i]\right],
\end{aligned}
$$

where we introduced the quantity $\mathcal{M}_i = \kappa m_i + \kappa_c$, with m_i the eigenvalues of the connectivity matrix, as discussed in Sec. 6.1. The expression of $\mathcal{Z}[\{\mathbf{j}_i\}]$ given in Eq. (6.48) can be obtained by standard methods as outlined in Appendix D.3. In particular, the generating functional can be readily used to derive the expressions of the unperturbed $\langle R_g^2\rangle_{f,0}$ and $\langle \boldsymbol{R}_{\text{ee}}\rangle_{f,0}$. These are given by

$$
\begin{aligned}
\langle R_g^2\rangle_{f,0} &= \frac{1}{N}\sum_{n=1}^{N-1}\langle\boldsymbol{\chi}_n^2\rangle_{f,0} = \frac{1}{N}\sum_{n=1}^{N-1}\sum_{\alpha=0}^{d-1}\left.\frac{\partial^2\mathcal{Z}[\{\mathbf{j}_i\}]}{\partial j_n^\alpha\partial j_n^\alpha}\right|_{\mathbf{j}_i=\mathbf{0}}\\
&= \frac{1}{N}\sum_{n=1}^{N-1}\left[\frac{d}{\beta\mathcal{M}_n}+\left(\frac{(\varphi_{n,N-1}-\varphi_{n,0})\boldsymbol{f}_s}{\mathcal{M}_n}\right)^2\right], \qquad (6.49)
\end{aligned}
$$

and

$$
\langle R_{\text{ee}}^\alpha\rangle_{f,0} = \sum_{n=0}^{N-1}(\varphi_{n,N-1}-\varphi_{n,0})\left.\frac{\partial\mathcal{Z}[\{\mathbf{j}_i\}]}{\partial j_n^\alpha}\right|_{\mathbf{j}_i=\mathbf{0}} = \sum_{n=0}^{N-1}\frac{(\varphi_{n,N-1}-\varphi_{n,0})^2}{\mathcal{M}_n}f\delta_{\alpha 0}\,, \qquad (6.50)
$$

where we assumed, without loss of generality, that the stretching force is directed along the x-axis (with unit vector $\boldsymbol{e}_1$), so that $\boldsymbol{f}_s = f\boldsymbol{e}_1$. The correction of order λ^2 to the unperturbed values in Eqs. (6.49) and (6.50) induced by the coupling of the polymer with the field depends on averages of the type $\langle\boldsymbol{\chi}_j^p\exp(i\boldsymbol{q}\cdot(\boldsymbol{X}_k-\boldsymbol{X}_n))\rangle$, with j,k,n generic indices in the set $\{0,1,...,N-1\}$, and the power $p\in\{0,1,2\}$. These averages can be computed again with the help of the generating functional $\mathcal{Z}[\{\mathbf{j}_i\}]$ as detailed in Appendix D.3. In this way we get:

$$
\begin{aligned}
&\big\langle R_g^2\big\rangle_{f,\lambda} - \big\langle R_g^2\big\rangle_{f,0} = \frac{\lambda^2\beta}{2N}\sum_{n=1}^{N-1}\sum_{i,j=0}^{N-1}\int\frac{\mathrm{d}^d q}{(2\pi)^d}|V_q|^2 G_{\boldsymbol{q}} \qquad (6.51)\\
&\times\left[\frac{2i\beta^{-1}\boldsymbol{f}_s\cdot\boldsymbol{q}\,(\varphi_{n,N-1}-\varphi_{n,0})\,(\varphi_{ni}-\varphi_{nj}) - q^2\beta^{-2}\,(\varphi_{ni}-\varphi_{nj})^2}{\mathcal{M}_n^2}\right]\\
&\times\exp\left\{-\frac{q^2}{2\beta}\sum_{l=0}^{N-1}\frac{(\varphi_{li}-\varphi_{lj})^2}{\mathcal{M}_l} + i\boldsymbol{f}_s\cdot\mathbf{q}\sum_{l=0}^{N-1}\frac{(\varphi_{li}-\varphi_{lj})\,(\varphi_{l,N-1}-\varphi_{l,0})}{\mathcal{M}_l}\right\} + \mathcal{O}(\lambda^4),
\end{aligned}
$$

and

$$\langle R^{\alpha}_{ee}\rangle_{f,\lambda} - \langle R^{\alpha}_{ee}\rangle_{f,0} = \tag{6.52}$$

$$\frac{\lambda^2\beta}{2}\sum_{n=1}^{N-1}\sum_{i,j=0}^{N-1}\int\frac{\mathrm{d}^d q}{(2\pi)^d}\frac{|V_q|^2 G_{\boldsymbol{q}}}{\mathcal{M}_n}\left[iq^{\alpha}\beta^{-1}(\varphi_{ni}-\varphi_{nj})(\varphi_{n,N-1}-\varphi_{n,0})\right]$$

$$\times\exp\left\{-\frac{q^2}{2\beta}\sum_{l=0}^{N-1}\frac{(\varphi_{li}-\varphi_{lj})^2}{\mathcal{M}_l}+i\boldsymbol{f}_s\cdot\mathbf{q}\sum_{l=0}^{N-1}\frac{(\varphi_{li}-\varphi_{lj})\,(\varphi_{l,N-1}-\varphi_{l,0})}{\mathcal{M}_l}\right\}+\mathcal{O}(\lambda^4).$$

The correction to the typical polymer size induced by the fluctuating order parameter ϕ, as described by Eqs. (6.51) and (6.52), is discussed in more details in the coming Sections. Specifically, in Sec. 6.4.2 we analyze the magnitude of such correction as a function of the correlation length of the field and of the polymerization degree N. In Sec. 6.4.3, instead, we study the dependence of Eqs. (6.51) and (6.52) on the stretching force $\boldsymbol{f}_s$.

6.4.2 Typical size in the absence of external forces

In the absence of external forces, i.e., for $\boldsymbol{f}_s = \mathbf{0}$, it is straightforward to verify that the correction to the average end-to-end distance $\langle \boldsymbol{R}_{\mathrm{ee}}\rangle$ due to the coupling with the field actually vanishes, as expected from simple symmetry arguments. In particular, for any given polymer configuration $\{\boldsymbol{X}_i\}$, the one obtained by the transformation $\{\boldsymbol{X}_i\} \to \{-\boldsymbol{X}_i\}$ has the same statistical weight but opposite end-to-end distance. In this case, when no stretching force is applied to the polymer, we focus on Eq. (6.51) for the gyration radius to study how the polymer size is affected by the underlying correlated medium.

The analytical result in Eq. (6.51) is shown in Fig. 6.4. In particular, we plot $\langle R_g^2\rangle_{0,\lambda}$ as a function of r (left panel) and of N (right panel). In the first case, we observe that the gyration radius of the polymer decreases when the medium develops long-range spatial correlations, i.e., for $r \to 0$. This has to do with the fact that the forces induced by a near-critical field are significant over a larger length scale. Importantly, as opposed to previous studies about polymeric macromolecules dispersed in a near-critical binary liquid mixtures [254, 255, 262], our theoretical model does not predict a re-expansion of the polymer when the field reaches the critical point. As pointed out in Ref. [262], the absence of this effect has to do with the field ϕ being described by a Gaussian theory. In the right panel of Fig. 6.4, instead, we show how the typical size of the polymer scales with the polymerization degree N, for a fixed value of the correlation length ξ_ϕ of the field. The value of the gyration radius is measured in units of the typical bond length l_0 in the uncoupled case, which can be obtained by specializing Eq. (6.49) to $N = 2$ and $\boldsymbol{f}_s = \mathbf{0}$, leading to

$$l_0^2 = dT/(2\tilde{\gamma}_1)\,. \tag{6.53}$$

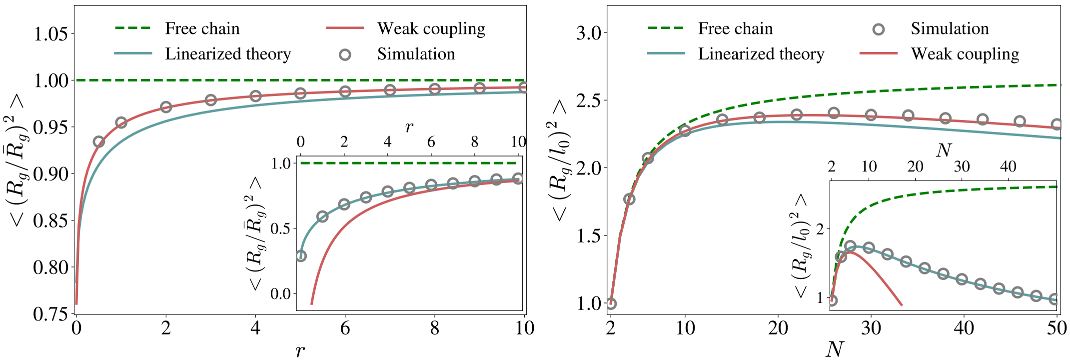

Figure 6.4: Typical size of the polymer at equilibrium, described by the mean-squared gyration radius $\langle R_g^2 \rangle$ in the absence of a stretching force. The results of numerical simulations in $d = 1$ (symbols) are compared with the theoretical predictions obtained with both the weak-coupling approximation (red lines, see Eq. (6.51)) and the linearized theory (light blue lines, see Eq. (6.54)). Left panel: $\langle R_g^2 \rangle$ of a linear chain with polymerization degree $N = 20$ as a function of $r = 1/\xi_\phi^2$. The value of $\langle R_g^2 \rangle$ is measured in units of $\bar{R}_g^2$, i.e. the gyration radius of a free chain with the same parameters (green dashed line). The figure shows that when the field approaches the critical point $r = 0$, the typical polymer size is reduced as a consequence of the larger field-mediated forces. The parameters used in the numerical simulations to obtain the data in the main plot are: $\kappa = 1$, $\nu = 1$, $T = 1$, $D = 1$, $R = 1$, $\lambda = 0.3$. In the inset: $\lambda = 1$ and $T = 0.1$. Right panel: $\langle R_g^2 \rangle$ of a linear chain as a function of N, measured in units of the typical bond length l_0 defined in Eq. (6.53). For a sufficiently large N, the attractive field-mediated forces induce a collapse of the chain, as shown by the non-monotonic behavior of the curves. The simulation parameters are the same as in the left panel, with $r = 1$. The choice of parameters in the main plots is such that the weak-coupling approximation produces better results than the linearized theory. Viceversa, the two insets show that upon increasing the coupling λ and decreasing the temperature T, the linearized theory is more accurate.

In particular, in the main plot of Fig. 6.4 (right panel), we have $\xi_\phi/l_0 \approx 2.5$, i.e., the field correlations live on a larger length scale than the typical bond length. For correlations lengths $\xi_\phi < l_0$, the effect of the field mediated forces would be less strong and the theoretical predictions would be closer to the free case. For sufficiently short chains, we observe that adding a monomer increases $\langle R_g^2\rangle_{0,\lambda}$. This expected behavior has an entropic origin and it is quantitatively similar to the one observed for a free chain decoupled from the field (dashed green line). However, beyond some threshold value for N, the pairwise-additive field-mediated forces dominate over the entropic effect, producing a decrease of $\langle R_g^2\rangle_{0,\lambda}$ as the number of monomers is increased. In the case of the ideal chain considered here, namely in the absence of excluded volume interactions and steric hindrance effects, the size of the polymer can actually become arbitrarily small as N increases. In a more realistic model, instead, the polymer would first collapse into a dense compact globule, and then its size would increase as $\sim N^{1/3}$ — as in the case of a polymer chain in a poor solvent, where the contacts with the solvent molecules are minimized [278, 279].

In both panels of Fig. 6.4, the theoretical predictions obtained with the weak-coupling approximation (solid red lines) are compared to those coming from the linearized theory (solid light blue lines). The latter can be readily obtained by analogy with Eq. (6.49) and considering that the main long-time effect of the field on the linearized dynamics of the higher order modes in Eq. (6.38) is the correction $\Gamma(0)$ to their relaxation rates $\tilde{\gamma}_j$. This implies that

$$\langle R_g^2\rangle_{0,\lambda}^L = \frac{1}{N}\sum_{n\neq 0}\langle \boldsymbol{\chi}_n^2\rangle_{0,\lambda}^L = \frac{1}{N}\sum_{n\neq 0}\frac{d\nu T}{\tilde{\gamma}_n + \Gamma(0)}\,, \tag{6.54}$$

where we introduced the symbol $\langle\cdots\rangle_{0,\lambda}^L$ to denote the average within the linear response theory in the absence of any stretching force. We recall here that the linearized theory is only based on the assumption that the Rouse modes are small, and thus it is in principle valid to any order in the interaction coupling λ. For this reason, it is more accurate than the weak-coupling theory upon increasing λ, as shown in the two insets of Fig. 6.4.

6.4.3 Force-extension curve

In this Section we analyze the response of the polymer to the stretching force $\boldsymbol{f}_s$, and show how the force-extension curve is modified by the coupling of the polymer with the correlated medium. The theoretical predictions for $\boldsymbol{R}_{\text{ee}}$ and R_g^2 reported in Eqs. (6.52) and (6.51) obtained within the weak-coupling approximation are plotted as a function of the stretching force f in Fig. 6.5. In particular, we observe that the correlations of the medium effectively increase the stiffness of the polymer, therefore introducing an additional resistance to the stretching. Indeed, for all values of f, the light blue lines corresponding

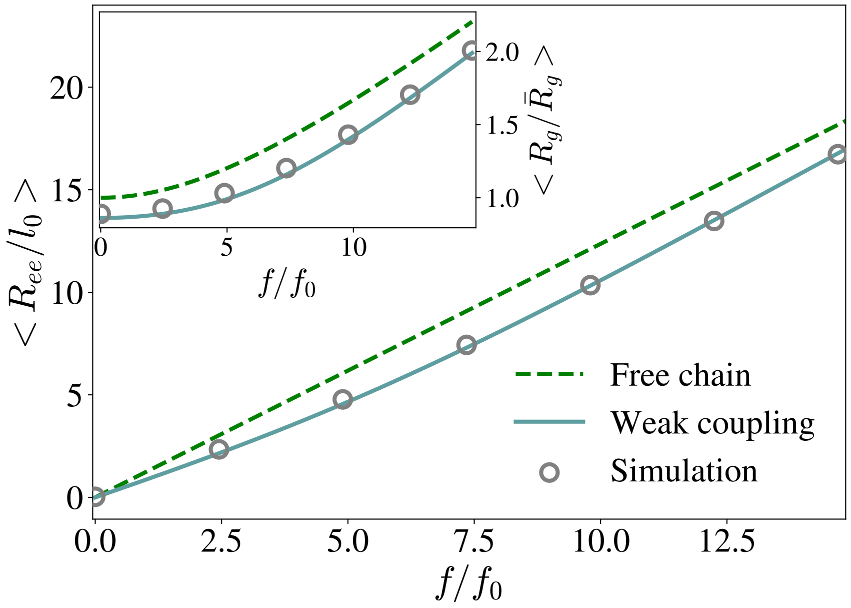

Figure 6.5: Force-extension curve of a linear polymer with $N = 20$ monomers coupled to a fluctuating field ϕ with correlation length $\xi_\phi = 1$, in $d = 1$ spatial dimensions. The main figure shows the response of the end-to-end distance R_{ee} to a stretching force f, measured in units of $f_0 = \kappa l_0$, with l_0 the typical bond length defined in Eq. (6.53). The results of numerical simulations (grey symbols) are compared to the theoretical predictions of Eq. (6.52) (light blue solid lines). Compared to the free case (dashed green line) described by Eq. (6.50), the coupling with the correlated medium introduces an additional resistance to the stretching force due to the attractive field-mediated forces. The R_{ee} is measured in units of l_0. In the inset we show the behavior of the gyration radius R_g as a function of the stretching force. Here, R_g is measured in units of $\bar{R}_g$, i.e., the value it assumes in the free and unstretched case. The parameters used in the numerical simulations are: $\kappa = 1$, $\nu = 1$, $T = 1$, $D = 1$, $R = 1$, $\lambda = 0.7$.

to the theoretical predictions in Eqs. (6.52) and (6.51) and the data obtained with numerical simulations (grey symbols), which are in very good agreement with each other, always lie below the dashed green lines, which refer to the free case. This actually happens because all monomers interact with the field with the same coupling sign $\sigma_i = \sigma$, and thus all field-mediated forces are attractive.

The correction introduced by the coupling to the field vanishes for large stretching forces f — compare with Eq. (6.52), where the integrand function becomes rapidly oscillating for large f, so that the integral vanishes. This can be physically rationalized by noting that, under an externally-imposed stretching, the typical monomer distance eventually exceeds the range of the field-mediated forces, which thus play a minor role. Note that in Fig. 6.5, differently from Fig. 6.4, we do not report the predictions of the linearized theory, because it relies on the assumption that the higher-order Rouse modes are sufficiently small, which is certainly not the case when a stretching force is applied.

Although the typical size of a polymer in a correlated medium has already been analyzed from a static point of view using more sophisticated models (see, e.g., Ref. [262]), our minimal model allows for an easier extension of the analysis to the dynamical properties, such as the relaxation of the internal structure of the polymer in response to a quenched stretching force. This analysis in not present in this Chapter and it will be done in the future.

6.5 Conclusions

In this Chapter we analyzed the behavior of a polymer molecule linearly coupled to a correlated medium described by a fluctuating scalar Gaussian field $\phi(\boldsymbol{x}, t)$. The reciprocal interaction between the polymer and the field is taken into account in their joint stochastic dynamics, which is chosen to satisfy detailed balance.

Working within the linear-response regime, we first studied the relaxation of the center of mass of the polymer toward its rest position in a confining potential. This relaxation turns out to be algebraic at long times, if the fluctuating order parameter $\phi(\boldsymbol{x}, t)$ supports slow relaxational modes, due either to criticality or to the presence of an underlying conservation law — see Sec. 6.3 and Fig. 6.3. Conversely, the internal structure of the chain described by higher order Rouse modes always displays an exponential relaxation, with a typical time scale that is shorter compared to the free case (in the case of attractive field-induced interactions), due to the effective attraction induced by the medium. Note that in the case where the monomers are characterized by interaction couplings $\lambda\sigma_i$ with different signs, the repulsive field-mediated forces can slow down the relaxation of the internal structure of the polymer. This aspect, however, is not analyzed in this Chapter.

The spatial range of these field-induced interactions depends on the correlation length of the field. Using a weak-coupling approximation, we then showed analytically that the gyration radius of the chain collapses as the field approaches the critical point, where such correlation length diverges. The theoretical predictions are in very good agreement with the numerical simulations. In addition, we studied how the typical polymer size depends on the polymerization degree N, showing that after an initial increase for small N due to entropic reasons, the dominant effect of the pairwise-additive field-induced interactions drives the polymer into a compact globule-like state. Within the weak-coupling approximation, in Sec.6.4.3 we analyzed the response of the polymer to a tensile force, observing an enhanced resistance of the polymer against the external stretching, whose origin is again to be attributed to the effective attractions between the monomers induced by the medium. Also in this case, this is due to the fact that all monomers interact with the field with the same coupling.

Further extensions of the model presented in this Chapter may address the steady state of the system in the presence of spatial confinement, where boundary conditions are imposed on the fluctuations of the correlated medium [69, 280], which is the typical setting in experimental realizations. Even more importantly, the model presented here opens the possibility of studying more complex dynamical settings where the field-induced forces may play a role in determining the nonequilibrium dynamics of the polymer. For instance, it would be interesting to characterize the dynamical response of the chain to a quenched stretching force, i.e., a force that is suddenly switched on (or off) at time $t = 0$. We expect that slow algebraic relaxations might emerge in the cases where the underlying medium is critical or conserved, and the external force produces an average displacement of the center of mass. What shown in Sec. 6.4 is the preliminary result of a study which will include the analysis of the aforementioned dynamical response. In addition, within the formulation of the model we adopted here, the joint stochastic dynamics of the polymer and the field was chosen so as to satisfy the detailed balance condition, so that the system is accordingly characterized by an equilibrium dynamics. An interesting extension to this aspect would thus be to consider a polymer chain in an active fluctuating correlated medium, whose fluctuations break detailed balance [230], and characterizing its behavior under non-equilibrium conditions.

Chapter 7

Odd tracer dynamics in soft-core media

7.1 Introduction

The transport of tracer particles in highly crowded environments is of fundamental interest in biological applications, such as in the crowded cytoplasm [281] or in the plasma membrane of cells [282]. Although at short distances molecular interactions always manifest strong diverging repulsion due to steric hindrance effects, *effective* soft interactions are known to emerge in numerous biophysical and soft matter systems [283, 284]. Some examples include polymer assemblies of various connectivity as star polymers [285], block-copolymer micelles [286] and microgels [287, 288]. A prototypical soft-interaction model is the *Gaussian-core model* (GCM), as pioneered by Stillinger and Weber [289–291] from 1976 onwards. This model found a widespread application when it was realized that it accurately describes the effective interaction between polymer coils [292–296] over a wide range of densities [297], and flexible dendrimers [298].

The GCM displays some interesting and seemingly counter-intuitive features that are sometimes referred to as static and dynamic anomalies [299–303]. For example, it has been shown that the single particle diffusivity can increase and the viscosity can decrease upon isothermal compression. The unexpected transport properties have been proved to be strongly correlated to an anomalous behavior of the short-range translational structural order [302]. The phase behavior of the GCM in the density-temperature space has been exhaustively investigated in the last few decades [294, 304, 305]. Specifically, it has been shown that there exist an upper freezing temperature above which the system is always fluid. Below this temperature, upon increasing the density, the system first freezes into a crystal structure and then exhibits a re-entrant melting transition [294, 304].

In equilibrium systems such as purely repulsive hard spheres [306–308], Yukawa-like or Lennard-Jones-like interacting particles [309–313], but also in systems with soft-core interactions like the GCM [302, 314], inter-particle interactions are genuinely found to reduce the self-diffusion of tracer particles compared to the interaction-free case. This generic qualitative reduction can only be turned into an interaction-enhanced self-diffusion by considering non-equilibrium conditions, such as those occurring in the case of tracer diffusion in non-reciprocal mixtures [315] or multi-temperature environments [316]. Only recently, it has been found that even in equilibrium systems, the self-diffusion of a tagged tracer particle can be enhanced by purely repulsive interactions with the host particles in the medium [142]. These systems go under the name of *odd diffusive* [113, 142] and are characterised by a broken time-reversal or spatial-inversion (parity) symmetry [317]. Relevant systems include, for example, charged Brownian particles subject to Lorentz force [318] at equilibrium or active chiral particles [113]. For additional cases, see, e.g., Ref. [319] and references therein. The microscopic cause of the enhanced self-diffusion was attributed to a mutual rolling of particles induced by the odd diffusion instead of an ordinary reflection after the interaction [142, 319] and associated with the non-Hermitian dynamics of the system [320]. Interaction-enhancement was later found also in related non-reciprocal systems [315], systems with transverse forces [321, 322] and skyrmionic systems [323].

In this Chapter, we study the transport properties of an odd-diffusive tracer immersed in a GCM medium via analytical and simulation methods. In our analysis, the host particles in the medium do not exhibit any oddness effect. In order to model the interactions with the medium we employ the field-theoretic approach developed by Dean and Kawasaki (see Sec. 2.9 and Refs. [72, 73]), which allows us to make accurate analytical predictions even in highly dense systems. By comparing our results with Brownian dynamics simulations we find remarkable agreement for three distinct regimes; depending on the oddness parameter κ, the interactions can either reduce the self-diffusion, enhance it or render the host-medium invisible for the tracer. We recover the diffusivity anomaly for the GCM (non-monotonicity of the self-diffusion coefficient upon increasing density of the medium) and find that in an odd-diffusive system this can be inverted in the enhancement region.

The remainder of this Chapter is organized as follows: in Sec. 7.2 we set up the model and derive the governing time-evolution equations for the fluctuating density field and for the tracer. In Sec. 7.3 we employ a weak-coupling approximation (similar in spirit to that discussed in Chapter 6) and evaluate the self-diffusion, presenting the results of both analytical and numerical approaches. In Sec. 7.4 we draw our conclusions and give an extended outlook on further applications of the effect. This Chapter is supplemented by the Appendix E, where we present a detailed derivation of the analytical predictions

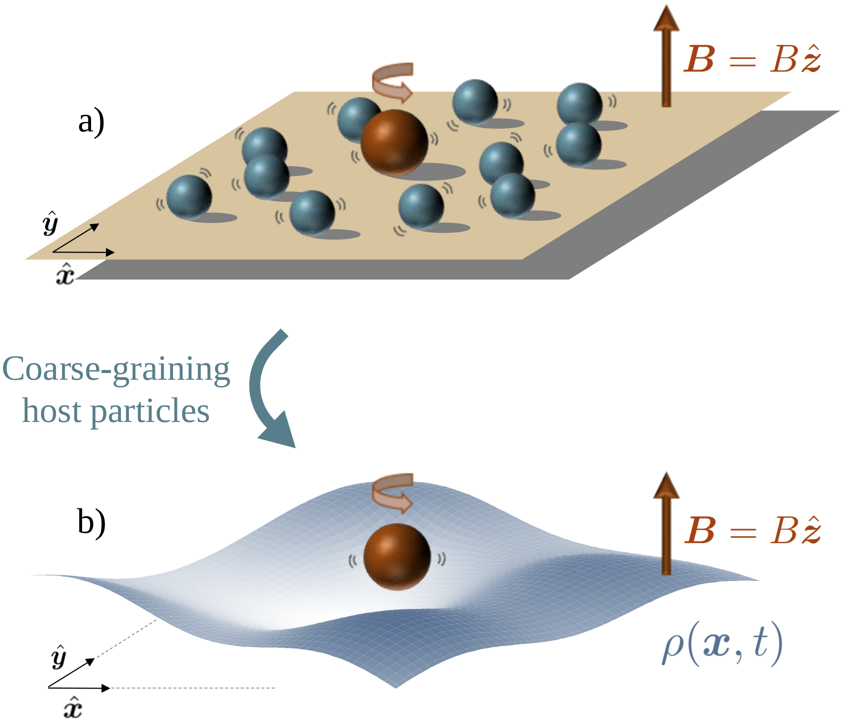

Figure 7.1: (a) Sketch of an odd tracer (brown particle) in $d = 2$ spatial dimensions under the effect of the Lorentz force generated by a magnetic field $\boldsymbol{B}$ oriented along the $\hat{\boldsymbol{z}}$ direction, coupled via soft-core interactions to a bath of (blue) host particles. Both the odd tracer and the host particles are subjected to thermal fluctuations. (b): Schematic of the mesoscopic description of the system. In this case, the host particles are effectively represented by the thermally fluctuating density field ρ.

reported here, as well as the details of the numerical simulations.

7.2 The model

We analyze the two−dimensional stochastic dynamics of an ensamble of $N + 1$ interacting particles whose position at time t is denoted by $\boldsymbol{X}_i(t) \in \mathbb{R}^2$, with $i \in \{0, \ldots, N\}$. The particle labeled by $\boldsymbol{X}_0$ is thought as electrically charged (see Sec. 2.10), and thus it experiences a Lorentz force generated by a magnetic field $\boldsymbol{B} = B\hat{\boldsymbol{z}}$ oriented along the z-axis, and it will be referred to as the *odd tracer* (see Fig. 7.1 for a sketch of the system). Indeed, as explained in Sec. 2.10, the effect of the magnetic field can be encoded in the friction tensor $\boldsymbol{\Gamma} = \gamma[\boldsymbol{1} - \kappa\boldsymbol{\varepsilon}]$ characterized by antisymmetric elements proportional to the dimensionless oddness parameter $\kappa = B/\gamma$, with γ the scalar friction coefficient and $\boldsymbol{\varepsilon}$ the Levi-Civita symbol in $d = 2$ dimensions. Although in the case presented here the oddness is due to the presence of a magnetic field, the derivation can be applied to more generic models characterized by a friction tensor Γ with anti-symmetric components. The stochastic dynamics of the odd tracer can be written as:

$$\begin{cases} \dot{\boldsymbol{X}}_0 &= \boldsymbol{V}_0, \\ m\dot{\boldsymbol{V}}_0 &= -\lambda_{\mathrm{t}} \sum_{j=1}^{N} \nabla\mathcal{U}(\boldsymbol{X}_0 - \boldsymbol{X}_j) - \boldsymbol{\Gamma}\boldsymbol{V}_0 + \sqrt{2T\gamma}\,\boldsymbol{\xi}_0, \end{cases} \tag{7.1}$$

where $\boldsymbol{V}_0(t)$ denotes the velocity of the odd tracer at time t, m its mass, λ_{t} is the coupling strength between the odd tracer and the remaining particles of the medium (host), and $\mathcal{U}$ is the inter-particle pair-wise potential. The stochastic term $\boldsymbol{\xi}_0$ belongs to a set of $N+1$ independent zero-mean Gaussian white noises $\{\boldsymbol{\xi}_i\}_{i=0}^{N}$ with unit variance. Note that we work in units such that the charge q of the odd particle and the Boltzmann constant k_{B} are set to 1. Moreover, we restrict our analysis to the case of bounded interaction potentials between the odd tracer and the host particles, characterized by $\nabla\mathcal{U}(\boldsymbol{0}) = 0$. The bounded potential $\mathcal{U}(\boldsymbol{x})$ will be generic throughout the derivation until otherwise specified. Although we are ultimately interested in investigating the self-diffusion of the odd tracer in the overdamped regime, where inertial effects can be neglected compared to viscous forces, we keep the time scale $\tau_\gamma = m/\gamma$ finite throughout the derivation, and take the limit $m \to 0$ at the end of the calculation. As shown in Appendix E.1 the dynamics for the velocity $\boldsymbol{V}_0$ in Eq. (7.1) can be formally solved and substituted in the equation for the position $\boldsymbol{X}_0$, leading to the following equation of motion for the position of the odd tracer

$$\begin{aligned} \dot{\boldsymbol{X}}_0 = &-\frac{\lambda_{\mathrm{t}}}{m}\int_{t_0}^{t} \mathrm{d}s\, \boldsymbol{G}(t-s) \sum_{j=1}^{N} \nabla\mathcal{U}(\boldsymbol{X}_0(s) - \boldsymbol{X}_j(s)) \\ &+ \boldsymbol{G}(t-t_0)\boldsymbol{V}_0(t_0) + \boldsymbol{\eta}(t) \end{aligned} \tag{7.2}$$

where the matrix $\boldsymbol{G}(u)$ is defined as:

$$\begin{aligned} \boldsymbol{G}(u) &= \mathrm{e}^{-|u|/\tau_\gamma}\boldsymbol{M}(u), \\ \boldsymbol{M}(u) &= \begin{pmatrix} \cos(u\kappa/\tau_\gamma) & \sin(u\kappa/\tau_\gamma) \\ -\sin(u\kappa/\tau_\gamma) & \cos(u\kappa/\tau_\gamma) \end{pmatrix}. \end{aligned} \tag{7.3}$$

with $\boldsymbol{M}(u)$ a rotation matrix. These expressions show that the odd diffusion introduces oscillations in the evolution of the particle position which decay on a time-scale τ_γ and in the limit of a normal-diffusive system ($\kappa \to 0$, i.e., in the absence of oddness) one retrieves $\boldsymbol{G}(u) \to \exp(-|u|/\tau_\gamma)\,\boldsymbol{1}$ as $\boldsymbol{M}(u) \to \boldsymbol{1}$. The memory introduced by the coarse-graining of the velocity variable appears in the convolution of $\boldsymbol{G}(u)$ with the interaction forces, as well as in the zero-mean Gaussian colored noise $\boldsymbol{\eta}(t)$

$$\boldsymbol{\eta}(t) = \frac{\sqrt{2T\gamma}}{m}\int_{t_0}^{t} \mathrm{d}s\, \boldsymbol{G}(t-s)\boldsymbol{\xi}_0(s), \tag{7.4}$$

with correlation

$$\langle \boldsymbol{\eta}(t) \otimes \boldsymbol{\eta}(s) \rangle = \frac{T}{m} \left[\mathrm{e}^{-\frac{|t-s|}{\tau\gamma}} - \mathrm{e}^{-\frac{t+s-2t_0}{\tau\gamma}} \right] \boldsymbol{M}(t-s). \tag{7.5}$$

At long times, the effect of the initial conditions is forgotten and the two-point correlation function becomes time-translation invariant, with:

$$\langle \boldsymbol{\eta}(t) \otimes \boldsymbol{\eta}(s) \rangle \overset{t,s \gg t_0}{\simeq} \frac{T}{m} \boldsymbol{G}(t-s) \,, \tag{7.6}$$

which corresponds to the one reported in Ref. [318]. In the same spirit of Refs. [315, 316], we want to adopt a coarse-grained description for the density of the host particles constituting the medium the odd tracer is coupled to. To this aim, following Ref. [72] and as discussed in Sec. 2.9, we introduce the fluctuating particle density $\rho(\boldsymbol{x}, t)$ of the host particles, defined in Eq. (2.85), and we use it to move from a microscopic to a mesoscopic description of the medium. It can be easily shown that the dynamics of the odd tracer couples to the fluctuating density $\rho(\boldsymbol{x}, t)$ in the following way:

$$\begin{aligned} \dot{\boldsymbol{X}}_0 = &- \frac{\lambda_{\mathrm{t}}}{m} \int_{t_0}^{t} \mathrm{d}s \, \boldsymbol{G}(t-s) \int \mathrm{d}\boldsymbol{x} \, \nabla \mathcal{U}(\boldsymbol{X}_0(s) - \boldsymbol{x}) \, \rho(\boldsymbol{x}, s) \\ &+ \boldsymbol{G}(t-t_0) \boldsymbol{V}_0(t_0) + \boldsymbol{\eta}(t) \, . \end{aligned} \tag{7.7}$$

In order to have a complete description of the system, one needs to derive a stochastic evolution equation for the density $\rho(\boldsymbol{x}, t)$. This can be obtained starting from the microscopic dynamics of the N host particles, which in the overdamped regime reads:

$$\dot{\boldsymbol{X}}_i = - \nu \lambda_{\mathrm{h}} \sum_{j=1}^{N} \nabla \mathcal{U}(\boldsymbol{X}_i - \boldsymbol{X}_j) - \nu \lambda_{\mathrm{t}} \nabla \mathcal{U}(\boldsymbol{X}_i - \boldsymbol{X}_0) + \sqrt{2T\nu} \, \boldsymbol{\xi}_i \tag{7.8}$$

with $i \in \{1, ..., N\}$ and $\nu = \gamma^{-1}$ the mobility coefficient. Note that, in this case, the stochastic dynamics in the overdamped regime can be easily derived as there is no ambiguity related to having an odd mobility. Furthermore, the coupling strengths λ_{h} and λ_{t} are taken to be distinct in that the host-host and host-tracer interactions can in principle be different. Analogously to Ref. [72] and as explained in Sec. 2.9, the stochastic dynamics of $\rho(\boldsymbol{x}, t)$ can be derived using the Itô Lemma, and is governed by the following continuity equation:

$$\dot{\rho}(\boldsymbol{x}, t) = - \nabla_{\boldsymbol{x}} \cdot \boldsymbol{\mathcal{J}} \,, \tag{7.9}$$

with the fluctuating flux

$$\begin{aligned} \boldsymbol{\mathcal{J}} = &- \nu \lambda_{\mathrm{h}} \int \mathrm{d}\boldsymbol{y} \, \rho(\boldsymbol{y}, t) \, \nabla \mathcal{U}(\boldsymbol{x} - \boldsymbol{y}) \, \rho(\boldsymbol{x}, t) \\ &- \nu \lambda_{\mathrm{t}} \nabla \mathcal{U}(\boldsymbol{x} - \boldsymbol{X}_0) \, \rho(\boldsymbol{x}, t) \\ &- T\nu \, \nabla \rho(\boldsymbol{x}, t) + \sqrt{2T\nu \, \rho(\boldsymbol{x}, t)} \, \boldsymbol{\Lambda}(\boldsymbol{x}, t). \end{aligned} \tag{7.10}$$

A few comments on the above equation are in order: the first line on the r.h.s. corresponds to the drift flux due to the soft interactions between the host particles which constitute the medium, whereas the second line involves the interaction between the density field of the host particles and the odd tracer at position $\boldsymbol{X}_0$. The last line comes, instead, from the coupling between the density $\rho(\boldsymbol{x},t)$ and the equilibrium thermal bath at temperature T. This involves the standard diffusive flux proportional to $\nabla\rho$ and a fluctuating contribution that depends on the zero-mean Gaussian white noise field $\boldsymbol{\Lambda}(\boldsymbol{x},t)$, the correlations of which are given in Eq. (2.95). Note that the noise $\sqrt{2T\nu\,\rho(\boldsymbol{x},t)}\,\boldsymbol{\Lambda}(\boldsymbol{x},t)$ is multiplicative as its amplitude depends on the fluctuating density itself. Moreover, Eq. (7.9) is non linear in the density ρ, and thus it is very challenging to make any analytical progress with it. To overcome this difficulty, it is rather common to assume that the density fluctuations are much smaller than the homogeneous bulk density (see, e.g., Refs. [275, 315, 316, 324]). In other words, after decomposing the fluctuating density as $\rho(\boldsymbol{x},t)=\rho_0+\phi(\boldsymbol{x},t)$, with ρ_0 the homogeneous state and $\phi(\boldsymbol{x},t)$ the fluctuations around that, we assume that $|\phi(\boldsymbol{x},t)|\ll\rho_0$. By expanding Eq. (7.9) at the lowest order in $\phi(\boldsymbol{x},t)/\rho_0$, one gets the following linearized dynamics for the field $\phi(\boldsymbol{x},t)$ [275]

$$\begin{aligned}\dot{\phi}(\boldsymbol{x},t) = \lambda_{\mathrm{h}}\nu\rho_0 &\int \mathrm{d}\boldsymbol{y}\,\phi(\boldsymbol{y},t)\,\nabla^2_{\boldsymbol{x}}\mathcal{U}(\boldsymbol{x}-\boldsymbol{y}) \\ &+ \lambda_{\mathrm{t}}\nu\rho_0\int \mathrm{d}\boldsymbol{y}\,\delta(\boldsymbol{y}-\boldsymbol{X}_0)\,\nabla^2_{\boldsymbol{x}}\mathcal{U}(\boldsymbol{x}-\boldsymbol{y}) \\ &+ T\nu\,\nabla^2\phi(\boldsymbol{x},t)+\zeta(\boldsymbol{x},t)\,,\end{aligned} \tag{7.11}$$

where we introduce the scalar zero-mean Gaussian white noise field $\zeta(\boldsymbol{x},t)$ with correlations:

$$\langle\zeta(\boldsymbol{x},t)\zeta(\boldsymbol{y},s)\rangle = -2T\nu\rho_0\nabla^2_{\boldsymbol{x}}\delta(t-s)\,\delta(\boldsymbol{x}-\boldsymbol{y}) \tag{7.12}$$

Note that, in this context, the field mobility coefficient is given by $\nu\rho_0$, . Interestingly, the dynamics of the density field fluctuations $\phi(\boldsymbol{x},t)$ in Eq. (7.11) can be cast into the standard form of a model-B like dynamics [54]

$$\dot{\phi}(\boldsymbol{x},t) = \nu\rho_0\,\nabla^2\frac{\delta\mathcal{F}}{\delta\phi(\boldsymbol{x},t)}+\zeta(\boldsymbol{x},t) \tag{7.13}$$

by introducing the appropriate effective free energy:

$$\begin{aligned}\mathcal{F}[\phi] = \frac{\lambda_{\mathrm{h}}}{2}&\int\mathrm{d}\boldsymbol{x}\int\mathrm{d}\boldsymbol{y}\,\phi(\boldsymbol{x},t)\,\mathcal{U}(\boldsymbol{x}-\boldsymbol{y})\,\phi(\boldsymbol{y},t) \\ &+\lambda_{\mathrm{t}}\int\mathrm{d}\boldsymbol{x}\int\mathrm{d}\boldsymbol{y}\,\delta(\boldsymbol{x}-\boldsymbol{X}_0)\,\mathcal{U}(\boldsymbol{x}-\boldsymbol{y})\,\phi(\boldsymbol{y},t) \\ &+\frac{T}{2\rho_0}\int\mathrm{d}\boldsymbol{x}\,\phi^2(\boldsymbol{x},t)\,.\end{aligned} \tag{7.14}$$

The first two lines of the effective free energy correspond to the energetic contributions related to the host-host and host-tracer particle interactions, respectively, whereas the last term has an entropic origin. Under the assumption of small density fluctuations, the microscopic equation of motion of the odd tracer can therefore be rewritten as:

$$\begin{aligned}\dot{\boldsymbol{X}}_0 = &-\frac{\lambda_\mathrm{t}}{m}\int_{t_0}^{t} \mathrm{d}s\, \boldsymbol{G}(t-s)\int \mathrm{d}\boldsymbol{x}\, \nabla\mathcal{U}(\boldsymbol{X}_0(s)-\boldsymbol{x})\,\phi(\boldsymbol{x},s) \\ &+\boldsymbol{G}(t-t_0)\boldsymbol{V}_0(t_0)+\boldsymbol{\eta}(t)\,.\end{aligned} \tag{7.15}$$

The structure of this stochastic dynamics is analogous to the one derived, in similar contexts, in Refs. [65–68, 325]. Note, however, that despite the linearization of Dean's equation, the theory remains non-linear in the position of the odd tracer $\boldsymbol{X}_0(t)$. Thus, in order to make analytical progress with Eq. (7.15), we consider in Sec. 7.3.1 a perturbative expansion of the tracer position $\boldsymbol{X}_0$ and the field ϕ in the interaction coupling λ_t. The analytical predictions obtained within this weak-coupling approach are tested a posteriori with Brownian dynamics simulations.

7.3 Self-diffusion of the odd tracer

With the help of the model presented in the previous Section, we analyze the self-diffusion coefficient of the odd tracer and investigate how this is affected by the soft-core interactions with the host particles. Collisions with the host particles have already proved to be useful for enhancing the self-diffusion coefficient of an odd tracer in both single and multi-species systems with hardcore repulsion [142]. As introduced at the end of Sec. 7.2, we use a perturbative approach in the coupling strength λ_t between the field $\phi(\boldsymbol{x},t)$ and the odd tracer to compute the mean-squared displacement of the latter and extract, from its long-time behavior, the self-diffusivity defined as:

$$D_\mathrm{s} = \lim_{(t-t_0)\to\infty} \frac{\langle|\boldsymbol{X}_0(t)-\boldsymbol{X}_0(t_0)|^2\rangle}{4(t-t_0)}\,. \tag{7.16}$$

To this purpose, it is convenient to rewrite the stochastic dynamics of the field $\phi(\boldsymbol{x},t)$ in terms of its Fourier modes $\phi_{\boldsymbol{q}}(t)$, which are defined as in Eq. (2.75). The field dynamics of Eq. (7.11) become

$$\dot{\phi}_{\boldsymbol{q}} = -\alpha_{\boldsymbol{q}}\phi_{\boldsymbol{q}} - \lambda_\mathrm{t}\,\nu\rho_0\, q^2\mathcal{U}_{\boldsymbol{q}}\,\mathrm{e}^{-i\boldsymbol{q}\cdot\boldsymbol{X}_0} + \zeta_{\boldsymbol{q}}(t)\,, \tag{7.17}$$

where we introduced the inverse relaxation time

$$\alpha_{\boldsymbol{q}} = \nu q^2[\lambda_\mathrm{h}\rho_0\,\mathcal{U}_{\boldsymbol{q}} + T] \tag{7.18}$$

of the $\boldsymbol{q}$-mode of the field and the Fourier transform of the noise $\zeta_{\boldsymbol{q}}(t)$ with correlation

$$\langle \zeta_{\boldsymbol{q}}(t)\zeta_{\boldsymbol{p}}(s)\rangle = 2T\nu\rho_0\, q^2(2\pi)^2\delta(\boldsymbol{q}+\boldsymbol{p})\,\delta(t-s)\,. \tag{7.19}$$

Notice that the relaxation time $1/\alpha_{\boldsymbol{q}}$ of $\phi_{\boldsymbol{q}}$ increases by approaching $q^2 \to 0$, eventually diverging for the $\boldsymbol{q} = \boldsymbol{0}$ mode. This is expected because Eq. (7.13) is a continuity equation, due to the fact that the field $\phi(\boldsymbol{x},t)$ is a locally conserved quantity. This conservation law implies that density fluctuations at large length scales relax very slowly. The coupling between the odd tracer and the field in Eq. (7.15) can also be rewritten in terms of the modes $\phi_{\boldsymbol{q}}(t)$ as follows:

$$\begin{aligned}\dot{\boldsymbol{X}}_0(t) = &-\frac{\lambda_{\mathrm{t}}}{m}\int_{t_0}^{t}\mathrm{d}s\,\boldsymbol{G}(t-s)\int\frac{\mathrm{d}\boldsymbol{q}}{(2\pi)^2}\,i\boldsymbol{q}\mathcal{U}_{\boldsymbol{q}}\,\phi_{\boldsymbol{q}}(s)\,\mathrm{e}^{i\boldsymbol{q}\cdot\boldsymbol{X}_0(s)}\\ &+\boldsymbol{G}(t-t_0)\boldsymbol{V}_0(t_0)+\boldsymbol{\eta}(t)\,.\end{aligned} \tag{7.20}$$

In the coming Section, we use Eq. (7.20) as the starting point for the weak-coupling approximation. In particular, we substitute the perturbative expansions for the tracer position $\boldsymbol{X}_0$ and the field ϕ given in Eqs. (7.21) and (7.22) into the dynamics in Eq. (7.20), and we collect together all terms of the same order in the interaction coupling λ_{t}.

7.3.1 Weak-coupling approximation

To compute the mean-squared displacement (MSD), we formally expand the tracer position and the density field in powers of the coupling strength λ_{t} of the tracer particle to the host field

$$\boldsymbol{X}_0(t) = \sum_{n=0}^{\infty}\lambda_{\mathrm{t}}^n\boldsymbol{X}_0^{(n)}(t)\,, \tag{7.21}$$

$$\phi_{\boldsymbol{q}}(t) = \sum_{n=0}^{\infty}\lambda_{\mathrm{t}}^n\phi_{\boldsymbol{q}}^{(n)}(t). \tag{7.22}$$

Within this perturbative approach and assuming that the initial position of the tracer is $\boldsymbol{X}_0(t_0) = \boldsymbol{0}$ without loss of generality, we have that the MSD of the tracer is given by

$$\begin{aligned}\langle|\boldsymbol{X}_0(t)|^2\rangle = &\left\langle\boldsymbol{X}_0^{(0)}(t)\cdot\boldsymbol{X}_0^{(0)}(t)\right\rangle\\ &+\lambda_{\mathrm{t}}^2\left(\left\langle\boldsymbol{X}_0^{(1)}(t)\cdot\boldsymbol{X}_0^{(1)}(t)\right\rangle+2\left\langle\boldsymbol{X}_0^{(0)}(t)\cdot\boldsymbol{X}_0^{(2)}(t)\right\rangle\right)\\ &+\mathcal{O}(\lambda_{\mathrm{t}}^4)\end{aligned} \tag{7.23}$$

Importantly, all contributions related to odd powers of λ_{t} vanish as the equation of motions are invariant under the transformation $(\lambda_{\mathrm{t}},\phi) \leftrightarrow (-\lambda_{\mathrm{t}},-\phi)$.

Accordingly, in order to evaluate the MSD, we have to solve the set of coupled stochastic dynamics of the tracer and the field, i.e., Eqs. (7.20) and (7.17), respectively, at orders λ_{t}^0, λ_{t}^1 and λ_{t}^2. At the lowest order $\mathcal{O}(\lambda_{\mathrm{t}}^0)$ we find

$$\dot{\boldsymbol{X}}_0^{(0)}(t) = \boldsymbol{G}(t-t_0)\boldsymbol{V}_0(t_0) + \boldsymbol{\eta}(t)\,, \tag{7.24}$$

which constitutes the time evolution of the interaction-free tracer particle and it is solved in Appendix E.2. The tracer evolution at the linear order $\mathcal{O}(\lambda_{\mathrm{t}})$ becomes

$$\dot{\boldsymbol{X}}_0^{(1)}(t) = -\frac{1}{m}\int_{t_0}^{t} \mathrm{d}s\; \boldsymbol{G}(t-s)\int \frac{\mathrm{d}\boldsymbol{q}}{(2\pi)^2}\, i\boldsymbol{q}\mathcal{U}_{\mathrm{t},\boldsymbol{q}}\phi_{\boldsymbol{q}}^{(0)}(s)\,\mathrm{e}^{i\boldsymbol{q}\cdot\boldsymbol{X}_0^{(0)}(s)}\,, \tag{7.25}$$

which depends on the free field $\phi_{\boldsymbol{q}}^{(0)}$ and on the position of the free tracer $\boldsymbol{X}_0^{(0)}$. Similarly, at order $\mathcal{O}(\lambda_{\mathrm{t}}^2)$ we find

$$\begin{aligned}\dot{\boldsymbol{X}}_0^{(2)}(t) = -\frac{1}{m}\int_{t_0}^{t} \mathrm{d}s\; \boldsymbol{G}(t-s)\int \frac{\mathrm{d}\boldsymbol{q}}{(2\pi)^2}\, i\boldsymbol{q}\mathcal{U}_{\mathrm{t},\boldsymbol{q}} \\ \times\left[\phi_{\boldsymbol{q}}^{(1)}(s) + i\boldsymbol{q}\cdot\boldsymbol{X}_0^{(1)}(s)\,\phi_{\boldsymbol{q}}^{(0)}(s)\right]\mathrm{e}^{i\boldsymbol{q}\cdot\boldsymbol{X}_0^{(0)}(s)},\end{aligned} \tag{7.26}$$

which again is related to the tracer position and the field at lower orders in the interaction coupling. Note that the weak-coupling approximation presented here is closely related to the one used for similar problems in Refs. [65, 66, 316, 325]. The relevant correlations within the small coupling approximations, $\langle \boldsymbol{X}_0^{(1)}(t)\cdot\boldsymbol{X}_0^{(1)}(t)\rangle$ and $\langle \boldsymbol{X}_0^{(0)}(t)\cdot\boldsymbol{X}_0^{(2)}(t)\rangle$, are evaluated in Appendix E.3.

7.3.2 Gaussian-core model

In this Section we specialize the analytical expressions derived in the previous Section to the case of the soft-core Gaussian interaction potential

$$\mathcal{U}(\boldsymbol{x}) = \frac{1}{2\pi\sigma^2}\exp\left(-\frac{\boldsymbol{x}^2}{2\sigma^2}\right), \tag{7.27}$$

where in the particle-based picture $\boldsymbol{x}$ denotes the center-to-center distance between two interacting particles. The parameter σ, which corresponds to the distance of the inflection point of the interaction potential from its maximum, sets the length scale of the strongest interaction force between the two particles. For this reason, we interpret σ as an effective particle radius, which, in turn, defines a particle area of $\pi\sigma^2$ and thus an effective area fraction

$$c = \pi\sigma^2 N/L^2\,, \tag{7.28}$$

with L the system size. In the framework of the mesoscopic field-theoretic description introduced in Sec. 7.2, σ determines the range of interaction between the odd-tracer and the fluctuating density field $\phi(\boldsymbol{x},t)$.

The first non-trivial perturbative correction to the MSD of the odd tracer, the expression of which is given in Eq. (7.23), is analyzed in detail in Appendix E.3. There, we derive the formal expression of the correlations $\langle \boldsymbol{X}_0^{(1)}(t) \cdot \boldsymbol{X}_0^{(1)}(t) \rangle$ and $\langle \boldsymbol{X}_0^{(0)}(t) \cdot \boldsymbol{X}_0^{(2)}(t) \rangle$ with a generic interaction potential $\mathcal{U}(\boldsymbol{x})$. Note that the derivation presented so far does not rely on any assumption about the mass of the odd-tracer. The reason behind this choice is two-fold: on the one hand, it is well-known that taking the small-mass limit $m \to 0$ at the level of the stochastic dynamics in Eq. (7.1) hides some subtleties due to the oddness of the tracer, and can potentially lead to wrong predictions for the fluxes in the systems (see e.g., Ref. [318]). For this reason, in order to study the overdamped regime of the odd-diffusive tracer, we find convenient to take the $m \to 0$ limit a posteriori. On the other hand, even though this is beyond the scope this Chapter, keeping a finite mass m for the tracer throughout the derivation paves the way for a thorough investigation of the role of mass in the odd-diffusive dynamics of interacting particles.

By specializing the field-induced correction to the MSD of the odd-tracer to the case of soft-core Gaussian interactions given in Eq. (7.27) and by using standard numerical integration schemes for its evaluation (see Appendix E.3 for details), we can analyze the extent to which the self-diffusion of the odd tracer is affected by the interactions with the host species. In Fig. 7.2 (left panel) we show the behavior of the self-diffusion coefficient D_s as a function of the oddness parameter κ. We represent with solid lines our theoretical predictions obtained within the weak coupling approximation, and with symbols the results of Brownian dynamics simulations (see Appendix E.4 for details). In particular, we observe that our weak-coupling theory (see Appendix E.3) predicts the existence of a critical oddness parameter $\kappa_c = 1$ such that, when $\kappa < \kappa_c = 1$, the self-diffusion of the odd tracer is suppressed compared to the value

$$D_0 = T\nu/(1+\kappa^2) \tag{7.29}$$

that characterizes a single free odd particle in the absence of interactions with the surrounding medium. This behavior is expected and reflects the intuition that in a crowded environment the motion of a diffusive tracer is hindered by the collisions with the other particles. Surprisingly, the combined effect of the particle interactions and the odd-diffusive motion of the tracer may result in an inversion of this tendency. Indeed, for sufficiently large κ, namely $\kappa > \kappa_c$, we observe an enhancement of the self-diffusion D_s compared to D_0. Notably, this proves that the described phenomenology, initially discovered in a system of interacting odd-diffusive hard-spheres in Ref. [142], does not rely on the specific choice of the interaction potential $\mathcal{U}$. At the same time, having soft-core interactions shifts the value of the critical oddness parameter to $\kappa_c = 1$, while this was $\kappa_c = 1/\sqrt{2}$ in the case of hard-spheres. This implies that a more pronounced chirality is required in order to enhance the transport properties of the odd tracer, because the effect of the collisions between the tracer and the host particles is milder with soft-interactions. Note that our weak-coupling approach predicts a critical oddness parameter $\kappa_c = 1$ that does not depend on the density c of the medium. While this appears to actually be the case for a sufficiently small interaction coupling λ_{t}, as reported in Fig. 7.2, an appreciable dependence on c of the critical oddness parameter emerges upon increasing λ_{t} (see Fig. 7.3).

One of the main advantages of the field-theoretic description adopted here compared to the geometric approach of Ref. [142], is that it carries over to the case of dense systems. In fact, in the main plot of Fig. 7.2 (left panel), different colors denote different area fractions c, from a very dilute case ($c = 5\%$, dark blue) to an intermediate density ($c = 50\%$, grey) and a very dense system ($c = 100\%$, yellow). It appears that the behavior of the self-diffusion as a function of c is far from being trivial. For example, if we focus on the region $\kappa < \kappa_c$ we realize that the self-diffusion D_{s} is larger when the tracer is dispersed in a very dense system ($c = 100\%$) than in the case of intermediate density ($c = 50\%$). This counter-intuitive phenomenon is actually well-known in the literature about the GCM (see e.g., Refs. [299, 302, 314]) and it has been associated to the structural anomaly that characterizes Gaussian-core fluids at high density. Indeed, due to the bounded nature of the interaction potential, different particles can possibly overlap, and when the density is sufficiently high, they can form transient clusters that lead to an overall increase of their mobility. In the inset of Fig. 7.2 (left panel), we confirm this picture by plotting the self-diffusion D_{s} over a wide range of area fractions (up to $c = 200\%$). For a normal diffusive tracer (i.e., $\kappa = 0$, blue lines and symbols), we confirm the non-monotonic anomalous behavior of D_{s} previously reported in Refs. [299, 302, 314]. Interestingly, when the oddness parameter κ exceeds the critical value κ_c (yellow line in the inset), we observe a opposite trend showing an initial increase in the self-diffusion for sufficiently dilute systems, followed by a decrease for densities above a certain threshold. Notably, the theoretical predictions are in excellent agreement with the results of Brownian dynamics simulations, especially for very dense systems. This is coherent with the fact that linearizing Dean's equation is allowed when the density fluctuations ϕ around the homogeneous bulk density ρ_0 are much smaller than ρ_0 itself.

In the right panel of Fig. 7.2 we plot the self-diffusion D_s as a function of the area fraction up to $c = 50\%$ for various values of the oddness parameter κ. Particularly interesting is the critical case $\kappa = \kappa_c$, for which the self-diffusion appears as insensitive to any variation of the system density. This effect could be rationalized by noting that the addition of host particles to the system has a two-fold effect on the tracer: on the one hand, it makes the surrounding environment more crowded, thus hindering the motion of the tracer. On the other, the collisions with the host particles provide a potential mechanism for speeding-up

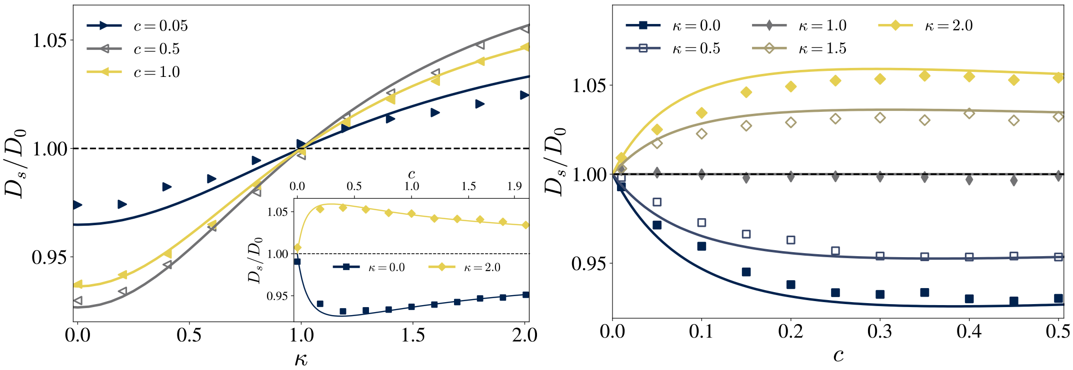

Figure 7.2: Long-time self-diffusion coefficient D_s of an odd tracer coupled to $N = 199$ normally diffusive host particles. In both panels, solid lines represent the analytical predictions (see Appendix E.3 for a detailed derivation) obtained within the weak-coupling approximation, whereas symbols denote the result of Brownian dynamics simulations (see Appendix E.4 for details). The value of D_s is measured in units of D_0 defined in Eq. (7.29), i.e. the self-diffusion coefficient of a single free odd particle. Left panel: Self-diffusion D_s as a function of the oddness parameter κ. The main plot shows that for sufficiently small values of κ, the self-diffusion is suppressed compared to the case of a free odd-tracer as intuitively expected in a crowded environment. Upon increasing κ beyond the critical value $\kappa_c = 1$, however, the interaction of the tracer with the host particles enhances its self-diffusion. In this panel, different colors denote different concentrations of particles, measured by the area fraction c defined in Eq. (7.28). The inset shows the values of D_s/D_0 for $\kappa = 0$ (blue line and symbols) and $\kappa = 2$ (yellow line and symbols) — corresponding to the two extremes of the range of values of κ considered in the main plot — as a function of c. This inset demonstrates that the suppression/enhancement of the self-diffusion persists over a remarkably wide range of system densities. Right panel: Self-diffusion D_s as function of the area fraction c. In this case, different colors stand for different values of the oddness parameter κ. Interestingly, at the critical value $\kappa_c = 1$, the odd tracer behaves as in the absence of host particles, independently of their density. The fact that at $\kappa = \kappa_c$ we observe $D_s \approx D_0$ for all densities c is related to the choice of a sufficiently small interaction coupling λ_t. Upon increasing λ_t this property disappears, as shown in Fig. 7.3. More details about the simulation parameters can be found in Appendix E.4.

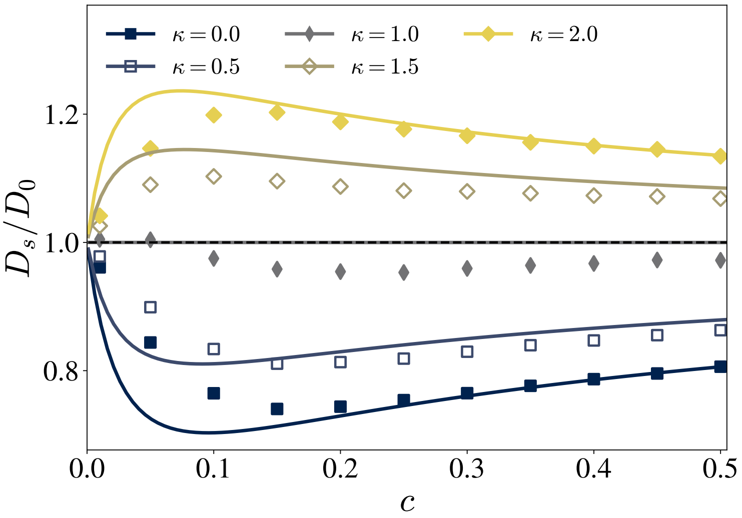

Figure 7.3: Self-diffusion coefficient D_{s} (measured in units of D_0) as a function of the area fraction c defined in Eq. (7.28) in the case of larger interaction coupling $\lambda_{\mathrm{t}} = 4 \cdot 2\pi\sigma^2$. Analogously to the inset of Fig. 7.2 (right panel), solid lines represent the analytical predictions whereas symbols are obtained with Brownian dynamics simulations. Different colors denote different values of the oddness parameter κ. In particular, we observe that for larger interaction coupling the enhancement of the self-diffusion for $\kappa > \kappa_c$ is much more pronounced (up to 20% of D_0) than in Fig. 7.2. Moreover, the largest enhancement is obtained with a lower density of host particles ($c \simeq 0.15$). Note that in this case, at $\kappa = \kappa_c$, the value of the self-diffusion D_s depends on the density c of the medium, as opposed to Fig. (7.2). Indeed, upon increasing the value of the interaction coupling λ_{t}, the accuracy of the predictions obtained with the weak-coupling approximation decreases.

the tracer's dynamics when the latter exhibits odd-diffusivity. At the critical value $\kappa = \kappa_c$ these two effects balance each other and the tracer effectively evolves as in the absence of interactions. As anticipated above, however, the fact that κ_c does not depend on the medium density c holds only in the weak-coupling regime, while it is not true anymore when the interaction coupling λ_{t} is increased (see Fig. 7.3). Furthermore, note that due to the complicated form of the analytical predictions reported in Appendix E.3, the value of $\kappa_c = 1$ does not explicitly appear from the calculations and it emerged from their numerical evaluation.

In Fig. 7.3 we show the extent to which a larger interaction coupling affects the self-diffusion coefficient of the odd tracer. Specifically, we observe that with a coupling λ_{t} that is 4 times lager than in Fig. 7.2, the self-diffusion can reach an enhancement of approximately 20% of the free value D_0. Since our theory is based on a weak-coupling approximation, it is expected to result into less accurate predictions when the interaction strength λ_t is increased. For this reason, we observe that the discrepancy between the analytical predictions and the simulation data increases in the low density limit. Despite the poorer agreement with the simulations in the very dilute regime, Fig. 7.3 shows that our theory is still able to correctly capture another qualitative feature caused by the larger interaction coupling, namely the shift of the onset of the diffusivity anomaly toward lower densities ($c \approx 15\%$).

7.4 Conclusions

In this Chapter, we studied the self-diffusion coefficient of an odd diffusive tracer interacting with an ensemble of normally diffusive host particles. The pairwise interaction between the particles was modeled by a bounded soft-core Gaussian potential, implying that different particles can potentially overlap. From a particle-based picture of the Gaussian-core model fluid, we moved to a field-theoretic description based on the Dean-Kawasaki equation [72, 73] (see also Chapter 2), where the host species are coarse-grained into a thermally fluctuating density field $\rho(\boldsymbol{x}, t)$, resulting in the stochastic evolution given in Eq. (7.9). Under the assumption that the interaction coupling λ_t between the density field and the odd tracer is sufficiently small, we obtained a perturbative expansion for the mean-squared displacement of the latter, which we truncated at the first non-trivial order $\mathcal{O}(\lambda_\mathrm{t}^2)$. From this expansion, we deduced the field-induced correction to the self-diffusion of the odd tracer. In particular, we showed that, upon increasing the oddness parameter κ, the collisions with the host particles have a substantially different effect on the transport properties of the odd tracer. Specifically, a critical value κ_c exists such that, for $\kappa < \kappa_c$, the self-diffusion is reduced compared to the interaction-free case by the hindering effect introduced by the host particles, whereas for $\kappa > \kappa_c$ the interaction with the host particles leads to an enhancement of the self-diffusion, causing a speed-up of the tracer dynamics. Moreover, we showed that this enhancement is maximized at a specific spatial density of the system (i.e., area fraction c in two dimensions), the value of which depends on the interaction coupling λ_t. The non-monotonic behavior of the self-diffusion as a function of the area fraction c for $\kappa > \kappa_c$ is opposite to that of normally diffusive Gaussian-core particles (see Fig. 7.2), the mobility of which first decreases and then increases upon isothermal compression (see, e.g., the self-diffusivity anomaly in Refs. [299–302, 314]). Finally, we showed that at the critical value $\kappa = \kappa_c$, the self-diffusion of the odd tracer is not affected by the collisions with the crowding particles. In particular, for sufficiently small interaction couplings λ_t, the value of κ_c does not depend on the density of the medium. It is natural to wonder which values of κ could be obtained for a real charged particle subject to a magnetic field

$\boldsymbol{B}$. Following Ref. [142], for a millimeter-sized granule with a surface charge density $\sigma = 1e\,\mathrm{nm}^{-2}$, with e the electronic charge, a viscosity of $\eta \approx 10^{-4}\,\mathrm{Pa\ s}$ (Propylene at room temperature), and $B = 1\,\mathrm{T}$, one gets $\kappa \approx 1$.

The model presented here can be extended to address a variety of related problems. For example, the Dean equation has been already generalized to the underdamped regime, by including in the description a momentum density field [326, 327]. A potentially interesting direction is that of deriving the fluctuating hydrodynamic equations for a system of interacting soft-core odd particles in the underdamped regime and study the dynamic behavior of a tracer in such an odd medium. Moreover, the derivation presented here can already be used for a systematic analysis of the role of the tracer mass on the transport properties of an odd tracer in a crowded environment.

The Gaussian-core model is known to exhibit numerous counter-intuitive anomalous features such as the aforementioned self-diffusivity anomaly, but also a density anomaly (consisting in an expansion upon isobaric cooling) and a structural order anomaly (i.e., the reduction of short-range translational order upon isothermal compression) [294, 299, 301–303]. It may be insightful to thoroughly investigate the influence of oddness on structural, transport and thermodynamics properties of Gaussian-core fluids.

A further extension of the model presented here can be used to describe the coupling of odd-diffusive particles with a binary mixture of purely repulsive Gaussian-core fluids, which has proved to exhibit fluid-fluid phase separation [328, 329]. Approaching the demixing point, the binary mixture would develop spatial correlations on arbitrarily large length scales and thus it could introduce fluctuation-induced forces between the odd-particles [55–57, 59]. The behavior of odd-particles in such correlated media is a future direction that might be worth exploring. Finally, in the formulation presented here, the odd tracer and the host particles (and thus the density field ρ) evolve according to an equilibrium dynamics. It may be interesting to analyze the transport properties of an odd tracer coupled to an active fluid featuring nonequilibrium fluctuations, where the detailed balance condition is violated.

Chapter 8

Conclusions and outlook

In the first part of this thesis (i.e., in Chapters 3, 4 and 5) we explored the complex non-equilibrium behavior of interacting active particles, of cargo-carrying self-propelled microswimmers and of polymeric systems when they are dispersed in environments characterized by a non-uniform degree of activity, with broad implications for experimental studies and applications in soft matter, biophysics and nanotechnology. In particular, in Chapter 3, we showed that the interplay between rotational diffusion and active chiral torques can lead to an emergent chemotactic-like behavior in dimers of interacting active chiral particles (see Fig. 3.2). By comparing the behavior of active chiral particles and active charged particles under the action of Lorentz force, we demonstrate that, despite they both belong to the same class of odd-diffusive systems, their response to a non-homogenous activity is qualitatively different. These results highlight the potential of active chiral particles in synthetic chemotaxis, providing insights into the design of autonomous systems that are able to steer towards specific target zones without the help of external stimuli. In Chapter 4 we showed that self-propelled cargo-carrying microswimmers interacting with traveling activity waves display a rich tactic behavior. In particular, by tuning the values of the parameters of the cargo, the active-passive complex can migrate along or against the direction of the activity wave propagation, as shown in Fig. 4.3. Due to the emerging possibility of controlling the directed motion of self-propelled particles with travelling tactic stimuli, these findings potentially suggest alternative strategies to innovate systems with targeted delivery at the microscale. In Chapter 5 we demonstrate that polymer chains dispersed in a non-uniform active bath can spontaneously separate in space by migrating into distinct regions with different level of activity (see Figs. 5.2, 5.3 and 5.4). This phenomenon, which relies on a nonequilibrium mechanism (and therefore it cannot occur at equilibrium), could be exploited for length-selective localization of polymer molecules or for their sorting based on their structural connectivity. Experimental validation with synthetic colloidal chains immersed in bacterial bath or with biomolecules would further support the relevance of these theoretical predictions. In all the aforementioned Chapters, the activity field is not affected by the interaction with the particles, nor it exhibits any sign of stochasticity due to thermal fluctuations. In modelling more realistic systems, however, these assumptions have to be relaxed. It would be interesting to analyse whether the phenomena described in Chapters 3, 4 and 5 would still occur if the particles and the fluctuating activity field influenced each other along their dynamical evolution.

In the second part of the thesis (Chapters 6 and 7) we investigated the dynamics of polymer chains and odd diffusive tracers coupled to fluctuating correlated media, and studied their structural, transport and relaxation properties. In particular, in Chapter 6 we examined the behavior of a polymer under harmonic confinement, coupled to a correlated medium described by a scalar Gaussian field. We proved that the relaxation of the center of mass of the polymer towards its equilibrium position exhibits an algebraic decay at long times if the field supports slow relaxation modes due to criticality or to underlying conservation laws, as shown in Fig. 6.3. Conversely, in the case in which all monomers interact with the field in the same way, the relaxation of the internal structure of the chain remains exponential, with a characteristic time scale which is reduced compared to the case with no interaction with the field, due to the attractive field-induced interactions between the monomers. Moreover, we showed how such field-mediated forces affect the typical size of the polymer and its response to a tensile stretching force. Although the model proposed here is a good starting point for understanding the influence of fluctuating correlated media on conformational and dynamic properties of polymer chains, it is based on the simplest possible polymer model. In particular, it neglects many interactions that should be taken into account in order to describe a more realistic polymer molecule. Specifically, it does not consider the excluded volume interaction between each pair of monomers, which account for steric hindrance effects, and it neglects the finite extensibility of the bonds as well as the bending rigidity of the chain. As a future perspective, it might be worth exploring the effect of field mediated forces on a more realistic polymer model.

In Chapter 7 we studied the self-diffusion of an odd tracer in a crowded environment of normally diffusive host particles. The soft interaction potential is chosen to be Gaussian, and thus particles are allowed to overlap. Within a field-theoretic framework based on the Dean-Kawasaki equation, where the host particles are coarse-grained into a fluctuating correlated density field, we analysed the self-diffusion of the odd tracer. Depending on the oddness parameter, we showed that the interactions between the tracer and the medium can either reduce or enhance the self-diffusion of the former (see Fig. 7.2). Moreover, we made contact with the existing literature on Gaussian-core model by describing how oddness affect the self-diffusivity anomaly at high density. In recent years, the study of chiral fluids has attracted a growing level of attention (see, e.g., Refs. [330, 331]). As future perspectives, it could be interesting to extend the analysis reported in Chapter 7 to the case of a medium composed by odd-diffusive host particles, in order to investigate how this affect the transport properties of a tracer. Moreover, one could study the effect of oddness on the structural order and phase behavior of such an odd Gaussian-core fluid. Another potentially interesting direction is to analyse to which extent the transport properties of the odd tracer are modified upon variation of the correlation length of the fluctuating density field.

Appendix A

Appendix of Chapter 3

This Appendix contains the detailed derivation of the results presented in Chapter 3. In Sec. A.1 we show how to obtain the steady state-density of the center of mass of a dimer made of two active chiral particles with opposite torques in a medium characterized by an activity field with small gradients. The derivation is specialized to the cases of two distinct interaction potentials: harmonic bond with zero rest length and rigid bond interaction. In Secs. A.2 and A.3 we deal with single active chiral particles and single active particles under Lorentz force, respectively. In particular, we show how to integrate out the orientational degree of freedom to get an effective FPE for their density distribution, and we point out under which conditions their effective dynamics are equivalent. Finally, in Sec. A.4 we show how to derive the steady state density of a dimer made of two oppositely charged active particles subjected to a magnetic field. Also in this case we work under the assumption that the non-uniform activity field features small spatial variations on length scales given by the persistence length and the typical size of the dimer.

A.1 Dimer of active chiral particles

In this Section we present a detailed derivation of the coarse graining procedure outlined in Chapter 3 for the case of two interacting active chiral particles with opposite torque. As a first step, we rewrite the stochastic equation of motion given in Eq. (3.1) in terms of the center-of-mass $\boldsymbol{R} = (\boldsymbol{X}_0 + \boldsymbol{X}_1)/2$ and the relative distance $\boldsymbol{r} = \boldsymbol{X}_0 - \boldsymbol{X}_1$ between the two monomers. This reads:

$$\begin{aligned}
\dot{\boldsymbol{R}} &= \frac{1}{2}\left[v_a(\boldsymbol{R}+\boldsymbol{r}/2)\boldsymbol{n}_0 + v_a(\boldsymbol{R}-\boldsymbol{r}/2)\boldsymbol{n}_1\right] + \sqrt{D_T}\boldsymbol{\xi}_1(t)\,,\\
\dot{\boldsymbol{r}} &= 2\nu\boldsymbol{F} + \left[v_a(\boldsymbol{R}+\boldsymbol{r}/2)\boldsymbol{n}_0 - v_a(\boldsymbol{R}-\boldsymbol{r}/2)\boldsymbol{n}_1\right] + \sqrt{4D_T}\boldsymbol{\xi}_2(t)\,,\\
\dot{\theta}_i &= \omega_i + \sqrt{2D_R}\eta_i(t)\,,
\end{aligned} \tag{A.1}$$

where the force $\boldsymbol{F} = -\nabla U(\boldsymbol{r})$ will be later on specialized to the case of rigid bond interaction or harmonic interaction with zero rest length. Here, as in Chapter 3, the stochastic terms $\{\boldsymbol{\xi}_i\}$ and $\{\eta_i\}$ are independent zero-mean Gaussian white noises with unit variance. The evolution of the one-time joint probability density $P(\boldsymbol{R}, \boldsymbol{r}, \theta_0, \theta_1, t)$ associated to the stochastic dynamics (A.1) is given in Eqs. (3.3), (3.4) and (3.5) of Chapter 3. To marginalize out the orientational degrees of freedom $\{\boldsymbol{n}_i\}$, we follows the standard procedure (see e.g. Refs. [24, 103, 126]) of expanding the joint probability density in eigenfunctions of the rotational operator $\mathcal{R}^2$. As reported in Chapter 3, this leads to the following expansion:

$$\begin{aligned}
P(\boldsymbol{R}, \boldsymbol{r}, \theta_1, \theta_2, t) = \frac{1}{\Omega_2^2}\Big[&\phi + \boldsymbol{\sigma}_0\cdot\boldsymbol{n}_0 + \boldsymbol{\sigma}_1\cdot\boldsymbol{n}_1 + \boldsymbol{\Sigma}:\boldsymbol{n}_0\boldsymbol{n}_1\\
&+ \boldsymbol{w}_1 : \Big(\boldsymbol{n}_0\boldsymbol{n}_0 - \frac{\mathbf{1}}{2}\Big) + \boldsymbol{w}_2 : \Big(\boldsymbol{n}_1\boldsymbol{n}_1 - \frac{\mathbf{1}}{2}\Big) + \boldsymbol{\Upsilon}\Big]\,,
\end{aligned} \tag{A.2}$$

with $\boldsymbol{\Upsilon}$ denoting higher order terms. In particular, the first eigenfunction of the rotational operator $\mathcal{R}^2$ are given by 1, $\{\boldsymbol{n}_i\}$, $\boldsymbol{n}_0\boldsymbol{n}_1$, $\{\boldsymbol{n}_i\boldsymbol{n}_i - \mathbf{1}/d\}$. In the following we derive the evolution equation of the expansion coefficients ϕ, $\{\boldsymbol{\sigma}_i\}$, $\boldsymbol{\Sigma}$ and $\{\boldsymbol{w}_i\}$ by projecting the FPE (3.3) onto their relative eigenfunctions. To this aim, we first introduce the scalar product

$$\langle fg\rangle = \int_0^{2\pi} \mathrm{d}\theta_0 \int_0^{2\pi} \mathrm{d}\theta_1 f(\theta_0, \theta_1) g(\theta_0, \theta_1) \tag{A.3}$$

between two arbitrary functions f, g of the polar angles θ_0 and θ_1. Using the cartesian multipole expansion (A.2), we can easily derive the following set of identities

$$\begin{aligned}
\langle P\rangle &= \phi\,,\\
\langle n_i^\alpha P\rangle &= \sigma_i^\alpha/2\,,\\
\langle n_i^\alpha n_i^\beta P\rangle &= \delta_{\alpha\beta}\phi/2\,,\\
\langle n_0^\alpha n_1^\beta P\rangle &= \Sigma_{\alpha\beta}/4\,,\\
\langle \mathcal{R}^2 P\rangle &= 0\,,\\
\langle n_i^\alpha \mathcal{R}^2 P\rangle &= -\sigma_i^\alpha/2\,,\\
\langle n_0^\alpha n_1^\beta \mathcal{R}^2 P\rangle &= -\Sigma_{\alpha\beta}/2\,,
\end{aligned} \tag{A.4}$$

that will be extensively used in the coming derivation. In the above expressions, as in the rest of this Appendix, the particle labels are denoted by latin letters, while greek letters correspond to the spatial components. We remind here that all expansion coefficients ϕ, $\{\boldsymbol{\sigma}_i\}$, $\boldsymbol{\Sigma}$ and $\{\boldsymbol{w}_i\}$ are functions of the center-of-mass position $\boldsymbol{R}$, the relative distance $\boldsymbol{r}$ and the time t. In addition to the identities in (A.4), it is useful to introduce some further relations. The first one is the following scalar product:

$$\begin{aligned}\langle n_i^\alpha \partial_{\theta_i} P\rangle &= \int \mathrm{d}\theta_0\,\mathrm{d}\theta_1\, n_i^\alpha \partial_{\theta_i} P = -\int \mathrm{d}\theta_0\,\mathrm{d}\theta_1\, \left(\partial_{\theta_i} n_i^\alpha\right) P \\ &= -\sum_\beta \int \mathrm{d}\theta_0\,\mathrm{d}\theta_1\, U_{\alpha\beta} n_i^\beta P = -\frac{1}{2}\sum_\beta U_{\alpha\beta}\sigma_i^\beta\,,\end{aligned} \tag{A.5}$$

where in the first equality we used integration by parts, and in the second we introduced the matrix

$$\boldsymbol{U} = \begin{pmatrix} 0 & -1 \\ 1 & 0 \end{pmatrix} \tag{A.6}$$

to rewrite the derivative of the vector $\boldsymbol{n}_i$ with respect to the polar angle as $\partial_{\theta_i}\boldsymbol{n}_i = \boldsymbol{U}\cdot\boldsymbol{n}_i$. In the last equality we used Eq. (A.4). The second relation that we want to prove is:

$$\begin{aligned}\langle n_0^\alpha n_1^\beta \partial_{\theta_0} P\rangle &= -\int \mathrm{d}\theta_0\,\mathrm{d}\theta_1\, \left(\partial_{\theta_0} n_0^\alpha\right) n_1^\beta P = -\sum_\gamma U_{\alpha\gamma}\int \mathrm{d}\theta_0\,\mathrm{d}\theta_1\, n_0^\gamma n_1^\beta P \\ &= -\frac{1}{4}\sum_\gamma U_{\alpha\gamma}\Sigma_{\gamma\beta}\,,\end{aligned} \tag{A.7}$$

where, again, we used integration by parts and Eq. (A.4). Analogously one can derive

$$\langle n_0^\alpha n_1^\beta \partial_{\theta_1} P\rangle = -\frac{1}{4}\sum_\gamma \Sigma_{\alpha\gamma}U^T_{\gamma\beta}\,. \tag{A.8}$$

With the help of the equalities derived above, we are now in the position to obtain the evolution equation of the expansion coefficients. In doing that, we will introduce our first approximation. Since we are working under the assumption that the activity field is a slowly varying function of space, i.e., it is characterized by small gradients, we can neglect the contribution to the effective coarse grained dynamics coming from the quadrupole moments $\{\boldsymbol{w}_i\}$, namely the local nematic order parameters. This approximation is common and well described in, e.g., Refs. [24, 103, 126]. Analogously, we neglect all terms $\boldsymbol{\Upsilon}$ in the multipole expansion (A.2) which are of higher order than $\{\boldsymbol{w}_i\}$. For the moment, we keep in our multipole expansion the term proportional to $\boldsymbol{\Sigma}$, and we show explicitly that it also gives a negligible contribution in the framework of the small gradient approximation. The first evolution equation we derive is the one for the coefficient $\phi(\boldsymbol{R}, \boldsymbol{r}, t)$. This can be obtained by projecting the FPE (3.3) onto the trivial eigenfunction 1, namely by computing $\partial_t \langle P \rangle$. This gives:

$$\begin{aligned}\partial_t \phi = &- \nabla_{\boldsymbol{R}} \cdot \left[\frac{1}{4} v_a \Big(\boldsymbol{R} + \boldsymbol{r}/2 \Big) \boldsymbol{\sigma}_0 + \frac{1}{4} v_a \Big(\boldsymbol{R} - \boldsymbol{r}/2 \Big) \boldsymbol{\sigma}_1 - \frac{D_T}{2} \nabla_{\boldsymbol{R}} \phi \right] \\ &- \nabla_{\boldsymbol{r}} \cdot \left[2\nu \boldsymbol{F} \phi + v_a \Big(\boldsymbol{R} + \boldsymbol{r}/2 \Big) \frac{\boldsymbol{\sigma}_0}{2} - v_a \Big(\boldsymbol{R} - \boldsymbol{r}/2 \Big) \frac{\boldsymbol{\sigma}_1}{2} - 2D_T \nabla_{\boldsymbol{r}} \phi \right] ,\end{aligned} \tag{A.9}$$

where the dependence of ϕ and $\{\boldsymbol{\sigma}_i\}$ on ($\boldsymbol{R}$, $\boldsymbol{r}$, t) has been dropped for the sake of space. Interestingly, $\phi(\boldsymbol{R}, \boldsymbol{r}, t)$ evolves according to a continuity equation and it describes the probability density of finding the two active particles in the configuration with center-of-mass $\boldsymbol{R}$ and relative distance $\boldsymbol{r}$ at time t. Accordingly, if we integrate Eq. (A.9) over $\boldsymbol{r}$, i.e., we marginalize out the relative distance between the two active monomers, we get an effective continuity equation for the coarse grained density $\rho(\boldsymbol{R}, t)$ defined in Eq. (3.7). This reads:

$$\partial_t \rho(\boldsymbol{R}, t) = -\nabla_{\boldsymbol{R}} \cdot \Big[\boldsymbol{J}_{\boldsymbol{\sigma}_1} + \boldsymbol{J}_{\boldsymbol{\sigma}_2} + \boldsymbol{J}_D \Big] \tag{A.10}$$

where the fluxes $\boldsymbol{J}_{\boldsymbol{\sigma}_i}$ and $\boldsymbol{J}_D$ are defined as:

$$\begin{aligned}\boldsymbol{J}_{\boldsymbol{\sigma}_i}(\boldsymbol{R}, t) &= \frac{1}{4} \int \mathrm{d}\boldsymbol{r} \, v_a \Big(\boldsymbol{X}_i(\boldsymbol{R}, \boldsymbol{r}) \Big) \boldsymbol{\sigma}_i \, , \\ \boldsymbol{J}_D(\boldsymbol{R}, t) &= -\frac{D_T}{2} \nabla_{\boldsymbol{R}} \rho \, .\end{aligned} \tag{A.11}$$

The fluxes $\boldsymbol{J}_{\boldsymbol{\sigma}_i}$ derive from the activity of the two monomers, and in particular from their average polarization, whereas $\boldsymbol{J}_D$ is the usual diffusive flux due to thermal fluctuations. Being a probability density, the field $\rho(\boldsymbol{R}, t)$ is locally conserved throughout its dynamics, and therefore it relaxes very slowly when perturbed over large length scales. The dynamics of the average polarizations $\{\boldsymbol{\sigma}_i\}$ can be derived by projecting the FPE (3.3) onto the polarity vectors $\{\boldsymbol{n}_i\}$. In particular, for the particle with position $\boldsymbol{X}_0$, we get:

$$\begin{aligned}&\frac{1}{2} \partial_t \sigma_0^\alpha = \\ &- \partial_\beta \Big[\frac{1}{2} v_a \Big(\boldsymbol{R} + \frac{\boldsymbol{r}}{2} \Big) \langle n_0^\alpha n_0^\beta P \rangle + \frac{1}{2} v_a \Big(\boldsymbol{R} - \frac{\boldsymbol{r}}{2} \Big) \langle n_0^\alpha n_1^\beta P \rangle - \frac{D_T}{2} \partial_\beta \frac{\sigma_1^\alpha}{2} \Big] \\ &- \partial'_\beta \Big[2\nu F_\beta \frac{\sigma_0^\alpha}{2} + v_a \Big(\boldsymbol{R} + \frac{\boldsymbol{r}}{2} \Big) \langle n_0^\alpha n_0^\beta P \rangle - v_a \Big(\boldsymbol{R} - \frac{\boldsymbol{r}}{2} \Big) \langle n_0^\alpha n_1^\beta P \rangle - 2D_T \partial'_\beta \frac{\sigma_0^\alpha}{2} \Big] \\ &- \omega \langle n_0^\alpha \partial_{\theta_0} P \rangle + \omega \langle n_0^\alpha \partial_{\theta_1} P \rangle + D_R \langle n_0^\alpha \mathcal{R}^2 P \rangle \, ,\end{aligned} \tag{A.12}$$

where we denoted with ∂_α and ∂'_α the α-component of $\nabla_{\boldsymbol{R}}$ and $\nabla_{\boldsymbol{r}}$, respectively, and summation over repeated indices is implied. By using the identities in (A.4), we obtain the following dynamics in vector notation:

$$\begin{aligned}\partial_t \boldsymbol{\sigma}_0 = &- \nabla_{\boldsymbol{R}} \cdot \Big[\frac{1}{2} v_a\Big(\boldsymbol{R} + \frac{\boldsymbol{r}}{2}\Big)\phi \mathbf{1} + \frac{1}{4} v_a\Big(\boldsymbol{R} - \frac{\boldsymbol{r}}{2}\Big)\boldsymbol{\Sigma}^T - \frac{D_T}{2}\nabla_{\boldsymbol{R}}\boldsymbol{\sigma}_0\Big] \\ &- \nabla_{\boldsymbol{r}} \cdot \Big[2\nu \boldsymbol{F}\boldsymbol{\sigma}_0 + v_a\Big(\boldsymbol{R} + \frac{\boldsymbol{r}}{2}\Big)\phi\mathbf{1} - \frac{1}{2} v_a\Big(\boldsymbol{R} - \frac{\boldsymbol{r}}{2}\Big)\boldsymbol{\Sigma}^T - 2D_T \nabla_{\boldsymbol{r}}\boldsymbol{\sigma}_0\Big] \\ &- \left(D_R \mathbf{1} - \omega \boldsymbol{U}\right)\boldsymbol{\sigma}_0 \,. \end{aligned} \tag{A.13}$$

Importantly, note that because of its evolution due to rotational diffusion and active torque, the average polarization $\boldsymbol{\sigma}_0$ does not evolve according to a continuity equation, as can be evinced by the presence of the sink term in the last line. This implies that the average polarity of the particles typically relax much faster than the coarse grained density $\rho(\boldsymbol{R}, t)$. Due to this time scale separation, we can approximate the polarization field $\boldsymbol{\sigma}_0(\boldsymbol{R}, \boldsymbol{r}, t)$ with its quasi-stationary expression:

$$\begin{aligned}&\boldsymbol{\sigma}_0 = \\ &- \left(D_R\mathbf{1} - \omega\boldsymbol{U}\right)^{-1} \cdot \Big\{\nabla_{\boldsymbol{R}} \cdot \Big[\frac{1}{2} v_a\Big(\boldsymbol{R} + \frac{\boldsymbol{r}}{2}\Big)\phi\mathbf{1} + \frac{1}{4} v_a\Big(\boldsymbol{R} - \frac{\boldsymbol{r}}{2}\Big)\boldsymbol{\Sigma}^T - \frac{D_T}{2}\nabla_{\boldsymbol{R}}\boldsymbol{\sigma}_0\Big] \\ &+ \nabla_{\boldsymbol{r}} \cdot \Big[2\nu\boldsymbol{F}\boldsymbol{\sigma}_0 + v_a\Big(\boldsymbol{R} + \frac{\boldsymbol{r}}{2}\Big)\phi\mathbf{1} - \frac{1}{2} v_a\Big(\boldsymbol{R} - \frac{\boldsymbol{r}}{2}\Big)\boldsymbol{\Sigma}^T - 2D_T\nabla_{\boldsymbol{r}}\boldsymbol{\sigma}_0\Big]\Big\} \,. \end{aligned} \tag{A.14}$$

Naturally, an analogous expression can be derived for the average polarization of the particle with position $\boldsymbol{X}_1$, and it is given by:

$$\begin{aligned}&\boldsymbol{\sigma}_1 = \\ &- \left(D_R\mathbf{1} + \omega\boldsymbol{U}\right)^{-1} \cdot \Big\{\nabla_{\boldsymbol{R}} \cdot \Big[\frac{1}{2} v_a\Big(\boldsymbol{R} - \frac{\boldsymbol{r}}{2}\Big)\phi\mathbf{1} + \frac{1}{4} v_a\Big(\boldsymbol{R} + \frac{\boldsymbol{r}}{2}\Big)\boldsymbol{\Sigma} - \frac{D_T}{2}\nabla_{\boldsymbol{R}}\boldsymbol{\sigma}_1\Big] \\ &+ \nabla_{\boldsymbol{r}} \cdot \Big[2\nu\boldsymbol{F}\boldsymbol{\sigma}_1 - v_a\Big(\boldsymbol{R} - \frac{\boldsymbol{r}}{2}\Big)\phi\mathbf{1} + \frac{1}{2} v_a\Big(\boldsymbol{R} + \frac{\boldsymbol{r}}{2}\Big)\boldsymbol{\Sigma} - 2D_T\nabla_{\boldsymbol{r}}\boldsymbol{\sigma}_1\Big]\Big\} \,. \end{aligned} \tag{A.15}$$

Finally, we can obtain the evolution equation for the tensor $\boldsymbol{\Sigma}$ by projecting the FPE (3.3) onto the dyadic product $\boldsymbol{n}_0\boldsymbol{n}_1$. The dynamics of its components is given by:

$$\begin{aligned}\frac{1}{4}\partial_t \Sigma_{\alpha\beta} = &-\partial_\gamma \Big[\frac{1}{2} v_a(\boldsymbol{X}_0)\langle n_0^\alpha n_1^\beta n_0^\gamma P\rangle + \frac{1}{2} v_a(\boldsymbol{X}_1)\langle n_0^\alpha n_1^\beta n_1^\gamma P\rangle - \frac{D_T}{2}\partial_\gamma \frac{\Sigma_{\alpha\beta}}{4}\Big] \\ &- \partial'_\gamma \Big[2\nu F_\gamma \frac{\Sigma_{\alpha\beta}}{4} + v_a(\boldsymbol{X}_0)\langle n_0^\alpha n_1^\beta n_0^\gamma P\rangle - v_a(\boldsymbol{X}_1)\langle n_0^\alpha n_1^\beta n_1^\gamma P\rangle - 2D_T\partial'_\gamma \frac{\Sigma_{\alpha,\beta}}{4}\Big] \\ &- \omega\langle n_0^\alpha n_1^\beta \partial_{\theta_0} P\rangle + \omega\langle n_0^\alpha n_1^\beta \partial_{\theta_1} P\rangle + D_R\langle n_0^\alpha n_1^\beta \mathcal{R}^2 P\rangle \end{aligned} \tag{A.16}$$

where again the summation over repeated indices is implied, and the position variables have to be interpreted as functions of $\boldsymbol{R}$ and $\boldsymbol{r}$. In this case, together with the identities in Eqs. (A.4), (A.5), (A.7) and (A.8) we also need to separately compute the scalar products

$$\begin{aligned}\langle n_0^\alpha n_1^\beta n_0^\gamma P\rangle &= \frac{1}{\Omega_2^2}\sum_\delta \sigma_1^\delta \langle n_0^\alpha n_1^\beta n_0^\gamma n_1^\delta\rangle = \frac{1}{4}\sigma_1^\beta \delta_{\alpha\gamma}\,,\\ \langle n_0^\alpha n_1^\beta n_1^\gamma P\rangle &= \frac{1}{\Omega_2^2}\sum_\delta \sigma_0^\delta \langle n_0^\alpha n_1^\beta n_1^\gamma n_0^\delta\rangle = \frac{1}{4}\sigma_0^\alpha \delta_{\beta\gamma}\,.\end{aligned} \tag{A.17}$$

In this way, by substituting all the scalar products in Eq. (A.16) we obtain:

$$\begin{aligned}\partial_t \Sigma_{\alpha\beta} = &-\partial_\gamma\left[\frac{1}{2}v_a\Big(\boldsymbol{R}+\frac{\boldsymbol{r}}{2}\Big)\sigma_1^\beta\delta_{\alpha\gamma} + \frac{1}{2}v_a\Big(\boldsymbol{R}-\frac{\boldsymbol{r}}{2}\Big)\sigma_0^\alpha\delta_{\beta\gamma} - \frac{D_T}{2}\partial_\gamma\Sigma_{\alpha\beta}\right]\\ &-\partial'_\gamma\left[2\nu F_\gamma\Sigma_{\alpha\beta} + v_a\Big(\boldsymbol{R}+\frac{\boldsymbol{r}}{2}\Big)\sigma_1^\beta\delta_{\alpha\gamma} - v_a\Big(\boldsymbol{R}-\frac{\boldsymbol{r}}{2}\Big)\sigma_0^\alpha\delta_{\beta\gamma} - 2D_T\partial'_\gamma\Sigma_{\alpha\beta}\right]\\ &+\omega U_{\alpha\gamma}\Sigma_{\gamma\beta} - \omega U_{\beta\gamma}\Sigma_{\alpha\gamma} - 2D_R\Sigma_{\alpha\beta}\,.\end{aligned} \tag{A.18}$$

As in the case of the average polarizations $\{\boldsymbol{\sigma}_i\}$, also the expansion coefficient $\boldsymbol{\Sigma}$ does not obey any conservation law, and relaxes much faster compared to the density $\rho(\boldsymbol{R},t)$. Considering its quasi-stationary configuration and combining with Eqs. (A.10), (A.14) and (A.15), it can be shown that it contributes to the flux (A.11) as a term of order $\mathcal{O}(\nabla_{\boldsymbol{R}}^2)$, and thus can be neglected if we truncate the effective dynamics (A.10) to the drift/diffusion order. For this reason, we drop the $\boldsymbol{\Sigma}$-dependent contributions to the quasi-stationary expressions of the average polarizations (A.14) and (A.15). In this way, we close the hierarchy of equations for the expansion coefficients and we reduce it to the three coupled differential equations for the fields $\rho(\boldsymbol{R},t)$ and $\{\boldsymbol{\sigma}_i(\boldsymbol{R},t)\}$. These are solved in the framework of the small gradient approximation. By combining Eqs. (A.11), (A.14) and (A.15), we can derive the expression of the fluxes in the effective dynamics (A.10). For example, for the flux $\boldsymbol{J}_{\boldsymbol{\sigma}_0}(\boldsymbol{R},t)$ we have:

$$\begin{aligned}\boldsymbol{J}_{\boldsymbol{\sigma}_0} = \frac{1}{4}\int \mathrm{d}\boldsymbol{r}\, v_a(\boldsymbol{X}_0)\boldsymbol{\sigma}_0 = -\frac{1}{4}\int \mathrm{d}\boldsymbol{r}\, v_a(\boldsymbol{X}_0)\\ \times\left(D_R\boldsymbol{1}-\omega\boldsymbol{U}\right)^{-1}\cdot\left\{\nabla_{\boldsymbol{R}}\cdot\left[\frac{1}{2}v_a(\boldsymbol{X}_0)\phi\boldsymbol{1}\right] + \nabla_{\boldsymbol{r}}\cdot\left[2\nu\boldsymbol{F}\boldsymbol{\sigma}_0 + v_a(\boldsymbol{X}_0)\phi\boldsymbol{1}\right]\right\}\,,\end{aligned} \tag{A.19}$$

where we neglected all terms leading to corrections of order $\mathcal{O}(\nabla_{\boldsymbol{R}}^2)$ or higher. Integrating by parts and using the identity $\nabla_{\boldsymbol{r}} = \frac{1}{2}\nabla_{\boldsymbol{R}} v_a(\boldsymbol{X}_0)$, we can separate the flux $\boldsymbol{J}_{\boldsymbol{\sigma}_0}$ into the sum of three contributions:

$$\begin{aligned}\boldsymbol{J}_{\boldsymbol{\sigma}_0} =& - \left(D_R\mathbf{1} - \omega\boldsymbol{U}\right)^{-1} \cdot \int \mathrm{d}\boldsymbol{r}\, \frac{1}{8} v_a(\boldsymbol{X}_0) \nabla_{\boldsymbol{R}} \cdot \Big[v_a(\boldsymbol{X}_0)\phi\mathbf{1}\Big] \\ &+ \left(D_R\mathbf{1} - \omega\boldsymbol{U}\right)^{-1} \cdot \int \mathrm{d}\boldsymbol{r}\, \frac{1}{8} \left[\nabla_{\boldsymbol{R}} v_a(\boldsymbol{X}_0)\right] v_a(\boldsymbol{X}_0)\phi \\ &+ \left(D_R\mathbf{1} - \omega\boldsymbol{U}\right)^{-1} \cdot \int \mathrm{d}\boldsymbol{r}\, \frac{\nu}{4} \left[\nabla_{\boldsymbol{R}} v_a(\boldsymbol{X}_0)\right] \cdot \boldsymbol{F}\boldsymbol{\sigma}_0\,,\end{aligned} \tag{A.20}$$

where the last integral still depends on the polarization field $\boldsymbol{\sigma}_0$. We call such integral $\boldsymbol{I}_0$, and we separately work it out in the following. In particular, by substituting again the quasi-static expression of $\boldsymbol{\sigma}_0$ into Eq. (A.20) and neglecting contributions of order $\mathcal{O}(\nabla^2_{\boldsymbol{R}})$ or higher, we get:

$$\begin{aligned}\boldsymbol{I}_0 &= \int \mathrm{d}\boldsymbol{r}\, \frac{\nu}{4} \left[\nabla_{\boldsymbol{R}} v_a(\boldsymbol{X}_0) \cdot \boldsymbol{F}\right] \boldsymbol{\sigma}_0 \\ &= -\frac{\nu}{4} \left(D_R\mathbf{1} - \omega\boldsymbol{U}\right)^{-1} \int \mathrm{d}\boldsymbol{r}\, \left[\nabla_{\boldsymbol{R}} v_a(\boldsymbol{X}_0) \cdot \boldsymbol{F}\right] \nabla_{\boldsymbol{r}} \cdot \Big[2\nu\boldsymbol{F}\boldsymbol{\sigma}_0 + v_a(\boldsymbol{X}_0)\phi\mathbf{1}\Big] \\ &= +\frac{\nu}{4} \left(D_R\mathbf{1} - \omega\boldsymbol{U}\right)^{-1} \int \mathrm{d}\boldsymbol{r}\, \nabla_{\boldsymbol{r}} \left[\nabla_{\boldsymbol{R}} v_a(\boldsymbol{X}_0) \cdot \boldsymbol{F}\right] \cdot \Big[2\nu\boldsymbol{F}\boldsymbol{\sigma}_0 + v_a(\boldsymbol{X}_0)\phi\mathbf{1}\Big] \\ &= +\frac{\nu}{4} \left(D_R\mathbf{1} - \omega\boldsymbol{U}\right)^{-1} \int \mathrm{d}\boldsymbol{r}\, \left[(\nabla_{\boldsymbol{r}}\boldsymbol{F}) \cdot \nabla_{\boldsymbol{R}} v_a(\boldsymbol{X}_0)\right] \cdot \Big[2\nu\boldsymbol{F}\boldsymbol{\sigma}_0 + v_a(\boldsymbol{X}_0)\phi\mathbf{1}\Big]\,,\end{aligned} \tag{A.21}$$

where we used integration by parts and in the last equality we neglected the term $\nabla_{\boldsymbol{r}}\nabla_{\boldsymbol{R}} v_a(\boldsymbol{X}_0) = \mathcal{O}(\nabla^2_{\boldsymbol{R}})$. In the following we consider the case of harmonic interaction potential with zero rest length and stiffness κ (for the case of rigid bond interaction see the Sec. A.1.1). In this case we have $\nabla_{\boldsymbol{r}}\boldsymbol{F} = -\kappa\mathbf{1}$, implying:

$$\begin{aligned}\boldsymbol{I}_0 &= -\frac{\kappa\nu}{4} \left(D_R\mathbf{1} - \omega\boldsymbol{U}\right)^{-1} \cdot \int \mathrm{d}\boldsymbol{r}\, \left[\nabla_{\boldsymbol{R}} v_a(\boldsymbol{X}_0)\right] \cdot \Big[2\nu\boldsymbol{F}\boldsymbol{\sigma}_0 + v_a(\boldsymbol{X}_0)\phi\mathbf{1}\Big] \\ &= -2\kappa\nu \left(D_R\mathbf{1} - \omega\boldsymbol{U}\right)^{-1} \cdot \left[\boldsymbol{I}_0 + \frac{1}{8} \int \mathrm{d}\boldsymbol{r}\, v_a(\boldsymbol{X}_0)\phi\nabla_{\boldsymbol{R}} v_a(\boldsymbol{X}_0)\right]\,.\end{aligned} \tag{A.22}$$

Solving for $\boldsymbol{I}_0$ we get:

$$\boldsymbol{I}_0 = -\frac{1}{8} \left[(1+\tau)\,\mathbf{1} - \Omega\tau\boldsymbol{U}\right]^{-1} \cdot \int \mathrm{d}\boldsymbol{r}\, v_a(\boldsymbol{X}_0)\phi\nabla_{\boldsymbol{R}} v_a(\boldsymbol{X}_0)\,, \tag{A.23}$$

where we introduced the dimensionless quantities $\tau = D_R/2\kappa\nu$ and $\Omega = \omega/D_R$ as in Chapter 3. The value of the integral $\boldsymbol{I}_0$ can then be substituted into Eq. (A.20). To compute the remaining integrals in Eq. (A.20) we make use once again of the small gradient approximation. Indeed, under this assumption, the activity field does not vary much on a typical length scale given by the distance between the active monomers. For this reason, we approximate the joint density as $\phi(\boldsymbol{R}, \boldsymbol{r}, t) \approx \rho(\boldsymbol{R}, t)\delta^d(\boldsymbol{r})$ inside the integrals, thus obtaining:

$$\boldsymbol{J}_{\boldsymbol{\sigma}_0} = \left(D_R \mathbf{1} - \omega \boldsymbol{U}\right)^{-1} \left[-\frac{v_a^2(\boldsymbol{R})}{8} \nabla \rho(\boldsymbol{R}) - \frac{\rho(\boldsymbol{R})}{16} \left[\left(1+\tau\right) \mathbf{1} - \Omega \tau \boldsymbol{U}\right]^{-1} \nabla v_a^2(\boldsymbol{R})\right] . \tag{A.24}$$

From the previous equation it appears that the activity field produces both an advective and a diffusive flux in the effective dynamics for the coarse grained density ρ. Following a similar derivation to the one presented for $\boldsymbol{J}_{\boldsymbol{\sigma}_0}$, we can work out the expression of the other flux:

$$\boldsymbol{J}_{\boldsymbol{\sigma}_1} = \left(D_R \mathbf{1} + \omega \boldsymbol{U}\right)^{-1} \left[-\frac{v_a^2(\boldsymbol{R})}{8} \nabla \rho(\boldsymbol{R}) - \frac{\rho(\boldsymbol{R})}{16} \left[\left(1+\tau\right) \mathbf{1} + \Omega \tau \boldsymbol{U}\right]^{-1} \nabla v_a^2(\boldsymbol{R})\right] . \tag{A.25}$$

From Eqs. (A.24) and (A.25) we see that the diffusive contribution to the fluxes $\boldsymbol{J}_{\boldsymbol{\sigma}_0}$ and $\boldsymbol{J}_{\boldsymbol{\sigma}_1}$ is not aligned with the density gradient due to the presence of the active torque ω. However, since the two polarities $\{\boldsymbol{n}_i\}$ rotate in opposite directions, the total flux is actually aligned with $\nabla \rho$, and therefore the center-of-mass does not feature a chiral motion. Indeed, with the help of the identities:

$$\sum_{\delta = \pm 1} \left(D_R \mathbf{1} + \delta \omega \boldsymbol{U}\right)^{-1} = \frac{2}{D_R} \frac{1}{1+\Omega^2} \mathbf{1} \tag{A.26}$$

and

$$\begin{aligned} &\sum_{\delta = \pm 1} \left(D_R \mathbf{1} + \delta \omega \boldsymbol{U}\right)^{-1} \left[\left(1+\tau\right) \mathbf{1} + \delta \Omega \tau \boldsymbol{U}\right]^{-1} \\ &= \frac{\frac{2}{D_R}\left[\left(1+\tau\right) - \Omega^2 \tau\right] \mathbf{1}}{\left[\left(1+\tau\right) - \Omega^2 \tau\right]^2 + \left[\Omega\left(1+\tau\right) + \Omega \tau\right]^2} , \end{aligned} \tag{A.27}$$

one can derive the total flux $\boldsymbol{J}_{\boldsymbol{\sigma}_0} + \boldsymbol{J}_{\boldsymbol{\sigma}_1} + \boldsymbol{J}_D$, obtaining the effective drift and diffusion terms reported in Eq. (3.9) of Chapter 3.

A.1.1 Case of rigid bond

In Chapter 3 we commented on the fact that the chemotactic transition relies on the soft interaction between the active monomers, allowing their typical distance to assume different values throughout the cycle described in Figure 3.1. In particular, we have claimed that the transition would disappear if the two monomers were connected by a rigid bond. We provide here a rigorous derivation of this statement by computing the chemotactic coupling ϵ in the case of rigid bond interaction. To this aim, we specialized the derivation presented in

Sec. A.1 to the interaction potential $U(\boldsymbol{r}) = \kappa(|\boldsymbol{r}| - l_0)^2/2$, where l_0 is the bond length. We will then take a posteriori the limit $\kappa \to \infty$. With the new interaction potential, we need to recompute the integral $\boldsymbol{I}_0$ defined in Eq. (A.21). To this aim we introduce the symmetric matrix $\boldsymbol{A} = \hat{\boldsymbol{r}}\hat{\boldsymbol{r}} + (\mathbf{1} - \hat{\boldsymbol{r}}\hat{\boldsymbol{r}})\,(1 - l_0/|\boldsymbol{r}|)$, where $\hat{\boldsymbol{r}}$ denotes the unit vector in the direction of the relative distance $\boldsymbol{r}$. The matrix $\boldsymbol{A}$ satisfies the identity $\nabla\boldsymbol{F} = -\kappa\boldsymbol{A}$. In this way we obtain:

$$\begin{aligned}
\boldsymbol{I}_0 &= \int \mathrm{d}\boldsymbol{r}\, \frac{\nu}{4}\left[\nabla_{\boldsymbol{R}} v_a(\boldsymbol{X}_0) \cdot \boldsymbol{F}\right] \boldsymbol{\sigma}_0 \\
&= \frac{\nu}{4}\left(D_R\mathbf{1} - \omega\boldsymbol{U}\right)^{-1} \int \mathrm{d}\boldsymbol{r}\, \left[\nabla_{\boldsymbol{R}} v_a(\boldsymbol{X}_0) \cdot (\nabla_{\boldsymbol{r}}\boldsymbol{F})\right] \cdot \Big[2\nu\boldsymbol{F}\boldsymbol{\sigma}_0 + v_a(\boldsymbol{X}_0)\phi\mathbf{1}\Big] = \\
&= \left(D_R\mathbf{1} - \omega\boldsymbol{U}\right)^{-1} \left[-2\kappa\nu\boldsymbol{I}_1 - \frac{\kappa\nu}{4}\int \mathrm{d}\boldsymbol{r}\, \nabla_{\boldsymbol{R}} v_a(\boldsymbol{X}_0) \cdot \boldsymbol{A}\, v_a(\boldsymbol{X}_0)\phi\right] = \\
&= -\frac{1}{8}\left[(1+\tau)\,\mathbf{1} - \Omega\tau\boldsymbol{U}\right]^{-1} \int \mathrm{d}\boldsymbol{r}\, v_a(\boldsymbol{X}_0)\phi\nabla_{\boldsymbol{R}} v_a(\boldsymbol{X}_0) \cdot \boldsymbol{A}\,,
\end{aligned} \tag{A.28}$$

where the dimensionless quantities $\tau = D_R/2\kappa\nu$ and $\Omega = \omega/D_R$ are defined as in Sec. A.1 and Chapter 3. Substituting the integral $\boldsymbol{I}_0$ into Eq. (A.20) we get:

$$\begin{aligned}
\boldsymbol{J}_{\boldsymbol{\sigma}_0} =& -\left(D_R\mathbf{1} - \omega\boldsymbol{U}\right)^{-1} \int \mathrm{d}\boldsymbol{r}\, \frac{1}{8} v_a\left(\boldsymbol{R}\right) \nabla_{\boldsymbol{R}} \cdot \Big[v_a\left(\boldsymbol{R}\right)\phi\mathbf{1}\Big] \\
&+ \left(D_R\mathbf{1} - \omega\boldsymbol{U}\right)^{-1} \int \mathrm{d}\boldsymbol{r}\, \frac{1}{8}\left[\nabla_{\boldsymbol{R}} v_a\left(\boldsymbol{R}\right)\right] v_a\left(\boldsymbol{R}\right)\phi + \\
&- \left(D_R\mathbf{1} - \omega\boldsymbol{U}\right)^{-1}\left[(1+\tau)\,\mathbf{1} - \Omega\tau\boldsymbol{U}\right]^{-1} \int \mathrm{d}\boldsymbol{r}\, \frac{1}{8} v_a\left(\boldsymbol{R}\right)\phi\nabla_{\boldsymbol{R}} v_a\left(\boldsymbol{R}\right) \cdot \boldsymbol{A}\,,
\end{aligned} \tag{A.29}$$

where the argument of the activity field has been approximated with the center-of-mass up to corrections of order $\mathcal{O}(\nabla^2_{\boldsymbol{R}})$. In the spirit of the small gradient assumption, we introduce another approximation in the integrals appearing in Eq. (A.29): since the variations of the activity field are small on the length scale given by the bond length l_0, we use $\phi(\boldsymbol{R}, \boldsymbol{r}, t) \approx \rho(\boldsymbol{R}, t)\delta\left(|\boldsymbol{r}| - l_0\right) 1/2\pi l_0$. Furthermore, in the rigid bond limit $\kappa \to \infty$, we have that:

$$\lim_{\kappa\to\infty}\left[(1+\tau)\,\mathbf{1} - \Omega\tau\boldsymbol{U}\right]^{-1} = \mathbf{1}\,. \tag{A.30}$$

With the previous approximations, the flux $\boldsymbol{J}_{\boldsymbol{\sigma}_0}$ reads:

$$\boldsymbol{J}_{\boldsymbol{\sigma}_0} = \left(D_R\mathbf{1} - \omega\boldsymbol{U}\right)^{-1}\Big\{-\frac{1}{8}v_a^2\left(\boldsymbol{R}\right)\nabla_{\boldsymbol{R}}\rho(\boldsymbol{R}) - \frac{1}{32}\rho(\boldsymbol{R})\nabla_{\boldsymbol{R}} v_a^2\left(\boldsymbol{R}\right)\Big\}. \tag{A.31}$$

An analogous expression can be obtained for $\boldsymbol{J}_{\boldsymbol{\sigma}_1}$, by simply sending $\omega \to -\omega$. Also in this case, we realize that the center-of-mass does not exhibit a chiral motion and its diffusive flux is aligned with the density gradient $\nabla\rho$ (this is expected as the two active particles have opposite chiralities). This can be seen by using Eq. (A.26) to compute the total flux $\boldsymbol{J}_{\boldsymbol{\sigma}_0} + \boldsymbol{J}_{\boldsymbol{\sigma}_1} + \boldsymbol{J}_D$. In this case, we obtain that the effective dynamics (A.10) of the coarse grained density ρ is characterized by the following drift and diffusion terms:

$$\begin{aligned} D(\boldsymbol{R}) &= \frac{1}{4D_R}\frac{1}{1+\Omega^2}v_a^2(\boldsymbol{R}) + \frac{D_T}{2}\,, \\ \boldsymbol{V}(\boldsymbol{R}) &= (1-\epsilon/2)\nabla_R D(\boldsymbol{R})\,, \end{aligned} \tag{A.32}$$

with the chemotactic coupling $\epsilon = 1/2$ that does not depend on the torque Ω as in Sec. A.1 and it is always positive. This implies that no chemotactic regime can be explored by a rigid dimer of this type.

A.2 Single active chiral particle

In this Section we derive the effective FPE of a single active chiral particle by marginalizing out its orientational degree of freedom. We start from the overdamped Langevin dynamics

$$\begin{cases} \dot{\boldsymbol{X}} = v_a(\boldsymbol{X})\boldsymbol{n}(\theta) + \sqrt{2D_T}\boldsymbol{\xi}(t) \\ \dot{\theta} = \omega(\boldsymbol{X}) + \sqrt{2D_R}\eta(t) \end{cases} \tag{A.33}$$

in the general case where both the activity field $v_a^C(\boldsymbol{X})$ and the active torque $\omega(\boldsymbol{X})$ are non-homogeneous functions of space. The self propulsion force is directed along the orientation vector $\boldsymbol{n}(\theta) = (\cos\theta, \sin\theta)$, and $\boldsymbol{\xi}(t)$, $\eta(t)$ are independent zero-mean Gaussian white noises with unit variance. Since the dynamics (A.33) is Markovian, the 1-time joint probability density $P(\boldsymbol{x}, \theta, t)$ evolves according to the following FPE:

$$\partial_t P(\boldsymbol{x},\theta,t) = -\nabla\cdot\left[v_a(\boldsymbol{x})\boldsymbol{n}(\theta)P - D_T\nabla P\right] - \partial_\theta\left[\omega(\boldsymbol{x})P\right] + D_R\partial_\theta^2 P\,. \tag{A.34}$$

To integrate out the rotational degree of freedom we expand the probability density in eigenfunctions of the operator ∂_θ^2 (as detailed in Sec. A.1). This leads to the cartesian multipole expansion:

$$P(\boldsymbol{x},\theta,t) = \frac{1}{\Omega_2}\left[\rho(\boldsymbol{x},t) + \boldsymbol{\sigma}(\boldsymbol{x},t)\cdot\boldsymbol{n} + \boldsymbol{w}(\boldsymbol{x},t) : (\boldsymbol{n}\boldsymbol{n} - \boldsymbol{1}/2) + \boldsymbol{\Upsilon}\right]\,, \tag{A.35}$$

with $\boldsymbol{\Upsilon}$ denoting higher order terms. Then we project Eq. (A.34) onto the eigenfunctions of ∂_θ^2. This procedure leads to a hierarchy of equations for the coefficients of the multipole expansion. The first two reads:

$$\begin{aligned}
\partial_t\rho(\boldsymbol{x},t) &= -\nabla\cdot\left[\frac{1}{2}v_a(\boldsymbol{x})\boldsymbol{\sigma} - D_T\nabla\rho\right],\\
\partial_t\boldsymbol{\sigma}(\boldsymbol{x},t) &= -\nabla\left[v_a(\boldsymbol{x})\rho\right] - \frac{1}{2}\nabla\cdot\left[v_a(\boldsymbol{x})\boldsymbol{w}\right] + D_T\nabla^2\boldsymbol{\sigma} - \left(D_R\mathbf{1} - \omega(\boldsymbol{x})\boldsymbol{U}\right)\boldsymbol{\sigma}\,,
\end{aligned} \tag{A.36}$$

with the anti-symmetric matrix $\boldsymbol{U}$ already defined in (A.6). Considering that $\boldsymbol{\sigma}(\boldsymbol{r},t)$ relaxes on a much smaller time scale than $\rho(\boldsymbol{r},t)$ and neglecting all terms proportional to $\mathcal{O}(\nabla^2)$ or higher order derivatives (small gradient approximation), we get:

$$\begin{aligned}
\partial_t\rho(\boldsymbol{x},t) &= -\nabla\cdot\left[\frac{1}{2}v_a(\boldsymbol{x})\boldsymbol{\sigma} - D_T\nabla\rho\right]\\
\boldsymbol{\sigma}(\boldsymbol{x},t) &= -\left(D_R\mathbf{1} - \omega(\boldsymbol{x})\boldsymbol{U}\right)^{-1}\nabla\left[v_a(\boldsymbol{x})\rho\right]
\end{aligned} \tag{A.37}$$

After defining the dimensionless parameter $\Omega(\boldsymbol{x}) = \omega(\boldsymbol{x})/D_R$, the matrix $\boldsymbol{M} = (\mathbf{1} - \Omega(\boldsymbol{x})\boldsymbol{U})$ and substituting the quasi-static expression of $\boldsymbol{\sigma}$ in the equation for the density ρ, we obtain the effective FPE

$$\partial_t\rho(\boldsymbol{x}) = -\nabla\cdot\left[\boldsymbol{V}^C(\boldsymbol{x})\rho(\boldsymbol{x}) - \boldsymbol{D}^C(\boldsymbol{x})\cdot\nabla\rho(\boldsymbol{x})\right] \tag{A.38}$$

characterized by the following drift and diffusion terms:

$$\begin{aligned}
\boldsymbol{V}^C(\boldsymbol{x}) &= -\frac{v_a(\boldsymbol{x})}{2D_R}\boldsymbol{M}^{-1}\nabla v_a(\boldsymbol{x})\,,\\
\boldsymbol{D}^C(\boldsymbol{x}) &= \frac{v_a^2(\boldsymbol{x})}{2D_R}\boldsymbol{M}^{-1} + D_T\mathbf{1}\,.
\end{aligned} \tag{A.39}$$

The odd-diffusive behavior of the active chiral particle is evident from the structure of its diffusion tensor, which contains off-diagonal elements with opposite sign.

A.3 Active particle under Lorentz force

An analogous derivation can be done for a single active charged particle subjected to a magnetic field. In $d = 2$ dimensions, its stochastic equation of motion reads:

$$\begin{cases}
\dot{\boldsymbol{X}} = \boldsymbol{v}\,,\\
m\dot{\boldsymbol{v}} = -\nu^{-1}\boldsymbol{\Gamma}\boldsymbol{v} + v_a(\boldsymbol{X})\boldsymbol{n}(\theta) + \sqrt{2T/\nu}\boldsymbol{\xi}\,,\\
\dot{\theta} = \sqrt{2D_R}\eta(t)\,,
\end{cases} \tag{A.40}$$

where m is the mass of the particle, $\boldsymbol{v}$ its velocity, and the effect of the magnetic field (which in full generality we take as possibly non-homogeneous in space) is included in the friction tensor

$$\boldsymbol{\Gamma} = \begin{pmatrix} 1 & -\kappa(\boldsymbol{r}) \\ \kappa(\boldsymbol{r}) & 1 \end{pmatrix} \tag{A.41}$$

characterized by anti-symmetric components proportional to the dimensionless oddness parameter $\kappa(\boldsymbol{r}) = qB(\boldsymbol{x})\nu$. As in the previous Section, we start our analysis from the FPE in the small mass limit (see, e.g., Refs. [116, 332] and the introductory Sec. 2.10):

$$\partial_t P(\boldsymbol{x}, \theta, t) = -\nabla \cdot \Big[\boldsymbol{\Gamma}^{-1}(\boldsymbol{x}) v_a(\boldsymbol{x}) \boldsymbol{n} P - D_T \boldsymbol{\Gamma}^{-1}(\boldsymbol{x}) \nabla P\Big] + D_R \partial_\theta^2 P, \tag{A.42}$$

and we derive the effective evolution equation for the density $\rho(\boldsymbol{x}, t)$ under the assumption of slowly varying activity field. Using again the decomposition in (A.35) and projecting (A.42) onto the eigenfunctions of ∂_θ^2 analogously to the previous Section, we obtain the following equations for the density ρ and the average polarization $\boldsymbol{\sigma}$:

$$\begin{aligned} \partial_t \rho(\boldsymbol{x}, t) &= -\nabla \cdot \left[\frac{v_a(\boldsymbol{x})}{2} \boldsymbol{\Gamma}^{-1} \boldsymbol{\sigma}(\boldsymbol{x}) - D_T \boldsymbol{\Gamma}^{-1} \nabla \rho(\boldsymbol{x})\right] \\ \partial_t \boldsymbol{\sigma}(\boldsymbol{x}, t) &= -\nabla \cdot \left[v_a(\boldsymbol{x}) \rho(\boldsymbol{x}) \boldsymbol{\Gamma}^{-1} - D_T \boldsymbol{\Gamma}^{-1} \nabla \boldsymbol{\sigma}(\boldsymbol{x})\right] - D_R \boldsymbol{\sigma}(\boldsymbol{x}) \end{aligned} \tag{A.43}$$

where all terms proportional to the quadrupole moment $\boldsymbol{w}$ have already been neglected. The equation for the average polarization can be further simplified considering that $\boldsymbol{\sigma}(\boldsymbol{r})$ relaxes on a much smaller time scale than $\rho(\boldsymbol{r})$ and that spatial gradients in the system are small. In particular, this leads to the quasi-stationary polarization

$$\boldsymbol{\sigma}(\boldsymbol{x}) = -\nabla \cdot \left[\frac{1}{D_R} v_a(\boldsymbol{x}) \rho(\boldsymbol{x}) \boldsymbol{\Gamma}^{-1}\right] \tag{A.44}$$

and the evolution of $\rho(\boldsymbol{r}, t)$ reads:

$$\begin{aligned} \partial_t \rho(\boldsymbol{r}) = -\nabla \cdot \Big[&- \frac{v_a(\boldsymbol{x})}{2D_R} \boldsymbol{\Gamma}^{-1} \nabla \cdot \left(\boldsymbol{\Gamma}^{-1} v_a(\boldsymbol{x})\right) \rho(\boldsymbol{x}) \\ &- \left(\frac{1}{2D_R} v_a^2(\boldsymbol{x}) \boldsymbol{\Gamma}^{-1} \cdot \left(\boldsymbol{\Gamma}^{-1}\right)^T + D_T \boldsymbol{\Gamma}^{-1}\right) \nabla \rho(\boldsymbol{x}) \Big] . \end{aligned} \tag{A.45}$$

Being $\boldsymbol{\Gamma}^{-1} \cdot \left(\boldsymbol{\Gamma}^{-1}\right)^T = \left(1 + \kappa^2(\boldsymbol{r})\right)^{-1} \mathbf{1}$, the drift and diffusion terms can be identified with

$$\begin{aligned} \boldsymbol{V}^B(\boldsymbol{x}) &= -\frac{v_a(\boldsymbol{x})}{2D_R} \boldsymbol{\Gamma}^{-1} \nabla \cdot \left(v_a(\boldsymbol{x}) \boldsymbol{\Gamma}^{-1}\right) , \\ \boldsymbol{D}^B(\boldsymbol{x}) &= \frac{1}{1 + \kappa^2(\boldsymbol{x})} \begin{pmatrix} \frac{v_a^2(\boldsymbol{x})}{2D_R} + D_T & D_T \kappa(\boldsymbol{x}) \\ -D_T \kappa(\boldsymbol{x}) & \frac{v_a^2(\boldsymbol{x})}{2D_R} + D_T \end{pmatrix} . \end{aligned} \tag{A.46}$$

Interestingly, we see that the activity field enhances the diagonal elements of the diffusion tensor, but not its anti-symmetric components. It is straightforward to show that in the case of uniform activity, magnetic field and active torque, the effective dynamics (A.45) and (A.38) can be mapped into one another by means of (3.17).

A.4 Active dimer under Lorentz force

In this Section we analyze the behavior of a dimer composed of two self-propelled charged particles (with opposite charges ±q) subjected to a magnetic field $\boldsymbol{B} = B\hat{\boldsymbol{z}}$ oriented along the z-axis. The dynamics of the dimer takes place in a two-dimensional medium perpendicular to the magnetic field, and characterized by a non-uniform activity field $v_a(\boldsymbol{x})$. The attractive interaction between the two active particles is modeled by a harmonic potential $U(\boldsymbol{x}) = \kappa_s \boldsymbol{x}^2/2$ with stiffness κ_s and zero rest length, but the derivation can be easily generalized to the case of finite rest length and rigid bond interaction. Moreover, in the present derivation we neglect the effect of the electrostatic interaction. The stochastic equation of motion of the dimer is given by the Langevin dynamics:

$$\begin{cases} \dot{\boldsymbol{X}}_i = \boldsymbol{v}_i \,, \\ m\dot{\boldsymbol{v}}_i = -\nabla_i U(\boldsymbol{X}_0 - \boldsymbol{X}_1) - \nu^{-1}\boldsymbol{\Gamma}_i \boldsymbol{v}_i + v_a(\boldsymbol{X})\boldsymbol{n}_i(\theta_i) + \sqrt{2T/\nu}\boldsymbol{\xi}_i \,, \\ \dot{\theta}_i = \sqrt{2D_R}\eta_i(t) \,, \end{cases} \tag{A.47}$$

with m the mass of the two self-propelled particles, $\boldsymbol{v}_i$ their velocities and $\boldsymbol{\Gamma}_i$ their effective friction tensors containing the effect of the Lorentz force generated by the magnetic field. Since the two particles have opposite charges, the tensors $\boldsymbol{\Gamma}_i$ are different and given by $\boldsymbol{\Gamma}_0 = [\mathbf{1} - \kappa\boldsymbol{\varepsilon}]$ and $\boldsymbol{\Gamma}_1 = [\mathbf{1} + \kappa\boldsymbol{\varepsilon}]$, with $\boldsymbol{\varepsilon}$ the 2-dimensional Levi-Civita symbol and $\kappa = qB\nu$ the dimensionless oddness parameter. As in the rest of this Appendix and in Chapter 3, the orientation vectors $\boldsymbol{n}_i = (\cos\theta_i, \sin\theta_i)$ are expressed in terms of the polar angles θ_i. The one-time joint probability density $P(\boldsymbol{X}_0, \boldsymbol{X}_1, \theta_0, \theta_1, t)$ in the overdamped regime evolves according to the following FPE:

$$\begin{aligned} \partial_t P(\boldsymbol{X}_0, \boldsymbol{X}_1, \theta_0, \theta_1, t) = &- \nabla_{\boldsymbol{X}_0} \cdot \left[\nu\boldsymbol{\Gamma}_0^{-1}\boldsymbol{F}P + \boldsymbol{\Gamma}_0^{-1} v_a(\boldsymbol{X}_0)\boldsymbol{n}_0 P - D_T \boldsymbol{\Gamma}_0^{-1}\nabla_{\boldsymbol{X}_0} P\right] \\ &- \nabla_{\boldsymbol{X}_1} \cdot \left[-\nu\boldsymbol{\Gamma}_1^{-1}\boldsymbol{F}P + \boldsymbol{\Gamma}_1^{-1} v_a(\boldsymbol{X}_1)\boldsymbol{n}_1 P - D_T \boldsymbol{\Gamma}_1^{-1}\nabla_{\boldsymbol{X}_1} P\right] \\ &+ D_R \left[\partial_{\theta_0}^2 + \partial_{\theta_1}^2\right] P \end{aligned} \tag{A.48}$$

where the force $F = -\nabla_{\boldsymbol{X}_0} U(\boldsymbol{X}_0 - \boldsymbol{X}_1)$ is due to the attractive interaction between the particles. Since the friction tensors $\boldsymbol{\Gamma}_i$ are different, we find convenient to rewrite Eq. (A.48) in terms of the center-of-friction $\boldsymbol{R}$ and the relative distance $\boldsymbol{r}$ defined as:

$$\begin{aligned}\boldsymbol{R} &= \frac{1}{2}\left[\boldsymbol{\Gamma}_0\boldsymbol{X}_0 + \boldsymbol{\Gamma}_1\boldsymbol{X}_1\right] \,, \\ \boldsymbol{r} &= \boldsymbol{X}_0 - \boldsymbol{X}_1 \,.\end{aligned} \tag{A.49}$$

With this new set of variables, the Fokker-Planck equation (A.48) can be rewritten as

$$\begin{aligned}&\partial_t P(\boldsymbol{R},\boldsymbol{r},\theta_0,\theta_1,t) = \\ &-\nabla_{\boldsymbol{R}}\cdot\left[\frac{1}{2}v_a(\boldsymbol{X}_0)\boldsymbol{n}_0 P + \frac{1}{2}v_a(\boldsymbol{X}_1)\boldsymbol{n}_1 P - \frac{D_T}{2}\nabla_{\boldsymbol{R}}P\right] + \\ &-\nabla_{\boldsymbol{r}}\cdot\left[\frac{2\nu}{1+\kappa^2}\boldsymbol{F}P + \boldsymbol{\Gamma}_0^{-1}v_a(\boldsymbol{X}_0)\boldsymbol{n}_0 P - \boldsymbol{\Gamma}_1^{-1}v_a(\boldsymbol{X}_1)\boldsymbol{n}_1 P - \frac{2D_T}{1+\kappa^2}\nabla_{\boldsymbol{r}}P\right] + \\ &+\frac{D_T}{2}\frac{4\kappa}{1+\kappa^2}\left(\partial_{r_x}\partial_{R_y} - \partial_{r_y}\partial_{R_x}\right)P + D_R\left[\partial^2_{\theta_0} + \partial^2_{\theta_1}\right]P \,,\end{aligned} \tag{A.50}$$

where the positions $\boldsymbol{X}_0$ and $\boldsymbol{X}_1$ have to be interpreted as functions of the center-of-friction and the relative distance, i.e. $\boldsymbol{X}_0 = \boldsymbol{R} + \frac{1}{2}\boldsymbol{\Gamma}_1\boldsymbol{r}$ and $\boldsymbol{X}_1 = \boldsymbol{R} - \frac{1}{2}\boldsymbol{\Gamma}_0\boldsymbol{r}$. The strategy to integrate out the orientational degrees of freedom is analogous to the one presented in Sec. A.1. Specifically, we expand the joint probability density in eigenfunctions of the rotational operator, obtaining the same Cartesian multipole expansion as in Eq. (A.2). The expansion is then truncated to the order of the dipole moments $\{\boldsymbol{\sigma}_i\}$, in that the higher order terms lead to corrections of order $\mathcal{O}(\nabla^2_{\boldsymbol{R}})$ in the probability flux of the coarse grained density $\rho(\boldsymbol{R},t)$. Projecting the FPE (A.50) onto the eigenfunctions 1 and $\{\boldsymbol{n}_i\}$, we obtain the evolution equation for the expansion coefficients ϕ and $\{\boldsymbol{\sigma}_i\}$. The first one reads

$$\begin{aligned}\partial_t\phi(\boldsymbol{R},\boldsymbol{r},t) = &-\nabla_{\boldsymbol{R}}\cdot\left[\frac{1}{4}v_a(\boldsymbol{X}_0)\boldsymbol{\sigma}_0 + \frac{1}{4}v_a(\boldsymbol{X}_1)\boldsymbol{\sigma}_1 - \frac{D_T}{2}\nabla_{\boldsymbol{R}}\phi\right] \\ &-\nabla_{\boldsymbol{r}}\cdot\left[\frac{2\nu\boldsymbol{F}\phi}{1+\kappa^2} + \boldsymbol{\Gamma}_0^{-1}v_a(\boldsymbol{X}_0)\frac{\boldsymbol{\sigma}_0}{2} - \boldsymbol{\Gamma}_1^{-1}v_a(\boldsymbol{X}_1)\frac{\boldsymbol{\sigma_1}}{2} - \frac{2D_T}{1+\kappa^2}\nabla_{\boldsymbol{r}}\phi\right] \\ &+\frac{D_T}{2}\frac{4\kappa}{1+\kappa^2}\left(\partial_{r_x}\partial_{R_y} - \partial_{r_y}\partial_{R_x}\right)\phi,\end{aligned} \tag{A.51}$$

and can be integrated over the relative distance $\boldsymbol{r}$ to get a continuity equation $\partial_t\rho = -\nabla_{\boldsymbol{R}}\boldsymbol{J}$ for the coarse grained density $\rho(\boldsymbol{R},t)$. Similarly to Sec. A.1, the total flux $\boldsymbol{J}$ can be decomposed as the summation of three contribution $\boldsymbol{J}_{\boldsymbol{\sigma}_0}$, $\boldsymbol{J}_{\boldsymbol{\sigma}_1}$ and $\boldsymbol{J}_D$. The first two are related to the average polarizations $\{\boldsymbol{\sigma}_i\}$ of the active particles, while the last one to thermal fluctuations. They are defined as:

$$\begin{aligned}
\boldsymbol{J}_{\boldsymbol{\sigma}_i} &= \frac{1}{4}\int \mathrm{d}\boldsymbol{r} v_a(\boldsymbol{X}_i)\boldsymbol{\sigma}_i \,, \\
\boldsymbol{J}_D &= \frac{D_T}{2}\nabla_{\boldsymbol{R}}\rho \,.
\end{aligned} \tag{A.52}$$

To make analytical progresses with the fluxes $\boldsymbol{J}_{\boldsymbol{\sigma}_i}$ we need to analyze the dipole moments $\boldsymbol{\sigma}_i$. In the following, we will explicitly derive the expression of $\boldsymbol{J}_{\boldsymbol{\sigma}_0}$. The flux $\boldsymbol{J}_{\boldsymbol{\sigma}_1}$ can be obtained with an analogous procedure. Projecting the FPE (A.50) onto $\boldsymbol{n}_0$ and using the truncated multipole expansion, we get the following evolution equation for the polarization $\boldsymbol{\sigma}_0$:

$$\begin{aligned}
\partial_t\boldsymbol{\sigma}_0 = &- \nabla_{\boldsymbol{R}} \cdot \left[\frac{1}{2}v_a(\boldsymbol{X}_0)\phi\mathbf{1} - \frac{D_T}{2}\nabla_{\boldsymbol{R}}\boldsymbol{\sigma}_0\right] \\
&- \nabla_{\boldsymbol{r}} \cdot \left[\frac{2\nu}{1+\kappa^2}\boldsymbol{F}\boldsymbol{\sigma}_0 + v_a(\boldsymbol{X}_0)\phi\boldsymbol{\Gamma}_0^{-1} - \frac{2D_T}{1+\kappa^2}\nabla_{\boldsymbol{r}}\boldsymbol{\sigma}_0\right] \\
&+ \frac{D_T}{2}\frac{4\kappa}{1+\kappa^2}\left(\partial_{r_x}\partial_{R_y} - \partial_{r_y}\partial_{R_x}\right)\boldsymbol{\sigma}_0 - D_R\boldsymbol{\sigma}_0 \,.
\end{aligned} \tag{A.53}$$

Similarly to Sec. A.1, the average polarization relaxes on a time scale $\sim 1/D_R$ much smaller compared to the density ρ, which is locally conserved throughout the dynamics. Thanks to this time scale separation we can obtain a quasi-static expression for $\boldsymbol{\sigma}_0$ by neglecting its time derivative $\partial_t\boldsymbol{\sigma}_0$. This leads to:

$$\begin{aligned}
\boldsymbol{\sigma}_0 = &- \frac{1}{D_R}\nabla_{\boldsymbol{R}} \cdot \left[\frac{1}{2}v_a(\boldsymbol{X}_0)\phi\mathbf{1} - \frac{D_T}{2}\nabla_{\boldsymbol{R}}\boldsymbol{\sigma}_0\right] \\
&- \frac{1}{D_R}\nabla_{\boldsymbol{r}} \cdot \left[\frac{2\nu}{1+\kappa^2}\boldsymbol{F}\boldsymbol{\sigma}_0 + v_a(\boldsymbol{X}_0)\phi\boldsymbol{\Gamma}_0^{-1} - \frac{2D_T}{1+\kappa^2}\nabla_{\boldsymbol{r}}\boldsymbol{\sigma}_0\right] \\
&+ \frac{1}{D_R}\frac{D_T}{2}\frac{4\kappa}{1+\kappa^2}\left(\partial_{r_x}\partial_{R_y} - \partial_{r_y}\partial_{R_x}\right)\boldsymbol{\sigma}_0 \,.
\end{aligned} \tag{A.54}$$

This expression can be substituted in the definition of the flux $\boldsymbol{J}_{\boldsymbol{\sigma}_0}$. Moreover, since we assume that the activity field is characterized by small gradients, we neglect all terms in the flux that contribute as $\mathcal{O}(\nabla_{\boldsymbol{R}}^2)$. In this way we get:

$$\begin{aligned}
\boldsymbol{J}_{\boldsymbol{\sigma}_0} = &- \frac{1}{8D_R}\int \mathrm{d}\boldsymbol{r}\, v_a(\boldsymbol{X}_0)\nabla_{\boldsymbol{R}}\left[v_a(\boldsymbol{X}_0)\phi\right] \\
&+ \frac{1}{8D_R}\int \mathrm{d}\boldsymbol{r}\, \left(\nabla_{\boldsymbol{R}} \cdot \boldsymbol{\Gamma}_1 v_a(\boldsymbol{X}_0)\right) \cdot \left[v_a(\boldsymbol{X}_0)\phi\boldsymbol{\Gamma}_0^{-1} + \frac{2\nu}{1+\kappa^2}\boldsymbol{F}\boldsymbol{\sigma}_0\right] \,.
\end{aligned} \tag{A.55}$$

Analogously to Sec. A.1 we can define the integral $\boldsymbol{I}_0$ as:

$$\boldsymbol{I}_0 = \int \mathrm{d}\boldsymbol{r}\, \left[\nabla_{\boldsymbol{R}} \cdot \boldsymbol{\Gamma}_1 v_a(\boldsymbol{X}_0)\right] \cdot \left[\boldsymbol{F}\boldsymbol{\sigma}_0\right] \,, \tag{A.56}$$

whose approximate solution can be obtained by substituting the quasi-static expression of the dipole moment $\boldsymbol{\sigma}_0$ given in (A.54) and neglecting all contributions of order $\mathcal{O}(\nabla^2_{\boldsymbol{R}})$. In this way we find:

$$
\begin{aligned}
\boldsymbol{I}_0 &= \frac{1}{D_R}\int \mathrm{d}\boldsymbol{r}\ \left[\nabla_{\boldsymbol{R}}\cdot(\boldsymbol{\Gamma}_1 v_a(\boldsymbol{X}_0))\cdot\boldsymbol{F}\right]\left\{-\nabla_{\boldsymbol{r}}\cdot\left[v_a(\boldsymbol{X}_0)\phi\boldsymbol{\Gamma}_0^{-1}+\frac{2\nu}{1+\kappa^2}\boldsymbol{F}\boldsymbol{\sigma}_0\right]\right\} \\
&= -\frac{\kappa_s}{D_R}\int \mathrm{d}\boldsymbol{r}\ \left[\nabla_{\boldsymbol{R}}\cdot(\boldsymbol{\Gamma}_1 v_a(\boldsymbol{X}_0))\cdot\boldsymbol{A}^T\right]\cdot\left[v_a(\boldsymbol{X}_0)\phi\boldsymbol{\Gamma}_0^{-1}+\frac{2\nu}{1+\kappa^2}\boldsymbol{F}\boldsymbol{\sigma}_0\right],
\end{aligned}
\tag{A.57}
$$

where in the last line we used integration by parts and the small gradient assumption. Moreover, we introduced the matrix $\boldsymbol{A}$ defined as $\nabla_{\boldsymbol{r}}\boldsymbol{F} = -\kappa_s\boldsymbol{A}$. In the case of harmonic interaction potential with zero rest length, we have $\boldsymbol{A} = \boldsymbol{1}$. In this case we find:

$$
\begin{aligned}
\boldsymbol{I}_0 &= -\frac{\kappa_s}{D_R}\frac{2\nu}{1+\kappa^2}\boldsymbol{I}_0 - \frac{\kappa_s}{D_R}\int \mathrm{d}\boldsymbol{r}\, v_a(\boldsymbol{X}_0)\phi\left(\nabla_{\boldsymbol{R}}v_a(\boldsymbol{X}_0)\right)\cdot\boldsymbol{\Gamma}_1\boldsymbol{\Gamma}_0^{-1} \\
&= -\frac{\kappa_s}{D_R}\frac{1}{1+\frac{\kappa_s}{D_R}\frac{2\nu}{1+\kappa^2}}\int \mathrm{d}\boldsymbol{r}\, v_a(\boldsymbol{X}_0)\phi\left(\nabla_{\boldsymbol{R}}v_a(\boldsymbol{X}_0)\right)\cdot\boldsymbol{\Gamma}_1\boldsymbol{\Gamma}_0^{-1}.
\end{aligned}
\tag{A.58}
$$

Substituting the integral $\boldsymbol{I}_0$ into (A.55) yields:

$$
\begin{aligned}
\boldsymbol{J}_{\boldsymbol{\sigma}_0} =& -\frac{1}{8D_R}\int \mathrm{d}\boldsymbol{r}\, v_a(\boldsymbol{X}_0)\nabla_{\boldsymbol{R}}\left[v_a(\boldsymbol{X}_0)\phi\right] \\
&+\frac{1}{8D_R}\left[1-\frac{1}{\tau(1+\kappa^2)+1}\right]\int \mathrm{d}\boldsymbol{r}\, v_a(\boldsymbol{X}_0)\phi\left(\nabla_{\boldsymbol{R}}v_a(\boldsymbol{X}_0)\right)\cdot\boldsymbol{\Gamma}_1\boldsymbol{\Gamma}_0^{-1},
\end{aligned}
\tag{A.59}
$$

where we introduced the dimensionless quantity $\tau = D_R/2\kappa_s\nu$ that measures the typical relaxation time of the relative distance $\boldsymbol{r}$ in units of the rotational diffusion time scale $1/D_R$. A similar equation can be found for the flux $\boldsymbol{J}_{\boldsymbol{\sigma}_1}$ and reads:

$$
\begin{aligned}
\boldsymbol{J}_{\boldsymbol{\sigma}_1} =& -\frac{1}{8D_R}\int \mathrm{d}\boldsymbol{r}\, v_a(\boldsymbol{X}_1)\nabla_{\boldsymbol{R}}\left[v_a(\boldsymbol{X}_1)\phi\right] \\
&+\frac{1}{8D_R}\left[1-\frac{1}{\tau(1+\kappa^2)+1}\right]\int \mathrm{d}\boldsymbol{r}\, v_a(\boldsymbol{X}_1)\phi\left(\nabla_{\boldsymbol{R}}v_a(\boldsymbol{X}_1)\right)\cdot\boldsymbol{\Gamma}_0\boldsymbol{\Gamma}_1^{-1}.
\end{aligned}
\tag{A.60}
$$

Finally, since we are working under the assumption that the activity field has small variations on the length scale given by the typical distance between the two particles, we can approximate the integrals above by using $\phi(\boldsymbol{R},t) \approx \rho(\boldsymbol{R},t)\delta^d(\boldsymbol{r})$. This approximation, together with the identity

$$
\boldsymbol{\Gamma}_1\boldsymbol{\Gamma}_0^{-1}+\boldsymbol{\Gamma}_0\boldsymbol{\Gamma}_1^{-1} = 2\frac{1-\kappa^2}{1+\kappa^2}\boldsymbol{1},
\tag{A.61}
$$

leads to the following expression for the total probability flux $\boldsymbol{J} = \boldsymbol{J}_{\boldsymbol{\sigma}_0} + \boldsymbol{J}_{\boldsymbol{\sigma}_1} + \boldsymbol{J}_D$ of the coarse grained density ρ:

$$\boldsymbol{J} = -\frac{\epsilon}{8D_R}\left(\nabla_{\boldsymbol{R}} v_a(\boldsymbol{R})^2\right)\rho(\boldsymbol{R}) - \left[\frac{1}{4D_R} v_a(\boldsymbol{R})^2 + \frac{D_T}{2}\right]\nabla_{\boldsymbol{R}}\rho(\boldsymbol{R})\,, \tag{A.62}$$

where the chemotactic coupling ϵ is given by

$$\epsilon = 1 - \frac{1-\kappa^2}{1+\kappa^2}\left[1 - \frac{1}{\tau(1+\kappa^2)+1}\right] \tag{A.63}$$

as reported in Eq. (3.21) of Chapter 3. In particular, the coupling ϵ is positive for any value of the magnetic field. This implies that is not possible to induce the preferential localization of this system in regions of high activity by changing the oddness parameter κ.

Appendix B

Appendix of Chapter 4

We provide here a detailed derivation of the analytical predictions reported in Chapter 4. In particular, in Sec. B.1 we derive the mode equations [i.e., (4.7) and (4.8) in Chapter 4] using the moment expansion technique. In Sec. B.2 we describe how a closure relation can be obtained within the small-gradient approximation, which allows one to obtain an equation of motion for the coarse-grained density of the microswimmer [Eq. (4.9) in Chapter 4]. In Sec. B.3 we prove analytically that the drift velocity of the microswimmer vanishes at $q = q_{\mathrm{th}}$. In Sec. B.4 we derive an equation of motion for the coarse-grained density of the microswimmer by using an alternative closure relation which is applicable to fast activity waves. We derive analytical expressions for the stationary density, stationary flux and average drift velocity. In Sec. B.5 we report the details about the numerical simulations.

B.1 Mode equations

In this Section, we show how to derive the mode equations using a moment expansion technique analogous to what is presented in Refs. [126, 173, 174]. We start the derivation from the Fokker-Planck equation (FPE) describing the evolution of $P(\boldsymbol{\chi}, \boldsymbol{r}, \boldsymbol{\eta}, t)$ (see Eq. (4.5)):

$$\begin{aligned}\partial_t P(\boldsymbol{\chi}, \boldsymbol{r}, \boldsymbol{\eta}, t) = &- \nabla_{\boldsymbol{\chi}} \cdot \left[-\boldsymbol{v}_w P + \frac{1}{1+q} v_{\mathrm{a}}\left(\boldsymbol{\chi}'\right) \boldsymbol{\eta} P - \frac{D}{1+q} \nabla_{\boldsymbol{\chi}} P\right] \\ &- \nabla_{\boldsymbol{r}} \cdot \left[-\frac{1+q}{q} \nu \nabla_{\boldsymbol{r}} U P + v_{\mathrm{a}}\left(\boldsymbol{\chi}'\right) \boldsymbol{\eta} P - \frac{1+q}{q} D \nabla_{\boldsymbol{r}} P\right] \\ &+ 1/(d\tau) \hat{\mathcal{L}}_{\boldsymbol{\eta}} P\end{aligned} \tag{B.1}$$

where we remind that

$$\boldsymbol{\chi}' = \boldsymbol{\chi} + q\boldsymbol{r}/(1+q) \tag{B.2}$$

is the position of the active carrier in the comoving frame and the operator $\hat{\mathcal{L}}_{\boldsymbol{\eta}}$ is defined as

$$\hat{\mathcal{L}}_{\boldsymbol{\eta}} f(\boldsymbol{\eta}) = \nabla^2_{\boldsymbol{\eta}} f(\boldsymbol{\eta}) + d\nabla_{\boldsymbol{\eta}} \cdot [\boldsymbol{\eta} f(\boldsymbol{\eta})] \ . \tag{B.3}$$

We now expand the joint probability density as

$$P(\boldsymbol{\chi}, \boldsymbol{r}, \boldsymbol{\eta}, t) = \sum_{\boldsymbol{n}} \phi_{\boldsymbol{n}}(\boldsymbol{\chi}, \boldsymbol{r}, t) u_{\boldsymbol{n}}(\boldsymbol{\eta}) \, , \tag{B.4}$$

where $\boldsymbol{n} = \{n_1, n_2, \ldots, n_d\}$ is a set of non-negative integers, while $\{u_{\boldsymbol{n}}(\boldsymbol{\eta})\}$ is the corresponding set of eigenfunctions of the operator $\hat{\mathcal{L}}_{\boldsymbol{\eta}}$, given by

$$u_{\boldsymbol{n}}(\boldsymbol{\eta}) = \exp\left\{-\frac{d\boldsymbol{\eta}^2}{2}\right\} \prod_{i=1}^{d} H_{n_i}(\sqrt{d}\,\eta_i) \, . \tag{B.5}$$

Here, $H_n(x)$ is the n-th Hermite polynomial in the probabilist convention [333]. They satisfy the following eigenvalue equation

$$\hat{\mathcal{L}}_{\boldsymbol{\eta}} u_{\boldsymbol{n}}(\boldsymbol{\eta}) = \lambda_{\boldsymbol{n}} u_{\boldsymbol{n}}(\boldsymbol{\eta}), \tag{B.6}$$

where the eigenvalues $\lambda_{\boldsymbol{n}}$ are given by

$$\lambda_{\boldsymbol{n}} = -d \sum_{i=1}^{d} n_i. \tag{B.7}$$

Moreover, it is convenient to introduce the family of auxiliary functions $\{\tilde{u}_{\boldsymbol{n}}(\boldsymbol{\eta})\}$ as

$$\tilde{u}_{\boldsymbol{n}}(\boldsymbol{\eta}) = (2\pi)^{-d/2} \prod_{i=1}^{d} \frac{H_{n_i}(\sqrt{d}\,\eta_i)}{n_i!}, \tag{B.8}$$

which are orthogonal to the eigenfunctions $\{u_{\boldsymbol{n}}(\boldsymbol{\eta})\}$, i.e.,

$$\int \mathrm{d}\boldsymbol{\eta}\, u_{\boldsymbol{n}}(\boldsymbol{\eta}) \tilde{u}_{\boldsymbol{m}}(\boldsymbol{\eta}) = d^{-d/2} \delta_{\boldsymbol{n},\boldsymbol{m}}, \tag{B.9}$$

where $\delta_{\boldsymbol{n},\boldsymbol{m}} = \prod_{i=1}^{d} \delta_{n_i,m_i}$. Multiplying Eq. (B.4) by $\tilde{u}_{\boldsymbol{0}}(\boldsymbol{\eta})$ and integrating over $\boldsymbol{\eta}$, we get

$$\int \mathrm{d}\boldsymbol{\eta}\, \tilde{u}_{\boldsymbol{0}}(\boldsymbol{\eta}) P(\boldsymbol{\chi}, \boldsymbol{r}, \boldsymbol{\eta}, t) = \sum_{\boldsymbol{n}} \phi_{\boldsymbol{n}}(\boldsymbol{\chi}, \boldsymbol{r}, t) \int \mathrm{d}\boldsymbol{\eta}\, \tilde{u}_{\boldsymbol{0}}(\boldsymbol{\eta}) u_{\boldsymbol{n}}(\boldsymbol{\eta}) = d^{-d/2} \phi_{\boldsymbol{0}}(\boldsymbol{\chi}, \boldsymbol{r}, t) \, , \tag{B.10}$$

and after using the definition of $\tilde{u}_{\boldsymbol{0}}(\boldsymbol{\eta})$ in the left hand side:

$$\varphi(\boldsymbol{\chi}, \boldsymbol{r}, t) \equiv \int d\boldsymbol{\eta}\, P(\boldsymbol{\chi}, \boldsymbol{r}, \boldsymbol{\eta}, t) = (2\pi/d)^{d/2} \phi_{\boldsymbol{0}}(\boldsymbol{\chi}, \boldsymbol{r}, t) \, . \tag{B.11}$$

Hence, the first coefficient $\phi_{\mathbf{0}}(\boldsymbol{\chi}, \boldsymbol{r}, t)$ of the expansion in (B.4) is related to the marginal density $\varphi(\boldsymbol{\chi}, \boldsymbol{r}, t)$. For later purposes, we recall that the Hermite polynomials satisfy the recurrence relation [333]

$$H_{n+1}(x) = xH_n(x) - H_n'(x), \tag{B.12}$$

and they form an Appell sequence, in that they can be obtained from one another using the following iterative formula:

$$H_n'(x) = nH_{n-1}(x). \tag{B.13}$$

In order to lighten the notation, below we will denote by $\boldsymbol{n}_{\alpha\pm}$ the vector $(n_1, .., n_\alpha \pm 1, ..., n_d)$. Then, by using the properties of Hermite polynomials (B.12) and (B.13) in equation (B.5), we obtain

$$\begin{aligned}
\eta_\alpha u_{\boldsymbol{n}}(\boldsymbol{\eta}) &= \frac{1}{\sqrt{d}} \exp\left\{-\frac{d\boldsymbol{\eta}^2}{2}\right\} \sqrt{d}\eta_\alpha H_{n_\alpha}\left(\sqrt{d}\eta_\alpha\right) \prod_{\beta\neq\alpha} H_{n_\beta}\left(\sqrt{d}\eta_\beta\right) \\
&= \frac{1}{\sqrt{d}} \exp\left\{-\frac{d\boldsymbol{\eta}^2}{2}\right\} \left[H_{n_\alpha+1}\left(\sqrt{d}\eta_\alpha\right) + n_\alpha H_{n_\alpha-1}\left(\sqrt{d}\eta_\alpha\right)\right] \prod_{\beta\neq\alpha} H_{n_\beta}\left(\sqrt{d}\eta_\beta\right) \\
&= \frac{1}{\sqrt{d}} u_{\boldsymbol{n}_{\alpha+}}(\boldsymbol{\eta}) + \frac{n_\alpha}{\sqrt{d}} u_{\boldsymbol{n}_{\alpha-}}(\boldsymbol{\eta})\,.
\end{aligned} \tag{B.14}$$

At this point we can project the FPE onto the $\{\tilde{u}_{\boldsymbol{n}}(\boldsymbol{\eta})\}$ and obtain a set of equations for the coefficients $\{\phi_{\boldsymbol{n}}(\boldsymbol{\chi}, \boldsymbol{r}, t)\}$. In the following, summation over repeated indices is implied. For convenience, we will split the Fokker-Planck operator into the three contributions

$$\partial_t P(\boldsymbol{\chi}, \boldsymbol{r}, \boldsymbol{\eta}, t) = \left(\hat{\mathcal{L}}_{\boldsymbol{\chi}} + \hat{\mathcal{L}}_{\boldsymbol{r}} + \frac{1}{d\tau}\hat{\mathcal{L}}_{\boldsymbol{\eta}}\right) P, \tag{B.15}$$

where $\hat{\mathcal{L}}_{\boldsymbol{\eta}}$ is defined in (B.3), while

$$\begin{aligned}
\hat{\mathcal{L}}_{\boldsymbol{\chi}} P &= -\partial_\alpha \left[\frac{1}{1+q} v_{\mathrm{a}} \left(\boldsymbol{\chi} + \frac{q}{1+q}\boldsymbol{r}\right) \eta_\alpha P - \frac{D}{1+q}\partial_\alpha P - v_w \delta_{\alpha,0} P\right], \\
\hat{\mathcal{L}}_{\boldsymbol{r}} P &= -\partial_\alpha' \left[-\frac{1+q}{q}\nu \partial_\alpha' U(\boldsymbol{r}) P + v_{\mathrm{a}} \left(\boldsymbol{\chi} + \frac{q}{1+q}\boldsymbol{r}\right) \eta_\alpha P - \frac{(1+q)}{q} D \partial_\alpha' P\right],
\end{aligned} \tag{B.16}$$

where we introduced the shorthand notation $\partial_\alpha \equiv \partial_{\chi_\alpha}$ and $\partial_\alpha' \equiv \partial_{r_\alpha}$. We separately project the various terms of the FPE onto $\tilde{u}_{\boldsymbol{m}}(\boldsymbol{\eta})$, starting from its l.h.s.:

$$\begin{aligned}
\int \mathrm{d}\boldsymbol{\eta}\, \tilde{u}_{\boldsymbol{m}}(\boldsymbol{\eta}) \partial_t P(\boldsymbol{\chi}, \boldsymbol{r}, \boldsymbol{\eta}, t) &= \partial_t \phi_{\boldsymbol{n}}(\boldsymbol{\chi}, \boldsymbol{r}, t) \int \mathrm{d}\boldsymbol{\eta}\, \tilde{u}_{\boldsymbol{m}}(\boldsymbol{\eta}) u_{\boldsymbol{n}}(\boldsymbol{\eta}) \\
&= d^{-d/2} \partial_t \phi_{\boldsymbol{m}}(\boldsymbol{\chi}, \boldsymbol{r}, t)\,.
\end{aligned} \tag{B.17}$$

For the first term on the r.h.s., i.e., $\hat{\mathcal{L}}_{\boldsymbol{\chi}}P$, we have (for simplicity, we do not indicate below the dependence of $\phi_{\boldsymbol{n}}$ on $\boldsymbol{\chi}$ and $\boldsymbol{r}$):

$$\begin{aligned}
&\int \mathrm{d}\boldsymbol{\eta}\, \tilde{u}_{\boldsymbol{m}}(\boldsymbol{\eta})\hat{\mathcal{L}}_{\boldsymbol{\chi}}P = \\
&= -\partial_\alpha \left[\frac{v_\mathrm{a}\left(\boldsymbol{\chi}'\right)\phi_{\boldsymbol{n}}}{1+q}\int \mathrm{d}\boldsymbol{\eta}\, \tilde{u}_{\boldsymbol{m}}(\boldsymbol{\eta})\eta_\alpha u_{\boldsymbol{n}}(\boldsymbol{\eta}) - \left(\frac{D\partial_\alpha\phi_{\boldsymbol{n}}}{1+q} + v_w\delta_{\alpha,0}\phi_{\boldsymbol{n}}\right)d^{-d/2}\delta_{\boldsymbol{n},\boldsymbol{m}}\right] \\
&= -\partial_\alpha \left\{\frac{v_\mathrm{a}\left(\boldsymbol{\chi}'\right)\phi_{\boldsymbol{n}}}{\sqrt{d}(1+q)}\int \mathrm{d}\boldsymbol{\eta}\, \tilde{u}_{\boldsymbol{m}}(\boldsymbol{\eta})\left[u_{\boldsymbol{n}_{\alpha+}} + n_\alpha u_{\boldsymbol{n}_{\alpha-}}\right] - \frac{Dd^{-d/2}}{1+q}\partial_\alpha\phi_{\boldsymbol{m}} - \frac{v_w\delta_{\alpha,0}}{d^{d/2}}\phi_{\boldsymbol{m}}\right\} \\
&= -\partial_\alpha \left\{\frac{d^{-(d+1)/2}}{1+q}v_\mathrm{a}\left(\boldsymbol{\chi}'\right)\left[\phi_{\boldsymbol{n}}\delta_{\boldsymbol{m},\boldsymbol{n}_{\alpha+}} + n_\alpha\phi_{\boldsymbol{n}}\delta_{\boldsymbol{m},\boldsymbol{n}_{\alpha-}}\right] - \frac{Dd^{-d/2}}{1+q}\partial_\alpha\phi_{\boldsymbol{m}} - \frac{v_w\delta_{\alpha,0}}{d^{d/2}}\phi_{\boldsymbol{m}}\right\} \\
&= -\partial_\alpha \left\{\frac{d^{-(d+1)/2}}{1+q}v_\mathrm{a}\left(\boldsymbol{\chi}'\right)\left[\phi_{\boldsymbol{m}_{\alpha-}} + (m_\alpha+1)\phi_{\boldsymbol{m}_{\alpha+}}\right] - \frac{Dd^{-d/2}}{1+q}\partial_\alpha\phi_{\boldsymbol{m}} - \frac{v_w\delta_{\alpha,0}}{d^{d/2}}\phi_{\boldsymbol{m}}\right\},
\end{aligned} \tag{B.18}$$

where we used $\delta_{\boldsymbol{m},\boldsymbol{n}_{\alpha-}} = \delta_{\boldsymbol{m}_{\alpha+},\boldsymbol{n}}$ and $\delta_{\boldsymbol{m},\boldsymbol{n}_{\alpha+}} = \delta_{\boldsymbol{m}_{\alpha-},\boldsymbol{n}}$. Similarly, the projection of the second term on the right hand side of Eq. (B.15), i.e., $\hat{\mathcal{L}}_{\boldsymbol{r}}P$, reads

$$\begin{aligned}
&d^{d/2}\int \mathrm{d}\boldsymbol{\eta}\, \tilde{u}_{\boldsymbol{m}}(\boldsymbol{\eta})\hat{\mathcal{L}}_{\boldsymbol{r}}P = \frac{(1+q)D}{q}\partial'^2_\alpha\phi_{\boldsymbol{m}} \\
&- \partial'_\alpha\left\{-\frac{(1+q)}{q}\nu\partial'_\alpha U(\boldsymbol{r})\phi_{\boldsymbol{m}} + \frac{v_\mathrm{a}\left(\boldsymbol{\chi}\right)}{d^{1/2}}\left[\phi_{\boldsymbol{m}_{\alpha-}} + (m_\alpha+1)\phi_{\boldsymbol{m}_{\alpha+}}\right]\right\}.
\end{aligned} \tag{B.19}$$

Finally, the last term $\frac{1}{d\tau}\hat{\mathcal{L}}_{\boldsymbol{\eta}}P$ of Eq. (B.15), contributes as

$$\frac{1}{d\tau}\int \mathrm{d}\boldsymbol{\eta}\, \tilde{u}_{\boldsymbol{m}}(\boldsymbol{\eta})\hat{\mathcal{L}}_{\boldsymbol{\eta}}P = \frac{1}{d\tau}\phi_{\boldsymbol{n}}\int \mathrm{d}\boldsymbol{\eta}\, \tilde{u}_{\boldsymbol{m}}(\boldsymbol{\eta})\hat{\mathcal{L}}_{\boldsymbol{\eta}}u_{\boldsymbol{n}}(\boldsymbol{\eta}) = \frac{d^{-d/2-1}}{\tau}\lambda_{\boldsymbol{m}}\phi_{\boldsymbol{m}}. \tag{B.20}$$

Collecting the contributions in Eqs. (B.18), (B.19), and (B.20), the FPE projection onto $\tilde{u}_{\boldsymbol{m}}(\boldsymbol{\eta})$ yields the following set of coupled equations for the coefficients

$$\begin{aligned}
&\partial_t\phi_{\boldsymbol{m}}(\boldsymbol{\chi},\boldsymbol{r},t) = \\
&-\partial_\alpha\left\{\frac{1}{\sqrt{d}(1+q)}v_\mathrm{a}\left(\boldsymbol{\chi}'\right)\left[\phi_{\boldsymbol{m}_{\alpha-}} + (m_\alpha+1)\phi_{\boldsymbol{m}_{\alpha+}}\right] - \frac{D}{1+q}\partial_\alpha\phi_{\boldsymbol{m}} - v_w\delta_{\alpha,0}\phi_{\boldsymbol{m}}\right\} \\
&-\partial'_\alpha\left\{-\frac{(1+q)}{q}\nu\partial'_\alpha U(\boldsymbol{r})\phi_{\boldsymbol{m}} + \frac{v_\mathrm{a}\left(\boldsymbol{\chi}'\right)}{\sqrt{d}}\left[\phi_{\boldsymbol{m}_{\alpha-}} + (m_\alpha+1)\phi_{\boldsymbol{m}_{\alpha+}}\right]\right\} \\
&+\frac{D(1+q)}{q}\partial'^2_\alpha\phi_{\boldsymbol{m}} + \frac{\lambda_{\boldsymbol{m}}}{d\tau}\phi_{\boldsymbol{m}}\,.
\end{aligned} \tag{B.21}$$

In particular, the dynamics of the first two modes $\varphi(\boldsymbol{\chi},\boldsymbol{r},t)$ and

$$\sigma_\alpha(\boldsymbol{\chi},\boldsymbol{r},t) \equiv \int \mathrm{d}\boldsymbol{\eta}\,\eta_\alpha P(\boldsymbol{\chi},\boldsymbol{r},\boldsymbol{\eta},t) = \left(\frac{2\pi}{d}\right)^{d/2}\frac{\phi_{\boldsymbol{0}_{\alpha+}}(\boldsymbol{\chi},\boldsymbol{r},t)}{\sqrt{d}}\,, \tag{B.22}$$

can be obtained by specialising Eq. (B.21) to the cases $\boldsymbol{m} = \boldsymbol{0}$ and $\boldsymbol{m} = \boldsymbol{0}_{\alpha+}$, finding

$$\begin{aligned}\partial_t \varphi(\boldsymbol{\chi}, \boldsymbol{r}, t) = &- \partial_\alpha \left[-v_w \delta_{\alpha,0} \varphi + \frac{v_\mathrm{a}(\boldsymbol{\chi}')\, \sigma_\alpha}{(1+q)} - \frac{D}{1+q} \partial_\alpha \varphi \right] \\ &- \partial'_\alpha \left[-\frac{(1+q)}{q} \nu \partial'_\alpha U \varphi + v_\mathrm{a}(\boldsymbol{\chi}')\, \sigma_\alpha - \frac{(1+q)D}{q} \partial'_\alpha \varphi \right],\end{aligned} \tag{B.23}$$

and

$$\begin{aligned}\partial_t \sigma_\alpha(\boldsymbol{\chi}, \boldsymbol{r}, t) = &- \partial_\beta \left[\frac{v_\mathrm{a}(\boldsymbol{\chi}')\, \varphi \delta_{\alpha,\beta}}{d(1+q)} - \frac{D}{1+q} \partial_\beta \sigma_\alpha - v_w \delta_{\beta,0} \sigma_\alpha \right] \\ &- \partial'_\beta \left[-\frac{(1+q)}{q} \nu \partial'_\beta U(\boldsymbol{r}) \sigma_\alpha + \frac{v_\mathrm{a}(\boldsymbol{\chi}')\, \varphi \delta_{\alpha,\beta}}{d} - \frac{(1+q)D}{q} \partial'_\beta \sigma_\alpha \right] \\ &- \tau^{-1} \sigma_\alpha + \Upsilon(\boldsymbol{\chi}, \boldsymbol{r}, t),\end{aligned} \tag{B.24}$$

with $\Upsilon(\boldsymbol{\chi}, \boldsymbol{r}, t)$ denoting the contributions due to higher-order modes. In order to simplify the notation, in the previous expression and in those which follow, the dependence on $(\boldsymbol{\chi}, \boldsymbol{r}, t)$ of φ and σ_α is understood if not explicitly indicated. In order to treat this hierarchy of equations, we adopt below two different approaches depending on the value of the phase velocity v_w of the activity wave compared to the activity field v_a itself.

B.2 Slow active traveling waves

In the case of slowly propagating waves $v_w \ll v_0$, the hierarchy formed by (B.23), (B.24) and the evolution equations for higher order modes, can be closed by assuming that the activity field v_a varies on length scales much larger than the persistence length $l_p = \tau v_0$ (small gradients approximation), and considering quasi-stationary higher-order modes at time scales longer than τ [126, 173, 174]. Under these approximations, the equation (B.24) for the polarization field σ_α can be rewritten as

$$\frac{\sigma_\alpha(\boldsymbol{\chi}, \boldsymbol{r}, t)}{\tau} = -\frac{\partial_\alpha \left[v_\mathrm{a}(\boldsymbol{\chi}')\, \varphi \right]}{(1+q)d} - \frac{\partial'_\alpha \left[v_\mathrm{a}(\boldsymbol{\chi}')\, \varphi \right]}{d} + \frac{(1+q)}{q} \nu \partial'_\beta \left[\partial'_\beta U \sigma_\alpha \right] + \mathcal{O}(\partial^2), \tag{B.25}$$

where $\mathcal{O}(\partial^2)$ denotes the contributions coming from higher-order powers of the gradient. The equation for $\sigma_\alpha(\boldsymbol{\chi}, \boldsymbol{r}, t)$ can be substituted into the continuity equation for the marginal density $\rho(\boldsymbol{\chi}, t) = \int \mathrm{d}\boldsymbol{r}\, \varphi(\boldsymbol{\chi}, \boldsymbol{r}, t)$, which can be obtained by integrating (B.23) over the relative distance $\boldsymbol{r}$, finding

$$\partial_t \rho(\boldsymbol{\chi}, t) = -\partial_\alpha \left[\int \mathrm{d}\boldsymbol{r}\, \frac{v_\mathrm{a}(\boldsymbol{\chi}')}{1+q} \sigma_\alpha(\boldsymbol{\chi}, \boldsymbol{r}, t) - v_w \delta_{\alpha,0} \rho(\boldsymbol{\chi}, t) - \frac{D}{1+q} \partial_\alpha \rho(\boldsymbol{\chi}, t) \right]. \tag{B.26}$$

On the r.h.s. of this equation one recognizes the probability current $J_\alpha(\boldsymbol{\chi},t)$, corresponding to the expression in square brackets. In addition to the diffusive term $\propto \boldsymbol{\nabla}\rho$ (with a renormalized diffusion coefficient $D/(1+q)$, as it refers to the diffusion of the center of friction) and to the current $\propto \boldsymbol{v}_w\rho$ due to the change of reference system, the additional contribution

$$I_\alpha(\boldsymbol{\chi},t) \equiv \frac{1}{1+q}\int \mathrm{d}\boldsymbol{r}\, v_{\mathrm{a}}(\boldsymbol{\chi}')\,\sigma_\alpha(\boldsymbol{\chi},\boldsymbol{r},t) \tag{B.27}$$

appears. By using the expression of the quasi-stationary polarization field (B.25), $I_\alpha(\boldsymbol{\chi},t)$ can be written as

$$\begin{aligned} &I_\alpha(\boldsymbol{\chi},t) = \\ &= \int \mathrm{d}\boldsymbol{r}\,\frac{\tau v_{\mathrm{a}}(\boldsymbol{\chi}')}{1+q}\left\{-\frac{\partial_\alpha\left[v_{\mathrm{a}}(\boldsymbol{\chi}')\,\varphi\right]}{d(1+q)} - \frac{\partial'_\alpha\left[v_{\mathrm{a}}(\boldsymbol{\chi}')\,\varphi\right]}{d} - \frac{(1+q)}{q}\nu\partial'_\beta\left[F_\beta(\boldsymbol{r})\sigma_\alpha\right]\right\}, \end{aligned} \tag{B.28}$$

where $F_\beta(\boldsymbol{r}) = -\partial_{\boldsymbol{r}_\beta}U(\boldsymbol{r})$. Integrating by part and using $\partial'_\alpha v_{\mathrm{a}}(\boldsymbol{\chi}') = \frac{q}{1+q}\partial_\alpha v_{\mathrm{a}}(\boldsymbol{\chi}')$, which follows from (B.2) and the definitions of ∂'_α and ∂_α given after (B.16), we can rewrite the previous expression as:

$$\begin{aligned} I_\alpha(\boldsymbol{\chi},t) &= \frac{\tau}{1+q}\int \mathrm{d}\boldsymbol{r}\, v_{\mathrm{a}}(\boldsymbol{\chi}')\left[-\frac{\partial_\alpha\left[v_{\mathrm{a}}(\boldsymbol{\chi}')\,\varphi\right]}{d(1+q)}\right] \\ &+ \frac{\tau}{1+q}\int \mathrm{d}\boldsymbol{r}\,\frac{q}{(1+q)d}\left[v_{\mathrm{a}}(\boldsymbol{\chi}')\,\varphi\right]\partial_\alpha v_{\mathrm{a}}(\boldsymbol{\chi}') \\ &+ \frac{\tau\nu}{1+q}\int \mathrm{d}\boldsymbol{r}\, F_\beta(\boldsymbol{r})\sigma_\alpha\partial_\beta v_{\mathrm{a}}(\boldsymbol{\chi}')\,. \end{aligned} \tag{B.29}$$

We define now the quantity Σ as

$$\Sigma(\boldsymbol{\chi},t) \equiv \int \mathrm{d}\boldsymbol{r}\, F_\beta(\boldsymbol{r})\sigma_\alpha(\boldsymbol{\chi},\boldsymbol{r},t)\partial_\beta v_{\mathrm{a}}(\boldsymbol{\chi}')\ . \tag{B.30}$$

By substituting (B.25) into the above expression for Σ and neglecting all terms of order $\mathcal{O}(\partial^2)$, we obtain:

$$\begin{aligned} \Sigma &= \int \mathrm{d}\boldsymbol{r}\,\tau F_\beta(\boldsymbol{r})\partial_\beta v_{\mathrm{a}}(\boldsymbol{\chi}')\left[-\frac{\partial'_\alpha\left[v_{\mathrm{a}}(\boldsymbol{\chi}')\,\varphi\right]}{d} - \frac{(1+q)}{q}\nu\partial'_\gamma\left[F_\gamma(\boldsymbol{r})\sigma_\alpha\right]\right] \\ &= \int \mathrm{d}\boldsymbol{r}\tau\left[\frac{v_{\mathrm{a}}(\boldsymbol{\chi}')\,\varphi}{d}\partial'_\alpha\left[F_\beta(\boldsymbol{r})\partial_\beta v_{\mathrm{a}}(\boldsymbol{\chi}')\right] + \frac{(1+q)}{q}\nu F_\gamma(\boldsymbol{r})\sigma_\alpha\partial'_\gamma\left[F_\beta(\boldsymbol{r})\partial_\beta v_{\mathrm{a}}(\boldsymbol{\chi}')\right]\right]. \end{aligned} \tag{B.31}$$

The last line can be further simplified by separately considering

$$\begin{aligned} \partial'_\alpha\left[F_\beta(\boldsymbol{r})\partial_\beta v_{\mathrm{a}}(\boldsymbol{\chi}')\right] &= \partial'_\alpha F_\beta(\boldsymbol{r})\partial_\beta v_{\mathrm{a}}(\boldsymbol{\chi}') + F_\beta(\boldsymbol{r})\partial'_\alpha\partial_\beta v_{\mathrm{a}}(\boldsymbol{\chi}') \\ &= \partial'_\alpha F_\beta(\boldsymbol{r})\partial_\beta v_{\mathrm{a}}(\boldsymbol{\chi}') + \frac{q}{1+q}F_\beta(\boldsymbol{r})\partial_\alpha\partial_\beta v_{\mathrm{a}}(\boldsymbol{\chi}') \\ &= \partial'_\alpha F_\beta(\boldsymbol{r})\partial_\beta v_{\mathrm{a}}(\boldsymbol{\chi}') + \mathcal{O}(\partial^2)\,. \end{aligned} \tag{B.32}$$

Moreover, since the attractive interaction between the cargo and the active particle is modeled by a harmonic potential with stiffness κ and zero rest length, we have that

$$\partial'_\alpha F_\beta(\boldsymbol{r}) = -\kappa\delta_{\alpha,\beta} = \partial'_\beta F_\alpha(\boldsymbol{r}). \tag{B.33}$$

Accordingly, (B.32) can be written as

$$\partial'_\alpha \left[F_\beta(\boldsymbol{r})\partial_\beta v_\mathrm{a}\left(\boldsymbol{\chi}'\right)\right] \simeq -\kappa\delta_{\alpha,\beta}\partial_\beta v_\mathrm{a}\left(\boldsymbol{\chi}'\right) = -\kappa\partial_\alpha v_\mathrm{a}\left(\boldsymbol{\chi}'\right), \tag{B.34}$$

and thus (B.31) becomes

$$\begin{aligned}\Sigma &= -\kappa\tau\int \mathrm{d}\boldsymbol{r}\left[\frac{v_\mathrm{a}\left(\boldsymbol{\chi}'\right)\varphi}{d}\partial_\alpha v_\mathrm{a}\left(\boldsymbol{\chi}'\right) + \frac{(1+q)}{q}\nu F_\gamma(\boldsymbol{r})\sigma_\alpha\partial_\gamma v_\mathrm{a}\left(\boldsymbol{\chi}'\right)\right] = \\ &= -\frac{\kappa\tau}{2d}\int \mathrm{d}\boldsymbol{r}\,\varphi\partial_\alpha v_\mathrm{a}^2\left(\boldsymbol{\chi}'\right) - \kappa\tau\nu\frac{(1+q)}{q}\Sigma,\end{aligned} \tag{B.35}$$

where, in the last line, we used the definition of Σ given in (B.30). Accordingly, the previous equation can be solved for Σ yielding

$$\Sigma(\boldsymbol{\chi},t) = -\frac{1}{2d}\frac{\gamma\tau/\tau_\mathrm{r}}{1+\frac{1+q}{q}\frac{\tau}{\tau_\mathrm{r}}}\int \mathrm{d}\boldsymbol{r}\,\varphi(\boldsymbol{\chi},\boldsymbol{r},t)\partial_\alpha v_\mathrm{a}^2\left(\boldsymbol{\chi}'\right), \tag{B.36}$$

where, as in Chapter 4, we introduced the typical time scale $\tau_\mathrm{r} = 1/\kappa\nu$. The expression of $\Sigma(\boldsymbol{\chi},t)$ can then be substituted into (B.29), giving

$$I_\alpha(\boldsymbol{\chi},t) = -\frac{\tau}{d(1+q)^2}\int \mathrm{d}\boldsymbol{r}\,v_\mathrm{a}^2\left(\boldsymbol{\chi}'\right)\partial_\alpha\varphi - \frac{1}{2}\frac{\tau}{d(1+q)^2}\epsilon\int \mathrm{d}\boldsymbol{r}\,\varphi\partial_\alpha v_\mathrm{a}^2\left(\boldsymbol{\chi}'\right), \tag{B.37}$$

where we introduced the tactic coupling

$$\epsilon = 1 - \frac{q}{1+\frac{1+q}{q}\frac{\tau}{\tau_\mathrm{r}}}, \tag{B.38}$$

reported in equation (4.11) of Chapter 4. Moreover, if the typical distance between the active carrier and the cargo is small compared to the persistence length, we can approximate $\varphi = \varphi(\boldsymbol{\chi},\boldsymbol{r},t)$ in the integrands above as:

$$\varphi(\boldsymbol{\chi},\boldsymbol{r},t) \approx \rho(\boldsymbol{\chi},t)\delta(\boldsymbol{r}). \tag{B.39}$$

Within this approximation, the total current $J_\alpha(\boldsymbol{\chi},t)$ introduced after (B.26) can be written as

$$J_\alpha(\boldsymbol{\chi},t) = V_{\mathrm{eff},\alpha}(\boldsymbol{\chi})\rho(\boldsymbol{\chi},t) - \partial_\alpha\left[D_\mathrm{eff}\rho(\boldsymbol{\chi},t)\right], \tag{B.40}$$

where the effective drift and diffusivity are, respectively, given by

$$V_{\mathrm{eff},\alpha}(\boldsymbol{\chi}) = (1-\epsilon/2)\partial_\alpha D_{\mathrm{eff}}(\boldsymbol{\chi}) - v_w\delta_{\alpha,0} \quad \text{and} \quad D_{\mathrm{eff}}(\boldsymbol{\chi}) = \frac{D}{1+q} + \frac{\tau v_{\mathrm{a}}^2(\boldsymbol{\chi})}{d(1+q)^2}, \tag{B.41}$$

which are reported in (4.10) of Chapter4. The stationary solution of the effective Fokker-Planck equation

$$\partial_t\rho(\boldsymbol{\chi},t) = -\nabla_{\boldsymbol{\chi}}\cdot\left[\boldsymbol{V}_{\mathrm{eff}}(\boldsymbol{\chi})\rho(\boldsymbol{\chi},t) - \nabla_{\boldsymbol{\chi}}(D_{\mathrm{eff}}(\boldsymbol{\chi})\rho(\boldsymbol{\chi},t))\right] \tag{B.42}$$

can be easily proved to be [167, 175, 176]

$$\frac{\rho(\boldsymbol{\chi})}{\rho_b} = \frac{L\, D_{\mathrm{eff}}^{-1}(\chi_0)\int_0^L \mathrm{d}x \exp\left\{-\int_{\chi_0}^{\chi_0+x}\mathrm{d}y\frac{V_{\mathrm{eff},0}(y)}{D_{\mathrm{eff}}(y)}\right\}}{\int_0^L \mathrm{d}u\int_0^L \mathrm{d}x\, D_{\mathrm{eff}}^{-1}(u)\exp\left\{-\int_u^{u+x}\mathrm{d}y\frac{V_{\mathrm{eff},0}(y)}{D_{\mathrm{eff}}(y)}\right\}} \tag{B.43}$$

in the case of periodic boundary conditions, as reported in Chapter 4. Moreover, the system can sustain a finite stationary flux in the comoving frame

$$J_0 = \frac{\rho_b L\left[1-\exp\left\{-\int_0^L \mathrm{d}y\frac{V_{\mathrm{eff},0}(y)}{D_{\mathrm{eff}}(y)}\right\}\right]}{\int_0^L \mathrm{d}u\int_0^L \mathrm{d}x\, D_{\mathrm{eff}}^{-1}(u)\exp\left\{-\int_u^{u+x}\mathrm{d}y\frac{V_{\mathrm{eff},0}(y)}{D_{\mathrm{eff}}(y)}\right\}} \tag{B.44}$$

along the direction $\boldsymbol{e}_0$, which can be used to compute the average drift velocity $v_d = J_0/\rho_b + v_w$ in the lab frame, as reported in (4.16) of Chapter 4.

B.3 Drift velocity with critical cargo

In this Section we show that the drift velocity v_d (given by (4.16)), derived in the limit of slowly propagating activity field $v_w \ll v_0$, vanishes if q takes the threshold value q_{th} reported in (4.13) of Chapter 4. In particular, when $q = q_{\mathrm{th}}$, the tactic coupling ϵ in (B.38) vanishes and the effective drift in (B.41) becomes

$$V_{\mathrm{eff},\alpha}(\boldsymbol{\chi}) = \partial_\alpha D_{\mathrm{eff}}(\boldsymbol{\chi}) - v_w\delta_{\alpha,0}\,. \tag{B.45}$$

This expression can be substituted in (B.44) to calculate the stationary current in the comoving frame. In particular, the denominator of that expression reads:

$$\begin{aligned}
&\int_0^L \mathrm{d}u\int_0^L \mathrm{d}x\, D_{\mathrm{eff}}^{-1}(u)\exp\left\{-\int_u^{u+x}\mathrm{d}y\,\left[\partial_\alpha \ln D_{\mathrm{eff}}(y) - \frac{v_w}{D_{\mathrm{eff}}(y)}\right]\right\}\\
&= \int_0^L \mathrm{d}u\int_0^L \mathrm{d}x\, D_{\mathrm{eff}}^{-1}(u+x)\exp\left\{\int_u^{u+x}\mathrm{d}y\,\frac{v_w}{D_{\mathrm{eff}}(y)}\right\}\\
&= \frac{1}{v_w}\int_0^L \mathrm{d}u\left[\exp\left\{\int_u^{u+L}\mathrm{d}y\,\frac{v_w}{D_{\mathrm{eff}}(y)}\right\}-1\right]\\
&= \frac{L}{v_w}\left[\exp\left\{\int_0^L \mathrm{d}y\,\frac{v_w}{D_{\mathrm{eff}}(y)}\right\}-1\right],
\end{aligned} \tag{B.46}$$

where in the last equality we used that the effective drift $D_{\text{eff}}(y)$ is a periodic function with period L. Analogously the numerator of (B.44) is given by:

$$\rho_b L \left[1 - \exp\left\{-\int_0^L \mathrm{d}y \frac{\partial_\alpha D_{\text{eff}}(y) - v_w}{D_{\text{eff}}(y)}\right\}\right] = \rho_b L \left[1 - \exp\left\{\int_0^L \mathrm{d}y \frac{v_w}{D_{\text{eff}}(y)}\right\}\right]. \tag{B.47}$$

Combining (B.46) and (B.47), the average drift velocity v_d reads:

$$v_d = \frac{J_0}{\rho_b} + v_w = v_w \frac{\rho_b L \left[1 - \exp\left\{\int_0^L \mathrm{d}y \frac{v_w}{D_{\text{eff}}(y)}\right\}\right]}{\rho_b L \left[\exp\left\{\int_0^L \mathrm{d}y \, \frac{v_w}{D_{\text{eff}}(y)}\right\} - 1\right]} + v_w = 0 \tag{B.48}$$

B.4 Fast active traveling waves

In this Section we derive analytical expressions for the stationary density, stationary current and average drift velocity in the regime of fast active traveling waves, i.e., for $v_w \gg v_0$. To this aim, we adopt a different strategy to close the hierarchy of equations governing the dynamics of the modes given by (B.23) and (B.24), which hinges on assuming a small activity v_0 compared to the wave velocity v_w. For simplicity, we present the derivation for the one-dimensional case $d = 1$ with the sinusoidal activity field reported in (4.14). The extension to the case with $d \neq 1$ is straightforward. To implement the new closure scheme, we start from the dynamics of the polarization field given by (B.24), which can be conveniently rewritten as:

$$\hat{\mathcal{L}}_\sigma \sigma(\chi, r, t) = -\frac{\partial_\chi \left[v_{\text{a}}(\chi')\varphi\right]}{(1+q)} - \partial_r \left[v_{\text{a}}(\chi')\varphi\right] + \Upsilon(\chi, r, t)\,, \tag{B.49}$$

where $\varphi = \varphi(\chi, r, t)$, the position χ' of the active carrier in the comoving frame is defined as in (B.2), specialized to $d = 1$, and $\Upsilon(\chi, r, t)$ includes the contributions of higher-order modes. In the previous equation, the operator $\hat{\mathcal{L}}_\sigma$ is defined as

$$\hat{\mathcal{L}}_\sigma = \partial_t + \frac{1}{\tau} - v_w \partial_\chi - \frac{D}{1+q}\partial_\chi^2 - \frac{(1+q)D}{q}\left[\partial_r^2 + \frac{1}{\ell^2}\partial_r r\right], \tag{B.50}$$

with the characteristic length $\ell = \sqrt{D\tau_{\text{r}}}$ and $\tau_{\text{r}} = 1/\nu\kappa$. We first determine the Green function $G(\chi, r, t; \chi_0, r_0, t_0)$ of the operator $\hat{\mathcal{L}}_\sigma$, defined as:

$$\hat{\mathcal{L}}_\sigma G(\chi, r, t; \chi_0, r_0, t_0) = \delta(\chi - \chi_0)\delta(r - r_0)\delta(t - t_0)\,. \tag{B.51}$$

Note that, due to the translational invariance of the operator $\hat{\mathcal{L}}_\sigma$ in the variables χ and t, one expects $G(\chi, r, t; \chi_0, r_0, t_0)$ to be a function of $\chi - \chi_0$ and $t - t_0$. The presence of the interparticle potential, instead, breaks the transaltional invariance of $\hat{\mathcal{L}}_\sigma$ with respect to r and therefore $G(\chi, r, t; \chi_0, r_0, t_0)$ depends separately on r and r_0. Accordingly, we can write $G(\chi, r, t; \chi_0, r_0, t_0) = G(\chi - \chi_0, r, t - t_0; 0, r_0, 0) \equiv G(\chi - \chi_0, r, t - t_0; r_0)$ where in the last equality we introduce a convenient shorthand notation. The function $G(\chi, r, t; r_0)$ can be conveniently determined by expanding it in the Fourier-Hermite basis

$$G(\chi, r, t; r_0) = \frac{1}{\ell} \sum_{n=0}^{\infty} \int \frac{\mathrm{d}\omega}{2\pi} \int \frac{\mathrm{d}\tilde{q}}{2\pi} \tilde{G}_n(\tilde{q}, \omega; r_0) e^{i\tilde{q}\chi + i\omega t} u_n(r), \tag{B.52}$$

where $u_n(r)$ is given by

$$u_n(r) = e^{-r^2/2\ell^2} H_n(r/\ell)\,, \tag{B.53}$$

and $H_n(x)$ is the n-th probabilist's Hermite polynomial. With this expansion, the l.h.s. of (B.51) becomes

$$\begin{aligned} \frac{1}{\ell} \sum_{n=0}^{\infty} \int \frac{\mathrm{d}\omega}{2\pi} \int \frac{\mathrm{d}\tilde{q}}{2\pi} &\left[i\omega + \tau^{-1} + \frac{D}{1+q}\tilde{q}^2 + i v_w \tilde{q} + \frac{(1+q)D}{q} \frac{n}{\ell^2} \right] \\ &\times \tilde{G}_n(\tilde{q}, \omega; r_0) e^{i\tilde{q}\chi + i\omega t} u_n(r), \end{aligned} \tag{B.54}$$

while its r.h.s. is

$$\frac{1}{\ell} \sum_{n=0}^{\infty} \int \frac{\mathrm{d}\omega}{2\pi} \int \frac{\mathrm{d}\tilde{q}}{2\pi} \tilde{u}_n(r_0) e^{i\tilde{q}\chi + i\omega t} u_n(r), \tag{B.55}$$

where we used the fact that $\delta(r - r_0)$ in (B.51) can be written as

$$\frac{1}{\ell} \sum_{n=0}^{\infty} \tilde{u}_n(r_0) u_n(r) = \delta(r - r_0)\,, \tag{B.56}$$

and the functions $\tilde{u}_n(r)$ are defined as:

$$\tilde{u}_n(r) = \frac{1}{\sqrt{2\pi} n!} H_n(r/\ell)\,. \tag{B.57}$$

Therefore, by comparing (B.54) with (B.55), the Green function in reciprocal space turns out to be given by

$$\tilde{G}_n(\tilde{q}, \omega; r_0) = \frac{\tilde{u}_n(r_0)}{i\omega + \tau^{-1} + \frac{D}{1+q}\tilde{q}^2 + i v_w \tilde{q} + \frac{(1+q)D}{q}\frac{n}{\ell^2}}\,. \tag{B.58}$$

After inserting this expression of $\tilde{G}_n(\tilde{q}, \omega; r_0)$ into (B.52), one can readily calculate the integral in ω via the residue theorem. The corresponding residue is a Gaussian function of $\tilde{q}$ and thus the corresponding integral is also straightforward, with the final result

$$G(\chi, r, t; r_0) = \frac{\Theta(t)}{\ell} \frac{\exp\left\{-\frac{t}{\tau} - \frac{(\chi+v_w t)^2}{4\frac{D}{1+q}t}\right\}}{\sqrt{4\pi\frac{D}{1+q}t}} \sum_{n=0}^{\infty} \exp\left\{-\frac{(1+q)Dn}{q\ell^2}t\right\} \tilde{u}_n(r_0) u_n(r), \tag{B.59}$$

where the Heaviside function Θ is defined such that $\Theta(t > 0) = 1$ and $\Theta(t \leq 0) = 0$. Before considering the last summation, we introduce the quantity

$$s = \exp\left\{-\frac{(1+q)}{q}\frac{Dt}{\ell^2}\right\} < 1\,. \tag{B.60}$$

In terms of s the remaining sum in (B.59) can be written as

$$\begin{aligned}\frac{1}{\ell}\sum_{n=0}^{\infty} s^n \tilde{u}_n(r_0) u_n(r) &= \frac{1}{\ell\sqrt{2\pi}} \exp\left\{-\frac{r^2}{2\ell^2}\right\} \sum_{n=0}^{\infty} \frac{s^n}{n!} H_n\left(\frac{r_0}{\ell}\right) H_n\left(\frac{r}{\ell}\right) \\ &= \frac{1}{\sqrt{2\pi\ell^2(1-s^2)}} \exp\left\{-\frac{(r-sr_0)^2}{2(1-s^2)\ell^2}\right\}\end{aligned} \tag{B.61}$$

where we used the expression of u_n and $\tilde{u}_n$ given in (B.53) and (B.57), respectively, and in the second equality we used Mehler's formula [333] for probabilist's Hermite polynomials, i.e.,

$$\sum_{n=0}^{\infty} \frac{s^n}{n!} H_n(x) H_n(y) = \frac{1}{\sqrt{1-s^2}} \exp\left\{-\frac{s^2(x^2+y^2) - 2sxy}{2(1-s^2)}\right\} \quad \text{for} \quad -1 < s < 1\,. \tag{B.62}$$

Accordingly, by using the equations (B.59), (B.60), and (B.61), the Green function in (B.51) reads:

$$G(\chi, r, t; r_0) = \Theta(t) \exp\{-t/\tau\} \frac{\exp\left\{-\frac{(\chi+v_w t)^2}{4Dt/(1+q)}\right\}}{\sqrt{4\pi Dt/(1+q)}} \frac{\exp\left\{-\frac{(r-sr_0)^2}{2(1-s^2)\ell^2}\right\}}{\sqrt{2\pi\ell^2(1-s^2)}}. \tag{B.63}$$

Once the Green function is known, one can determine $\sigma(\chi, r, t)$ by computing the convolution integral over χ_0, t_0, and r_0 of the product between $G(\chi - \chi_0, r, t - t_0; r_0)$ and the r.h.s. of (B.49) evaluated for $\chi = \chi_0$, $r = r_0$, and $t = t_0$. At this stage, we are ready to compute the contribution to the flux in (B.26) given by (B.27), specialized to the case $d = 1$. In particular, one has

$$
\begin{aligned}
I(\chi, t) = & \\
& - \int dr\, v_{\mathrm{a}}\left(\chi'\right) \int_{-\infty}^{\infty} d\chi_0 dr_0 dt_0\, G(\chi - \chi_0, r, t - t_0; r_0) \frac{\partial_{\chi_0}\left[v_{\mathrm{a}}(\chi_0 + \frac{qr_0}{1+q})\varphi(\chi_0, r_0, t_0)\right]}{(1+q)^2} \\
& - \int dr\, v_{\mathrm{a}}\left(\chi'\right) \int_{-\infty}^{\infty} d\chi_0 dr_0 dt_0\, G(\chi - \chi_0, r, t - t_0; r_0) \frac{\partial_{r_0}\left[v_{\mathrm{a}}(\chi_0 + \frac{qr_0}{1+q})\varphi(\chi_0, r_0, t_0)\right]}{(1+q)} \\
& + \int dr\, v_{\mathrm{a}}\left(\chi'\right) \int_{-\infty}^{\infty} d\chi_0 dr_0 dt_0\, G(\chi - \chi_0, r, t - t_0; r_0) \frac{\Upsilon(\chi_0, r_0, t_0)}{(1+q)}.
\end{aligned}
\tag{B.64}
$$

The latter quantity can be computed under the approximation of small activity field compared to v_w, by keeping only terms of the lowest order in v_0. For this reason, we neglect the contribution coming from higher-order modes $\Upsilon(\chi, r, t)$, thus closing the hierarchy, and we evaluate the first two integrals by assuming that the density field

$$
\varphi(\chi_0, r_0, t_0) = \rho_b \frac{e^{-r_0^2/2\ell^2}}{\sqrt{2\pi\ell^2}} + \mathcal{O}(v_0/v_w) \tag{B.65}
$$

is approximately equal to the one at equilibrium, i.e., for $v_{\mathrm{a}} \propto v_0 = 0$, with ρ_b the bulk density. In this way, all integrals appearing in the first two lines are standard Gaussian integrals, and can be easily calculated. As a result, $I(\chi, t)$ is actually independent of time (as φ in Eq. (B.65)) and is given by

$$
\begin{aligned}
I(\chi) = & - \frac{\rho_b \tau v_0^2 \exp\left(-\frac{q^2\ell^2}{2\lambda^2(1+q)^2}\right)}{\lambda(1+q)^2} \left[\frac{\cos(\chi/\lambda + \psi_0)}{|z_0|} - q \frac{\cos\left(\chi/\lambda\right)}{\left(1 + \frac{(1+q)\tau D}{q\ell^2}\right)} \right. \\
& \left. + \exp\left(-\frac{q^2\ell^2}{2\lambda^2(1+q)^2}\right) \sum_{n=0}^{\infty} \frac{1}{n!} \left[\frac{q^2\ell^2}{\lambda^2(1+q)^2}\right]^n \left[f_n(\chi) + q f_{n+1}(\chi)\right] \right],
\end{aligned}
\tag{B.66}
$$

with

$$
f_n(\chi) = \frac{(-1)^n \sin(2\chi/\lambda + \psi_n) - \sin\psi_n}{2|z_n|}, \tag{B.67}
$$

and where ψ_n and $|z_n|$ are the phase and the modulus, respectively, of the complex number

$$
z_n = 1 + \frac{\tau D}{\lambda^2(1+q)} + \frac{(1+q)\tau D}{q\ell^2} n + i\frac{\tau v_w}{\lambda}. \tag{B.68}
$$

In order to compute the marginal probability density $\rho(\chi)$ in the steady state, we impose that the probability current in (B.26) equals a constant J. Therefore, one has to solve the following differential equation,

$$\frac{D}{1+q}\partial_\chi \rho(\chi) + v_w \rho(\chi) = I(\chi) - J, \tag{B.69}$$

with $I(\chi)$ given in (B.66). This can be done by first computing the Green function G_1, defined by

$$\left(\frac{D}{1+q}\partial_\chi + v_w\right) G_1(\chi - \chi_0) = \delta(\chi - \chi_0), \tag{B.70}$$

which reads (in the case of $v_w > 0$)

$$G_1(\chi - \chi_0) = \frac{(1+q)}{D}\Theta(\chi - \chi_0)\exp\left\{-\frac{(1+q)v_w}{D}(\chi - \chi_0)\right\}, \tag{B.71}$$

and then the following convolution:

$$\rho(\chi) = \frac{(1+q)}{D}\int_{-\infty}^{\chi} d\chi' \exp\left\{-\frac{(1+q)v_w}{D}(\chi - \chi')\right\} I(\chi') - \frac{J}{v_w}. \tag{B.72}$$

The contribution coming from the homogeneous solution of (B.69) vanishes under periodic boundary conditions. Also in this case, the convolution involves Gaussian integrals, the standard calculation of which is not reported here for the sake of space. As a result, the stationary density $\rho(\chi)$ can be expressed as

$$\begin{aligned}\rho(\chi) = -\frac{\rho_b \tau v_0^2}{D\lambda(1+q)} e^{-\frac{q^2\ell^2}{2\lambda^2(1+q)^2}} \Bigg[& \frac{\cos(\chi/\lambda + \psi_0 + \varphi(\lambda))}{|\zeta(\lambda)||z_0|} - \frac{q\cos\left(\chi/\lambda + \varphi(\lambda)\right)}{|\zeta(\lambda)|\left(1 + \frac{(1+q)\tau D}{q\ell^2}\right)} \\ & + \exp\left(-\frac{q^2\ell^2}{2\lambda^2(1+q)^2}\right)\sum_{n=0}^{\infty}\frac{1}{n!}\left(\frac{q^2\ell^2}{\lambda^2(1+q)^2}\right)^n \left[g_n(\chi) + q g_{n+1}(\chi)\right]\Bigg] - \frac{J}{v_w},\end{aligned} \tag{B.73}$$

where the functions $\{g_n(\chi)\}$ are defined as

$$g_n(\chi) = \frac{(-1)^n \sin(2\chi/\lambda + \psi_n + \varphi(\lambda/2))}{2|\zeta(\lambda/2)||z_n|} - \frac{\sin(\psi_n)}{2\frac{(1+q)v_w}{D}|z_n|}, \tag{B.74}$$

and where $\varphi(\lambda)$ and $|\zeta(\lambda)|$ are the phase and the modulus, respectively, of the λ-dependent complex number

$$\zeta(\lambda) = \frac{(1+q)v_w}{D} - i\lambda^{-1}. \tag{B.75}$$

Moreover, by imposing the normalization of the marginal density $\rho(\chi)$, we find the expression of the stationary flux J in the comoving frame:

$$J = -\frac{v_w}{L}\left[1 - \frac{\tau v_0^2 e^{-\frac{q^2\ell^2}{\lambda^2(1+q)^2}}}{2v_w\lambda(1+q)^2}\sum_{n=0}^{\infty}\frac{\left(\frac{q^2\ell^2}{\lambda^2(1+q)^2}\right)^n}{n!}\left(\frac{\sin(\psi_n)}{|z_n|} + \frac{q\sin(\psi_{n+1})}{|z_{n+1}|}\right)\right], \tag{B.76}$$

and, as a consequence, the average drift velocity:

$$\frac{v_d}{v_0} = \frac{l_p}{2\lambda(1+q)^2} e^{-\frac{q^2\ell^2}{\lambda^2(1+q)^2}} \sum_{n=0}^{\infty} \frac{\left(\frac{q^2\ell^2}{\lambda^2(1+q)^2}\right)^n}{n!} \left(\frac{\sin(\psi_n)}{|z_n|} + \frac{q\sin(\psi_{n+1})}{|z_{n+1}|} \right). \tag{B.77}$$

The previous equation is reported in Chapter 4 in the limit of small thermal diffusivity $D\tau_{\mathrm{r}} \ll \lambda^2$ (see equation (4.21)).

B.5 Simulation details

All numerical data presented in Chapter 4 have been obtained from Brownian-dynamics simulations of the discretized version of the stochastic equation of motion (4.1), using the Euler-Maruyama scheme with integration timestep $\Delta t = 0.01$. In particular, the stationary density of the center-of-friction reported in Figure 4.2 has been numerically estimated on a time series coming from a single simulation of duration 10^8 steps, using periodic boundary conditions with a cell size of $L = 10$. Other simulation parameters were: $v_w = 10^{-2}$, $v_0 = 1.0$, $\tau = 0.1$, $\kappa = 5$, $\gamma = 1.0$, $D = 10^{-3}$ (note that $k_BT = \gamma D = 10^{-3}$), $\lambda = 10/(4\pi)$, $q_{\mathrm{high}} = 4$ and $q_{\mathrm{low}} = 1$. The numerical results about the drift velocity in both cases of slow and fast propagating activity wave, shown in Figures 4.3 and 4.4, were obtained by computing $(\chi(t) + v_w t - \chi(0))/t$ for each of $N = 10^3$ independent stochastic trajectories of length $t = 10^6\Delta t$ with open boundary conditions, and averaging such a quantity over different realizations. In this case we used $D = 10^{-2}$.

Appendix C

Appendix of Chapter 5

We provide here a detailed derivation of the analytical predictions reported in Chapter 5. In particular, in Sec. C.1 we marginalize out the active degrees of freedom by using a moment expansion and obtain a hierarchy of coupled differential equations for the expansion coefficients. A closure scheme for this hierarchy is presented in Sec C.2. This relies on the separation of time scales between the evolution of the probability density of the polymer structure and that of higher-order expansion coefficients, as well as on the assumption that the activity field is characterized by small gradients. The effective evolution equation for the density of the center-of-mass of the polymer (Equation (5.10) of Chapter 5) is derived in Sec C.2. In Sec. C.3 we consider a more realistic model of a polymer chain that includes excluded volume interaction (to account for steric hindrance effects) and finite extensibility of the bonds. We show by means of numerical simulations that the phenomenology presented in the case of ideal chains is not altered by these additional interactions. In Sec. C.4 we comment on the fact that the polymers' separation described in Chapter 5 is a pure nonequilibrium effect, which would disappear if the underlying stochastic dynamics satisfied the detailed balance condition. Finally, in Sec. C.5 we report the details of the numerical simulations carried out to obtain the results presented in Chapter 5 as well as in this Appendix.

C.1 Moment expansion

In order to determine the spatial regions of the bath in which the chain tends to localize, we apply a two-step coarse-graining procedure to the dynamics of the system. First, we marginalize the 1-time joint probability density $\mathcal{P}(\{\boldsymbol{\chi}\}, \{\boldsymbol{\eta}\}, t)$ over the orientation vectors $\{\boldsymbol{\eta}\}$ associated to the active forces and obtain an exact evolution equation for the marginal density

$$\varrho(\{\boldsymbol{\chi}\},t) \equiv \int \prod_{i=0}^{N-1} \mathrm{d}\boldsymbol{\eta}_i \mathcal{P}(\{\boldsymbol{\chi}\},\{\boldsymbol{\eta}\},t). \tag{C.1}$$

As a second step, under some assumptions which will be introduced in the following, we integrate out the information concerning the internal structure of the chain (i.e., the Rouse modes $\{\boldsymbol{\chi}_i\}$ with $i>0$)[84], thus getting the marginal density $\rho_0(\boldsymbol{\chi}_0,t)$ of the rescaled center-of-mass $\boldsymbol{\chi}_0$ which is defined as

$$\rho_0(\boldsymbol{\chi}_0,t) \equiv \int \prod_{i=1}^{N-1} \mathrm{d}\boldsymbol{\chi}_i \, \varrho(\{\boldsymbol{\chi}\},t). \tag{C.2}$$

To marginalize the active degrees of freedom $\{\boldsymbol{\eta}\}$, we first expand the joint probability density $\mathcal{P}(\{\boldsymbol{\chi}\},\{\boldsymbol{\eta}\},t)$ into the eigenfunctions of the operator $\mathcal{L}_{\boldsymbol{\eta}}$ which contributes to the dynamics of $\mathcal{P}$ according to Equation (5.8). It can be shown that the latter is diagonalized by the following set of functions:

$$u_{\boldsymbol{n}}(\{\boldsymbol{\eta}\}) = \frac{\exp\left\{-\frac{d\sum_j \boldsymbol{\eta}_j^2}{2}\right\} \prod_{i=0}^{N-1}\prod_{\alpha=1}^{d} H_{n_{i\alpha}}\left(\sqrt{d}\eta_{i\alpha}\right)}{(2\pi/d)^{Nd/2}}, \tag{C.3}$$

where $\boldsymbol{n}$ denotes an $N\times d$ matrix of non-negative integers used to label the eigenfunctions and $H_n(x)$ is the n-th Hermite polynomial in the probabilist convention [333]. The corresponding eigenvalues $\lambda_{\boldsymbol{n}}$ are proportional to the inverse persistence time $1/\tau$:

$$\lambda_{\boldsymbol{n}} = -\tau^{-1}\sum_{i=0}^{N-1}\sum_{\alpha=1}^{d} n_{i\alpha}\,. \tag{C.4}$$

Accordingly, the joint probability density $\mathcal{P}(\{\boldsymbol{\chi}\},\{\boldsymbol{\eta}\},t)$ can be rewritten as a weighted combination of the basis elements $\{u_{\boldsymbol{n}}(\{\boldsymbol{\eta}\})\}$:

$$\mathcal{P}(\{\boldsymbol{\chi}\},\{\boldsymbol{\eta}\},t) = \sum_{\boldsymbol{n}\in\mathbb{N}_0^{N\times d}} \phi_{\boldsymbol{n}}(\{\boldsymbol{\chi}\},t)u_{\boldsymbol{n}}(\{\boldsymbol{\eta}\})\,, \tag{C.5}$$

where the dependence on the Rouse modes and time is now brought in by the expansion coefficients $\{\phi_{\boldsymbol{n}}(\{\boldsymbol{\chi}\},t)\}$. In order to derive their governing equations, we find convenient to first introduce the set of auxiliary functions $\{\tilde{u}_{\boldsymbol{n}}(\{\boldsymbol{\eta}\})\}$ defined as:

$$\tilde{u}_{\boldsymbol{n}}(\{\boldsymbol{\eta}\}) = \prod_{i=0}^{N-1}\prod_{\alpha=1}^{d} \frac{H_{n_{i\alpha}}\left(\sqrt{d}\,\eta_{i\alpha}\right)}{n_{i\alpha}!}, \tag{C.6}$$

which satisfy the following orthonormality relation with the eigenfunctions (C.3):

$$\int \prod_{i=0}^{N-1} \mathrm{d}\boldsymbol{\eta}_i \, \tilde{u}_{\boldsymbol{m}} u_{\boldsymbol{n}} = \prod_{i=0}^{N-1} \prod_{\alpha=1}^{d} \delta_{n_{i\alpha}, m_{i\alpha}} = \delta_{\boldsymbol{n},\boldsymbol{m}}. \tag{C.7}$$

With the help of Eqs. (C.5), (C.6), and (C.7), it can be easily shown that the lowest-order coefficient $\phi_{\boldsymbol{0}}(\{\boldsymbol{\chi}\}, t)$ is nothing but the marginal distribution $\varrho(\{\boldsymbol{\chi}\}, t)$:

$$\begin{aligned} \varrho(\{\boldsymbol{\chi}\}, t) &= \int \prod_{i=0}^{N-1} \mathrm{d}\boldsymbol{\eta}_i \, \tilde{u}_{\boldsymbol{0}} \mathcal{P}(\{\boldsymbol{\chi}\}, \{\boldsymbol{\eta}\}, t) \\ &= \sum_{\boldsymbol{n}} \phi_{\boldsymbol{n}}(\{\boldsymbol{\chi}\}, t) \int \prod_{i=0}^{N-1} \mathrm{d}\boldsymbol{\eta}_i \, \tilde{u}_{\boldsymbol{0}} u_{\boldsymbol{n}} \\ &= \phi_{\boldsymbol{0}}(\{\boldsymbol{\chi}\}, t) \, . \end{aligned} \tag{C.8}$$

Accordingly, the information about the conformation of the polymer and its preferential accumulation in specific regions of the non-homogeneous active bath is encoded in $\phi_{\boldsymbol{0}}(\{\boldsymbol{\chi}\}, t)$. In order to derive the evolution equations for the coefficients $\{\phi_{\boldsymbol{n}}(\{\boldsymbol{\chi}\}, t)\}$, we introduce the following inner product between two generic functions f, g of the orientation vectors $\{\boldsymbol{\eta}\}$:

$$\langle f(\{\boldsymbol{\eta}\}); g(\{\boldsymbol{\eta}\}) \rangle \equiv \int \prod_{i=0}^{N-1} \mathrm{d}\boldsymbol{\eta}_i f(\{\boldsymbol{\eta}\}) g(\{\boldsymbol{\eta}\}); \tag{C.9}$$

then, we project the FP equation given by (5.8) onto the auxiliary functions $\{\tilde{u}_{\boldsymbol{n}}(\{\boldsymbol{\eta}\})\}$, finding

$$\partial_t \phi_{\boldsymbol{n}}(\{\boldsymbol{\eta}\}) = \langle \tilde{u}_{\boldsymbol{n}}; \partial_t \mathcal{P} \rangle = \langle \tilde{u}_{\boldsymbol{n}}; (\mathcal{L}_0 + \mathcal{L}_{\mathrm{a}} + \mathcal{L}_{\boldsymbol{\eta}}) \mathcal{P} \rangle. \tag{C.10}$$

The right hand side of (C.10) can be evaluated after recalling that all Hermite polynomials can be built by iteratively applying the following recurrence relation, starting from $H_0(x) = 1$ [333],

$$H_{n+1}(x) = x H_n(x) - H_n'(x), \tag{C.11}$$

and that they form a so-called Appell sequence, as they satisfy

$$H_n'(x) = n H_{n-1}(x). \tag{C.12}$$

These two identities can be combined to obtain useful relations between Hermite polynomials of different orders. To set the notation for the upcoming derivation, we find convenient to extend the definition of $u_{\boldsymbol{n}}$, $\tilde{u}_{\boldsymbol{n}}$ and $\phi_{\boldsymbol{n}}$ to the case with $\boldsymbol{n} \in \mathbb{Z}^{N\times d}$, assuming that $u_{\boldsymbol{n}} = \tilde{u}_{\boldsymbol{n}} = \phi_{\boldsymbol{n}} = 0$ if the matrix $\boldsymbol{n}$ contains at least one negative element. Moreover, we introduce the raising and lowering operators $b^{\dagger}_{i\alpha}$, $b_{i\alpha} : \mathbb{Z}^{N\times d} \longrightarrow \mathbb{Z}^{N\times d}$, which act on an $N \times d$ matrix $\boldsymbol{n}$ by increasing/decreasing its (i,α)-component by a unit. With the help of Eqs. (C.11) and (C.12), the following useful identity can be obtained:

$$\eta_{i\alpha} H_{n_{i\alpha}}(\sqrt{d}\eta_{i\alpha}) = \frac{H_{n_{i\alpha}+1}(\sqrt{d}\eta_{i\alpha}) + n_{i\alpha} H_{n_{i\alpha}-1}(\sqrt{d}\eta_{i\alpha})}{\sqrt{d}}, \tag{C.13}$$

which implies:

$$\eta_{i\alpha} u_{\boldsymbol{n}} = d^{-1/2}\big[u_{b^{\dagger}_{i\alpha}\boldsymbol{n}} + n_{i\alpha} u_{b_{i\alpha}\boldsymbol{n}}\big]. \tag{C.14}$$

Using the identities introduced above, we are now in the position of evaluating the right hand side of (C.10). To avoid cumbersome expressions, we separately determine the contributions due to the three operators $\mathcal{L}_0$, $\mathcal{L}_{\mathrm{a}}$, and $\mathcal{L}_{\boldsymbol{\eta}}$ defined in (5.9). As $\mathcal{L}_0$ does not explicitly depend on the orientation vectors $\{\boldsymbol{\eta}_i\}$, it is straightforward to show that:

$$\langle \tilde{u}_{\boldsymbol{n}}; \mathcal{L}_0 \mathcal{P}\rangle = \sum_{\boldsymbol{m}} \langle \tilde{u}_{\boldsymbol{n}}; u_{\boldsymbol{m}}\rangle \mathcal{L}_0 \phi_{\boldsymbol{m}} = \mathcal{L}_0 \phi_{\boldsymbol{n}}. \tag{C.15}$$

The projection of $\mathcal{L}_{\boldsymbol{\eta}}\mathcal{P}$ onto $\tilde{u}_{\boldsymbol{n}}$ can be easily computed by exploiting the fact that $\mathcal{L}_{\boldsymbol{\eta}}$ does not depend on the Rouse modes and it is diagonalized by the eigenfunctions $\{u_{\boldsymbol{n}}\}$:

$$\langle \tilde{u}_{\boldsymbol{n}}; \mathcal{L}_{\boldsymbol{\eta}} \mathcal{P}\rangle = \sum_{\boldsymbol{m}} \phi_{\boldsymbol{m}} \langle \tilde{u}_{\boldsymbol{n}}; \mathcal{L}_{\boldsymbol{\eta}} u_{\boldsymbol{m}}\rangle = \lambda_{\boldsymbol{n}} \phi_{\boldsymbol{n}}. \tag{C.16}$$

Deriving the contribution coming from the projection of $\mathcal{L}_{\mathrm{a}}\mathcal{P}$ is slightly more complicate, as it contains information about the coupling between the Rouse modes and the orientation vectors. It reads

$$\begin{aligned} \langle \tilde{u}_{\boldsymbol{n}}; \mathcal{L}_{\mathrm{a}} \mathcal{P}\rangle &= -\partial_{i\alpha}\varphi_{ij} \mathrm{v}(\boldsymbol{X}_j) \sum_{\boldsymbol{m}} \phi_{\boldsymbol{m}} \langle \tilde{u}_{\boldsymbol{n}}; \eta_{j\alpha} u_{\boldsymbol{m}}\rangle \\ &= -\partial_{i\alpha}\varphi_{ij} \mathrm{v}(\boldsymbol{X}_j) \frac{1}{\sqrt{d}} [\phi_{b_{j\alpha}\boldsymbol{n}} + (n_{j\alpha}+1)\phi_{b^{\dagger}_{j\alpha}\boldsymbol{n}}], \end{aligned} \tag{C.17}$$

where summation over repeated indices is implied and we used the identity (C.14) in order to evaluate the inner product in the right hand side of the first line:

$$\begin{aligned} \sqrt{d}\,\langle \tilde{u}_{\boldsymbol{n}}; \eta_{j\alpha} u_{\boldsymbol{m}}\rangle &= \langle \tilde{u}_{\boldsymbol{m}}; u_{b^{\dagger}_{j\alpha}\boldsymbol{m}}\rangle + n_{j\alpha} \langle \tilde{u}_{\boldsymbol{m}}; u_{b_{j\alpha}\boldsymbol{m}}\rangle \\ &= \delta_{\boldsymbol{n}, b^{\dagger}_{j\alpha}\boldsymbol{m}} + m_{j\alpha} \delta_{\boldsymbol{n}, b_{j\alpha}\boldsymbol{m}} \\ &= \delta_{b_{j\alpha}\boldsymbol{n}, \boldsymbol{m}} + (n_{j\alpha}+1) \delta_{b^{\dagger}_{j\alpha}\boldsymbol{n}, \boldsymbol{m}}. \end{aligned} \tag{C.18}$$

The projection in Eq. (C.10) generates a system of coupled partial differential equations for $\{\phi_{\boldsymbol{n}}(\{\boldsymbol{\chi}\},t)\}$ with a hierarchical structure

$$\partial_t \phi_{\boldsymbol{n}} = \mathcal{L}_0 \phi_{\boldsymbol{n}} + \lambda_{\boldsymbol{n}} \phi_{\boldsymbol{n}} - \partial_{i\alpha} \varphi_{ij} \mathrm{v}(\boldsymbol{X}_j) \frac{1}{\sqrt{d}} [\phi_{b_{j\alpha}\boldsymbol{n}} + (n_{j\alpha}+1)\phi_{b^\dagger_{j\alpha}\boldsymbol{n}}] \,, \tag{C.19}$$

which bears similarities to hydrodynamic theories. For this reason, Eq. (C.19) is sometimes referred to as a generalized hydrodynamic hierarchy [25, 146], even though our model neglects any explicit hydrodynamic effect due to the interaction of the polymer with the surrounding fluid.

It is possible to show that the expansion coefficients $\{\phi_{\boldsymbol{n}}(\{\boldsymbol{\chi}\},t)\}$ are related to the conditional moments of the orientation vectors given a fixed polymer configuration $\{\boldsymbol{\chi}\}$. In fact, the following equalities hold:

$$\begin{aligned} \varrho &= \varrho\langle 1 |\, \{\boldsymbol{\chi}\}\rangle = \phi_{\boldsymbol{0}} \,, \\ \sigma_{i\alpha} &\equiv \varrho\langle \eta_{i\alpha} |\, \{\boldsymbol{\chi}\}\rangle = \frac{1}{\sqrt{d}} \phi_{b^\dagger_{i\alpha}\boldsymbol{0}} \,, \\ Q_{ij\alpha\beta} &\equiv \varrho\langle \eta_{i\alpha}\eta_{j\beta} - \frac{\delta_{ij}\delta_{\alpha\beta}}{d} |\, \{\boldsymbol{\chi}\}\rangle \\ &= d^{-1}[1+\delta_{ij}\delta_{\alpha\beta}] \phi_{b^\dagger_{i\alpha} b^\dagger_{j\beta}\boldsymbol{0}} \,, \end{aligned} \tag{C.20}$$

with $\boldsymbol{0}$ the $N \times d$ matrix with all entries equal to zero, and where we introduced the rank-2 tensor $\sigma_{i\alpha}$ and rank-4 tensor $Q_{ij\alpha\beta}$. Analogous formulas which relate higher-order conditional moments and expansion coefficients can be derived. The vector field $\boldsymbol{\sigma}_i(\{\boldsymbol{\chi}\})$ represents the typical orientation of the active force acting on the i-th monomer when the whole chain assumes the configuration $\{\boldsymbol{\chi}\}$. Note that this average polarization does not trivially vanish in the steady state due to the non-homogeneity which characterizes the active bath. Similarly, when $i = j$, the field $\boldsymbol{Q}_{ij}(\{\boldsymbol{\chi}\})$ is proportional to the nematic tensor of the orientation vector $\boldsymbol{\eta}_i$ at fixed polymer configuration $\{\boldsymbol{\chi}\}$, whereas for $i \neq j$ it depends on the conditional correlation of the directions of the active forces exerted on monomers i and j. Analogous definitions of local polar and nematic order parameters are commonly employed in other contexts, see e.g. [115, 127, 146, 334]. The evolution of the zeroth- and first-order expansion coefficients can be obtained by specializing Eq. (C.19) to $\boldsymbol{n} = \boldsymbol{0}$ and $\boldsymbol{n} = b^\dagger_{i\alpha}\boldsymbol{0}$, respectively, and is given by:

$$\begin{aligned} \partial_t \varrho &= -\partial_{i\alpha} \Big[-\gamma_i \chi_{i\alpha} \varrho - D \partial_{i\alpha} \varrho + \varphi_{ij} \mathrm{v}(\boldsymbol{X}_j) \sigma_{j\alpha} \Big] \,, \\ \partial_t \sigma_{i\alpha} &= -\partial_{l\beta} \Big[\varphi_{lj} \mathrm{v}(\boldsymbol{X}_j) \Big(\frac{\delta_{ij}\delta_{\alpha\beta}}{d} \varrho + Q_{ji\alpha\beta} \Big) \Big] + \mathcal{L}_0 \sigma_{i\alpha} - \tau^{-1} \sigma_{i\alpha} \,. \end{aligned} \tag{C.21}$$

where we recall that $\boldsymbol{X}_j = \sum_k \varphi^{-1}_{jk} \boldsymbol{\chi}_k$. A few remarks on these equations are needed. The marginal density ϱ is a locally conserved quantity, hence its evolution takes the form of a continuity equation $\partial_t \varrho = -\partial_{i\alpha} J_{i\alpha}$, where

$$J_{i\alpha} = -\gamma_i \chi_{i\alpha} \varrho + \varphi_{ij} \mathrm{v}(\boldsymbol{X}_j) \sigma_{j\alpha} - D \partial_{i\alpha} \varrho \tag{C.22}$$

denotes the (i, α)-component of the probability flux in the $N \times d$ dimensional Rouse space. The first two terms on the right hand side of Eq. (C.22) correspond to the drift component of the flux $J_{i\alpha}$. They originate from the internal interactions along the polymer backbones and the average polarity of the active forces, respectively. On the other hand, the last term on the right hand side of Eq. (C.22) arises from fluctuations due to thermal diffusion. It can be readily shown that the marginal densities $\rho_i(\boldsymbol{\chi}_i, t)$ defined as

$$\rho_i(\boldsymbol{\chi}_i, t) \equiv \int \prod_{j \neq i} \mathrm{d}\boldsymbol{\chi}_j \, \varrho(\{\boldsymbol{\chi}\}, t), \tag{C.23}$$

also evolve according to continuity equations $\partial_t \rho_i = -\partial_\alpha \mathcal{J}_{i\alpha}$, with flux

$$\begin{aligned} \mathcal{J}_{i\alpha} &\equiv \int \prod_{h \neq i} \mathrm{d}\boldsymbol{\chi}_h J_{i\alpha} \\ &= -\gamma_i \chi_{i\alpha} \rho_i + \varphi_{ij} \int \prod_{h \neq i} \mathrm{d}\boldsymbol{\chi}_h \mathrm{v}(\boldsymbol{X}_j) \sigma_{j\alpha} - D \partial_{i\alpha} \rho_i \,. \end{aligned} \tag{C.24}$$

Due to the fact that the probability density is locally conserved, both ϱ and $\{\rho_i\}$ can be seen as slow modes of the generalized hydrodynamic theory, i.e., they exhibit a slow relaxation when subject to large-wavelength perturbations. On the contrary, $\sigma_{i\alpha}$ does not obey any conservation law and its relaxation occurs on a typical time scale given by the persistence time τ, even when perturbed on very large length scales. For this reason, it is identified as a fast mode. Analogously, all equations governing the evolution of the higher-order modes associated to the expansion coefficients $\phi_{\boldsymbol{n}}$ will be characterized by a damping term $\propto \lambda_{\boldsymbol{n}} \phi_{\boldsymbol{n}}$ [see Eq. (C.19)], and thus by an inverse relaxation time $|\lambda_{\boldsymbol{n}}|$. In particular, the time scale separation between slow and fast modes can be used to make analytical progresses with the aforementioned generalized hydrodynamic theory. More precisely, for any given time t, one can assume that the fast modes have relaxed to their quasi-stationary state at fixed density field $\varrho(\{\boldsymbol{\chi}\}, t)$. The accuracy of this adiabatic approximation, which is used in the rest of the paper to close the hierarchy of the equations governing the evolution of the generalized hydrodynamic modes, is strongly dependent on the reorientational dynamics of the active forces. In particular, if their persistence time increases, the accuracy of the quasi-static approximation decreases.

C.2 Small gradient approximation

In this Section we derive the effective Fokker-Planck equation (5.10) for the marginal probability density $\rho_0(\boldsymbol{\chi}_0, t)$ by applying a gradient expansion approach up to the drift/diffusion order (i.e., we neglect terms of order $\mathcal{O}(\nabla_0^2)$ or higher in the flux $\mathcal{J}_{0\alpha}$). We start by considering the evolution of the tensor $Q_{ij\alpha\beta}$ obtained combining Eqs. (C.20) and (C.19):

$$\begin{aligned}\partial_t Q_{ij\alpha\beta} = {} & \mathcal{L}_0 Q_{ij\alpha\beta} - (2/\tau) Q_{ij\alpha\beta} \\ & - \partial_{k\gamma}\varphi_{kh}\mathrm{v}(\boldsymbol{X}_h) d^{-1}[\delta_{hi}\delta_{\gamma\alpha}\sigma_{j\beta} + \delta_{hj}\delta_{\gamma\beta}\sigma_{i\alpha}] \\ & - \partial_{k\gamma}\varphi_{kh}\mathrm{v}(\boldsymbol{X}_h)\Sigma_{ijh\alpha\beta\gamma}\,,\end{aligned} \tag{C.25}$$

where we used $\lambda_{b^\dagger_{i\alpha}b^\dagger_{j\beta}\mathbf{0}} = -2/\tau$, the identity

$$(1 + \delta_{ij}\delta_{\alpha\beta})\phi_{b_{h\gamma}b^\dagger_{i\alpha}b^\dagger_{j\beta}\mathbf{0}} = d^{1/2}[\delta_{hi}\delta_{\gamma\alpha}\sigma_{j\beta} + \delta_{hj}\delta_{\gamma\beta}\sigma_{i\alpha}]\,, \tag{C.26}$$

and we introduced the tensor $\Sigma_{ijh\alpha\beta\gamma}$ related to the third order expansion coefficient $\phi_{b^\dagger_{h\gamma}b^\dagger_{i\alpha}b^\dagger_{j\beta}\mathbf{0}}$, the expression of which is actually not needed below. Imposing $\partial_t Q_{ij\alpha\beta} = 0$ due to the time-scale separation between slow and fast modes, we get the following compact equation for $Q_{ij\alpha\beta}$:

$$Q_{ij\alpha\beta} = \partial_{k\gamma}\Upsilon_{ijk\alpha\beta\gamma}, \tag{C.27}$$

where $\Upsilon_{ijk\alpha\beta\gamma} = \Upsilon_{ijk\alpha\beta\gamma}[\boldsymbol{\sigma}, \boldsymbol{Q}, ...]$ is a functional of all the fast modes and it corresponds to the flux of the local nematic order parameter tensor $\boldsymbol{Q}$. Its exact expression, which can be obtained from (C.25), is actually irrelevant for the rest of the derivation. What matters is that the tensor $Q_{ij\alpha\beta}$ is a quantity of order $\mathcal{O}(\{\nabla_k\})$ or higher, where the notation $\mathcal{O}(\{\nabla_k\})$ indicates dependence on first-order gradients with respect to all Rouse modes $\{\boldsymbol{\chi}_k\}$. Note, however, that our gradient expansion is based on the assumption that the probability densities and fluxes (and thus the modes) exhibit small variations when the center-of-mass of the polymer is displaced, but not when its internal structure is changed. Combining Eqs. (C.27) and (C.21), and applying again the quasistatic approximation $\partial_t\sigma_{i\alpha} = 0$, we obtain the following equation for $\sigma_{i\alpha}$:

$$\begin{aligned}\sigma_{i\alpha} = & -\tau/d\,\partial_{l\alpha}\varphi_{li}\mathrm{v}(\boldsymbol{X}_i)\varrho \\ & + \tau\partial_{j\beta}\gamma_j\chi_{j\beta}\sigma_{i\alpha} \\ & - \tau\partial_{l\beta}\varphi_{lj}\mathrm{v}(\boldsymbol{X}_j)\partial_{k\gamma}\Upsilon_{ijk\alpha\beta\gamma} \\ & + \tau D\partial_{j\beta}\partial_{j\beta}\sigma_{i\alpha}.\end{aligned} \tag{C.28}$$

Let us now consider the probability flux $\mathcal{J}_{0\alpha}$ related to the marginal density $\rho_0(\boldsymbol{\chi}_0, t)$, the definition of which is given in Eq. (C.24). In particular, we focus on the second contribution on the right hand side of that equation, which originates from the interaction of the polymer with the active bath:

$$\mathcal{J}^{\mathrm{act}}_{0\alpha} \equiv \varphi_{0i}\int\prod_{h\neq 0}\mathrm{d}\boldsymbol{\chi}_h\mathrm{v}(\boldsymbol{X}_i)\sigma_{i\alpha}, \tag{C.29}$$

and combine it with the expression of the quasistatic mode $\sigma_{i\alpha}$ in Eq. (C.28). The last line of Eq. (C.28) contributes to the flux with a term proportional to:

$$\begin{aligned}
&\varphi_{0i}\int\prod_{h\neq 0}\mathrm{d}\boldsymbol{\chi}_h \mathrm{v}(\boldsymbol{X}_i)\partial_{j\beta}\partial_{j\beta}\sigma_{i\alpha}\\
&=\varphi_{0i}\int\prod_{h\neq 0}\mathrm{d}\boldsymbol{\chi}_h[\mathrm{v}(\boldsymbol{X}_i)\nabla_0^2\sigma_{i\alpha}+\sigma_{i\alpha}\sum_{j\neq 0}\nabla_j^2\mathrm{v}(\boldsymbol{X}_i)]\\
&=\mathcal{O}(\nabla_0^2),
\end{aligned}\tag{C.30}$$

where we used integration by parts from first to second line, and the following identity

$$\partial_{j\beta}\mathrm{v}(\boldsymbol{X}_i)=\partial_{j\beta}\mathrm{v}(\varphi_{ki}\boldsymbol{\chi}_k)=\frac{\partial \mathrm{v}}{\partial\varphi_{ki}\chi_{k\alpha}}\partial_{j\beta}\varphi_{li}\chi_{l\alpha}=\sqrt{N}\varphi_{ji}\partial_{0\beta}\mathrm{v}(\boldsymbol{X}_i),\tag{C.31}$$

to show that each Laplacian $\nabla_j^2\mathrm{v}(\boldsymbol{X}_i)$ in Eq. (C.30) can be also rewritten as a term of order $\mathcal{O}(\nabla_0^2)$. Hence, the contribution to the flux $\mathcal{J}_{0\alpha}^{\mathrm{act}}$ related to Eq. (C.30) is negligible under the assumptions we made. Analogously, also the third line of Eq. (C.28) can be shown to produce terms of order $\mathcal{O}(\nabla_0^2)$ once plugged into Eq. (C.29), due to

$$\begin{aligned}
&\int\prod_{h\neq 0}\mathrm{d}\boldsymbol{\chi}_h \mathrm{v}(\boldsymbol{X}_i)\partial_{l\beta}\mathrm{v}(\boldsymbol{X}_j)\partial_{k\gamma}\Upsilon_{ijk\alpha\beta\gamma}\\
&=\mathcal{O}(\nabla_0^2)-\sum_{k\neq 0}\int\prod_{h\neq 0}\mathrm{d}\boldsymbol{\chi}_h\Upsilon_{ijk\alpha\beta\gamma}\partial_{k\gamma}\mathrm{v}(\boldsymbol{X}_i)\partial_{l\beta}\mathrm{v}(\boldsymbol{X}_j)\\
&=\mathcal{O}(\nabla_0^2),
\end{aligned}\tag{C.32}$$

where we used again integration by parts and Eq. (C.31). This implies that the information about higher-order modes is not relevant if we are only interested in deriving an effective drift/diffusion equation for ρ_0. We now focus on the terms of Eq. (C.28) that lead to non-vanishing contributions to the flux $\mathcal{J}_{0\alpha}^{\mathrm{act}}$. Substituting the first line of (C.28) into (C.29) we get:

$$\mathcal{J}_{0\alpha}^{\mathrm{act},1}\equiv-\tau/d\,\varphi_{0i}\int\prod_{h\neq 0}\mathrm{d}\boldsymbol{\chi}_h \mathrm{v}(\boldsymbol{X}_i)\partial_{l\alpha}\varphi_{li}\mathrm{v}(\boldsymbol{X}_i)\varrho\,.\tag{C.33}$$

We find convenient to divide the implicit sum over the index l in this expression into the terms with $l = 0$ and $l \neq 0$. For $l \neq 0$, we get:

$$\begin{aligned}
&-(\tau/d)\varphi_{0i}\sum_{l\neq 0}\int\prod_{h\neq 0}\mathrm{d}\boldsymbol{\chi}_h \mathrm{v}(\boldsymbol{X}_i)\partial_{l\alpha}\varphi_{li}\mathrm{v}(\boldsymbol{X}_i)\varrho \\
&= \frac{\tau}{2d}\varphi_{0i}\sum_{l\neq 0}\int\prod_{h\neq 0}\mathrm{d}\boldsymbol{\chi}_h\sqrt{N}\varphi_{li}\varphi_{li}\varrho\,\partial_{0\alpha}\mathrm{v}^2(\boldsymbol{X}_i) \\
&= \frac{\tau}{2d}\partial_{0\alpha}\mathrm{v}^2\Big(\frac{\boldsymbol{\chi}_0}{\sqrt{N}}\Big)\sum_{l\neq 0}\sqrt{N}\varphi_{0i}\varphi_{li}\varphi_{li}\rho_0 + \mathcal{O}(\nabla_0^2) \\
&= \frac{(N-1)\tau}{2d}\rho_0\partial_{0\alpha}\mathrm{v}^2\Big(\frac{\boldsymbol{\chi}_0}{\sqrt{N}}\Big) + \mathcal{O}(\nabla_0^2),
\end{aligned} \tag{C.34}$$

where the first equality follows from integration by parts and Eq. (C.31), the second equality is obtained by Taylor expanding $\partial_{0\alpha}\mathrm{v}^2(\boldsymbol{X}_i)$ as

$$\partial_{0\alpha}\mathrm{v}^2(\boldsymbol{X}_i) = \partial_{0\alpha}\mathrm{v}^2(\varphi_{ji}\boldsymbol{\chi}_j) = \partial_{0\alpha}\mathrm{v}^2(\varphi_{0i}\boldsymbol{\chi}_0) + \mathcal{O}(\nabla_0^2), \tag{C.35}$$

and by using the definition of ρ_0 given in Eq. (C.2). The last line of Eq. (C.34), instead, results from using the following identity

$$\sum_i\sum_{l\neq 0}\varphi_{0i}\varphi_{li}\varphi_{li} = \sum_{l\neq 0}\delta_{ll}/\sqrt{N} = (N-1)/\sqrt{N}, \tag{C.36}$$

based on the fact that the matrix φ_{ij} is orthogonal, i.e., $\varphi_{ji} = \varphi_{ij}^{-1}$, and the entries of its first row are $\varphi_{0i} = N^{-1/2}$ for all values of $i \in \{0, 1, ..., N-1\}$. For $l = 0$, instead, Eq. (C.33) reads

$$\begin{aligned}
&-(\tau/d)\varphi_{0i}\int\prod_{h\neq 0}\mathrm{d}\boldsymbol{\chi}_h\mathrm{v}(\boldsymbol{X}_i)\partial_{0\alpha}\varphi_{0i}\mathrm{v}(\boldsymbol{X}_i)\varrho \\
&= -\frac{\tau}{2d}\rho_0\partial_{0\alpha}\mathrm{v}^2\Big(\frac{\boldsymbol{\chi}_0}{\sqrt{N}}\Big) - \frac{\tau}{d}\mathrm{v}^2\Big(\frac{\boldsymbol{\chi}_0}{\sqrt{N}}\Big)\partial_{0\alpha}\rho_0 + \mathcal{O}(\nabla_0^2)\,.
\end{aligned} \tag{C.37}$$

Combining Eq. (C.34) and Eq. (C.37) one has:

$$\mathcal{J}_{0\alpha}^{\mathrm{act},1} = \frac{(N-2)\tau}{2d}\rho_0\partial_{0\alpha}\mathrm{v}^2\Big(\frac{\boldsymbol{\chi}_0}{\sqrt{N}}\Big) - \frac{\tau}{d}\mathrm{v}^2\Big(\frac{\boldsymbol{\chi}_0}{\sqrt{N}}\Big)\partial_{0\alpha}\rho_0 + \mathcal{O}(\nabla_0^2). \tag{C.38}$$

Finally, the last contribution to the flux $\mathcal{J}_{0\alpha}^{\mathrm{act}}$ comes from inserting the second line of (C.28) into (C.29). We denote this contribution by $\mathcal{J}_{0\alpha}^{\mathrm{act},2}$, the expression of which is

$$\begin{aligned}
\mathcal{J}_{0\alpha}^{\mathrm{act},2} &= \sum_j \mathcal{I}_{j\alpha}\,, \\
\mathcal{I}_{j\alpha} &\equiv -\tau\varphi_{0i}\int\prod_{h\neq 0}\mathrm{d}\boldsymbol{\chi}_h[\partial_{j\beta}\mathrm{v}(\boldsymbol{X}_i)]\gamma_j\chi_{j\beta}\sigma_{i\alpha},
\end{aligned} \tag{C.39}$$

where the right hand side of the second line is not implicitly summed over j. Using again (C.28) and neglecting all terms of order $\mathcal{O}(\nabla_0^2)$, we can derive a self-consistent equation for $\mathcal{I}_{j\alpha}$. As a first step we rewrite $\mathcal{I}_{j\alpha}$ as:

$$\begin{aligned}\mathcal{I}_{j\alpha} = {} & \frac{\tau^2}{d}\,\varphi_{0i}\int\prod_{h\neq 0}\mathrm{d}\boldsymbol{\chi}_h[\partial_{j\beta}\mathrm{v}(\boldsymbol{X}_i)]\gamma_j\chi_{j\beta}\partial_{l\alpha}\varphi_{li}\mathrm{v}(\boldsymbol{X}_i)\varrho \\ & -\tau^2\varphi_{0i}\int\prod_{h\neq 0}\mathrm{d}\boldsymbol{\chi}_h[\partial_{j\beta}\mathrm{v}(\boldsymbol{X}_i)]\gamma_j\chi_{j\beta}\partial_{l\gamma}\gamma_l\chi_{l\gamma}\sigma_{i\alpha} \\ & +\mathcal{O}(\nabla_0^2).\end{aligned} \tag{C.40}$$

The first line can be simplified as follows:

$$\begin{aligned} & \frac{\tau^2}{d}\,\varphi_{0i}\int\prod_{h\neq 0}\mathrm{d}\boldsymbol{\chi}_h[\partial_{j\beta}\mathrm{v}(\boldsymbol{X}_i)]\gamma_j\chi_{j\beta}\partial_{l\alpha}\varphi_{li}\mathrm{v}(\boldsymbol{X}_i)\varrho \\ & = -\frac{\tau^2}{d}\,\varphi_{0i}\int\prod_{h\neq 0}\mathrm{d}\boldsymbol{\chi}_h[\partial_{j\alpha}\mathrm{v}(\boldsymbol{X}_i)]\gamma_j\varphi_{ji}\mathrm{v}(\boldsymbol{X}_i)\varrho+\mathcal{O}(\nabla_0^2) \\ & = -\frac{\tau^2}{2d}\,\sqrt{N}\varphi_{0i}\varphi_{ji}\varphi_{ji}\gamma_j\rho_0\partial_{0\alpha}\mathrm{v}^2\Big(\frac{\boldsymbol{\chi}_0}{\sqrt{N}}\Big)+\mathcal{O}(\nabla_0^2) \\ & = -\frac{\tau^2\gamma_j}{2d}\,\rho_0\partial_{0\alpha}\mathrm{v}^2\Big(\frac{\boldsymbol{\chi}_0}{\sqrt{N}}\Big)+\mathcal{O}(\nabla_0^2),\end{aligned} \tag{C.41}$$

where we used integration by parts and Eqs. (C.31), (C.35), and (C.36). The second line of (C.40) can be rewritten as:

$$\begin{aligned} & -\tau^2\varphi_{0i}\int\prod_{h\neq 0}\mathrm{d}\boldsymbol{\chi}_h[\partial_{j\beta}\mathrm{v}(\boldsymbol{X}_i)]\gamma_j\chi_{j\beta}\partial_{l\gamma}\gamma_l\chi_{l\gamma}\sigma_{i\alpha} \\ & = \tau^2\varphi_{0i}\int\prod_{h\neq 0}\mathrm{d}\boldsymbol{\chi}_h[\partial_{j\beta}\mathrm{v}(\boldsymbol{X}_i)]\gamma_j\gamma_j\chi_{j\beta}\sigma_{i\alpha}+\mathcal{O}(\nabla_0^2) \\ & = -\tau\gamma_j\mathcal{I}_{j\alpha}+\mathcal{O}(\nabla_0^2)\,.\end{aligned} \tag{C.42}$$

Equations (C.41), (C.42), (C.40), and (C.39) can eventually be combined to get

$$\begin{aligned}\mathcal{J}_{0\alpha}^{\mathrm{act},2} & = \sum_j\mathcal{I}_{j\alpha} \\ & = -\frac{\tau}{2d}\left[\sum_{j=0}^{N-1}\frac{\tau\gamma_j}{1+\tau\gamma_j}\right]\rho\partial_{0\alpha}\mathrm{v}^2\Big(\frac{\boldsymbol{\chi}_0}{\sqrt{N}}\Big)+\mathcal{O}(\nabla_0^2) \\ & = -\frac{\tau}{2d}[N-2+\epsilon]\rho\partial_{0\alpha}\mathrm{v}^2\Big(\frac{\boldsymbol{\chi}_0}{\sqrt{N}}\Big)+\mathcal{O}(\nabla_0^2),\end{aligned} \tag{C.43}$$

where ϵ is defined in (5.13). Putting together the contributions derived in Eqs. (C.33) and (C.43), we can finally write down the expression of the probability flux $\mathcal{J}_{0\alpha}$ related to the marginal density ρ_0, given by

$$\begin{aligned}\mathcal{J}_{0\alpha} &= \mathcal{J}_{0\alpha}^{\text{act},1} + \mathcal{J}_{0\alpha}^{\text{act},2} - D\partial_{0\alpha}\rho_0 \\ &= -\frac{\tau\epsilon}{2d}\rho_0\partial_{0\alpha}\mathrm{v}^2\Big(\frac{\boldsymbol{\chi}_0}{\sqrt{N}}\Big) - \Big[D + \frac{\tau}{d}\mathrm{v}^2\Big(\frac{\boldsymbol{\chi}_0}{\sqrt{N}}\Big)\Big]\partial_{0\alpha}\rho_0 + \mathcal{O}(\nabla_0^2).\end{aligned} \tag{C.44}$$

After applying the chain rule to the second line of Eq. (C.44), we can identify the drift and diffusion component of the flux with:

$$\begin{aligned}\boldsymbol{\mathcal{J}}_0^{\text{drift}} &= \frac{\tau(2-\epsilon)}{2d}\rho_0\nabla_0\mathrm{v}^2\Big(\frac{\boldsymbol{\chi}_0}{\sqrt{N}}\Big), \\ \boldsymbol{\mathcal{J}}_0^{\text{diff}} &= -\nabla_0\Big(\Big[D + \frac{\tau}{d}\mathrm{v}^2\Big(\frac{\boldsymbol{\chi}_0}{\sqrt{N}}\Big)\Big]\rho_0\Big),\end{aligned} \tag{C.45}$$

from which Eq. (5.10) of Chapter 5 follows.

C.3 Excluded volume and finite extensibility

The theoretical predictions derived so far are based on the simplest possible polymer model, i.e., that of an ideal fully flexible harmonic chain. In the present Section we consider a more realistic system characterized by excluded volume interactions among the monomers and a finite extensibility of the bonds, and we investigate the extent to which the predictions presented in Chapter 5 are affected by these additional interactions. In particular, we run Brownian dynamics simulations of linear chains with polymerization degree N, with excluded volume repulsion modeled by a truncated and shifted Lennard-Jones (or WCA [335]) interaction potential $V_{LJ}(r)$ given by:

$$V_{LJ}(r) = \begin{cases} 4\varepsilon_{LJ}\left[\left(\frac{\sigma}{r}\right)^{12} - \left(\frac{\sigma}{r}\right)^{6}\right] + \varepsilon_{LJ} & \text{if } r < 2^{1/6}\sigma\ , \\ 0 & \text{else.} \end{cases} \tag{C.46}$$

Moreover, we change the harmonic interaction potential between connected monomers with the following Finitely Extensible Nonlinear Elastic (FENE) potential [336]:

$$V_{FE}(r) = \begin{cases} -\frac{\kappa_f\Delta^2}{2}\ln\left[1 - \left(\frac{r-r_0}{\Delta}\right)^2\right] & \text{if } |r-r_0| < \Delta\ , \\ +\infty & \text{else,} \end{cases} \tag{C.47}$$

where κ_f denotes the stiffness of the interaction, r_0 the equilibrium bond length and Δ the maximal stretching length. To analyze the changes due to such interactions, we compute the stationary distribution of the center of mass for

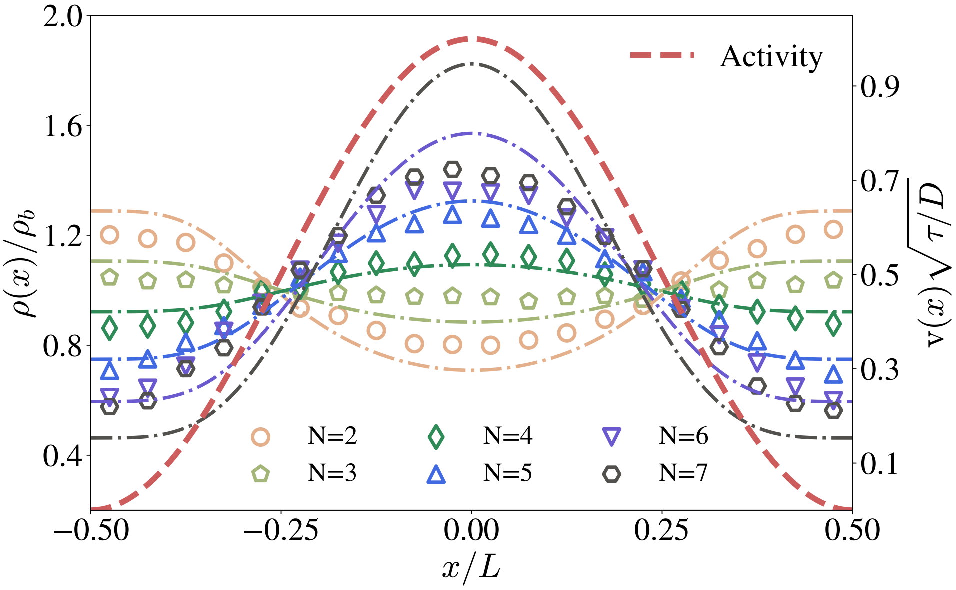

Figure C.1: Stationary probability distribution of the center of mass of linear chains with $N \in \{2, 3, ..., 7\}$ monomers, excluded volume interaction and FENE bonds. The sinusoidal activity field (red dashed line) is the same as in Figures 5.2 and 5.3. The dashed-dotted lines represent the theoretical predictions obtained with ideal (phantom) harmonic chains. The parameters of the FENE potential are: $\kappa_f = 10$, $\Delta = 0.5$, $r_0 = 1.5$. The Lennard Jones parameters are: $\varepsilon_{LJ} = 1.0$, $\sigma = 1.0$. All the other parameters are the same as in Figure 5.2.

all considered linear chains, with the same sinusoidal activity field as that used in Figures 5.2 and 5.3. As a result, we obtain the histograms reported in Figure C.1. Although we do not expect a quantitative matching between these numerical data and the theoretical predictions derived for the ideal Rouse model, it is instructive to compare them. For this reason, Figure C.1 shows with dashed-dotted lines the steady state density of an ideal phantom chain, reported in Eq. (5.15), and with symbols the results of the molecular dynamics simulations with both excluded volume interaction and FENE potential. A few comments on Figure C.1 are in order. Within the range of values of the parameters chosen in all the simulations considered here, the transition from localization in regions with low activity to that in regions with high activity occurs at a fairly small polymerization degree N. Specifically, in Figure C.1, a tetramer ($N = 4$) is already able to accumulate where the bath activity is higher. Moreover, intuitively, one would expect the steric hindrance to play a minor role for very short chains. Indeed, with the choice of parameters done in Figure C.1, not only the transition is not affected by the additional interactions, but also the difference between the simulation data and the theoretical predictions for ideal chains is quite small, at least up to $N = 4$. Above the transition point, where the polymers localize in the region of high activity, the steric hindrance is more relevant and the quantitative difference with the ideal case increases. Specifically, one can see that the excluded volume interaction reduces the efficiency of the localization in high activity regions. Notice that in the simulations performed in order to obtain Figure C.1, the Lennard-Jones parameter σ_{LJ} is comparable with the typical bond length. Interestingly enough, this shows that the localization properties of a polymer in a non-uniform active bath are not qualitatively affected by the presence of steric hindrance effects and thus that our results are robust even with more realistic interaction potentials.

C.4 Non-equilibrium separation

In this Section we argue that the chemotactic-like transition that leads to a spontaneous separation of polymers with different length and/or connectivity is a pure non-equilibrium effect. In other words, restoring the fluctuation-dissipation relation by adding a suitable friction memory kernel to the stochastic equation of motion would substantially alter the behavior of the polymer compared to the case discussed in Chapter 5. In the following, we try to justify this statement by considering the simpler scenario of a single particle in a non-uniform activity field, where the rotational dynamics of the orientation vector is modified so that the detailed balance condition is satisfied. More precisely, let us consider the following underdamped dynamics of a tracer particle with position $\boldsymbol{X}(t)$, velocity $\boldsymbol{v}(t)$ and orientation vector $\boldsymbol{\eta}(t)$:

$$\begin{aligned} \dot{\boldsymbol{X}} &= \boldsymbol{v}\,, \\ m\dot{\boldsymbol{v}} &= -\gamma\boldsymbol{v} - \nabla U(\boldsymbol{X}) + f_a(\boldsymbol{X})\boldsymbol{\eta} + \boldsymbol{\xi}\,, \\ \dot{\boldsymbol{\eta}} &= -\tau^{-1}\boldsymbol{\eta} - \sigma f_a(\boldsymbol{X})\boldsymbol{v} + \boldsymbol{\zeta}\,, \end{aligned} \tag{C.48}$$

where γ is a friction coefficient, $U(\boldsymbol{x})$ an external potential, $\boldsymbol{\xi}$ and $\boldsymbol{\zeta}$ zero-mean Gaussian white noises with correlation

$$\langle \xi_\alpha(t)\xi_\beta(s)\rangle = 2T\gamma\delta_{\alpha\beta}\delta(t-s)\,, \tag{C.49}$$

$$\langle \zeta_\alpha(t)\zeta_\beta(s)\rangle = 2T/\tau\delta_{\alpha\beta}\delta(t-s)\,, \tag{C.50}$$

and where we introduced the binary variable $\sigma \in \{0, 1\}$. The stochastic variable $\boldsymbol{\eta}$ is treated as an effective velocity variable with a unit mass-like coefficient. Note that for $\sigma = 0$ the dynamics reduces to the underdamped regime of the active Ornstein-Uhlenbeck particle. In this case, being $\sigma = 0$, the orientation vector $\boldsymbol{\eta}$ is an *enslaved* variable that does not depend on the position and the velocity of the particle, and the related active force $f_a(\boldsymbol{X})\boldsymbol{\eta}$ is not balanced by any additional dissipation in the system. Conversely, when $\sigma = 1$, the evolution of $\boldsymbol{\eta}$ depends on both $\boldsymbol{X}$ and $\boldsymbol{v}$. Interestingly, the evolution of $\boldsymbol{\eta}$ can be formally determined and substituted in the equation of motion for the velocity, yielding the non-Markovian dynamics:

$$\begin{aligned} m\dot{\boldsymbol{v}} &= -\gamma \boldsymbol{v} - \nabla U(\boldsymbol{X}) + f_a(\boldsymbol{X}(t)) \int_{t_0}^{t} \mathrm{d}s\, e^{-(t-s)/\tau} [-\sigma f_a(\boldsymbol{X}(s))\boldsymbol{v}(s) + \boldsymbol{\zeta}(s)] + \boldsymbol{\xi} \\ &= -\int_{t_0}^{t} \mathrm{d}s\, \Gamma(\boldsymbol{X}(t), \boldsymbol{X}(s), t-s)\boldsymbol{v}(s) - \nabla U(\boldsymbol{X}(t)) + \Xi(\boldsymbol{X}(t), t)\,, \end{aligned} \tag{C.51}$$

where we introduced the (in general non-linear) friction memory kernel $\Gamma(\boldsymbol{x}, \boldsymbol{y}, t)$ and the colored noise $\Xi(\boldsymbol{x}, t)$ defined as:

$$\Gamma(\boldsymbol{x}, \boldsymbol{y}, t) = 2\gamma\delta(t) + \sigma f_a(\boldsymbol{x}) f_a(\boldsymbol{y}) e^{-t/\tau}\Theta(t)\,, \tag{C.52}$$

$$\Xi(\boldsymbol{x}, t) = \boldsymbol{\xi} + f_a(\boldsymbol{x}) \int_{t_0}^{t} \mathrm{d}s\, e^{-(t-s)/\tau} \boldsymbol{\zeta}(s)\,, \tag{C.53}$$

where $\Theta(t)$ is the Heaviside step function. As we are interested in the long-time (stationary) properties of the dynamics, we assumed without loss of generality that, at the initial time $t = t_0$, the orientation vector assumes the value $\boldsymbol{\eta}(t_0) = \boldsymbol{0}$. It is easy to show that at every fixed positions $\boldsymbol{x}$ and $\boldsymbol{y}$, the friction memory kernel $\Gamma(\boldsymbol{x}, \boldsymbol{y}, t)$ and the colored noise $\Xi(\boldsymbol{x}, t)$ satisfy a fluctuation-dissipation relation, as the noise correlation and the memory kernel are proportional to each other by the temperature T. Although related to a very different problem, a similar derivation can be found for example in Section 3 of Ref. [65]. In order to determine the stationary probability density of the particle position, however, it is more convenient to consider the Markovian dynamics in Eq. (C.48). In particular, when $\sigma = 1$, the associated Fokker-Planck equation for the one-time probability density $\mathcal{P}(\boldsymbol{x}, \boldsymbol{v}, \boldsymbol{\eta}, t)$ reads:

$$\begin{aligned} \partial_t \mathcal{P} = -\boldsymbol{v} \cdot \nabla_{\boldsymbol{x}} \mathcal{P} - \nabla_{\boldsymbol{v}} \cdot \left[-\frac{\gamma \boldsymbol{v} \mathcal{P}}{m} - \frac{\nabla_{\boldsymbol{x}} U(\boldsymbol{x}) \mathcal{P}}{m} + \frac{f_a(\boldsymbol{x}) \boldsymbol{\eta} \mathcal{P}}{m} - \frac{T\gamma}{m^2} \nabla_{\boldsymbol{v}} \mathcal{P} \right] \\ - \nabla_{\boldsymbol{\eta}} \cdot \left[-\tau^{-1} \boldsymbol{\eta} \mathcal{P} - f_a(\boldsymbol{x}) \boldsymbol{v} \mathcal{P} - \frac{T}{\tau} \nabla_{\boldsymbol{\eta}} \mathcal{P} \right]\,. \end{aligned} \tag{C.54}$$

It is easy to verify that the above equation is solved, in the steady state, by the Boltzmann-like probability density:

$$P(\boldsymbol{x}, \boldsymbol{v}, \boldsymbol{\eta}) \propto \exp\left[-\beta \left(U(\boldsymbol{x}) + \frac{m\boldsymbol{v}^{\boldsymbol{2}}}{2} + \frac{\boldsymbol{\eta}^2}{2} \right) \right] \tag{C.55}$$

with $\beta = 1/T$ the inverse temperature. This implies that the stationary marginal density of the position $P(\boldsymbol{x}) \propto \exp(-\beta U(\boldsymbol{x}))$ only depends on the external potential $U(\boldsymbol{x})$ and not on the field $f_a(\boldsymbol{x})$. In other words, the time-correlated active forces do not alter the steady state distribution of the particle as long as the associated energy injections are balanced by additional dissipation modeled by a suitable friction memory kernel in the stochastic dynamics. An analogous reasoning extends to the case of a polymer chain in a non-uniform active bath. In particular, if the fluctuation-dissipation relation is restored, the chemotactic-like transition discussed in Chapter 5 disappears.

C.5 Numerical simulations

All numerical data reported in Chapter 5 as well as in this Appendix, have been obtained by running Brownian dynamics simulations of the stochastic equation of motion in Eq. (5.2), and of the Ornstein-Uhlenbeck processes (5.4) governing the stochastic evolution of the orientation vectors $\{\boldsymbol{\eta}\}$. For the discretization, we used the standard Euler-Maruyama scheme with an integration time step $\Delta t = 0.001$. In particular, the discretized equation of motion reads:

$$
\begin{aligned}
X_i^\alpha(t+\Delta t) &= X_i^\alpha(t) + \Delta t \left[-\gamma \sum_j M_{ij} X_j^\alpha(t) + \mathrm{v}(\boldsymbol{X}_i(t)) \eta_i^\alpha(t) \right] \\
&\quad + \sqrt{2\Delta t D}\, \xi_i^\alpha(t)\,, \\
\eta_i^\alpha(t+\Delta t) &= \eta_i^\alpha(t) - \frac{\Delta t}{\tau} \eta_i^\alpha(t) + \sqrt{\frac{2\Delta t}{\tau d}}\, \zeta_i^\alpha(t),
\end{aligned}
\tag{C.56}
$$

where $X_i^\alpha(t)$ denotes the position of the α-component of the i-th monomer at time t, $\eta_i^\alpha(t)$ the α-component of its orientation vector and $\xi_i^\alpha(t)$ and $\zeta_i^\alpha(t)$ are uncorrelated Gaussian random variables with zero mean and unit variance. Note that the stochastic dynamics has been interpreted according to the Itô prescription for convenience, but there are no spurious effects associated to this choice because the stochastic dynamics is characterized by additive noise. Each numerical simulation has a duration of $n = 2 \cdot 10^9$ steps and the error bars are within the symbol size. In the Brownian dynamics simulation associated to Figure 5.4, the first well separated state occurred after $\sim 10^4$ integration steps.

Appendix D

Appendix of Chapter 6

In this Appendix we present a theoretical derivation of the predictions reported in Chapter 6, as well as a detailed description of the numerical simulations. In particular, in Sec. D.1 we derive the asymptotic behavior of the linear memory kernel $\Gamma(t)$ introduced in Chapter 6, by analyzing the analytic structure of its Laplace transform. This analysis is useful to study the long-time behavior of the center-of-mass of the polymer, which is done is Sec. D.2. Here, we derive the algebraic decay that characterizes the relaxation of the center-of-mass when the polymer is coupled to a critical or conserved field. In Sec. D.3 we derive the first non-trivial perturbative correction of order λ^2 to the mean-squared gyration radius and to the end-to-end distance of the polymer at equilibrium. In this derivation, we consider the potential presence of an external tensile force applied to the terminal monomers of a linear chain. The results obtained here are used in Chapter 6 to plot the typical size of the polymer as a function of its polymerization degree and of the correlation length of the field, as well as the force-extension curve. Finally, in Sec. D.4 we report the details of the numerical simulations used to test our analytical predictions.

D.1 Asymptotic analysis of the memory kernel

In this Section we analyze the long-time behavior of the memory kernel $\Gamma(t)$ in Eq. (6.29), which can be easily deduced by inspecting the analytic structure of the corresponding Laplace transform [68, 277]. The latter can be immediately found using Eq. (6.21), and reads

$$\hat{\Gamma}(z) = \frac{ND\nu\lambda^2}{d} \int \frac{\mathrm{d}^d q}{(2\pi)^d} \frac{q^{2+a}|V_{\boldsymbol{q}}|^2}{\alpha_{\boldsymbol{q}}(z+\alpha_{\boldsymbol{q}})}. \tag{D.1}$$

This function is non-analytic for all the points $z \in \mathbb{C}$ that render the denominator $(z + \alpha_q) = 0$. Since $\alpha_{\boldsymbol{q}} = Dq^a(q^2 + r)$, at the critical point (i.e. $r = 0$) the function $\hat{\Gamma}(z)$ exhibits a branch cut along the real negative semiaxis in the complex z plane. As there are no other singularities, the behavior of $\hat{\Gamma}(z)$ around the branching point $z_0 = 0$ will generically determine the long-time behavior of $\Gamma(t)$ [68]. In particular, if

$$\hat{\Gamma}(z) \sim \sum_j a_j (z - z_0)^{\lambda_j} \tag{D.2}$$

for some λ_j around the branching point z_0, then

$$\Gamma(t) \sim e^{z_0 t} \sum_j \frac{a_j}{\Gamma_E(-\lambda_j)\, t^{1+\lambda_j}}, \tag{D.3}$$

as can be easily understood by taking the inverse Laplace transform term by term. If $z_0 = 0$, this generates an algebraic decay at long times. Note that the very same scenario occurs for the off-critical model B, i.e. $a = 2$ and $r > 0$, because the branching point is still $z_0 = 0$. By contrast, for the off-critical model A (i.e. $a = 0$ and $r > 0$) the function in Eq. (D.1) presents a branch cut at the left of $z_0 = -Dr$. Expanding around the new branching point as in Eqs. (D.2) and (D.3) will thus generate an exponential prefactor $e^{z_0 t} = e^{-Drt}$ superimposed to the algebraic tail.

As we are about to show, expanding $\hat{\Gamma}(z)$ around the branching point z_0 can be easily achieved even by keeping the interaction potential $V(\mathbf{x})$ generic, under the mild simplifying assumptions that it is rotationally invariant, normalized to unity, and depends on a single length scale R (such as in Eq. (6.4)). However, for later convenience and to make contact with the notation of Ref. [68], in the following we will not analyze $\hat{\Gamma}(z)$ directly, but rather introduce $\Gamma(t) = \int_t^\infty \mathrm{d}u\, \mathcal{K}(u)$, so that

$$\begin{aligned} \mathcal{K}(t) &= \frac{ND\nu\lambda^2}{d} \int \frac{\mathrm{d}^d q}{(2\pi)^d}\, q^{2+a} |V_{\boldsymbol{q}}|^2 G_{\boldsymbol{q}}(t) \\ \mapsto \hat{\mathcal{K}}(z) &= \frac{ND\nu\lambda^2}{d} \int \frac{\mathrm{d}^d q}{(2\pi)^d}\, \frac{q^{2+a}|V_{\boldsymbol{q}}|^2}{z + \alpha_{\boldsymbol{q}}}, \end{aligned} \tag{D.4}$$

and in particular

$$\hat{\Gamma}(z) = -\frac{\hat{\mathcal{K}}(z) - \hat{\mathcal{K}}(0)}{z}. \tag{D.5}$$

Note that the function $\hat{\mathcal{K}}(z)$ in Eq. (D.4) has the same analiticity properties as $\hat{\Gamma}(z)$, apart from an additional factor $1/z$.

Let us start from the critical case $r = 0$, and expand $\hat{\mathcal{K}}(z)$ around $z_0 = 0$. Using polar coordinates and changing variables as $y = Dq^{a+2}/z$, one finds from Eq. (D.1)

$$\hat{\mathcal{K}}(z) = N\lambda^2 \nu c_d (zD)^{d/(2+a)} \int_0^\infty \frac{\mathrm{d}y\, y^{d/(2+a)}}{1+y} |V_{(zy/D)^{\frac{1}{2+a}}}|^2 \sim z^{d/(2+a)}. \tag{D.6}$$

In the last step we expanded the integrand for small z by using the normalization condition $V_q = 1 + \mathcal{O}(q^2)$ of the interaction potential, while

$$c_d = 2^{1-d}/[d\pi^{d/2}\Gamma_E(d/2)] \tag{D.7}$$

is a numerical constant, accounting for the integration over the angular variables, with Γ_E the Euler gamma function. Using Eq. (D.5) we deduce that for small z

$$\hat{\Gamma}(z) \sim z^{d/(2+a)-1}, \tag{D.8}$$

and comparing with (D.3) and (D.2) we can conclude that at long times

$$\Gamma(t) \sim t^{-d/(2+a)}. \tag{D.9}$$

This corresponds to the result reported in Eqs. (6.32) and (6.33), for $a = 0, 2$, respectively.

Let us now analyze the off-critical case $r > 0$. For model B, i.e. $a = 2$, the branching point is still $z_0 = 0$, so that using again polar coordinates and changing variables to $y \equiv Dq^2/z$ we find from Eq. (D.1)

$$\hat{\mathcal{K}}(z) = N\lambda^2\nu c_d \int_0^\infty \frac{\mathrm{d}y\,|V_{(zy/D)^{1/2}}|^2}{1 + y(r + zy/D)} \left(\frac{zy}{D}\right)^{1+\frac{d}{2}} \sim z^{1+\frac{d}{2}}. \tag{D.10}$$

Using Eqs. (D.3), (D.2) and (D.5) we thus get

$$\hat{\Gamma}(z) \sim z^{\frac{d}{2}} \quad \longrightarrow \quad \Gamma(t) \sim t^{-(1+\frac{d}{2})}, \tag{D.11}$$

as reported in Eq. (6.32).

Finally we address the off-critical case in model A. In this case the branching point is $z_0 = -Dr$, and expanding $\hat{\mathcal{K}}(z)$ around it yields

$$\begin{aligned}\hat{\mathcal{K}}(z) &= N\lambda^2\nu D c_d \left(\frac{z + Dr}{D}\right)^{\frac{d}{2}} \int_0^\infty \frac{\mathrm{d}y\, y^{d/2}}{1+y} |V_{\sqrt{y(z/D+r)}}|^2 \\ &\sim (z + Dr)^{\frac{d}{2}},\end{aligned} \tag{D.12}$$

where we called $y = Dq^2/(z + Dr)$, and in the last step we expanded in small powers of $(z + Dr)$. By contrast, note that expanding the same expression around $z = 0$ we would get $\hat{\mathcal{K}}(z) = \hat{\mathcal{K}}(0) + \mathcal{O}(z)$, meaning that the function $\hat{\Gamma}(z)$ in Eq. (D.5) is *not* singular in $z = 0$. The singularity in $z = z_0 = -Dr$ thus still dominates the long-time asymptotics of $\Gamma(t)$, which follows from Eqs. (D.3), (D.2) and (D.5) as

$$\hat{\Gamma}(z) \sim (z + Dr)^{\frac{d}{2}} \quad \longrightarrow \quad \Gamma(t) \sim e^{-Drt} t^{-(1+\frac{d}{2})}, \tag{D.13}$$

as reported in Eq. (6.32).

D.2 Asymptotic analysis of the center-of-mass

The evolution of the mean center-of-mass position of the polymer $\langle \chi_0^\alpha(t)\rangle$, starting from the initial condition $\bar{\chi}_0$ at time $t_0 = 0$, is given in the Laplace domain by Eq. (6.41). The latter can be rephrased, in terms of the function $\hat{\mathcal{K}}(z)$ introduced in Eq.(D.4), as

$$\hat{\chi}_0^\alpha(z) = \frac{\bar{\chi}_0}{z + \tilde{\gamma}_0 - [\hat{\mathcal{K}}(z) - \hat{\mathcal{K}}(0)]}. \tag{D.14}$$

This function exhibits two types of singularities in the complex z plane: (i) a branch cut starting from the branching point z_0, where $\hat{\mathcal{K}}(z)$ is non-analytic, as discussed in the previous Section; and (ii) the zero(s) $z = z^*$ of the denominator, implicitly defined by the condition

$$\mathcal{D}(z^*) = z^* + \tilde{\gamma}_0 - [\hat{\mathcal{K}}(z^*) - \hat{\mathcal{K}}(0)] \equiv 0. \tag{D.15}$$

Note that these are simple poles: to see this, it is enough to take the derivative

$$\mathcal{D}'(z) = 1 - \hat{\mathcal{K}}'(z) = 1 + \frac{ND\nu\lambda^2}{d}\int \frac{\mathrm{d}^d q}{(2\pi)^d}\,\frac{q^{2+a}|V_{\boldsymbol{q}}|^2}{(z+\alpha_{\boldsymbol{q}})^2}, \tag{D.16}$$

where we used Eq. (D.4), and note that it can never be $\mathcal{D}'(z^*) = 0$. Moreover, note that it must be $\operatorname{Re} z^*, \operatorname{Re} z_0 < 0$ in order for $\langle \chi_0^\alpha(t)\rangle$ to decay to zero at large times. The closest to the imaginary axis $\operatorname{Re} z = 0$ among z_0 and z^* then generically determines the long-time asymptotic behavior of $\langle \chi_0^\alpha(t)\rangle$ [68, 277].

Again, it proves convenient to inspect first the critical case $r = 0$, for which the branching point $z_0 = 0$ necessarily dominates the long-time asymptotics of $\hat{\chi}_0^\alpha(z)$ in Eq. (D.14). Expanding the latter around $z_0 = 0$ gives

$$\hat{\chi}_0^\alpha(z) = \bar{\chi}_0 \sum_{n=0}^{\infty} \left[\hat{\mathcal{K}}(z) - z\right]^n \left[\hat{\mathcal{K}}(0) + \tilde{\gamma}_0\right]^{-(n+1)} \sim z^{d/(2+a)}, \tag{D.17}$$

where in the last step we used Eq. (D.6). Comparing with Eqs. (D.3) and (D.2) then yields

$$\langle \chi_0^\alpha(t)\rangle \sim t^{-1-d/(2+a)}, \tag{D.18}$$

as reported in Eqs. (6.43) and (6.42).

The situation is analogous for the off-critical model B, i.e. $a = 2$ and $r > 0$, as the branching point is still $z_0 = 0$. Using the asymptotic behavior of $\hat{\mathcal{K}}(z)$ given in Eq. (D.10) in the second step of (D.17) this time gives

$$\hat{\chi}_0^\alpha(z) \sim z^{1+\frac{d}{2}} \quad \longrightarrow \quad \langle \chi_0^\alpha(t)\rangle \sim t^{-2-d/2}, \tag{D.19}$$

as stated in Eq.(6.42).

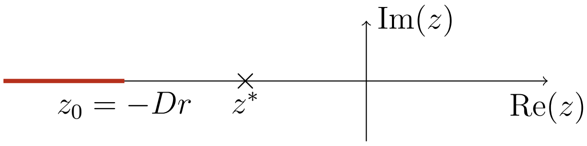

Figure D.1: Sketch of the analytic structure in the complex z plane of the function $\hat{\chi}_0^\alpha(z)$ in Eq. (D.14), for the off-critical case of model A, and for $r \gg \tilde{\gamma}_0/D$. This features a branch cut (red) terminating in $z = z_0$, and a simple real pole in $z = z^*$, which is a root of Eq. (D.15). The latter dominates the long-time asymptotics of $\langle \chi_0^\alpha(t) \rangle$, as described in Sec. D.2.

The off-critical case in model A (i.e. $r > 0$ and $a = 0$) is more delicate, because the relative positions of the branching point $z_0 = -Dr$ and the pole(s) z^* may change depending on the value of r. For sufficiently small $r \ll \tilde{\gamma}_0/D$, the branching point z_0 will still lie closer to the imaginary axis than the pole(s) z^*. The leading asymptotic behavior of $\chi_0^\alpha(t)$ can thus be found by expanding $\hat{\chi}_0^\alpha(z)$ in Eq. (D.14) around $z_0 = -Dr$. Using Eq. (D.12) gives

$$\hat{\chi}_0^\alpha(z) \sim (z + Dr)^{\frac{d}{2}}, \tag{D.20}$$

and comparing with Eqs. (D.3) and (D.2) then yields

$$\langle \chi_0^\alpha(t) \rangle \sim e^{-Drt} t^{-(1+\frac{d}{2})}, \tag{D.21}$$

as reported in (6.43).

In the opposite limit $r \gg \tilde{\gamma}_0/D$, the analytic structure of the function $\hat{\chi}_0^\alpha(z)$ in Eq. (D.14) can be inspected by plotting its real or imaginary part using e.g. `Mathematica`, for selected choices of the interaction potential V_q. By choosing a Gaussian V_q as in Eq. (6.4) and for $d = 1, 2, 3$ (but also for a Yukawa-like potential $V_q = 1/(1 + q^2 R^2)$ [68]), the resulting analytic structure resembles the one sketched in Figure D.1, with a single real pole z^* at the right of the branch cut. This simple pole dominates the long-time behavior of $\langle \chi_0^\alpha(t) \rangle$, which thus generically reads [68, 277]

$$\langle \chi_0^\alpha(t) \rangle \sim e^{z^* t}, \tag{D.22}$$

with $z^* < 0$ given implicitly from Eq. (D.15).

Finally, we note that the asymptotic behavior of the center of mass $\chi_0^\alpha(t)$ studied here coincides with that of a single particle at position $X(t)$ relaxing towards the center of a harmonic potential of stiffness $\tilde{\gamma}_0$, which was derived in [66] within a weak-coupling approximation for small λ (see Eqs. (33) and (34) therein, and the Erratum), and later in [68] within linear response (see Appendix C therein). In particular, for the off-critical model A it was found perturbatively in Ref. [66] that $X(t) \sim \lambda^2 t e^{-\tilde{\gamma}_0 t} + \mathcal{O}(\lambda^4)$, for $Dr > \tilde{\gamma}_0$. In hindsight, this is compatible with the behavior found above in Eq. (D.22), as can be checked by using that for small λ (see Eq. (D.15))

$$z^* = -\tilde{\gamma}_0 + \lambda^2 \left[\hat{\mathcal{K}}(-\tilde{\gamma}_0) - \hat{\mathcal{K}}(0)\right] + \mathcal{O}(\lambda^4). \tag{D.23}$$

D.3 Perturbative correction to the gyration radius

In this Section we derive the expression of the generating functional $\mathcal{Z}[\{\mathbf{j}_i\}]$ reported in Eq. (6.48), and we use it to obtain the theoretical predictions on the typical polymer size in Eqs. (6.51) and (6.52) in the framework of the weak-coupling approximation. By taking appropriate derivatives of $\mathcal{Z}[\{\mathbf{j}_i\}]$ we compute the covariance between the R_g^2 (or $\boldsymbol{R}_{\text{ee}}$) and the effective Hamiltonian $\mathcal{H}_{\text{eff}}$, which constitute the first non-trivial corrections of order λ^2 to the unperturbed values $\langle R_g^2\rangle_{f,0}$ and $\langle \boldsymbol{R}_{\text{ee}}\rangle_{f,0}$. After rewriting the Hamiltonian $\mathcal{H}_0$ in terms of the Rouse modes $\{\boldsymbol{\chi}_i\}$ as

$$\mathcal{H}_0 = \frac{\kappa}{2}\sum_{ij} M_{ij}\boldsymbol{X}_i \cdot \boldsymbol{X}_j + \frac{\kappa_c}{2}\sum_i \boldsymbol{X}_i^2 = \frac{1}{2}\sum_i \mathcal{M}_i \boldsymbol{\chi}_i^2 , \tag{D.24}$$

we use the definition of the generating functional given in Eq. (6.48) to obtain:

$$\begin{aligned}\mathcal{Z}[\{\mathbf{j}_i\}] &= \left\langle \exp\left(\sum_i \mathbf{j}_i \cdot \boldsymbol{\chi}_i\right)\right\rangle_{f,0} &\text{(D.25)}\\ &= \frac{1}{\mathcal{N}}\prod_{j=0}^{N-1}\int \mathrm{d}\boldsymbol{\chi}_j \exp\left[-\frac{\beta}{2}\mathcal{M}_i\boldsymbol{\chi}_j^2 - \boldsymbol{\chi}_j\cdot[\beta(\varphi_{j,N-1}-\varphi_{j,0}) - \mathbf{j}_j]\right]\\ &= \exp\left[\frac{1}{2\beta}\sum_i \frac{1}{\mathcal{M}_i}[\mathbf{j}_i^2 + 2\beta(\varphi_{i,N-1}-\varphi_{i,0})\boldsymbol{f}_s\cdot\mathbf{j}_i]\right] ,\end{aligned}$$

where $\mathcal{N}$ denotes the normalization factor given by $\mathcal{N} = \mathcal{Z}[\{\mathbf{j}_i = \mathbf{0}\}]$, and the integral in the second line can be easily solved being a standard multivariate Gaussian integral. In order to compute the covariance between R_g^2 and $\mathcal{H}_{\text{eff}}$, we first of all need to evaluate $\langle\mathcal{H}_{\text{eff}}\rangle_{f,0}$, which depends on the following averages:

$$\left\langle \exp\left(i\boldsymbol{q}\sum_k(\varphi_{ki}-\varphi_{kj})\boldsymbol{\chi}_k\right)\right\rangle = \mathcal{Z}[\{\mathbf{j}_k = i\boldsymbol{q}(\varphi_{ki}-\varphi_{kj})\}] , \tag{D.26}$$

with generic indices i and j. Thus we have:

$$\langle\mathcal{H}_{\text{eff}}\rangle_{f,0} = -\frac{\lambda^2}{2}\sum_{ij}\int\frac{\mathrm{d}^d q}{(2\pi)^d}|V_q|^2 G_{\boldsymbol{q}}\left[\mathcal{Z}[\{\mathbf{j}_k = i\boldsymbol{q}(\varphi_{ki}-\varphi_{kj})\}] - 1\right] . \tag{D.27}$$

Secondly, we need the correlation between the gyration radius and the effective Hamiltonian, i.e. $\langle R_g^2 \mathcal{H}_{\text{eff}} \rangle_{f,0}$. Since the R_g^2 is a weighted combination of the Rouse amplitudes $\boldsymbol{\chi}_j^2$, such correlation requires the knowledge of the following average:

$$\langle \boldsymbol{\chi}_n^2 e^{i\mathbf{q}\cdot\sum_k(\varphi_{ki}-\varphi_{kj})\boldsymbol{\chi}_k} \rangle_{f,0} = \sum_\alpha \left.\frac{\partial^2 \mathcal{Z}[\{\mathbf{j}_k\}]}{\partial j_n^\alpha \partial j_n^\alpha}\right|_{\mathbf{j}_k = i\mathbf{q}(\varphi_{ki}-\varphi_{kj})} =$$
$$\left[\frac{d}{\beta\mathcal{M}_n} + \left(\frac{i\boldsymbol{q}/\beta(\varphi_{ni}-\varphi_{nj}) + \boldsymbol{f}_s(\varphi_{n,N-1}-\varphi_{n,0})}{\mathcal{M}_n}\right)^2\right] \mathcal{Z}[\{\mathbf{j}_k = i\boldsymbol{q}(\varphi_{ki}-\varphi_{kj})\}] \,. \tag{D.28}$$

Combining Eqs. (6.47), (6.49), (D.27) and (D.28), we get the first non-trivial perturbative correction to the gyration radius R_g^2 reported in Eq. (6.51). In the case of the $\boldsymbol{R}_{\text{ee}}$, being the latter a linear combination of the Rouse modes as shown in (6.45), its correlation $\langle \boldsymbol{R}_{\text{ee}} \mathcal{H}_{\text{eff}} \rangle_{f,0}$ with the effective Hamiltonian depends on the average:

$$\begin{aligned}\langle \chi_n^\alpha e^{i\mathbf{q}\cdot\sum_k(\varphi_{ki}-\varphi_{kj})\boldsymbol{\chi}_k} \rangle_{f,0} &= \left.\frac{\partial \mathcal{Z}[\{\mathbf{j}_k\}]}{\partial j_n^\alpha}\right|_{\mathbf{j}_k = i\boldsymbol{q}(\varphi_{ki}-\varphi_{kj})} \\ &= \frac{\mathrm{j}_n^\alpha + \beta f_s^\alpha(\varphi_{i,N-1}-\varphi_{i,0})}{\beta\mathcal{M}_n} \mathcal{Z}[\{\mathbf{j}_k = i\boldsymbol{q}(\varphi_{ki}-\varphi_{kj})\}] \,.\end{aligned} \tag{D.29}$$

The above equation can be combined with Eqs. (6.47), (6.50), (D.27) to obtain the result reported in Eq. (6.52).

D.4 Details of the numerical simulation

All theoretical predictions derived in Chapter 6 are compared with numerical simulations of the stochastic equations of motion given in Eqs. (6.6) and (6.12). In particular, the stochastic dynamics of the polymer is simulated in real space, whereas the evolution of the fluctuating order parameter ϕ is simulated in Fourier space (see e.g. [62, 325]). This requires introducing a momentum cutoff for the modes of the field, given by $q_c = 2\pi n_c/L$ with L the box size, and n_c an integer cutoff that determines the number of simulated modes. Specifically, in $d = 1$ the number of modes is $n_c + 1$, with wave vectors $q = 2\pi n/L$ and $n \in \{0, 1, 2, ..., n_c\}$. In $d = 2$, instead, we simulate $(n_c + 1)(2n_c + 1)$ modes, namely those related to the wave vectors $\boldsymbol{q} = (2\pi n_x/L, 2\pi n_y/L)$ with $n_x \in \{0, 1, 2, ..., n_c\}$ and $n_y \in \{-n_c, -n_c+1, ..., n_c-1, n_c\}$. Note that the modes $\phi_{\boldsymbol{q}}$ with $\boldsymbol{q}$ living on the left half-plane of the momentum space can be automatically obtained as $\phi_{-\boldsymbol{q}} = \phi_{\boldsymbol{q}}^*$, being $\phi(\boldsymbol{x}, t)$ a real scalar field. In particular, we used $n_c = 40$ with box size $L = 50$ in all figures but Figure 6.3, where we used instead $n_c = 640$ and $L = 1600$. Indeed, in the latter case, capturing the long-time power-law relaxation of the center of mass requires including in the simulation Fourier modes with a wave vector sufficiently close to $\boldsymbol{q} = 0$, i.e. those modes characterized by a slower relaxation time. For this reason, a larger system size is needed to observe the algebraic decay that appears in the vicinity of the critical point.

The stochastic differential equations (6.6) and (6.12) are integrated with the standard Euler-Maruyama scheme with integration timestep $\Delta t = 0.001$. The discretized dynamics of the polymer is given by:

$$\begin{aligned} \boldsymbol{X}_i(t+\Delta t) - \boldsymbol{X}_i(t) = -\Delta t\gamma \sum_j M_{ij}\boldsymbol{X}_j(t) - \Delta t\gamma_c \boldsymbol{X}_i(t) + \boldsymbol{\xi}_i(t) \\ - \Delta t\nu\lambda\sigma_i L^d \sum_{\boldsymbol{n}\in S} V_{-\boldsymbol{n}}\left(\frac{2\pi\boldsymbol{n}}{L}\right)\phi^R_{\boldsymbol{n}}(t)\sin\left(\frac{2\pi\boldsymbol{n}\cdot\boldsymbol{X}_i(t)}{L}\right) \\ - \Delta t\nu\lambda\sigma_i L^d \sum_{\boldsymbol{n}\in S} V_{-\boldsymbol{n}}\left(\frac{2\pi\boldsymbol{n}}{L}\right)\phi^I_{\boldsymbol{n}}(t)\cos\left(\frac{2\pi\boldsymbol{n}\cdot\boldsymbol{X}_i(t)}{L}\right), \end{aligned} \tag{D.30}$$

where the set S is defined as $S = \{-n_c, -n_c+1, ..., n_c-1, n_c\}^2$, the noises $\{\boldsymbol{\xi}_i(t)\}$ are independent zero-mean Gaussian random variables with standard deviation $\sqrt{2\nu T\Delta t}$ and $\phi^R_{\boldsymbol{n}}$, and $\phi^I_{\boldsymbol{n}}$ are the real and the imaginary part of the mode $\phi_{\boldsymbol{n}}$, respectively. The potential $V_{\boldsymbol{n}}$ is given by

$$\begin{aligned} V_{\boldsymbol{n}} &= \frac{(2\pi R^2)^{-d/2}}{L^d}\int_{\mathcal{D}} \mathrm{d}^d\boldsymbol{x}\exp\left(-\boldsymbol{x}^2/2R^2 - i2\pi\boldsymbol{n}\cdot\boldsymbol{x}/L\right) \\ &\simeq \frac{1}{L^d}\exp\left[-\frac{1}{2}\left(\frac{2\pi}{L}\right)^2\boldsymbol{n}^2R^2\right], \end{aligned} \tag{D.31}$$

with integration domain $\mathcal{D} = [-L, L]^d$, and where we assumed that the box size L is much bigger than the range of interaction between each monomer and the field, i.e. $L \gg R$. The discretized dynamics of the field is given by:

$$\begin{aligned} \phi^R_{\boldsymbol{n}}(t+\Delta t) - \phi^R_{\boldsymbol{n}}(t) = &- \Delta t\alpha_{\boldsymbol{q}}\phi^R_{\boldsymbol{n}}(t) + \zeta^R_{\boldsymbol{n}}(t) \\ &+ \Delta t D\lambda V_{\boldsymbol{n}} q^a \sum_j \sigma_j\cos\left(\frac{2\pi\boldsymbol{n}\cdot\boldsymbol{X}_j(t)}{L}\right), \end{aligned} \tag{D.32}$$

and

$$\begin{aligned} \phi^I_{\boldsymbol{n}}(t+\Delta t) - \phi^I_{\boldsymbol{n}}(t) = &- \Delta t\alpha_{\boldsymbol{q}}\phi^I_{\boldsymbol{n}}(t) + \zeta^I_{\boldsymbol{n}}(t) \\ &- \Delta t D\lambda V_{\boldsymbol{n}} q^a \sum_j \sigma_j\sin\left(\frac{2\pi\boldsymbol{n}\cdot\boldsymbol{X}_j(t)}{L}\right), \end{aligned} \tag{D.33}$$

with $\boldsymbol{q} = 2\pi\boldsymbol{n}/L$. The noises $\{\zeta^R_{\boldsymbol{n}}(t)\}$ and $\{\zeta^I_{\boldsymbol{n}}(t)\}$ are zero-mean Gaussian random variables with correlations

$$\langle\zeta^{R,I}_{\boldsymbol{n}}(t)\zeta^{R,I}_{\boldsymbol{m}}(s)\rangle = \frac{DT}{L^d}\left(\frac{2\pi|\boldsymbol{n}|}{L}\right)^a\delta(t-s)[\delta_{\boldsymbol{n},\boldsymbol{m}} \pm \delta_{\boldsymbol{n},-\boldsymbol{m}}]. \tag{D.34}$$

Appendix E

Appendix of Chapter 7

E.1 Velocity marginalization

In this Appendix, we derive the equation of motion for the position of the odd tracer in Eq. (7.2) by integrating out the velocity variable $\boldsymbol{V}_0(t)$. Wherever they appear, repeated indices imply summation according to Einstein notation. To marginalize the velocity, we define the new variable $\boldsymbol{U}_0(t) = \boldsymbol{S}^{-1}\boldsymbol{V}_0(t)$, which is related to the velocity $\boldsymbol{V}_0(t)$ by the linear transformation $\boldsymbol{S}$. The latter has the property to diagonalize the friction tensor $\boldsymbol{\Gamma}$, and satisfies the following relation

$$\boldsymbol{S}^{-1}\,\boldsymbol{\Gamma}\boldsymbol{S} = \boldsymbol{L}\,, \tag{E.1}$$

with $\boldsymbol{L}, \boldsymbol{S} \in \mathbb{C}^{2\times 2}$. In particular, $\boldsymbol{L}$ is diagonal and contains the eigenvalues of the friction tensor $L_{00} \equiv \ell_0 = \gamma(1 - i\kappa)$ and $L_{11} \equiv \ell_1 = \gamma(1 + i\kappa)$, where i denotes the imaginary unit, and

$$\boldsymbol{S} = \frac{1}{\sqrt{2}}\begin{pmatrix} -i & i \\ 1 & 1 \end{pmatrix}\,. \tag{E.2}$$

Note that the emergence of complex eigenvalues is due to the oscillatory behavior introduced by the oddness κ. In the new variable, the velocity dynamics can be formally solved yielding:

$$\begin{aligned} \boldsymbol{U}_0(t) &= \mathrm{e}^{-\frac{(t-t_0)}{m}\boldsymbol{L}}\,\boldsymbol{U}_0(t_0) \\ &- \frac{\lambda_\mathrm{t}}{m}\int_{t_0}^{t}\mathrm{d}s\,\mathrm{e}^{-\frac{(t-s)}{m}\boldsymbol{L}}\sum_{j=0}^{N}\boldsymbol{S}^{-1}\,\nabla\mathcal{U}(\boldsymbol{X}_0(s) - \boldsymbol{X}_j(s)) \\ &+ \frac{1}{m}\int_{t_0}^{t}\mathrm{d}s\,\mathrm{e}^{-\frac{(t-s)}{m}\boldsymbol{L}}\,\boldsymbol{S}^{-1}\,\boldsymbol{\xi}_0(s). \end{aligned} \tag{E.3}$$

The expression for $\boldsymbol{U}_0(t)$ can be inverted back into the original variables to find the stochastic dynamics of the position $\dot{\boldsymbol{X}}_0(t) = \boldsymbol{S}\boldsymbol{U}_0(t)$. Using the identity

$$S_{\alpha\beta}S^{-1}_{\beta\sigma}\, f_\sigma(s) \exp\left(-\frac{\ell_\beta}{m}(t-s)\right) = G_{\alpha\beta}(t-s)\, f_\beta(s) \tag{E.4}$$

with $\boldsymbol{f}(s)$ a generic 2-dimensional vector, $s < t$ and $\boldsymbol{G}(u)$ defined in Eq. (7.3), Eq. (7.2) is finally obtained. As described in Eq. (7.4), the evolution of the position of the odd tracer depends on the colored noise $\boldsymbol{\eta}(t)$, which is given by the convolution of the function $\boldsymbol{G}(u)$ with the white noise $\boldsymbol{\xi}_0$. The correlation of $\boldsymbol{\eta}(t)$ can be computed as

$$\begin{aligned}
\langle \boldsymbol{\eta}(t) \otimes \boldsymbol{\eta}(s) \rangle &= \frac{2T\gamma}{m^2}\int_{t_0}^{t} \mathrm{d}t' \int_{t_0}^{s} \mathrm{d}s'\, \boldsymbol{G}(t-t')\, \boldsymbol{G}^{\mathrm{T}}(s-s')\, \delta(t'-s') \\
&= \frac{2T\gamma}{m^2}\int_{t_0}^{\min(t,s)} \mathrm{d}t'\, \boldsymbol{G}(t-t')\, \boldsymbol{G}^{\mathrm{T}}(s-t') \\
&= \frac{T}{m}\left[\mathrm{e}^{-\frac{|t-s|}{\tau_\gamma}} - \mathrm{e}^{-\frac{t+s-2t_0}{\tau_\gamma}}\right] \boldsymbol{M}(t-s),
\end{aligned}$$

which corresponds to the correlation reported in Eq. (7.5). For the matrix product in the above calculation we used the relation

$$\boldsymbol{G}(t-t')\, \boldsymbol{G}^{T}(s-t') = \mathrm{e}^{-(t+s-2t')/\tau_\gamma}\, \boldsymbol{M}(t-s), \tag{E.5}$$

which easily can be shown with the help of trigonometric identities.

E.2 The interaction-free case

For later purposes, it is convenient to first analyze the case where the coupling between the odd tracer and the density field is switched off. We denote the position of the free odd tracer as $\boldsymbol{X}_0^{(0)}$, and the free field as $\phi_{\boldsymbol{q}}^{(0)}$.

E.2.1 Free dynamics of the odd tracer

In the absence of the coupling to the density field, i.e. with $\lambda_{\mathrm{t}} = 0$, the stochastic dynamics of the odd tracer can be exactly solved, and gives

$$\boldsymbol{X}_0^{(0)}(t) = \int_{t_0}^{t} \mathrm{d}s\, \boldsymbol{G}(s-t_0)\, \boldsymbol{V}_0(t_0) + \int_{t_0}^{t} \mathrm{d}s\, \boldsymbol{\eta}(s), \tag{E.6}$$

where we assumed that the odd tracer initially sits at the origin $\boldsymbol{X}_0^{(0)}(t_0) = \boldsymbol{0}$ without loss of generality. Note that $\boldsymbol{V}_0(t_0)$ is a fixed value and therefore does not need a perturbative expansion. As the position variable of the tracer follows a Gaussian process, we can characterize it by computing its mean $\boldsymbol{\mu}_0(t)$

$$\boldsymbol{\mu}_0(t) = m\,\boldsymbol{A}(t-t_0)\boldsymbol{V}_0(t_0), \tag{E.7}$$

and the two-point connected correlation $\boldsymbol{C}(t,s)$

$$\begin{aligned}\boldsymbol{C}(t,s) &\equiv \left\langle \boldsymbol{X}_0^{(0)}(t)\otimes\boldsymbol{X}_0^{(0)}(s)\right\rangle - \left\langle \boldsymbol{X}_0^{(0)}(t)\right\rangle \otimes \left\langle \boldsymbol{X}_0^{(0)}(s)\right\rangle \\ &= \frac{2T\nu}{1+\kappa^2}\,[\min(s,t)-t_0]\,\mathbf{1} - mT\left[\boldsymbol{\Gamma}^{-1}\boldsymbol{A}(s-t_0)+\boldsymbol{\Gamma}^{-1}\boldsymbol{A}(t-t_0)\right] \\ &\quad + mT\left[\Theta(t-s)\,\boldsymbol{\Gamma}^{-1}\boldsymbol{A}(t-s)+\Theta(s-t)\,(\boldsymbol{\Gamma}^{-1}\boldsymbol{A}(s-t))^{\mathrm{T}}\right] \\ &\quad - mT\boldsymbol{A}(t-t_0)\boldsymbol{A}^{\mathrm{T}}(s-t_0),\end{aligned} \tag{E.8}$$

where we introduced the abbreviation $\boldsymbol{A}(u)=\boldsymbol{\Gamma}^{-1}[\mathbf{1}-\boldsymbol{G}(u)]$ and denoted by $\boldsymbol{a}\otimes\boldsymbol{b}=a_\alpha b_\beta$ the outer product between two vectors $\boldsymbol{a}$, $\boldsymbol{b}$. Note that the connected correlation satisfies $\boldsymbol{C}(t,s)=\boldsymbol{C}^{\mathrm{T}}(s,t)$. Once $\boldsymbol{\mu}_0(t)$ and $\boldsymbol{C}(t,s)$ are known, we can compute the generating functional $\mathcal{Z}[\boldsymbol{j}]$ of the n-point correlations for the position of the odd tracer in the free case ($\lambda=0$)

$$\mathcal{Z}[\boldsymbol{j}] = \left\langle \exp\left\{\int \mathrm{d}t\,\boldsymbol{j}(t)\cdot\boldsymbol{X}_0^{(0)}(t)\right\}\right\rangle, \tag{E.9}$$

where $\boldsymbol{j}(t)$ is an auxiliary field and the average is taken with respect to the following Gaussian path probability

$$\mathcal{P}_0[\boldsymbol{x}] \propto \exp\left\{-\frac{1}{2}\int \mathrm{d}t\int \mathrm{d}s\,[\boldsymbol{x}(t)-\boldsymbol{\mu}_0(t)]\cdot\boldsymbol{C}(t,s)\cdot[\boldsymbol{x}(t)-\boldsymbol{\mu}_0(t)]\right\}. \tag{E.10}$$

Solving the functional Gaussian integral in Eq. (E.9) leads to the following expression for the generating functional

$$\mathcal{Z}[\boldsymbol{j}] = \exp\left\{\frac{1}{2}\int \mathrm{d}t\int \mathrm{d}s\,\boldsymbol{j}(t)\cdot\boldsymbol{C}(t,s)\cdot\boldsymbol{j}(s)+\int \mathrm{d}t\,\boldsymbol{j}(t)\cdot\boldsymbol{\mu}_0(t)\right\}, \tag{E.11}$$

which can be used to derive the full statistics of $\boldsymbol{X}_0^{(0)}$ by taking appropriate derivatives.

E.2.2 Free dynamics of the density field

In the absence of interaction with the tracer particle, the dynamics of the free field in Fourier space $\phi_{\boldsymbol{q}}^{(0)}$ follows an Ornstein-Uhlenbeck process and it is solved by

$$\phi_{\boldsymbol{q}}^{(0)}(t) = \phi_{\boldsymbol{q}}^{(0)}(t_0)\,\mathrm{e}^{-\alpha_{\boldsymbol{q}}(t-t_0)} + \int_{t_0}^{t}\mathrm{d}s\,\mathrm{e}^{-\alpha_{\boldsymbol{q}}(t-s)}\,\zeta_{\boldsymbol{q}}(s). \tag{E.12}$$

Note that in our notation $\phi_{\boldsymbol{q}}(t) = \int \mathrm{d}\boldsymbol{x}\ \phi(\boldsymbol{x},t)\ \exp(-i\boldsymbol{x}\cdot\boldsymbol{q})$ denotes the (two-dimensional) Fourier transformation of a field $\phi(\boldsymbol{x},t)$ with respect to the wave vector $\boldsymbol{q}$. From Eq. (E.12) we can compute the two-point correlations of the free field as

$$\begin{aligned}\left\langle \phi^{(0)}_{\boldsymbol{q}}(t)\,\phi^{(0)}_{\boldsymbol{p}}(s)\right\rangle &= \left\langle \phi^{(0)}_{\boldsymbol{q}}(t_0)\,\phi^{(0)}_{\boldsymbol{p}}(t_0)\right\rangle\ \mathrm{e}^{-\alpha_{\boldsymbol{q}}(t-t_0)}\ \mathrm{e}^{-\alpha_{\boldsymbol{p}}(s-t_0)} \\ &\quad + T\,\frac{(2\pi)^2\,\delta(\boldsymbol{q}+\boldsymbol{p})}{\lambda_{\mathrm{h}}\mathcal{U}_{\boldsymbol{q}} + T/\rho_0}\left[\mathrm{e}^{-\alpha_{\boldsymbol{q}}|t-s|} - \mathrm{e}^{-\alpha_{\boldsymbol{q}}(t+s-2t_0)}\right], \end{aligned} \tag{E.13}$$

where we used that $\mathcal{U}_{\boldsymbol{q}} = \mathcal{U}_{-\boldsymbol{q}}$ which holds for any symmetric interaction potential. When $t = s$ and the field had enough time to relax (formally $t_0 \to -\infty$), the two-point correlator yields

$$\left\langle \phi^{(0)}_{\boldsymbol{q}}(t)\,\phi^{(0)}_{\boldsymbol{p}}(t)\right\rangle = T\,\frac{(2\pi)^2\,\delta(\boldsymbol{q}+\boldsymbol{p})}{\lambda_{\mathrm{h}}\mathcal{U}_{\boldsymbol{q}} + T/\rho_0}\,. \tag{E.14}$$

Thus, if we assume that the field is distributed according to its equilibrium distribution before being put in contact with the odd tracer at time $t = t_0$, we have that $\langle \phi^{(0)}_{\boldsymbol{q}}(t_0)\,\phi^{(0)}_{\boldsymbol{p}}(t_0)\rangle$ is given by (E.14). Under this equilibration assumption, Eq. (E.13) can be written as

$$\begin{aligned}\left\langle \phi^{(0)}_{\boldsymbol{q}}(t)\,\phi^{(0)}_{\boldsymbol{q}'}(s)\right\rangle &= T\,\frac{(2\pi)^2\delta(\boldsymbol{q}+\boldsymbol{p})}{\lambda_{\mathrm{h}}\mathcal{U}_{\boldsymbol{q}} + T/\rho_0}\mathrm{e}^{-\alpha_{\boldsymbol{q}}|t-s|} \\ &\equiv (2\pi)^2\delta(\boldsymbol{q}+\boldsymbol{p})\,C_{\phi_{\boldsymbol{q}}}(t-s), \end{aligned} \tag{E.15}$$

which defines the stationary time-translational invariant correlator $C_{\phi_{\boldsymbol{q}}}$ of the free field $\phi^{(0)}_{\boldsymbol{q}}$.

E.3 Weak-coupling approximation

In this Appendix, we compute the first non-trivial perturbative correction to the mean squared displacement, which due to symmetry arguments is of second order in the interaction coupling λ_{t}. In the case where the tracer is initialized at the origin, i.e. $\boldsymbol{X}_0(t_0) = \boldsymbol{0}$, this is formally given by Eq. (7.23). To evaluate such correction we need to separately compute the correlations $\langle \boldsymbol{X}^{(1)}_0(t)\cdot\boldsymbol{X}^{(1)}_0(t)\rangle$ and $\langle \boldsymbol{X}^{(0)}_0(t)\cdot\boldsymbol{X}^{(2)}_0(t)\rangle$. To evaluate the first, we formally solve the stochastic dynamics in Eq. (7.25) to get

$$\begin{aligned}\left\langle \boldsymbol{X}^{(1)}_0(t)\cdot\boldsymbol{X}^{(1)}_0(t)\right\rangle &= -\frac{1}{m^2}\int\frac{d\boldsymbol{q}}{(2\pi)^2}\int\frac{d\boldsymbol{p}}{(2\pi)^2}\,q_\beta p_\gamma\,\mathcal{U}_{\boldsymbol{q}}\mathcal{U}_{\boldsymbol{p}} \\ \times\int_{t_0}^{t}\mathrm{d}s\int_{t_0}^{s}\mathrm{d}u\int_{t_0}^{t}\mathrm{d}s'\int_{t_0}^{t}\mathrm{d}u'\,G_{\alpha\beta}(s-u)\,G_{\alpha\gamma}(s'-u') \\ \times\left\langle \phi^{(0)}_{\boldsymbol{q}}(u)\,\phi^{(0)}_{\boldsymbol{p}}(u')\,\mathrm{e}^{i\boldsymbol{q}\cdot\boldsymbol{X}^{(0)}_0(u)+i\boldsymbol{p}\cdot\boldsymbol{X}^{(0)}_0(u')}\right\rangle. \end{aligned} \tag{E.16}$$

As the average in the last line only involves the position of the free tracer $\boldsymbol{X}_0^{(0)}$ and the free field $\phi_{\boldsymbol{q}}^{(0)}$, it can be factorized as follows

$$\begin{aligned}
&\left\langle \phi_{\boldsymbol{q}}^{(0)}(u)\, \phi_{\boldsymbol{p}}^{(0)}(u')\, \mathrm{e}^{i\boldsymbol{q}\cdot\boldsymbol{X}_0^{(0)}(u)+i\boldsymbol{p}\cdot\boldsymbol{X}_0^{(0)}(u')}\right\rangle \\
&\quad= \left\langle \phi_{\boldsymbol{q}}^{(0)}(u)\, \phi_{\boldsymbol{p}}^{(0)}(u')\right\rangle \left\langle \mathrm{e}^{i\boldsymbol{q}\cdot\boldsymbol{X}_0^{(0)}(u)+i\boldsymbol{p}\cdot\boldsymbol{X}_0^{(0)}(u')}\right\rangle \\
&\quad= (2\pi)^2\delta(\boldsymbol{q}+\boldsymbol{p})\, C_{\phi_{\boldsymbol{q}}}(u-u')\, \mathcal{Q}_{\boldsymbol{q}}(u,u')\,, \qquad \text{(E.17)}
\end{aligned}$$

where we used Eq. (E.15) and we introduced the two-time quantity $\mathcal{Q}$, which can be obtained from the generating functional as

$$\begin{aligned}
\mathcal{Q}_{\boldsymbol{q}}(u,u') &\equiv \mathcal{Z}[\boldsymbol{j} = i\boldsymbol{q}(\delta(t-u)-\delta(t-u'))] \qquad \text{(E.18)}\\
&= \exp\Big\{ -\frac{1}{2}\boldsymbol{q}\cdot[\boldsymbol{C}(u,u)+\boldsymbol{C}(u',u')-\boldsymbol{C}(u',u)-\boldsymbol{C}(u,u')]\cdot\boldsymbol{q} \\
&\qquad + i\boldsymbol{q}\cdot[\boldsymbol{\mu}_0(u)-\boldsymbol{\mu}_0(u')]\Big\}\,.
\end{aligned}$$

Therefore, the correlation $\langle \boldsymbol{X}_0^{(1)}(t)\cdot\boldsymbol{X}_0^{(1)}(t)\rangle$ can be rewritten as

$$\begin{aligned}
\left\langle \boldsymbol{X}_0^{(1)}(t)\cdot\boldsymbol{X}_0^{(1)}(t)\right\rangle &= \frac{1}{m^2}\int \frac{d\boldsymbol{q}}{(2\pi)^2}\, q_\beta q_\gamma\, |\mathcal{U}_{\boldsymbol{q}}|^2 \\
\times \int_{t_0}^{t}\mathrm{d}s\int_{t_0}^{s}\mathrm{d}u\int_{t_0}^{t}\mathrm{d}s'\int_{t_0}^{s'}&\mathrm{d}u'\, G_{\alpha\beta}(s-u)G_{\alpha\gamma}(s'-u') \\
\times\, C_{\phi_{\boldsymbol{q}}}(u-u')\, \mathcal{Q}_{\boldsymbol{q}}(u,u'). \qquad \text{(E.19)}
\end{aligned}$$

Before calculating $\langle \boldsymbol{X}_0^{(0)}(t)\cdot\boldsymbol{X}_0^{(2)}(t)\rangle$ it is convenient to solve the dynamics of $\phi_{\boldsymbol{q}}^{(1)}$, obtaining

$$\phi_{\boldsymbol{q}}^{(1)}(t) = -\nu\rho_0\, q^2\mathcal{U}_{\boldsymbol{q}}\int_{t_0}^{t}\mathrm{d}s\, \mathrm{e}^{-\alpha_{\boldsymbol{q}}(t-s)}\, \mathrm{e}^{-i\boldsymbol{q}\cdot\boldsymbol{X}_0^{(0)}(s)}\,, \qquad \text{(E.20)}$$

where we used $\phi_{\boldsymbol{q}}^{(n)}(t_0)=0$ for all $n\geq 1$. This is justified as we already assumed for Eq. (E.14) that the initial condition of the field is drawn from its equilibrium distribution in absence of the coupling with the tracer. With the help of the identity

$$\begin{aligned}
\left\langle X_0^{(0)}(t)\, \mathrm{e}^{-i\boldsymbol{q}\cdot[\boldsymbol{X}_0^{(0)}(u')-\boldsymbol{X}_0^{(0)}(u)]}\right\rangle &= \left.\frac{\delta\mathcal{Z}[\{\boldsymbol{j}\}]}{\delta j^\alpha(t)}\right|_{\boldsymbol{j}(t)=-i\boldsymbol{q}[\delta(t-u')-\delta(t-u)]} \\
&= \mathcal{Q}_{\boldsymbol{q}}(u,u')\ \left[(\boldsymbol{C}(t,u)-\boldsymbol{C}(t,u'))i\boldsymbol{q}+\boldsymbol{\mu}_0(t)\right]\,, \\
&\qquad \text{(E.21)}
\end{aligned}$$

the correlation $\langle \boldsymbol{X}_0^{(0)}(t) \cdot \boldsymbol{X}_0^{(2)}(t)\rangle$ can now be evaluated to be

$$\begin{aligned}\langle \boldsymbol{X}_0^{(0)}(t) \cdot \boldsymbol{X}_0^{(2)}(t)\rangle &= \frac{i\nu\rho_0}{m} \int \frac{\mathrm{d}\boldsymbol{q}}{(2\pi)^2} q_\beta q^2 |\mathcal{U}_{\boldsymbol{q}}|^2 \int_{t_0}^{t} \mathrm{d}s' \int_{t_0}^{s'} \mathrm{d}u' \int_{t_0}^{u'} dv'\; G_{\alpha\beta}(s'-u') \\ &\quad \times \mathrm{e}^{-\alpha_{\boldsymbol{q}}(u'-v')} \left[(C_{\alpha\gamma}(t,u') - C_{\alpha\gamma}(t,v'))\, iq_\gamma + \mu_0^\alpha(t)\right] \mathcal{Q}_{\boldsymbol{q}}(u',v') \\ &\quad + \frac{i}{m^2} \int \frac{\mathrm{d}\boldsymbol{q}}{(2\pi)^2} q^\beta q^\delta q^\epsilon |\mathcal{U}_{\boldsymbol{q}}|^2 \int_{t_0}^{t} \mathrm{d}s' \int_{t_0}^{s'} \mathrm{d}u' \int_{t_0}^{u'} \mathrm{d}v' \int_{t_0}^{v'} \mathrm{d}w'\; G_{\alpha\beta}(s'-u') \\ &\quad \times G_{\delta\epsilon}(v'-w') \left[(C_{\alpha\gamma}(t,u') - C_{\alpha\gamma}(t,w'))\, iq_\gamma + \mu_0^\alpha(t)\right] C_{\phi_{\boldsymbol{q}}}(u'-w')\, \mathcal{Q}_{\boldsymbol{q}}(u',w').\end{aligned} \tag{E.22}$$

The expression for the correlations given in Eqs. (E.19) and (E.22) are very lengthy and do not admit an efficient numerical evaluation due to the nested time-integrals. However, these integrals can be analytically evaluated within the small mass limit that characterizes the overdamped regime. We can simplify the expression of $\mathcal{Q}_{\boldsymbol{q}}(t,s)$ given in Eq. (E.18) by neglecting all contributions proportional to mass in its exponent and find

$$\mathcal{Q}_{\boldsymbol{q}}(t,s) \xrightarrow{m\to 0} \mathrm{e}^{-q^2 D_0 |t-s| + i\boldsymbol{q}\cdot(\boldsymbol{\mu}_0(t) - \boldsymbol{\mu}_0(s))}\,, \tag{E.23}$$

which renders $\mathcal{Q}_{\boldsymbol{q}}$ an exponential function of the two times t and s only. Here, we used the bare diffusion of the odd tracer particle given by $D_0 = T\nu/(1+\kappa^2)$. Since also the two-point correlator $\boldsymbol{C}(t,s)$ of Eq. (E.10), the function $\boldsymbol{G}(t)$ as defined in Eq. (7.3) and the free field correlator $C_{\phi_{\boldsymbol{q}}}(t)$ of Eq. (E.15) can be rewritten as (complex) exponentials upon using suitable trigonometric identities, the nested time-integrals in Eqs. (E.19) and (E.22) can thus be solved analytically. Note that the validity of this seemingly uncontrolled approximation is checked a posteriori by comparing the theoretical predictions with numerical simulations. By further specializing the calculation to the long-time limit $t_0 \to -\infty$, we can rewrite the correlation in Eq. (E.19) as

$$\left\langle \boldsymbol{X}_0^{(1)}(t) \cdot \boldsymbol{X}_0^{(1)}(t) \right\rangle = \frac{2T\nu\rho_0}{m^2}(t-t_0) \int \frac{\mathrm{d}\boldsymbol{q}}{(2\pi)^2} \frac{q^4 |\mathcal{U}_{\boldsymbol{q}}|^2}{\alpha_{\boldsymbol{q}}} \mathrm{Re}[f_{\boldsymbol{q}}]\,, \tag{E.24}$$

where $\mathrm{Re}[f_{\boldsymbol{q}}]$ denotes the real part of the momentum-dependent complex number $f_{\boldsymbol{q}}$ defined as

$$f_{\boldsymbol{q}} = \frac{\tau_\gamma^2}{\tilde{\alpha}_{\boldsymbol{q}} \left[1 - (i\kappa - \tau_\gamma \tilde{\alpha}_{\boldsymbol{q}})^2\right]} - \frac{\tau_\gamma^4\, \tilde{\alpha}_{\boldsymbol{q}}}{(1+i\kappa)\left[(1+i\kappa)^2 - (\tau_\gamma \tilde{\alpha}_{\boldsymbol{q}})^2\right]}\,. \tag{E.25}$$

To make the notation more compact, we further defined the new inverse time scale as $\tilde{\alpha}_{\boldsymbol{q}} \equiv \alpha_{\boldsymbol{q}} + T\nu q^2/(1+\kappa^2)$. The correlation given in Eq. (E.22) analogously can be rewritten as

$$\begin{aligned}\left\langle \boldsymbol{X}_0^{(0)}(t)\cdot\boldsymbol{X}_0^{(2)}(t)\right\rangle =& -\frac{2D_0\nu^2\rho_0}{(1+\kappa^2)}(t-t_0)\int\frac{\mathrm{d}\boldsymbol{q}}{(2\pi)^2}\,\frac{q^4|\mathcal{U}_{\boldsymbol{q}}|^2}{\tilde{\alpha}_{\boldsymbol{q}}}\\ &-\frac{2\nu\rho_0}{m}D_0^2(t-t_0)\int\frac{\mathrm{d}\boldsymbol{q}}{(2\pi)^2}\,\frac{q^6|\mathcal{U}_{\boldsymbol{q}}|^2}{\alpha_{\boldsymbol{q}}}\mathrm{Re}[g_{\boldsymbol{q}}]\,, \end{aligned}\tag{E.26}$$

where we introduced the complex number $g_{\boldsymbol{q}}$ defined as

$$g_{\boldsymbol{q}}=\frac{\tau_\gamma\,(2\tau_\gamma\,\tilde{\alpha}_{\boldsymbol{q}}+1-i\kappa)}{\tilde{\alpha}_{\boldsymbol{q}}^2\,(\tau_\gamma\,\tilde{\alpha}_{\boldsymbol{q}}+1-i\kappa)^2}\,. \tag{E.27}$$

The remaining momentum integrals of Eqs. (E.19) and (E.22) due to the inverse Fourier transform can be finally performed numerically (e.g. using `Mathematica`). For the numerical evaluation, we truncated the integration domain $\mathbb{R}^2$ of the momentum-integral into $[-q_b,q_b]^2$, by introducing the momentum cut-off $q_b=300$. This choice strongly depends on the specific interaction potential, as well as on the other parameters of the model (see Appendix E.4 for more details). Here, we use a Gaussian interaction potential that displays an exponential decay on a momentum scale much smaller than q_b. We approved the validity of this approximation by testing the numerical integration for insensitivity against a variation of q_b around the chosen value. By combining the numerical evaluation of Eqs. (E.19) and (E.22) with the formal expression of the first non-trivial perturbative correction to the MSD given in Eq. (7.23), we obtain the results shown in Figs. 7.2, 7.3 and E.1.

E.4 Simulation details

In this Section we report the details of the Brownian dynamics simulations and of the numerical evaluation of the first non-trivial perturbative correction to the MSD of the odd-tracer.

E.4.1 Brownian dynamics simulations

We simulate the stochastic dynamics of the i-th particle according to the underdamped Langevin equation

$$\frac{\mathrm{d}\boldsymbol{X}_i(t)}{\mathrm{d}t}=\boldsymbol{V}_i(t), \tag{E.28}$$

$$m_i\frac{\mathrm{d}\boldsymbol{V}_i(t)}{\mathrm{d}t}=-\gamma_i(\boldsymbol{1}-\kappa_i\boldsymbol{\epsilon})\,\boldsymbol{V}_i(t)+\boldsymbol{F}_i(t)+\sqrt{2\gamma_i k_{\mathrm{B}}T}\,\boldsymbol{\xi}_i(t), \tag{E.29}$$

where $\boldsymbol{X}_i(t),\boldsymbol{V}_i(t)$ are the ith particle position and velocity, respectively. In total, we have $N=200$ particles, where the $i=0$ particle models the odd-diffusive tracer ($\kappa_0\neq 0$) and all other particles form the set of normal-diffusive

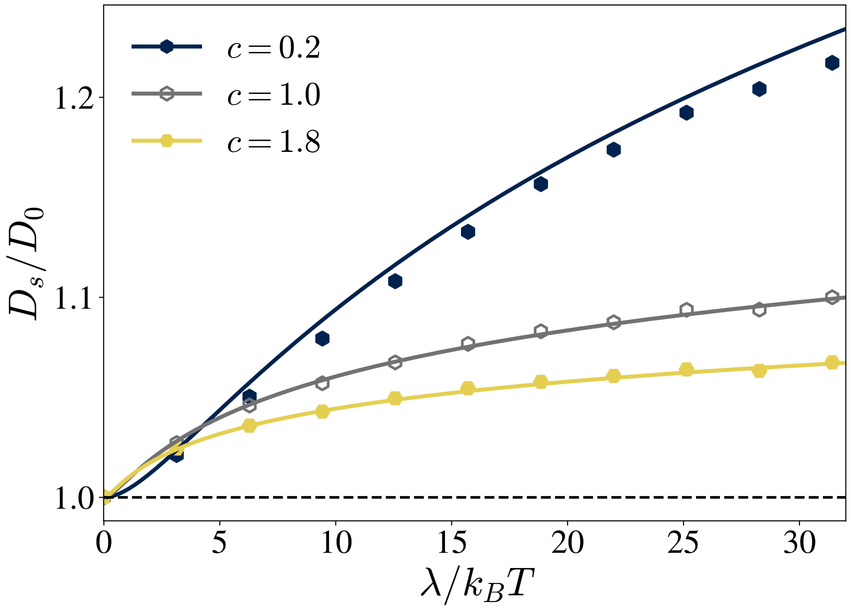

Figure E.1: Reduced self-diffusion D_s/D_0 as a function of the dimensionless coupling parameter $\lambda/k_\mathrm{B}T$. The area fractions c are reported in the legend and the oddness parameter of the tracer is $\kappa = 2$. Despite our theory (solid lines) is supposed to be valid within the weak-coupling approximation, we observe a very good agreement with simulations data (symbols) also for fairly high interaction couplings, especially at high density.

host particles ($\kappa_i = 0$, $i = 1, \ldots, 199$). The coefficients γ_i, m_i denote the particles' friction and mass, respectively, and are assumed to be equal for the tracer and the host particles, i.e. $\gamma_i = 1.0$ and $m_i = 0.01$. In units such that the Boltzmann constant k_B is set to unity, the temperature of the thermal bath is taken to be $T = 1.0$. $\boldsymbol{\xi}_i(t)$ is a zero-mean Gaussian white noise with correlations $\langle \xi_{i,\alpha}(t)\xi_{j,\beta}(t')\rangle = \delta_{ij}\,\delta_{\alpha\beta}\,\delta(t-t')$. Note that Latin indices i, j represent particle labels, and Greek indices α, β represent spatial coordinates. The conservative force $\boldsymbol{F}_i(t)$ exerted on particle i is given by the sum of pairwise interaction forces $\boldsymbol{F}_i(t) = \sum_{j=0}^{N} \boldsymbol{f}_{ij}(t)$, where $\boldsymbol{f}_{ij}$ derives from a (normalized) Gaussian interaction potential $\boldsymbol{f}_{ij} = -\lambda\nabla\mathcal{U}(R_{ij})$ if $R_{ij} < \delta_c$ and is zero if $R_{ij} > \delta_c$. Here, $R_{ij} = |\boldsymbol{X}_i(t) - \boldsymbol{X}_j(t)|$ is the inter-particle distance, and δ_c denotes a cut-off length scale that we use to truncate the interaction potential $\mathcal{U}(R_{ij})$ to reduce the computational time. In particular, if δ_c is sufficiently larger than typical decay length of $\mathcal{U}(R_{ij})$, the error introduced by this approximation is negligible. For the Gaussian interaction potential reported in Eq. (7.27), we choose the parameter $\sigma = 1.0$. Note that σ is used as an effective particle radius, from where we deduce the effective concentration of particles $c = \pi\sigma^2 N/V$, where V is the volume of the simulation box. The cut-off distance of the interaction force is chosen as $\delta_c = 4\sigma$.

The interaction energy scale in units of the thermal energy $k_{\mathrm{B}}T$ is set by the coupling λ, which is taken as a fit parameter. For a comparison of theoretical predictions and simulation results, see Fig. E.1, where different coupling λ are tested. Our analytical predictions are expected to be valid in a regime where the coupling between the tracer and the host particle is sufficiently small. However, from Fig. E.1 it can be seen that at high density ($c = 1.0$ and $c = 1.8$) the whole range of coupling tested produces very accurate results. At low density $c = 0.2$, indeed the mismatch between the theory and the numerical data increases with λ. As a compromise between the accuracy of analytical predictions and the magnitude of the effects shown in the figures of Chapter 7, we opted for $\lambda = 2\pi\sigma^2$. Note that this value is such that the maximum of the interaction energy $\lambda\mathcal{U}(R_{ij})$ is equal to the thermal energy $k_{\mathrm{B}}T$.

To solve the first order stochastic differential equation (E.29) we use the standard Euler-Maruyama scheme, where $\boldsymbol{X}_i(t_{n+1})$ and $\boldsymbol{V}_i(t_{n+1})$ are calculated from $\boldsymbol{X}_i(t_n)$ and $\boldsymbol{V}_i(t_n)$ and $t_{n+1} = t_n + \Delta t$ with $\Delta t = 10^{-3}$. The thermal noise is accounted for by $\sqrt{2\gamma_i T\Delta t}\,\mathcal{N}(0, \mathbf{1})$, where $\mathcal{N}(0, \mathbf{1})$ is a two-dimensional random vector drawn from a multivariate normal distribution with zero mean and covariance matrix given by the identity matrix $\mathbf{1}$. Note that the discretized stochastic equations of motion are interpreted according to the Itô prescription, implying that the standard deviation of the noise is proportional to $\sqrt{\Delta t}$. To simulate Eq. (E.29) we use a square box of length L with periodic boundary conditions ($V = L^2$), where the box length is determined so as to reproduce the desired density of particles c, i.e., $L = \sqrt{\pi\sigma^2 N/c}$. As the interaction force is non-divergent for $R_{ij} \to 0$ and particle overlaps are possible, we initialize the position of the $N = 200$ particles according to a uniform distribution over the finite box. After an initial equilibration process of $n_{\mathrm{eq}} = 10^7$ time-steps, we start recording the stochastic trajectory for a total duration of $n_{\mathrm{tot}} = 4 \times 10^8$ time-steps, which corresponds to a trajectory length of $T = 4 \times 10^5$ in real-time units. For efficient computation, we used a neighbor-list implementation for the evaluation of the interaction forces, with a buffer radius δ_{buff} which has been optimized so to minimize the computational time. Over the broad range of densities simulated, a buffer-radius of $\delta_{\mathrm{buff}} \approx 2\delta_c$ turned out to be the most efficient.

E.4.2 MSD numerical evaluation

To evaluate the diffusion coefficient we calculate the time-averaged mean-squared displacement (TAMSD) [337] for each (independent) trajectory i according to

$$\overline{\delta_i^2(\Delta, T)} = \frac{1}{T - \Delta}\int_0^{T-\Delta} \mathrm{d}t \; |\boldsymbol{X}_{0,i}(t + \Delta) - \boldsymbol{X}_{0,i}(t)|^2, \tag{E.30}$$

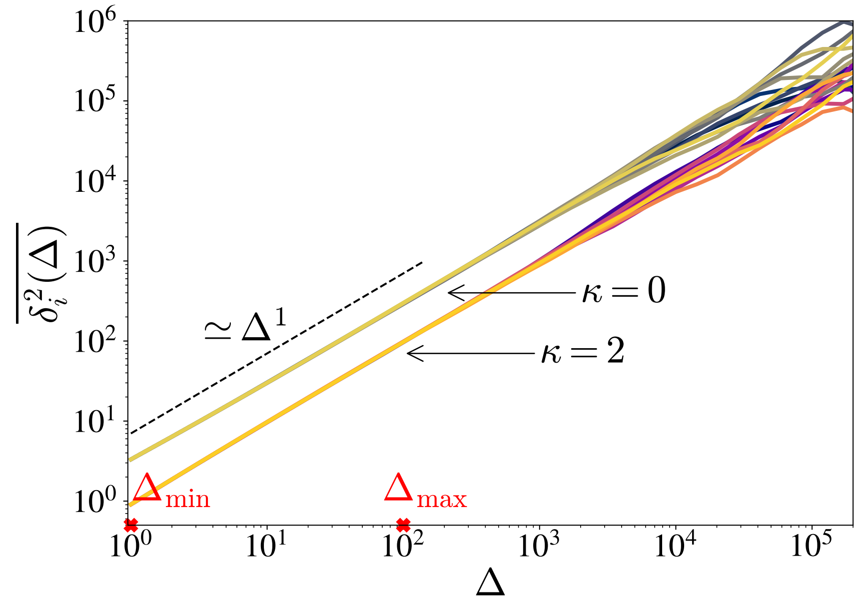

Figure E.2: Typical TAMSD $\overline{\delta_i^2(\Delta)}$ curves as a function of lag-time Δ related to $i = 1, \ldots, 10$ trajectories in the case of $N = 200$ interacting particles with density $c = 0.1$ and $\kappa = 0, 2$. The extreme values $\Delta_{\min} = 1$ and $\Delta_{\max} = 100$ mark the interval of lag times Δ (in real-time units) which are used for ensemble averaging the TAMSDs.

where $\boldsymbol{X}_{0,i}(t)$ is the the position of the tracer particle at time t in trajectory i. As the system under consideration is ergodic, we can ensemble-average over the $i = 1, \ldots, i_{\max}$ independent trajectories to obtain the estimate for the mean-squared displacement (MSD) [338], which is formally defined as

$$\begin{aligned} \left\langle |\mathbf{X}_0(t) - \mathbf{X}_0(0)|^2 \right\rangle &= \lim_{T\to\infty} \left\langle \overline{\delta_i^2(\Delta = t, T)} \right\rangle \\ &= \lim_{T\to\infty} \frac{1}{i_{\max}} \sum_{i=1}^{i_{\max}} \overline{\delta_i^2(t = \Delta, T)}. \end{aligned} \tag{E.31}$$

By taking T big it is legit to assume that the initial conditions play no role in the evaluation of the long-time MSD. Hence, for the sake of simplicity, we impose $\mathbf{X}_0(t_0) = \mathbf{0}$. We observe from Fig. E.2 that the most reliable Δ-range from where to extract the MSD is $1 = \Delta_{\min} \leq \Delta \leq \Delta_{\max} = 100$. The MSD is then used to deduce the self-diffusion coefficient D_{s} by fitting a linear time-dependence $\langle |\mathbf{X}_0(t)|^2 \rangle = 4\, D_{\mathrm{s}}\, t^1$, where we take $N_\Delta = 40$ logarithmically equidistant lag-times to fit the MSD and ensemble average over $i_{\max} = 10$ independent trajectories.

Acknowledgements

First and foremost, I would like to express my gratitude to my two supervisors, Andrea Gambassi and Edgar Roldan, for fostering my scientific growth and for their invaluable guidance throughout this journey. I am deeply grateful to Abhinav Sharma for maintaining our fruitful collaboration over the years, for his constant support, and for our many stimulating discussions and interactions, both scientific and philosophical. A special thank you goes to Davide Venturelli and Erik Kalz for our collaborations and shared projects. It has been a privilege to work alongside you, and I look forward to keep collaborating with you in the future.

A sincere thank you to Jens-Uwe Sommer for our insightful scientific discussions and for making my visit to the IPF Dresden possible. I am also thankful to Pascal Martin and Achille Joliot—visiting your experimental lab at the Curie Institute in Paris was a unique and enriching experience. I owe a huge debt of gratitude to Ralf Metzler for hosting me in his group at the University of Potsdam for three months; I will always remember the warm welcome from the group and the wonderful working environment. I would also like to thank Hartmut Löwen for our collaboration and for hosting me at the University of Düsseldorf.

I am immensely grateful to all the amazing people at SISSA who have accompanied me on this journey: Mattia, Piero, Alex, Romina, Eddy, all the members of the SBP group and the entire SISSA community. Thanks to my friend and flatmate Fabrizio for our brief but intense experience in Via Giulia 48, full of memorable moments and challenges. Thank you to Andrea, Chiara and Lorenzo for sharing in our daily sport activities, which truly helped me in the last challenging months. A special thank you goes to Antonio Francesco, Stefano, Maurizio, and Luigi—your sincere friendship means the world to me.

Finally, my deepest thanks go to Carolina and my family, my guiding lights, without whom none of this would have been possible.

Bibliography

[1] R. Brown, "XXVII. A brief account of microscopical observations made in the months of June, July and August 1827, on the particles contained in the pollen of plants; and on the general existence of active molecules in organic and inorganic bodies.", Philos. Mag. **4**, 161–173 (1828).

[2] S. G. Brush, "A history of random processes: i. Brownian movement from brown to perrin", Arch. Hist. Exact Sci. **5**, 1–36 (1968).

[3] A. Einstein, "Über die von der molekularkinetischen Theorie der Wärme geforderte Bewegung von in ruhenden Flüssigkeiten suspendierten Teilchen", Ann. Phys. (Berl.) **4**, 549–560 (1905).

[4] M. Smoluchowski, *Essai d'une théorie cinétique du mouvement Brownien et des milieux troublés* (Acad. Litterarum Cracoviensis, 1906).

[5] M. Smoluchowski, "Sur le chemin moyen parcouru par les molécules d'un gaz et sur son rapport avec la théorie de la diffusion", Pisma Mariana Smoluchowskiego **1**, 479–489 (1924).

[6] P. Langevin, "Sur la théorie du mouvement brownien", CR Acad. Sci. Paris **146**, 530–533 (1908).

[7] J. Perrin, "Mouvement brownien et réalité moléculaire", Ann. Chim. Phys. **18**, 5–114 (1909).

[8] G. Ford, M. Kac, and P. Mazur, "Statistical mechanics of assemblies of coupled oscillators", J. Math. Phys. **6**, 504–515 (1965).

[9] C. W. Gardiner, *Handbook of stochastic methods*, Vol. 3 (springer Berlin, 1985).

[10] M. E. Cates and J. Tailleur, "Motility-induced phase separation", Annu. Rev. Condens. Matter Phys. **6**, 219–244 (2015).

[11] I. S. Aranson, "Bacterial active matter", Rep. Prog. Phys. **85**, 076601 (2022).

[12] T. Guérin, J. Prost, P. Martin, and J.-F. Joanny, "Coordination and collective properties of molecular motors: theory", Curr. Opin. Cell Biol. **22**, 14–20 (2010).

[13]C. Bechinger, R. Di Leonardo, H. Löwen, C. Reichhardt, G. Volpe, and G. Volpe, "Active Particles in Complex and Crowded Environments", Rev. Mod. Phys. **88**, 045006 (2016).

[14]W. F. Paxton, S. Sundararajan, T. E. Mallouk, and A. Sen, "Chemical locomotion", Angew. Chem. **45**, 5420–5429 (2006).

[15]D. Bray, *Cell movements: from molecules to motility* (Garland Science, 2000).

[16]E. Lauga, "Bacterial hydrodynamics", Annu. Rev. Fluid Mech. **48**, 105–130 (2016).

[17]E. Lauga and T. R. Powers, "The hydrodynamics of swimming microorganisms", Rep. Prog. Phys. **72**, 096601 (2009).

[18]E. A. Gillies, R. M. Cannon, R. B. Green, and A. A. Pacey, "Hydrodynamic propulsion of human sperm", J. Fluid Mech. **625**, 445–474 (2009).

[19]A. Zöttl and H. Stark, "Emergent behavior in active colloids", J. Phys. Condens. Matter **28**, 253001 (2016).

[20]J. R. Howse, R. A. Jones, A. J. Ryan, T. Gough, R. Vafabakhsh, and R. Golestanian, "Self-motile colloidal particles: from directed propulsion to random walk", Phys. Rev. Lett. **99**, 048102 (2007).

[21]L. F. Valadares, Y.-G. Tao, N. S. Zacharia, V. Kitaev, F. Galembeck, R. Kapral, and G. A. Ozin, "Catalytic nanomotors: self-propelled sphere dimers", Small **6**, 565–572 (2010).

[22]I. Theurkauff, C. Cottin-Bizonne, J. Palacci, C. Ybert, and L. Bocquet, "Dynamic clustering in active colloidal suspensions with chemical signaling", Phys. Rev. Lett. **108**, 268303 (2012).

[23]H.-R. Jiang, N. Yoshinaga, and M. Sano, "Active motion of a Janus particle by self-thermophoresis in a defocused laser beam", Phys. Rev. Lett. **105**, 268302 (2010).

[24]A. P. Solon, M. E. Cates, and J. Tailleur, "Active Brownian particles and run-and-tumble particles: a comparative study", Eur. Phys. J.: Spec. Top. **224**, 1231–1262 (2015).

[25]M. E. Cates and J. Tailleur, "When are active Brownian particles and run-and-tumble particles equivalent? Consequences for motility-induced phase separation", EPL **101**, 20010 (2013).

[26]J. Tailleur and M. E. Cates, "Statistical mechanics of interacting run-and-tumble bacteria", Phys. Rev. Lett. **100**, 218103 (2008).

[27]D. Martin, J. O'Byrne, M. E. Cates, É. Fodor, C. Nardini, J. Tailleur, and F. Van Wijland, "Statistical mechanics of active Ornstein-Uhlenbeck particles", Phys. Rev. E **103**, 032607 (2021).

[28]J. Elgeti and G. Gompper, "Run-and-tumble dynamics of self-propelled particles in confinement", EPL **109**, 58003 (2015).

[29]C. Nardini, É. Fodor, E. Tjhung, F. Van Wijland, J. Tailleur, and M. E. Cates, "Entropy production in field theories without time-reversal symmetry: quantifying the non-equilibrium character of active matter", Phys. Rev. X **7**, 021007 (2017).

[30]L. Caprini, U. Marini Bettolo Marconi, A. Puglisi, and A. Vulpiani, "The entropy production of Ornstein–Uhlenbeck active particles: a path integral method for correlations", J. Stat. Mech.: Theory Exp. **2019**, 053203 (2019).

[31]I. Buttinoni, J. Bialké, F. Kümmel, H. Löwen, C. Bechinger, and T. Speck, "Dynamical clustering and phase separation in suspensions of self-propelled colloidal particles", Phys. Rev. Lett. **110**, 238301 (2013).

[32]Y. Fily and M. C. Marchetti, "Athermal phase separation of self-propelled particles with no alignment", Phys. Rev. Lett. **108**, 235702 (2012).

[33]G. S. Redner, M. F. Hagan, and A. Baskaran, "Structure and dynamics of a phase-separating active colloidal fluid", Phys. Rev. Lett. **110**, 055701 (2013).

[34]O. Pohl and H. Stark, "Dynamic clustering and chemotactic collapse of self-phoretic active particles", Phys. Rev. Lett. **112**, 238303 (2014).

[35]O. Pohl and H. Stark, "Self-phoretic active particles interacting by diffusiophoresis: a numerical study of the collapsed state and dynamic clustering", Eur. Phys. J. E **38**, 1 (2015).

[36]H. Stark, "Artificial chemotaxis of self-phoretic active colloids: collective behavior", Acc. Chem. Res. **51**, 2681–2688 (2018).

[37]H. C. Berg and D. A. Brown, "Chemotaxis in Escherichia Coli analysed by three-dimensional tracking", Nature **239**, 500–504 (1972).

[38]Z. Eidi, F. Mohammad-Rafiee, M. Khorrami, and A. Gholami, "Modelling of dictyostelium discoideum movement in a linear gradient of chemoattractant", Soft Matter **13**, 8209–8222 (2017).

[39]H. V. Ramírez-Gómez, V. Jimenez Sabinina, M. Velázquez Pérez, C. Beltran, J. Carneiro, C. D. Wood, I. Tuval, A. Darszon, and A. Guerrero, "Sperm chemotaxis is driven by the slope of the chemoattractant concentration field", Elife **9**, e50532 (2020).

[40]C. Lozano, B. Ten Hagen, H. Löwen, and C. Bechinger, "Phototaxis of synthetic microswimmers in optical landscapes", Nat. Commun. **7**, 12828 (2016).

[41]S. Jahanshahi, C. Lozano, B. Liebchen, H. Löwen, and C. Bechinger, "Realization of a motility-trap for active particles", Commun. Phys. **3**, 127 (2020).

[42]J. Taktikos, H. Stark, and V. Zaburdaev, "How the motility pattern of bacteria affects their dispersal and chemotaxis", PloS one **8**, e81936 (2013).

[43] J. Adler, "Chemoreceptors in bacteria: studies of chemotaxis reveal systems that detect attractants independently of their metabolism.", Science **166**, 1588–1597 (1969).

[44] H. C. Berg and E. M. Purcell, "Physics of chemoreception", Biophys. J. **20**, 193–219 (1977).

[45] S. M. Block, J. E. Segall, and H. C. Berg, "Impulse responses in bacterial chemotaxis", Cell **31**, 215–226 (1982).

[46] J. E. Segall, S. M. Block, and H. C. Berg, "Temporal comparisons in bacterial chemotaxis.", Proc. Natl. Acad. Sci. USA **83**, 8987–8991 (1986).

[47] D. B. Dusenbery, "Efficiency and the role of adaptation in klinokinesis", J. Theor. Biol. **136**, 281–293 (1989).

[48] H. Keller and A. Zimmermann, "Orthokinetic and klinokinetic responses of human polymorphonuclear leucocytes", Cell Motil. **5**, 447–461 (1985).

[49] G. Fraenkel and D. Gunn, *The orientation of Animals: Kineses Taxes and Compass Reactions* (Dover Publications, New York, 1961).

[50] M. J. Schnitzer, "Theory of continuum random walks and application to chemotaxis", Phys. Rev. E **48**, 2553 (1993).

[51] H. Mori, "Transport, collective motion, and Brownian motion", Prog. Theor. Phys. **33**, 423–455 (1965).

[52] S. Nordholm and R. Zwanzig, "A systematic derivation of exact generalized Brownian motion theory", J. Stat. Phys. **13**, 347–371 (1975).

[53] T. G. Mason and D. A. Weitz, "Optical Measurements of Frequency-Dependent Linear Viscoelastic Moduli of Complex Fluids", Phys. Rev. Lett. **74**, 1250–1253 (1995).

[54] U. C. Täuber, *Critical dynamics: a field theory approach to equilibrium and non-equilibrium scaling behavior* (Cambridge University Press, 2014).

[55] A. Gambassi, A. Maciołek, C. Hertlein, U. Nellen, L. Helden, C. Bechinger, and S. Dietrich, "Critical Casimir effect in classical binary liquid mixtures", Phys. Rev. E **80**, 061143 (2009).

[56] I. A. Martínez, C. Devailly, A. Petrosyan, and S. Ciliberto, "Energy transfer between colloids via critical interactions", Entropy **19**, 77 (2017).

[57] C. Hertlein, L. Helden, A. Gambassi, S. Dietrich, and C. Bechinger, "Direct measurement of critical Casimir forces", Nature **451**, 172–175 (2008).

[58] S. Paladugu, A. Callegari, Y. Tuna, L. Barth, S. Dietrich, A. Gambassi, and G. Volpe, "Nonadditivity of critical Casimir forces", Nat. Commun. **7**, 11403 (2016).

[59]A. Magazzù, A. Callegari, J. P. Staforelli, A. Gambassi, S. Dietrich, and G. Volpe, "Controlling the dynamics of colloidal particles by critical Casimir forces", Soft Matter **15**, 2152–2162 (2019).

[60]H. B. Casimir, "On the attraction between two perfectly conducting plates", in Proc. Kon. Ned. Akad. Wet. Vol. 51 (1948), pp. 793–795.

[61]V. Démery and D. S. Dean, "Thermal Casimir drag in fluctuating classical fields", Phys. Rev. E **84**, 010103 (2011).

[62]V. Démery and D. S. Dean, "Perturbative path-integral study of active- and passive-tracer diffusion in fluctuating fields", Phys. Rev. E **84**, 011148 (2011).

[63]V. Démery, "Diffusion of a particle quadratically coupled to a thermally fluctuating field", Phys. Rev. E **87**, 052105 (2013).

[64]D. S. Dean and V. Démery, "Diffusion of active tracers in fluctuating fields", J. Phys. Condens. Matter **23**, 234114 (2011).

[65]U. Basu, V. Démery, and A. Gambassi, "Dynamics of a colloidal particle coupled to a Gaussian field: from a confinement-dependent to a non-linear memory", SciPost Phys. **13**, 078 (2022).

[66]D. Venturelli, F. Ferraro, and A. Gambassi, "Nonequilibrium relaxation of a trapped particle in a near-critical Gaussian field", Phys. Rev. E **105**, 054125 (2022).

[67]D. Venturelli and A. Gambassi, "Inducing oscillations of trapped particles in a near-critical Gaussian field", Phys. Rev. E **106**, 044112 (2022).

[68]D. Venturelli and A. Gambassi, "Memory-induced oscillations of a driven particle in a dissipative correlated medium", New J. Phys. **25**, 093025 (2023).

[69]D. Venturelli and M. Gross, "Tracer particle in a confined correlated medium: an adiabatic elimination method", J. Stat. Mech.: Theo. Exp. **2022**, 123210 (2022).

[70]D. Venturelli, "Stochastic dynamics in complex landscapes: from fluctuating fields to quenched disorder", PhD thesis (SISSA, 2023).

[71]D. Venturelli, S. A. M. Loos, B. Walter, É. Roldán, and A. Gambassi, "Stochastic thermodynamics of a probe in a fluctuating correlated field", EPL **146**, 27001 (2024).

[72]D. S. Dean, "Langevin equation for the density of a system of interacting Langevin processes", J. Phys. A: Math. Gen. **29**, L613 (1996).

[73]K. Kawasaki, "Microscopic analyses of the dynamical density functional equation of dense fluids", J. Stat. Phys **93**, 527–546 (1998).

[74]H. Risken, *The Fokker-Planck Equation* (Springer, 1996).

[75]C. Aron, G. Biroli, and L. F. Cugliandolo, “Symmetries of generating functionals of Langevin processes with colored multiplicative noise”, J. Stat. Mech.: Theory Exp. **2010**, P11018 (2010).

[76]C. Aron, D. G. Barci, L. F. Cugliandolo, Z. G. Arenas, and G. S. Lozano, “Dynamical symmetries of Markov processes with multiplicative white noise”, J. Stat. Mech.: Theory Exp. **2016**, 053207 (2016).

[77]N. G. Van Kampen, *Stochastic processes in physics and chemistry* (Elsevier, 1992).

[78]A. D. Fokker, “Die mittlere Energie rotierender elektrischer Dipole im Strahlungsfeld”, Ann. Phys. (Berl.) **348**, 810–820 (1914).

[79]M. Planck, “Uber einen Satz der statistischen Dynamik und seine Erweiterung in der Quantentheorie”, Sitzungsber. Preuss. Akad. Wiss., 324–341 (1917).

[80]A. V. Straube and F. Höfling, “Langevin equations and a geometric integration scheme for the overdamped limit of homogeneous rotational Brownian motion”, preprint arXiv:2403.04501 (2024).

[81]G. E. Uhlenbeck and L. S. Ornstein, “On the theory of the Brownian motion”, Phys. Rev. **36**, 823 (1930).

[82]J.-U. Sommer and A. Blumen, “On the statistics of generalized Gaussian structures: Collapse and random external fields”, J. Phys. A Math. Gen. **28**, 6669 (1995).

[83]P. E. Rouse, “A theory of the linear viscoelastic properties of dilute solutions of coiling polymers”, J. Chem. Phys. **21**, 1272–1280 (1953).

[84]M. Doi and S. F. Edwards, *The theory of polymer dynamics* (Oxford University Press, 1988).

[85]B. H. Zimm, “Dynamics of polymer molecules in dilute solution: viscoelasticity, flow birefringence and dielectric loss”, J. Chem. Phys. **24**, 269–278 (1956).

[86]P. C. Hohenberg and B. I. Halperin, “Theory of dynamic critical phenomena”, Rev. Mod. Phys. **49**, 435–479 (1977).

[87]T. Ahamed, A. C. Costa, and G. J. Stephens, “Capturing the continuous complexity of cehavior in C. Elegans”, Nat. Phys. **17**, 275–283 (2021).

[88]A. C. Costa, T. Ahamed, and G. J. Stephens, “Adaptive, locally linear models of complex dynamics”, Proc. Natl. Acad. Sci. U.S.A. **116**, 1501–1510 (2019).

[89]G. H. Wadhams and J. P. Armitage, “Making sense of it all: bacterial chemotaxis”, Nat. Rev. Mol. Cell Biol. **5**, 1024–1037 (2004).

[90]Y. Tu, “Quantitative modeling of bacterial chemotaxis: signal amplification and accurate adaptation”, Annu. Rev. Biophys. **42**, 337–359 (2013).

[91]S. Sengupta, C. A. Parent, and J. E. Bear, "The principles of directed cell migration", Nat. Rev. Mol. Cell Biol. **22**, 529–547 (2021).

[92]H. C. Berg, *E. coli in Motion* (Springer Science and Business Media, 2008).

[93]M. E. Cates, "Diffusive transport without detailed balance in motile bacteria: does microbiology need statistical physics?", Rep. Prog. Phys. **75**, 042601 (2012).

[94]J. R. Howse, R. A. L. Jones, A. J. Ryan, T. Gough, R. Vafabakhsh, and R. Golestanian, "Self-Motile Colloidal Particles: From Directed Propulsion to Random Walk", Phys. Rev. Lett. **99**, 048102 (2007).

[95]W. Gao, A. Pei, R. Dong, and J. Wang, "Catalytic Iridium-Based Janus Micromotors Powered by Ultralow Levels of Chemical Fuels", J. Am. Chem. Soc. **136**, 2276–2279 (2014).

[96]A.-Y. Jee, Y.-K. Cho, S. Granick, and T. Tlusty, "Catalytic enzymes are active matter", Proc. Natl. Acad. Sci. U.S.A. **115**, E10812–E10821 (2018).

[97]J. Stenhammar, R. Wittkowski, D. Marenduzzo, and M. E. Cates, "Light-induced self-assembly of active rectification devices", Sci. Adv. **2**, e1501850 (2016).

[98]L. Caprini, U. Marini Bettolo Marconi, R. Wittmann, and H. Löwen, "Dynamics of active particles with space-dependent swim velocity", Soft Matter **18**, 1412–1422 (2022).

[99]A. Sharma and J. M. Brader, "Brownian Systems with Spatially Inhomogeneous Activity", Phys. Rev. E **96**, 032604 (2017).

[100]T. Mano, J.-B. Delfau, J. Iwasawa, and M. Sano, "Optimal run-and-tumble–based transportation of a Janus particle with active steering", Proc. Natl. Acad. Sci. U.S.A. **114**, E2580–E2589 (2017).

[101]B. Qian, D. Montiel, A. Bregulla, F. Cichos, and H. Yang, "Harnessing Thermal Fluctuations for Purposeful Activities: The Manipulation of Single Micro-swimmers by Adaptive Photon Nudging", Chem. Sci. **4**, 1420–1429 (2013).

[102]H. Massana-Cid, G. Frangipane, C. Maggi, and R. Di Leonardo, "Rectification and confinement of photokinetic bacteria in an optical feedback loop", Nat. Commun. **13**, 2740 (2022).

[103]H. D. Vuijk, H. Merlitz, M. Lang, A. Sharma, and J.-U. Sommer, "Chemotaxis of Cargo-Carrying Self-Propelled Particles", Phys. Rev. Lett. **126**, 208102 (2021).

[104]R. G. Winkler, J. Elgeti, and G. Gompper, "Active Polymers — Emergent Conformational and Dynamical Properties: A Brief Review", J. Phys. Soc. Jpn. **86**, 101014 (2017).

[105]S. M. Mousavi, G. Gompper, and R. G. Winkler, “Active Brownian ring polymers”, J. Chem. Phys. **150**, 064913 (2019).

[106]R. G. Winkler and G. Gompper, “The physics of active polymers and filaments”, J. Chem. Phys. **153**, 040901 (2020).

[107]A. Martín-Gómez, T. Eisenstecken, G. Gompper, and R. G. Winkler, “Active Brownian Filaments with Hydrodynamic Interactions: Conformations and Dynamics”, Soft Matter **15**, 3957–3969 (2019).

[108]T. Eisenstecken and R. G. Winkler, “Path integral description of semiflexible active Brownian polymers”, J. Chem. Phys. **156** (2022).

[109]A. Kaiser, S. Babel, B. ten Hagen, C. von Ferber, and H. Löwen, “How does a flexible chain of active particles swell?”, J. Chem. Phys. **142**, 124905 (2015).

[110]S. Ebbens, R. A. L. Jones, A. J. Ryan, R. Golestanian, and J. R. Howse, “Self-assembled autonomous runners and tumblers”, Phys. Rev. E **82**, 015304 (2010).

[111]H. Löwen, “Active colloidal molecules”, EPL **121**, 58001 (2018).

[112]H. D. Vuijk, S. Klempahn, H. Merlitz, J.-U. Sommer, and A. Sharma, “Active colloidal molecules in activity gradients”, Phys. Rev. E **106**, 014617 (2022).

[113]C. Hargus, J. M. Epstein, and K. K. Mandadapu, “Odd diffusivity of chiral random motion”, Phys. Rev. Lett. **127**, 178001 (2021).

[114]C. Hargus, “Odd transport phenomena in active matter”, PhD thesis (UC Berkeley, 2022).

[115]E. Kalz, A. Sharma, and R. Metzler, “Field theory of active chiral hard disks: a first-principles approach to steric interactions”, J. Phys. A: Math. Theor. **57**, 265002 (2024).

[116]H. D. Vuijk, J. U. Sommer, H. Merlitz, J. M. Brader, and A. Sharma, “Lorentz forces induce inhomogeneity and flux in active systems”, Phys. Rev. Res. **2**, 013320 (2020).

[117]I. Abdoli, H. D. Vuijk, J.-U. Sommer, J. M. Brader, and A. Sharma, “Nondiffusive fluxes in a Brownian system with Lorentz force”, Phys. Rev. E **101**, 012120 (2020).

[118]I. Abdoli, H. D. Vuijk, R. Wittmann, J. U. Sommer, J. M. Brader, and A. Sharma, “Stationary state in Brownian systems with Lorentz force”, Phys. Rev. Res. **2**, 023381 (2020).

[119]I. Abdoli, E. Kalz, H. D. Vuijk, R. Wittmann, J.-U. Sommer, J. M. Brader, and A. Sharma, “Correlations in Multithermostat Brownian Systems with Lorentz Force”, New J. Phys. **22**, 093057 (2020).

[120]P. L. Muzzeddu, H. D. Vuijk, H. Löwen, J.-U. Sommer, and A. Sharma, "Active chiral molecules in activity gradients", J. Chem. Phys. **157**, 134902 (2022).

[121]R. Golestanian, "Anomalous Diffusion of Symmetric and Asymmetric Active Colloids", Phys. Rev. Lett. **102**, 188305 (2009).

[122]M. N. Popescu, M. Tasinkevych, and S. Dietrich, "Pulling and pushing a cargo with a catalytically active carrier", EPL **95**, 28004 (2011).

[123]M. N. Popescu, W. E. Uspal, Z. Eskandari, M. Tasinkevych, and S. Dietrich, "Effective squirmer models for self-phoretic chemically active spherical colloids", Eur. Phys. J. E **41**, 145 (2018).

[124]S. Y. Reigh and R. Kapral, "Catalytic dimer nanomotors: continuum theory and microscopic dynamics", Soft Matter **11**, 3149–3158 (2015).

[125]S. Y. Reigh, P. Chuphal, S. Thakur, and R. Kapral, "Diffusiophoretically induced interactions between chemically active and inert particles", Soft Matter **14**, 6043–6057 (2018).

[126]M. E. Cates and J. Tailleur, "When are active Brownian particles and run-and-tumble particles equivalent? Consequences for motility-induced phase separation", EPL **101**, 20010 (2013).

[127]P.-G. De Gennes and J. Prost, *The physics of liquid crystals* (Oxford university press, 1993).

[128]J. A. Kromer, N. de la Cruz, and B. M. Friedrich, "Chemokinetic scattering, trapping, and avoidance of active Brownian particles", Phys. Rev. Lett. **124**, 118101 (2020).

[129]C. Lozano and C. Bechinger, "Diffusing wave paradox of phototactic particles in traveling light pulses", Nat. Commun. **10**, 2495 (2019).

[130]Q. Chen, S. C. Bae, and S. Granick, "Directed self-assembly of a colloidal Kagome lattice", Nature **469**, 381–384 (2011).

[131]E. Bianchi, R. Blaak, and C. N. Likos, "Patchy colloids: state of the art and perspectives", Phys. Chem. Chem. Phys. **13**, 6397 (2011).

[132]S. Sacanna, W. T. M. Irvine, P. M. Chaikin, and D. J. Pine, "Lock and key colloids", Nature **464**, 575–578 (2010).

[133]S. C. Glotzer and M. J. Solomon, "Anisotropy of building blocks and their assembly into complex structures", Nat. Mater. **6**, 557–562 (2007).

[134]J. Zhang, J. Yan, and S. Granick, "Directed Self-Assembly Pathways of Active Colloidal Clusters", Angew. Chem. **128**, 5252–5255 (2016).

[135]M. N. Popescu, "Chemically Active Particles: From One to Few on the Way to Many", Langmuir **36**, 6861–6870 (2020).

[136] E. Altshuler, J. M. Pastor, A. Garcimartín, I. Zuriguel, and D. Maza, "Vibrot, a simple device for the conversion of vibration into rotation mediated by friction: preliminary evaluation", PloS one **8**, e67838 (2013).

[137] C. Scholz, S. D'Silva, and T. Pöschel, "Ratcheting and tumbling motion of vibrots", New J. Phys. **18**, 123001 (2016).

[138] C. Scholz and T. Pöschel, "Velocity distribution of a homogeneously driven two-dimensional granular gas", Phys. Rev. Lett. **118**, 198003 (2017).

[139] M. Broseghini, C. Ceccolini, C. Della Volpe, and S. Siboni, "The notched stick, an ancient vibrot example", PloS one **14**, e0218666 (2019).

[140] C. Scholz, M. Engel, and T. Pöschel, "Rotating robots move collectively and self-organize", Nat. Commun. **9**, 1–8 (2018).

[141] C. Scholz, A. Ldov, T. Pöschel, M. Engel, and H. Löwen, "Surfactants and rotelles in active chiral fluids", Sci. Adv. **7**, eabf8998 (2021).

[142] E. Kalz, H. D. Vuijk, I. Abdoli, J.-U. Sommer, H. Löwen, and A. Sharma, "Collisions enhance self-diffusion in odd-diffusive systems", Phys. Rev. Lett. **129**, 090601 (2022).

[143] R. Shinde, J. U. Sommer, H. Löwen, and A. Sharma, "Strongly enhanced dynamics of a charged Rouse dimer by an external magnetic field", PNAS Nexus **1**, pgac119 (2022).

[144] F. Jülicher, A. Ajdari, and J. Prost, "Modeling molecular motors", Rev. Mod. Phys. **69**, 1269 (1997).

[145] P. Hänggi and F. Marchesoni, "Artificial Brownian motors: Controlling transport on the nanoscale", Rev. Mod. Phys. **81**, 387 (2009).

[146] M. C. Marchetti, J.-F. Joanny, S. Ramaswamy, T. B. Liverpool, J. Prost, M. Rao, and R. A. Simha, "Hydrodynamics of soft active matter", Rev. Mod. Phys. **85**, 1143 (2013).

[147] G. Fenteany and M. Glogauer, "Cytoskeletal remodeling in leukocyte function", Curr. Opin. Hematol. **11**, 15–24 (2004).

[148] Y. Kanai, N. Dohmae, and N. Hirokawa, "Kinesin transports RNA: isolation and characterization of an RNA-transporting granule", Neuron **43**, 513–525 (2004).

[149] B. M. Friedrich and F. Jülicher, "Chemotaxis of sperm cells", Proc. Natl. Acad. Sci. **104**, 13256–13261 (2007).

[150] L. Reinišová, S. Hermanová, and M. Pumera, "Micro/nanomachines: what is needed for them to become a real force in cancer therapy?", Nanoscale **11**, 6519–6532 (2019).

[151] S. Ebbens, "Active colloids: Progress and challenges towards realising autonomous applications", Curr. Op. Coll. Inter. Sci. **21**, 14–23 (2016).

[152] M. García, J. Orozco, M. Guix, W. Gao, S. Sattayasamitsathit, A. Escarpa, A. Merkoçi, and J. Wang, “Micromotor-based lab-on-chip immunoassays”, Nanoscale **5**, 1325–1331 (2013).

[153] S. Sánchez, L. Soler, and J. Katuri, “Chemically powered micro- and nanomotors”, Angew. Chem. **54**, 1414–1444 (2015).

[154] A. V. Singh, Z. Hosseinidoust, B.-W. Park, O. Yasa, and M. Sitti, “Microemulsion-based soft bacteria-driven microswimmers for active cargo delivery”, ACS Nano **11**, 9759–9769 (2017).

[155] Y. Alapan, O. Yasa, O. Schauer, J. Giltinan, A. F. Tabak, V. Sourjik, and M. Sitti, “Soft erythrocyte-based bacterial microswimmers for cargo delivery”, Sci. Robot. **3**, 4423 (2018).

[156] L. Vaccari, M. Molaei, R. L. Leheny, and K. J. Stebe, “Cargo carrying bacteria at interfaces”, Soft Matter **14**, 5643–5653 (2018).

[157] O. I. Sentürk, O. Schauer, F. Chen, V. Sourjik, and S. V. Wegner, “Red/far-red light switchable cargo attachment and release in bacteria-driven microswimmers”, Adv. Health. Mat. **9**, 1900956 (2020).

[158] P. R. Fisher, R. Merkl, and G. Gerisch, “Quantitative analysis of cell motility and chemotaxis in dictyostelium discoideum by using an image processing system and a novel chemotaxis chamber providing stationary chemical gradients”, J. Cell. Biol. **108**, 973–984 (1989).

[159] J.-L. Martiel and A. Goldbeter, “A model based on receptor desensitization for cyclic amp signaling in dictyostelium cells”, Biophys. J. **52**, 807–828 (1987).

[160] K. J. Tomchik and P. N. Devreotes, “Adenosine 3’, 5’-monophosphate waves in dictyostelium discoideum: a demonstration by isotope dilution—fluorography”, Science **212**, 443–446 (1981).

[161] R. E. Goldstein, “Traveling-wave chemotaxis”, Phys. Rev. Lett. **77**, 775–778 (1996).

[162] T. Gregor, K. Fujimoto, N. Masaki, and S. Sawai, “The onset of collective behavior in social amoebae”, Science **328**, 1021–1025 (2010).

[163] T. Höfer, P. Maini, J. Sherratt, M. Chaplain, P. Chauvet, D. Metevier, P. Montes, and J. Murray, “A resolution of the chemotactic wave paradox”, App. Math. Lett. **7**, 1–5 (1994).

[164] A. Geiseler, P. Hänggi, F. Marchesoni, C. Mulhern, and S. Savel’ev, “Chemotaxis of artificial microswimmers in active density waves”, Phys. Rev. E **94**, 012613 (2016).

[165] A. Geiseler, P. Hänggi, and F. Marchesoni, “Self-Polarizing Microswimmers in Active Density Waves”, Sci. Rep. **7**, 41884 (2017).

[166] A. Geiseler, "Artificial microswimmers in spatio-temporally modulated activating media", PhD thesis (University of Augsburg, 2017).

[167] H. Merlitz, H. D. Vuijk, J. Brader, A. Sharma, and J.-U. Sommer, "Linear response approach to active Brownian particles in time-varying activity fields", J. Chem. Phys. **148**, 194116 (2018).

[168] L. Baraban, M. Tasinkevich, M. N. Popescu, S. Sanchez, S. Dietrich, and O. Schmidt, "Transport of cargo by catalytic Janus micro-motors", Soft Matter **8**, 48–52 (2012).

[169] L. Caprini, E. Hernández-García, C. López, and U. Marini Bettolo Marconi, "A comparative study between two models of active cluster crystals", Sci. Rep. **9**, 1–13 (2019).

[170] L. Caprini, A. R. Sprenger, H. Löwen, and R. Wittmann, "The parental active model: a unifying stochastic description of self-propulsion", J. Chem. Phys. **156**, 071102 (2022).

[171] A. Gopal, É. Roldán, and S. Ruffo, "Energetics of critical oscillators in active bacterial baths", J. Phys. A **54**, 164001 (2021).

[172] P. L. Muzzeddu, É. Roldán, A. Gambassi, and A. Sharma, "Taxis of cargo-carrying microswimmers in traveling activity waves", EPL **142**, 67001 (2023).

[173] A. P. Solon, M. E. Cates, and J. Tailleur, "Active Brownian particles and run-and-tumble particles: a comparative study", Eur. Phys. J. Spec. Top. **224**, 1231–1262 (2015).

[174] T. Adeleke-Larodo, "Non-equilibrium dynamics of active enzymes.", PhD thesis (University of Oxford, 2020).

[175] P. Hänggi, P. Talkner, and M. Borkovec, "Reaction-rate theory: fifty years after Kramers", Rev. Mod. Phys. **62**, 251 (1990).

[176] N. S. Goel and N. Richter-Dyn, *Stochastic models in biology* (Elsevier, 2016).

[177] A. Sharma and J. M. Brader, "Communication: Green-Kubo approach to the average swim speed in active Brownian systems", J. Chem. Phys. **145**, 161101 (2016).

[178] S. Dal Cengio, D. Levis, and I. Pagonabarraga, "Linear response theory and Green-Kubo relations for active matter", Phys. Rev. Lett. **123**, 238003 (2019).

[179] H. R. Vutukuri, A. F. Demirörs, B. Peng, P. D. J. van Oostrum, A. Imhof, and A. van Blaaderen, "Colloidal analogues of charged and uncharged polymer chains with tunable stiffness", Angew. Chem. Int. Ed. Engl. **51**, 11249–11253 (2012).

[180] H. R. Vutukuri, B. Bet, R. van Roij, M. Dijkstra, and W. T. S. Huck, "Rational design and dynamics of self-propelled colloidal bead chains: from rotators to flagella", Scientific Reports **7**, 16758 (2017).

[181] R. García-Millán and G. Pruessner, "Run-and-tumble motion in a harmonic potential: field theory and entropy production", J. Stat. Mech. **2021**, 063203 (2021).

[182] L. Baraban, D. Makarov, R. Streubel, I. Mönch, D. Grimm, S. Sanchez, and O. G. Schmidt, "Catalytic Janus Motors on Microfluidic Chip: Deterministic Motion for Targeted Cargo Delivery", ACS Nano **6**, 3383–3389 (2012).

[183] D. Akin, J. Sturgis, K. Ragheb, D. Sherman, K. Burkholder, J. P. Robinson, A. K. Bhunia, S. Mohammed, and R. Bashir, "Bacteria-mediated delivery of nanoparticles and cargo into cells", Nat. Nanotech. **2**, 441–449 (2007).

[184] M. Medina-Sánchez, L. Schwarz, A. K. Meyer, F. Hebenstreit, and O. G. Schmidt, "Cellular cargo delivery: toward assisted fertilization by sperm-carrying micromotors", Nano Lett. **16**, 555–561 (2016).

[185] V. Magdanz, M. Medina-Sánchez, L. Schwarz, H. Xu, J. Elgeti, and O. G. Schmidt, "Spermatozoa as functional components of robotic microswimmers", Adv. Mat. **29**, 1606301 (2017).

[186] S. Di Talia and M. Vergassola, "Waves in embryonic development", Annu. Rev. Biophys. **51**, 327–353 (2022).

[187] X. Fang, K. Kruse, T. Lu, and J. Wang, "Nonequilibrium physics in biology", Rev. Mod. Phys. **91**, 045004 (2019).

[188] E. L. F. Holzbaur and Y. E. Goldman, "Coordination of molecular motors: from in vitro assays to intracellular dynamics", Curr. Opin. Cell Biol. **22**, 4–13 (2010).

[189] F. Jülicher and J. Prost, "Cooperative molecular motors", Phys. Rev. Lett. **75**, 2618–2621 (1995).

[190] D. B. Kearns, "A field guide to bacterial swarming motility", Nat. Rev. Microbiol. **8**, 634–644 (2010).

[191] J. Toner and Y. Tu, "Long-range order in a two-dimensional dynamical XY model: how birds fly together", Phys. Rev. Lett. **75**, 4326–4329 (1995).

[192] J. Toner and Y. Tu, "Flocks, herds, and schools: a quantitative theory of flocking", Phys. Rev. E **58**, 4828–4858 (1998).

[193] J. Toner, Y. Tu, and S. Ramaswamy, "Hydrodynamics and phases of flocks", Ann. Phys. **318**, 170–244 (2005).

[194] F. Jülicher, S. W. Grill, and G. Salbreux, "Hydrodynamic theory of active matter", Rep. Prog. Phys. **81**, 076601 (2018).

[195] G. Gompper, R. G. Winkler, et al., "The 2020 motile active matter roadmap", J. Phys. Condens. Matter **32**, 193001 (2020).

[196] É. Fodor, C. Nardini, M. E. Cates, J. Tailleur, P. Visco, and F. Van Wijland, "How far from equilibrium is active matter?", Phys. Rev. Lett. **117**, 038103 (2016).

[197] G. De Magistris and D. Marenduzzo, "An introduction to the physics of active matter", Phys. A: Stat. Mech. Appl. **418**, 65–77 (2015).

[198] M. Polin, I. Tuval, K. Drescher, J. P. Gollub, and R. E. Goldstein, "Chlamydomonas swims with two "gears" in a eukaryotic version of run-and-tumble locomotion", Science **325**, 487–490 (2009).

[199] V. F. Geyer, F. Jülicher, J. Howard, and B. M. Friedrich, "Cell-body rocking is a dominant mechanism for flagellar synchronization in a swimming alga", Proc. Natl. Acad. Sci. **110**, 18058–18063 (2013).

[200] J. Elgeti, R. G. Winkler, and G. Gompper, "Physics of microswimmers—single particle motion and collective behavior: a review", Rep. Prog. Phys. **78**, 056601 (2015).

[201] J. Howard, "The movement of kinesin along microtubules", Annu. Rev. Physiol. **58**, 703–729 (1996).

[202] A. Deblais, A. C. Maggs, D. Bonn, and S. Woutersen, "Phase separation by entanglement of active polymerlike worms", Phys. Rev. Lett. **124**, 208006 (2020).

[203] A. Deblais, S. Woutersen, and D. Bonn, "Rheology of entangled active polymer-like t. tubifex worms", Phys. Rev. Lett. **124**, 188002 (2020).

[204] R. Dreyfus, J. Baudry, M. L. Roper, M. Fermigier, H. A. Stone, and J. Bibette, "Microscopic artificial swimmers", Nature **437**, 862–865 (2005).

[205] A. Najafi and R. Golestanian, "Simple swimmer at low Reynolds number: three linked spheres", Phys. Rev. E **69**, 062901 (2004).

[206] B. J. Williams, S. V. Anand, J. Rajagopalan, and M. T. A. Saif, "A self-propelled biohybrid swimmer at low reynolds number", Nat. Commun. **5**, 3081 (2014).

[207] B. Alberts, *Molecular biology of the cell* (Garland science, 2017).

[208] S. C. Weber, A. J. Spakowitz, and J. A. Theriot, "Nonthermal ATP-dependent fluctuations contribute to the in vivo motion of chromosomal loci", Proc. Natl. Acad. Sci. **109**, 7338–7343 (2012).

[209] C. J. Anderson, G. Briand, O. Dauchot, and A. Fernández-Nieves, "Polymer-chain configurations in active and passive baths", Phys. Rev. E **106**, 064606 (2022).

[210] C. Zhang, C. Xie, W. Feng, H. Luo, Y. Liu, and G. Jing, “Configurational dynamics of flexible filaments in bacterial active baths”, New J. Phys. **25**, 043029 (2023).

[211] A. Kaiser and H. Löwen, “Unusual swelling of a polymer in a bacterial bath”, J. Chem. Phys. **141** (2014).

[212] J. Harder, C. Valeriani, and A. Cacciuto, “Activity-induced collapse and reexpansion of rigid polymers”, Phys. Rev. E **90**, 062312 (2014).

[213] J. Shin, A. G. Cherstvy, W. K. Kim, and R. Metzler, “Facilitation of polymer looping and giant polymer diffusivity in crowded solutions of active particles”, New J. Phys. **17**, 113008 (2015).

[214] S. M. Mousavi, G. Gompper, and R. G. Winkler, “Active bath-induced localization and collapse of passive semiflexible polymers”, J. Chem. Phys. **155** (2021).

[215] V. Bianco, E. Locatelli, and P. Malgaretti, “Globulelike conformation and enhanced diffusion of active polymers”, Phys. Rev. Lett. **121**, 217802 (2018).

[216] M. Foglino, E. Locatelli, C. Brackley, D. Michieletto, C. Likos, and D. Marenduzzo, “Non-equilibrium effects of molecular motors on polymers”, Soft Matter **15**, 5995–6005 (2019).

[217] S. K. Anand and S. P. Singh, “Structure and dynamics of a self-propelled semiflexible filament”, Phys. Rev. E **98**, 042501 (2018).

[218] E. Locatelli, V. Bianco, and P. Malgaretti, “Activity-induced collapse and arrest of active polymer rings”, Phys. Rev. Lett. **126**, 097801 (2021).

[219] C. A. Philipps, G. Gompper, and R. G. Winkler, “Tangentially driven active polar linear polymers—an analytical study”, J. Chem. Phys. **157**, 194904 (2022).

[220] R. E. Isele-Holder, J. Elgeti, and G. Gompper, “Self-propelled worm-like filaments: spontaneous spiral formation, structure, and dynamics”, Soft Matter **11**, 7181–7190 (2015).

[221] D. Osmanović and Y. Rabin, “Dynamics of active Rouse chains”, Soft Matter **13**, 963–968 (2017).

[222] D. Osmanović, “Properties of Rouse polymers with actively driven regions”, J. Chem. Phys. **149**, 164911 (2018).

[223] S. Brahmachari, T. Markovich, F. C. MacKintosh, and J. N. Onuchic, “Temporally correlated active forces drive segregation and enhanced dynamics in chromosome polymers”, PRX Life **2**, 033003 (2024).

[224] H. Vandebroek and C. Vanderzande, “Dynamics of a polymer in an active and viscoelastic bath”, Phys. Rev. E **92**, 060601 (2015).

[225]S. Put, T. Sakaue, and C. Vanderzande, “Active dynamics and spatially coherent motion in chromosomes subject to enzymatic force dipoles”, Phys. Rev. E **99**, 032421 (2019).

[226]B. Liebchen and H. Löwen, “Optimal navigation strategies for active particles”, EPL **127**, 34003 (2019).

[227]L. Caprini, U. Marini Bettolo Marconi, R. Wittmann, and H. Löwen, “Active particles driven by competing spatially dependent self-propulsion and external force”, SciPost Physics **13**, 065 (2022).

[228]A. Wysocki, A. K. Dasanna, and H. Rieger, “Interacting particles in an activity landscape”, New J. Phys. **24**, 093013 (2022).

[229]N. A. Söker, S. Auschra, V. Holubec, K. Kroy, and F. Cichos, “How activity landscapes polarize microswimmers without alignment forces”, Phys. Rev. Lett. **126**, 228001 (2021).

[230]P. L. Muzzeddu, A. Gambassi, J.-U. Sommer, and A. Sharma, “Migration and separation of polymers in non-uniform active baths”, arXiv preprint arXiv:2403.05914 (2024).

[231]P. Sajeesh and A. K. Sen, “Particle separation and sorting in microfluidic devices: a review”, Microfluid. Nanofluidics **17**, 1–52 (2014).

[232]M. Kreysing, L. Keil, S. Lanzmich, and D. Braun, “Heat flux across an open pore enables the continuous replication and selection of oligonucleotides towards increasing length”, Nat. Chem. **7**, 203–208 (2015).

[233]J. Shin, A. G. Cherstvy, W. K. Kim, and V. Zaburdaev, “Elasticity-based polymer sorting in active fluids: a Brownian dynamics study”, Phys. Chem. Chem. Phys. **19**, 18338–18347 (2017).

[234]R. Mhanna, Y. Gao, I. Van Tol, E. Springer, N. Wu, and D. W. Marr, “Chain assembly kinetics from magnetic colloidal spheres”, Langmuir **38**, 5730–5737 (2022).

[235]F. Martinez-Pedrero, A. Cebers, and P. Tierno, “Orientational dynamics of colloidal ribbons self-assembled from microscopic magnetic ellipsoids”, Soft Matter **12**, 3688–3695 (2016).

[236]H. Massana-Cid, C. Maggi, G. Frangipane, and R. Di Leonardo, “Rectification and confinement of photokinetic bacteria in an optical feedback loop”, Nat. Commun. **13**, 2740 (2022).

[237]H. Massana-Cid, C. Maggi, N. Gnan, G. Frangipane, and R. Di Leonardo, “Multiple temperatures and melting of a colloidal active crystal”, Nat. Commun. **15**, 6574 (2024).

[238]M. Almonacid, W. W. Ahmed, M. Bussonnier, P. Mailly, T. Betz, R. Voituriez, N. S. Gov, and M.-H. Verlhac, “Active diffusion positions the nucleus in mouse oocytes”, Nat. Cell Biol. **17**, 470–479 (2015).

[239] B. Cadot, V. Gache, and E. R. Gomes, “Moving and positioning the nucleus in skeletal muscle–one step at a time”, Nucleus **6**, 373–381 (2015).

[240] T. P. Lele, R. B. Dickinson, and G. G. Gundersen, “Mechanical principles of nuclear shaping and positioning”, J. Cell Biol. **217**, 3330–3342 (2018).

[241] A. Kirillova and L. Ionov, “Shape-changing polymers for biomedical applications”, J. Mater. Chem. B **7**, 1597–1624 (2019).

[242] A. S. Hoffman, “Stimuli-responsive polymers: biomedical applications and challenges for clinical translation”, Adv. Drug Deliv. Rev. **65**, 10–16 (2013).

[243] B. Jeong and A. Gutowska, “Lessons from nature: stimuli-responsive polymers and their biomedical applications”, Trends Biotechnol. **20**, 305–311 (2002).

[244] D. Mukherji, C. M. Marques, and K. Kremer, “Smart responsive polymers: fundamentals and design principles”, Annu. Rev. Condens. Matter Phys. **11**, 271–299 (2020).

[245] M. R. Aguilar and J. San Román, *Smart polymers and their applications* (Woodhead Publishing, 2019).

[246] I. Y. Galaev and B. Mattiasson, “‘Smart’ polymers and what they could do in biotechnology and medicine”, Trends Biotechnol. **17**, 335–340 (1999).

[247] A. Kumar, A. Srivastava, I. Y. Galaev, and B. Mattiasson, “Smart polymers: physical forms and bioengineering applications”, Prog. Polym. Sci. **32**, 1205–1237 (2007).

[248] C. P. Brangwynne, P. Tompa, and R. V. Pappu, “Polymer physics of intracellular phase transitions”, Nat. Phys. **11**, 899–904 (2015).

[249] F. C. MacKintosh, J. Käs, and P. A. Janmey, “Elasticity of semiflexible biopolymer networks”, Phys. Rev. Lett. **75**, 4425–4428 (1995).

[250] F. Tanaka, T. Koga, and F. M. Winnik, “Temperature-responsive polymers in mixed solvents: competitive hydrogen bonds cause cononsolvency”, Phys. Rev. Lett. **101**, 028302 (2008).

[251] J.-L. Viovy, “Electrophoresis of DNA and other polyelectrolytes: physical mechanisms”, Rev. Mod. Phys. **72**, 813–872 (2000).

[252] A. M. Chiariello, C. Annunziatella, S. Bianco, A. Esposito, and M. Nicodemi, “Polymer physics of chromosome large-scale 3D organisation”, Sci. Rep. **6**, 29775 (2016).

[253] Q. Wen and P. A. Janmey, “Polymer physics of the cytoskeleton”, Curr. Opin. Solid State Mater. Sci. **15**, 177–182 (2011).

[254] P. De Gennes, “Conformation of a polymer chain in certain mixed solvents”, J. Physique Lett. **37**, 59–61 (1976).

[255] F. Brochard and P. D. Gennes, “Collapse of one polymer coil in a mixture of solvents”, Ferroelectrics **30**, 33–47 (1980).

[256] J. J. Magda, G. H. Fredrickson, R. G. Larson, and E. Helfand, “Dimensions of a polymer chain in a mixed solvent”, Macromolecules **21**, 726–732 (1988).

[257] D. Mukherji, C. M. Marques, and K. Kremer, “Polymer collapse in miscible good solvents is a generic phenomenon driven by preferential adsorption”, Nat. Commun. **5**, 4882 (2014).

[258] X. Zheng, M. A. Anisimov, J. V. Sengers, and M. He, “Unusual transformation of polymer coils in a mixed solvent close to the critical point”, Phys. Rev. Lett. **121**, 207802 (2018).

[259] P. Venkatesu, “Polymer modifies the critical region of the coexisting liquid phases”, J. Phys. Chem. B **110**, 17339–17346 (2006).

[260] T. Araki, “Conformational changes of polyelectrolyte chains in solvent mixtures”, Soft Matter **12**, 6111–6119 (2016).

[261] K. To, C. A. Kim, and H. J. Choi, “Abnormal scattering of polymer in binary solvent”, Physica A **254**, 292–299 (1998).

[262] T. Vilgis, A. Sans, and G. Jannink, “Conformation of a polymer chain dissolved in a critical fluid”, J. Phys. II France **3**, 1779–1786 (1993).

[263] A. Dua and B. J. Cherayil, “Polymer collapse in supercritical solvents”, J. Chem. Phys. **111**, 3274–3277 (1999).

[264] S. F. Edwards and P. Singh, “Size of a polymer molecule in solution. Part 1.—Excluded volume problem”, J. Chem. Soc. Farad. T. 2 **75**, 1001–1019 (1979).

[265] M. Stapper and T. A. Vilgis, “Behavior of a polymer chain in a critical binary solvent”, EPL **42**, 7 (1998).

[266] A. Negadi, A. Sans-Pennincks, M. Benmouna, and T. A. Vilgis, “Mean-field-theory for polymers in mixed solvents. thermodynamic and structural properties”, Macromol. Theor. Simul. **8**, 285–295 (1999).

[267] A. Negadi, T. A. Vilgis, and M. Benmouna, “Dynamic relaxations of polymers in mixed solvents”, Macromol. Theor. Simul. **9**, 628–640 (2000).

[268] V. V. Vasilevskaya, P. G. Khalatur, and A. R. Khokhlov, “Conformation of a polymer chain near the solvent critical region. II. Monte Carlo simulation”, J. Chem. Phys. **109**, 5119–5125 (1998).

[269] T. Sumi, N. Imazaki, and H. Sekino, “Critical Casimir effect in a polymer chain in supercritical solvents”, Phys. Rev. E **79**, 030801 (2009).

[270] W. Theobald, A. Sans-Penninckx, G. Meier, and T. A. Vilgis, “Evidence for chain shrinkage in binary polymer blends: light scattering experiments and theory”, Phys. Rev. E **55**, 5723 (1997).

[271]K. To and H. J. Choi, “Polymer conformation near the critical point of a binary mixture”, Phys. Rev. Lett. **80**, 536 (1998).

[272]L. He, G. Cheng, and Y. B. Melnichenko, “Partial collapse and reswelling of a polymer in the critical demixing region of good solvents”, Phys. Rev. Lett. **109**, 067801 (2012).

[273]J.-B. Fournier, “Field-mediated interactions of passive and conformation-active particles: multibody and retardation effects”, Soft Matter **18**, 2634–2645 (2022).

[274]S. Dietrich, “Critical Casimir forces in soft matter”, Soft Matter **20**, 3212–3242 (2024).

[275]V. Démery, O. Bénichou, and H. Jacquin, “Generalized Langevin equations for a driven tracer in dense soft colloids: construction and applications”, New J. Phys. **16**, 053032 (2014).

[276]I. Di Terlizzi, F. Ritort, and M. Baiesi, “Explicit solution of the generalised Langevin equation”, J. Stat. Phys. **181**, 1609 (2020).

[277]T. E. Hull and C. Froese, “Asymptotic behaviour of the inverse of a Laplace transform”, Canadian J. Math. **7**, 116–125 (1955).

[278]M. Rubinstein and R. H. Colby, *Polymer physics* (Oxford University Press, 2003).

[279]P.-G. De Gennes, *Scaling concepts in polymer physics* (Cornell University Press, 1979).

[280]M. Gross, “Dynamics and steady states of a tracer particle in a confined critical fluid”, J. Stat. Mech. **2021**, 063209 (2021).

[281]F. Höfling and T. Franosch, “Anomalous transport in the crowded world of biological cells”, Rep. Prog. Phys. **76**, 046602 (2013).

[282]S. Ramadurai, A. Holt, V. Krasnikov, G. van den Bogaart, J. A. Killian, and B. Poolman, “Lateral diffusion of membrane proteins”, J. Am. Chem. Soc. **131**, 12650–12656 (2009).

[283]C. N. Likos, “Effective interactions in soft condensed matter physics”, Phys. Rep. **348**, 267–439 (2001).

[284]D. Vlassopoulos and M. Cloitre, “Tunable rheology of dense soft deformable colloids”, Curr. Opin. Colloid Interface Sci. **19**, 561–574 (2014).

[285]C. N. Likos, H. Löwen, M. Watzlawek, B. Abbas, O. Jucknischke, J. Allgaier, and D. Richter, “Star polymers viewed as ultrasoft colloidal particles”, Phys. Rev. Lett. **80**, 4450–4453 (1998).

[286]J. Buitenhuis and S. Förster, “Block copolymer micelles: viscoelasticity and interaction potential of soft spheres”, J. Chem. Phys. **107**, 262–272 (1997).

[287]M. J. Bergman, N. Gnan, M. Obiols-Rabasa, J.-M. Meijer, L. Rovigatti, E. Zaccarelli, and P. Schurtenberger, “A new look at effective interactions between microgel particles”, Nat. Commun. **9**, 5039 (2018).

[288]D. Heyes and A. Brańka, “Interactions between microgel particles”, Soft Matter **5**, 2681–2685 (2009).

[289]F. H. Stillinger, “Phase transitions in the Gaussian core system”, J. Chem. Phys. **65**, 3968–3974 (1976).

[290]F. H. Stillinger and T. A. Weber, “Study of melting and freezing in the Gaussian core model by molecular dynamics simulation”, J. Chem. Phys. **68**, 3837–3844 (1978).

[291]F. H. Stillinger and T. A. Weber, “Lindemann melting criterion and the Gaussian core model”, Phys. Rev. B **22**, 3790 (1980).

[292]P. J. Flory and W. R. Krigbaum, “Statistical mechanics of dilute polymer solutions. II”, J. Chem. Phys **18**, 1086–1094 (1950).

[293]A. A. Louis, R. Finken, and J.-P. Hansen, “The structure of colloid-polymer mixtures”, EPL **46**, 741 (1999).

[294]A. Lang, C. N. Likos, M. Watzlawek, and H. Löwen, “Fluid and solid phases of the Gaussian core model”, J. Phys. Condens. Matter **12**, 5087 (2000).

[295]C. N. Likos, A. Lang, M. Watzlawek, and H. Löwen, “Criterion for determining clustering versus reentrant melting behavior for bounded interaction potentials”, Phys. Rev. E **63**, 031206 (2001).

[296]P. G. Bolhuis, A. A. Louis, J. P. Hansen, and E. J. Meijer, “Accurate effective pair potentials for polymer solutions”, J. Chem. Phys **114**, 4296–4311 (2001).

[297]A. A. Louis, P. G. Bolhuis, J. P. Hansen, and E. J. Meijer, “Can polymer coils be modeled as “soft colloids”?”, Phys. Rev. Lett. **85**, 2522–2525 (2000).

[298]C. N. Likos, M. Schmidt, H. Löwen, M. Ballauff, D. Pötschke, and P. Lindner, “Soft interaction between dissolved flexible dendrimers: theory and experiment”, Macromolecules **34**, 2914–2920 (2001).

[299]P. Mausbach and H.-O. May, “Static and dynamic anomalies in the Gaussian core model liquid”, Fluid Ph. Equilibria **249**, 17–23 (2006).

[300]P. Mausbach and H.-O. May, “Transport anomalies in the Gaussian core model fluid”, Z. Phys. Chem. **223**, 1035–1046 (2009).

[301]L. A. Shall and S. A. Egorov, “Structural and dynamical anomalies of a Gaussian core fluid: A mode-coupling theory study”, J. Chem. Phys. **132**, 184504 (2010).

[302]W. P. Krekelberg, T. Kumar, J. Mittal, J. R. Errington, and T. M. Truskett, “Anomalous structure and dynamics of the Gaussian-core fluid”, Phys. Rev. E **79**, 031203 (2009).

[303] C. Speranza, S. Prestipino, and P. V. Giaquinta, "Thermodynamic and structural anomalies of the Gaussian-core model in one dimension", Mol. Phys. **109**, 3001–3013 (2011).

[304] F. H. Stillinger and D. K. Stillinger, "Negative thermal expansion in the Gaussian core model", Physica A **244**, 358–369 (1997).

[305] V. Sposini, C. N. Likos, and M. Camargo, "Glassy phases of the Gaussian core model", Soft Matter **19**, 9531–9540 (2023).

[306] S. Hanna, W. Hess, and R. Klein, "Self-diffusion of spherical Brownian particles with hard-core interaction", Physica A **111**, 181–199 (1982).

[307] A. Imhof and J. K. G. Dhont, "Long-time self-diffusion in binary colloidal hard-sphere dispersions", Phys. Rev. E **52**, 6344 (1995).

[308] B. U. Felderhof and R. B. Jones, "Cluster expansion of the diffusion kernel of a suspension of interacting Brownian particles", Phys. A: Stat. Mech. Appl. **121**, 329–344 (1983).

[309] H. Löwen and G. Szamel, "Long-time self-diffusion coefficient in colloidal suspensions: theory versus simulation", J. Phys. Condens. Matter **5**, 2295 (1993).

[310] J. Kushick and B. J. Berne, "Role of attractive forces in self-diffusion in dense Lennard-Jones fluids", J. Chem. Phys. **59**, 3732–3736 (1973).

[311] S. D. Bembenek and G. Szamel, "The role of attractive interactions in self-diffusion", J. Phys. Chem. B **104**, 10647–10652 (2000).

[312] T. Yamaguchi, N. Matubayasi, and M. Nakahara, "A mode-coupling approach to the attractive interaction effect on the solute diffusion in liquids", J. Chem. Phys. **115**, 422–432 (2001).

[313] K. F. Seefeldt and M. J. Solomon, "Self-diffusion in dilute colloidal suspensions with attractive potential interactions", Phys. Rev. E **67**, 050402 (2003).

[314] H. H. Wensink, H. Löwen, M. Rex, C. N. Likos, and S. van Teeffelen, "Long-time self-diffusion for Brownian Gaussian-core particles", Comp. Phys. Commun. **179**, 77–81 (2008).

[315] A. Benois, M. Jardat, V. Dahirel, V. Démery, J. Agudo-Canalejo, R. Golestanian, and P. Illien, "Enhanced diffusion of tracer particles in nonreciprocal mixtures", Phys. Rev. E **108**, 054606 (2023).

[316] M. Jardat, V. Dahirel, and P. Illien, "Diffusion of a tracer in a dense mixture of soft particles connected to different thermostats", Phys. Rev. E **106**, 064608 (2022).

[317] M. Fruchart, C. Scheibner, and V. Vitelli, "Odd viscosity and odd elasticity", Annu. Rev. Condens. Matter Phys. **14**, 471–510 (2023).

[318] H.-M. Chun, X. Durang, and J. D. Noh, “Emergence of nonwhite noise in Langevin dynamics with magnetic Lorentz force”, Phys. Rev. E **97**, 032117 (2018).

[319] A. Langer, A. Sharma, R. Metzler, and E. Kalz, “The dance of odd-diffusive particles: a Fourier approach”, preprint arXiv:2407.13290 (2024).

[320] E. Kalz, H. D. Vuijk, J.-U. Sommer, R. Metzler, and A. Sharma, “Oscillatory force autocorrelations in equilibrium odd-diffusive systems”, Phys. Rev. Lett **132**, 057102 (2024).

[321] F. Ghimenti, L. Berthier, G. Szamel, and F. van Wijland, “Irreversible Boltzmann samplers in dense liquids: weak-coupling approximation and mode-coupling theory”, preprint arXiv:2404.14863 (2024).

[322] F. Ghimenti, L. Berthier, G. Szamel, and F. van Wijland, “Sampling efficiency of transverse forces in dense liquids”, Phys. Rev. Lett. **131**, 257101 (2023).

[323] D. Schick, M. Weißenhofer, L. Rózsa, J. Rothörl, P. Virnau, and U. Nowak, “Two levels of topology in skyrmion lattice dynamics”, Phys. Rev. Res. **6**, 013097 (2024).

[324] A. Poncet, O. Bénichou, V. Démery, and G. Oshanin, “Universal long ranged correlations in driven binary mixtures”, Phys. Rev. Lett. **118**, 118002 (2017).

[325] V. Démery and A. Gambassi, “Non-Gaussian fluctuations of a probe coupled to a Gaussian field”, Phys. Rev. E **108**, 044604 (2023).

[326] T. Nakamura and A. Yoshimori, “Derivation of the nonlinear fluctuating hydrodynamic equation from the underdamped Langevin equation”, J. Phys. A: Math. Theo. **42**, 065001 (2009).

[327] M. A. Durán-Olivencia, P. Yatsyshin, B. D. Goddard, and S. Kalliadasis, “General framework for fluctuating dynamic density functional theory”, New J. Phys. **19**, 123022 (2017).

[328] A. J. Archer and R. Evans, “Binary Gaussian core model: fluid-fluid phase separation and interfacial properties”, Phys. Rev. E **64**, 041501 (2001).

[329] A. A. Louis, P. G. Bolhuis, and J. P. Hansen, “Mean-field fluid behavior of the Gaussian core model”, Phys. Rev. E **62**, 7961 (2000).

[330] C. Hargus, K. Klymko, J. M. Epstein, and K. K. Mandadapu, “Time reversal symmetry breaking and odd viscosity in active fluids: green–kubo and nemd results”, J. Chem. Phys. **152**, 201102 (2020).

[331] C. Duclut, S. Bo, R. Lier, J. Armas, P. Surówka, and F. Jülicher, “Probe particles in odd active viscoelastic fluids: How activity and dissipation determine linear stability”, Phys. Rev. E **109**, 044126 (2024).

[332] I. Abdoli and A. Sharma, "Stochastic resetting of active Brownian particles with Lorentz force", Soft Matter **17**, 1307–1316 (2021).

[333] M. Abramowitz, I. A. Stegun, and R. H. Romer, *Handbook of mathematical functions with formulas, graphs, and mathematical tables* (American Association of Physics Teachers, 1988).

[334] P. M. Chaikin, T. C. Lubensky, and T. A. Witten, *Principles of condensed matter physics* (Cambridge University Press, 1995).

[335] J. D. Weeks, D. Chandler, and H. C. Andersen, "Role of Repulsive Forces in Determining the Equilibrium Structure of Simple Liquids", J.Chem. Phys. **54**, 5237–5247 (1971).

[336] H. R. Warner Jr, "Kinetic theory and rheology of dilute suspensions of finitely extendible dumbbells", Ind. Eng. Chem. Res. **11**, 379–387 (1972).

[337] Y. He, S. Burov, R. Metzler, and E. Barkai, "Random time-scale invariant diffusion and transport coefficients", Phys. Rev. Lett **101**, 058101 (2008).

[338] S. Burov, J.-H. Jeon, R. Metzler, and E. Barkai, "Single particle tracking in systems showing anomalous diffusion: the role of weak ergodicity breaking", Phys. Chem. Chem. Phys. **13**, 1800–1812 (2011).